Development, characterization and modeling of interfaces for high efficiency silicon heterojunction solar cells

vorgelegt von
Diplom-Physiker
Renaud Varache
aus Clermont-Ferrand (Frankreich)

Von der Fakultät IV - Elektrotechnik und Informatik
der Technischen Universität Berlin
zur Erlangung des akademischen Grades

Doktor der Naturwissenschaften
- Dr. rer. nat. –

genehmigte Dissertation

Promotionsausschuss:

Vorsitzender:	Prof. Frédéric Aniel	Gutachter:	Prof. Bernd Rech
Gutachter:	Prof. Bernd Szyszka	Zusätzl. Miglied:	Dr. Jean-Paul Kleider
Gutachter:	Dr. Ivan Gordon	Zusätzl. Miglied:	Dr. Lars Korte
Gutachter:	Dr. Stefaan de Wolf	Zusätzl. Miglied:	Dr. Marie-Estelle Gueunier-Farret

Tag der wissenschaftlichen Aussprache: 20. November 2012

Berlin 2013

D83

Development, characterization and modeling of interfaces for high efficiency silicon heterojunction solar cells

Renaud VARACHE

November 2012

A dissertation submitted to the University Paris 11
and to the Technical University of Berlin
in partial fulfilment of the requirements
for the degree of Doctor of Philosophy

Thesis comittee:

Prof. Frédéric Aniel (IEF - Univ. Paris-Sud 11)
Prof. Bernd Szyszka (Technical Univ. Berlin)
Prof. Bernd Rech (HZB - Technical Univ. Berlin; supervisor)
Dr. Jean-Paul Kleider (LGEP - CNRS; supervisor)
Dr. Stefaan De Wolf (EPFL - PVLab)
Dr. Ivan Gordon (IMEC)
Dr. Lars Korte (HZB)
Dr. Marie-Estelle Gueunier-Farret (LGEP - Univ. Paris-Sud 11)

UNIVERSITE PARIS-SUD

ÉCOLE DOCTORALE : STITS
Laboratoire de Génie Electrique de Paris/Helmholtz Zentrum Berlin

***DISCIPLINE** PHYSIQUE*

THÈSE DE DOCTORAT

soutenue le 20/11/2012

par

Renaud VARACHE

Développement, caractérisation et modélisation d'interfaces pour cellules solaires à haut rendement à base d'hétérojonctions de silicium

Directeur de thèse :	Jean-Paul KLEIDER	Directeur de recherche CNRS (LGEP)
Co-directeur de thèse :	Bernd RECH	Professeur (TU Berlin - HZB)

Composition du jury :

Président du jury :	Frédéric ANIEL	Professeur (UPS - IEF)
Rapporteurs :	Ivan GORDON	Chef de projets (IMEC)
	Stefaan DE WOLF	Chef de projets (EPFL - PVLab)
Examinateurs :	Jean-Paul KLEIDER	Directeur de recherche CNRS (LGEP)
	Bernd RECH	Professeur (TU Berlin - HZB)
	Bernd SZYSZKA	Professeur (TU Berlin - HZB)
	Marie-Estelle GUEUNIER-FARRET	Maître de conférence (UPS – LGEP)
	Lars KORTE	Chef de projets (HZB)

Abstract

The interface between amorphous silicon (*a*-Si:H) and crystalline silicon (*c*-Si) is the building block of high efficiency solar cells based on low temperature fabrication processes. Three properties of the interface determine the performance of silicon heterojunction solar cells: band offsets between *a*-Si:H and *c*-Si, interface defects and band bending in *c*-Si. These three points are addressed in this thesis.

First, an analytical model for the calculation of the band bending in *c*-Si is developed. It assumes a constant density of states (DOS) in the *a*-Si:H band gap. The influence of most parameters of the structure on the band bending is studied: band offsets, DOS in *a*-Si:H, interface defects, etc. The presence of quantum confinement at the interface is discussed. Analytical calculations and temperature dependent planar conductance measurements are compared such that the band offsets on both (p)*a*-Si:H/(n)*c*-Si and (n)*a*-Si:H/(p)*c*-Si can be estimated: the valence band offset amounts 0.36 eV while the conduction band offset is 0.15 eV. In addition, it is shown that the valence band offset is independent of temperature whereas the conduction band offset follows the evolutions of *c*-Si and *a*-Si:H band gaps with temperature. A discussion of these results in the frame of the branch point theory for band line-up leads to the conclusion that the branch point in *a*-Si:H is independent of the doping. Then, analytical calculations are developed further to take into account the real solar cell structure where the *a*-Si:H/*c*-Si structure is in contact with a transparent conductive oxide and an undoped buffer layer is present at the interface. Measurements of the planar conductance and of the interface passivation quality are interpreted in the light of analytical calculations and numerical simulations to open a way towards a method for the optimization of silicon heterojunction solar cells. It is particularly shown that a trade-off has to be found between a good passivation quality and a significant band bending. This can be realized by tuning the buffer layer properties (thickness, doping), the TCO-contact (high work function) and the emitter (defect density and thickness). Interestingly, an emitter with a high DOS leads to better cell performances.

Finally, a new type of interface has been developed, that was not applied to heterojunction solar cells so far. The *c*-Si surface has been oxidized in deionized water at 80 °C before the (p)*a*-Si:H emitter deposition such that (p)*a*-Si:H/SiO_2/(n)*c*-Si structures were obtained. A tunneling current model has been developed, implemented in the 1D numerical device simulator AFORS-HET and used to study the effect of a wide band gap interfacial layer (as it is the case for SiO_2) on cell performance: the fill-factor and the short-circuit current are dramatically reduced for thick and high barriers. However, a SiO_2 layer has only little impact on optical properties. Fabricated samples show a passivation quality halfway between samples with no buffer layer and with an (i)*a*-Si:H buffer layer: this is explained by the presence of a negative fixed charge in the oxide. The band bending in (n)*c*-Si is higher with an oxide layer than with an (i)*a*-Si:H buffer layer. Solar cells demonstrate that this new concept has the potential to achieve high power conversion efficiencies: for non-optimized structures, an open-circuit voltage higher than 650 mV has been demonstrated, while the oxide does not seem to create a barrier to charge transport.

Résumé

L'interface entre le silicium amorphe (*a*-Si :H) et le silicium cristallin (*c*-Si) est un constituent clés de cellules solaires à haut rendement reposant sur des procédés à basse température. Trois propriétés de l'interface déterminent le rendement des cellules solaires à hétérojonction de silicium : les décalages de bandes entre *a*-Si :H et *c*-Si, les défauts d'interface et la courbure de bande dans *c*-Si. Ces trois aspects sont traités dans ces travaux de thèse.

Dans un premier temps, un calcul analytique de la courbure de bande dans *c*-Si est développé. Il repose sur l'approximation d'une densité d'états (DE) constante dans la bande interdite de *a*-Si :H. L'influence des principaux paramêtres de la structure sur la courbure de bande est étudiée : décalage de bande, densité d'états dans *a*-Si :H, défauts d'interface, etc. La présence d'un effet de confinement quantique est discutée. Grâce à une comparaison entre ces calculs et des mesures de conductance planaire en fonction de la température sur des structures (p)*a*-Si :H/(n)*c*-Si et (n)*a*-Si :H/(p)*c*-Si, les décalages de bande de valence et de conduction ont pu être estimés à 0.36 eV et 0.15 eV respectivement. En outre, il est montré que le décalage de la bande de valence est indépendant de la température, alors que le décalage de la bande de conduction suit les évolutions des bandes interdites de *c*-Si et *a*-Si :H. Ces mesures tendent à prouver que le 'branch point' dans *a*-Si :H est indépendant du dopage.

Ensuite, les calculs analytiques sont approfondis pour prendre en compte différents aspects de la structure complète incorporée dans les cellules : contact avec un oxyde transparent conducteur, présence d'une couche d'*a*-Si :H non-dopée à l'interface. Grâce à des mesures de conductance planaire conjuguées à des mesures de la qualité de passivation de l'interface, et à l'aide de simulations numériques, des pistes pour optimiser les cellules à hétérojonction sont commentées. En particulier, il est montré qu'un optimum doit être trouvé entre une bonne passivation et une courbure de bande suffisante. Ceci peut être accompli par un réglage fin des propriétés de la couche tampon (épaisseur, dopage), du contact (travail de sortie élevé) et de l'émetteur (p)*a*-Si :H (densité de défauts et épaisseur). En particulier, un émetteur avec une DE importante peut conduire paradoxalement à de meilleures performances.

Enfin, un nouveau type d'interface a été développé. La surface de *c*-Si a été oxydée volontairement dans de l'eau pure dé-ionisée à 80 °C avant le dépôt de (p)*a*-Si :H afin d'obtenir une structure (p)*a*-Si :H/SiO_2/(n)*c*-Si. A l'aide d'un modèle de courant par effet tunnel implémenté dans le logiciel de simulation numérique AFORS-HET, l'effet d'une couche à grande bande interdite (comme c'est le cas pour SiO_2) sur les performances de cellules est étudié : le facteur de forme et le courant de court-circuit sont extrêmement réduits. En revanche, une couche de SiO_2 n'a que peu d'impact sur les propriétés optiques de la structure. Expérimentalement, les échantillons réalisés montrent une qualité de passivation à mi-chemin entre le cas sans couche tampon et le cas avec (i)*a*-Si :H : ceci est expliqué par la présence d'une charge fixe négative dans l'oxyde. La courbure de bande dans *c*-Si est moins affectée par la présence d'une couche d'oxyde que d'une couche de (i)*a*-Si :H. Les cellules solaires réalisées démontrent que le concept a le potentiel d'aboutir à de hauts rendements : sur des structures non-optimisées, une tension de circuit ouvert supérieure à 650 mV a été démontrée, alors que l'oxyde ne semble pas limiter le transport de charge.

Zusammenfassung

Die elektronische Qualität der Grenzfläche zwischen amorphem und kristallinem Silizium ist der entscheidende Baustein von amorph-kristallinen Wafer-Solarzellen mit hohen Wirkungsgraden, die bei niedrigen Temperaturen hergestellt werden. Drei Eigenschaften der Grenzfläche bestimmen die Energiewandeleffizienz der Silizium-Heteroübergang-Solarzellen: der Sprung (offset) in den Bandkanten *a*-Si:H und *c*-Si, Grenzflächen-Defekte und die Band-Verbiegung im *c*-Si. Diese drei Aspekte bilden den Schwerpunkt dieser Arbeit.
Zunächst wird ein analytisches Modell entwickelt, das die Band-Verbiegung in *c*-Si berechnet. Die Zustandsdichte-Verteilung (ZDV) in der *a*-Si:H Band-Lücke wird als konstant angenommen. Der Einfluss folgender Struktur-Eigenschaften auf die Bandverbiegung wird untersucht: Band-Verschiebung, ZDV im *a*-Si:H, Grenzflächen-Defekte, etc. Der Effekt des quantenmechanischen Confinements an der Grenzfläche wird diskutiert. Analytische Berechnungen werden mit temperaturabhängigen Messungen der planaren Leitfähigkeit verglichen. Hieraus lassen sich die Sprünge der Valenz- bzw. Leitungsband-Kanten mittels Untersuchungen an (p)*a*-Si:H/(n)*c*-Si bzw. (n)*a*-Si:H/(p)*c*-Si Strukturen bestimmen: Werte von 0.36 eV bzw. 0.15 eV wurden gemessen. Die Valenzband-Offset ist temperaturunabhängig, während der Leitungsband-Offset den Bandlücken-Variationen folgt. Es wird gefunden, dass der Ladungsneutralpunkt (branch point) in *a*-Si:H unabhängig von der Dotierung ist.
Anschliessend wird das analytische Modell verbessert, um zwei Aspekte der Solarzellen-Struktur besser zu simulieren: den Kontakt mit einem transparenten leitfähigen Oxid und die Anwesenheit einer ultra-dünnen intrinsischen *a*-Si:H Pufferschicht. Messungen der planaren Leitfähigkeit werden durch Berechnungen der Bandverbiegung mit diesem verbesserten Modell ausgewertet. Es wird gezeigt, dass ein Mittelweg zwischen einer guten Passivierung und einer hohen Band-Verbiegung gesucht werden muss. Das kann durch die Optimierung der Pufferschicht-Eigenschaften (Dicke, Dotierung), des leitfähigen Oxids (hohe Austrittsarbeit) und des (p)*a*-Si:H Emitters (Dicke und ZDV) bewerkstelligt werden. Insbesondere kann eine hohe Zustandsdichte im Emitter positiv für die Zellen sein.
Schließlich wurde eine Präparationsmethode für ultradünne Tunneloxide entwickelt,die für Heteroübergang Solarzellen benutzt wurde. Die *c*-Si Oberfläche wurde in deionisierten 80 °C warmen Wasser oxidiert und darauf mittels PECVD eine dotierte *a*-Si:H-Schicht deponiert: dadurch wird eine (p)*a*-Si:H/SiO_2/(n)*c*-Si Struktur hergestellt. Ein Tunnelstrom-Modell wurde entwickelt, in der Simulations-Software AFORS-HET implementiert und benutzt, um den Einfluss einer Grenzflächen-Barriere auf den Stromtransport in Solarzellen zu bestimmen. Für dicke und hohe Barrieren wird der Strom drastisch reduziert. Allerdings hat das Oxid keinen negativen Einfluss auf das optische Verhalten. Experimentell wird gefunden, dass oxidierte Proben eine bessere Passivierungs-Qualität zeigen als Proben ohne Pufferschicht. Dieser Befund wird durch eine höhere negative Festladung erklärt. In den oxidierten Proben ist die Band-Verbiegung höher als in Proben mit einer (i)*a*-Si:H Pufferschicht. Solarzellen wiesen nach, dass das neue Konzept das Potenzial hat, hohe Wirkungsgrade zu erreichen: bei un-optimierten Proben wurde eine Leerlauf-Spannung von mehr als 650 mV gezeigt, der Füllfaktor der Zellen zeigt, dass das Oxid keine Barriere für den Ladungstransport bildet.

For my part, I travel not to go anywhere, but to go.
I travel for travel's sake.
The great affair is to move; to feel the needs
and hitches of our life more nearly;
to come down off this feather-bed of civilisation,
and find the globe granite underfoot and strewn with cutting flints.

Quant à moi, je voyage non pour aller quelque part,
mais pour marcher. Je voyage pour le plaisir de voyager.
L'important est de bouger, d'éprouver de plus près
les nécessités et les embarras de la vie,
de quitter le lit douillet de la civilisation,
de sentir sous mes pieds le granit terrestre et les silex épars avec leurs coupants.

Travels with a Donkey in the Cevennes
Voyages avec un âne dans les Cévennes
Robert Louis Stevenson, born on 13th of November 1850 in Edinburgh, Scotland.

A mes parents...

Contents

Contents xv

List of symbols and abbreviations xix

Introduction 1

1 Basics of the amorphous silicon/crystalline silicon heterojunction 5
1.1 Materials properties . . . 6
1.1.1 Mono-crystalline silicon for photovoltaic applications . . . 6
1.1.1.1 Basic properties . . . 6
1.1.1.2 Charge generation and recombination mechanisms in *c*-Si . . . 7
1.1.2 Hydrogenated amorphous silicon . . . 10
1.1.2.1 Basic properties . . . 10
1.1.2.2 Bulk defects and recombination in *a*-Si:H . . . 11
1.2 The amorphous silicon/crystalline silicon interface . . . 14
1.2.1 Band offsets . . . 14
1.2.1.1 Experimental determination of band offsets . . . 14
1.2.1.2 Theoretical predictions . . . 15
1.2.2 Interface defects and recombination . . . 18
1.2.3 Band bending in *c*-Si and inversion layer . . . 20
1.2.3.1 Origin of the band bending in *c*-Si . . . 20
1.2.3.2 Inversion layer: the (p)*c*-Si/(n)*c*-Si induced diode . . . 22
1.3 Summary and conclusions . . . 22

2 Samples preparation & characterization and modeling tools 25
2.1 Amorphous silicon/crystalline silicon heterojunction preparation . . . 26
2.1.1 Preparation of the *c*-Si surface . . . 26

2.1.2 *a*-Si:H deposition . . . 27
2.1.3 Formation of electrical contacts . . . 28
2.2 Characterization techniques . . . 29
2.2.1 Band bending measurement . . . 29
2.2.1.1 Surface photo-voltage: SPV . . . 30
2.2.1.2 Planar conductance: focus on the rectifying *a*-Si:H/*c*-Si heterojunction . . . 35
2.2.2 Interface defect probing . . . 37
2.2.2.1 Voltage dependent surface photo-voltage . . . 37
2.2.2.2 Photo-conductance decay . . . 38
2.2.2.3 Modulated Photo-luminescence . . . 40
2.2.2.4 First measurement examples and comparison . . . 42
2.2.3 Assessing solar cell performance: current-voltage characteristics and spectral response . . . 45
2.2.3.1 Current-voltage characteristics . . . 45
2.2.3.2 Quantum efficiency . . . 46
2.3 Simulation tool: AFORS-HET . . . 47
2.3.1 Generalities . . . 47
2.3.2 Bulk materials modeling . . . 47
2.3.3 Interface modeling . . . 49
2.3.4 AFORS-HET development . . . 50
2.3.5 Standard cell structures for simulations . . . 51
2.4 Chapter conclusion . . . 52

3 Determination of the band offsets at the amorphous silicon/crystalline silicon heterocontact 53
3.1 Analytical calculations of the band bending in *c*-Si . . . 54
3.1.1 Equilibrium band diagram . . . 54
3.1.2 Calculation of the charge components: Q_{c-Si}, $Q_{a-Si:H}$ and Q_{int} . . . 56
3.1.2.1 Charge in *c*-Si: Q_{c-Si} . . . 56
3.1.2.2 Charge in *a*-Si:H: $Q_{a-Si:H}$ . . . 61
3.1.2.3 Charge in interface defects: Q_{int} . . . 63
3.1.3 Solution of the charge neutrality equation . . . 64
3.1.4 Validation with AFORS-HET . . . 67
3.1.5 Hole sheet density: band bending and temperature dependence . . . 69
3.1.5.1 Hole sheet density and band bending . . . 69
3.1.5.2 Hole sheet density and temperature dependence . . . 71
3.1.6 Dependence of P_s on key parameters . . . 72
3.1.7 Quantum confinement at the *a*-Si:H/*c*-Si interface . . . 74
3.2 Experiments and extraction of band offsets . . . 77
3.2.1 Temperature dependent planar conductance measurement analysis . . . 77

3.2.2 Qualitative analysis: temperature dependence of band offsets 79
3.2.3 Quantitative analysis: extraction of band offsets 82
3.3 Comparison with modern band line-up theories 86
3.3.1 Review on dipoles at the *a*-Si:H/*c*-Si interface 86
3.3.2 The branch point in *a*-Si:H 87
3.4 Chapter conclusion 89

4 Simulation-based guidelines to open-circuit voltage maximization in *a*-Si:H/*c*-Si solar cells 91
4.1 Band bending and open circuit voltage 92
4.2 Analytical calculations of φ_{c-Si}: influence of thin *a*-Si:H emitter and buffer layers 94
4.2.1 Calculation of the charge in a thin *a*-Si:H emitter layer 95
4.2.1.1 Neumann conditions 96
4.2.1.2 Dirichlet conditions 97
4.2.1.3 Charge at the *a*-Si:H surface 98
4.2.2 Calculation of the charge in an interfacial *a*-Si:H buffer layer 99
4.3 Interplay between thickness and density of states in the (p)*a*-Si:H emitter . . . 101
4.3.1 Experimental evidence of surface effects 101
4.3.2 Emitter density of states/thickness interplay 103
4.3.3 Beneficial high emitter density of states 105
4.4 Experiment: variation of the (i)*a*-Si:H thickness and doping in *a*-Si:H/*c*-Si solar cells 108
4.4.1 (i)*a*-Si:H thickness variations 109
4.4.2 Buffer layer doping variations 111
4.4.3 Discussion 111
4.5 Chapter conclusion 115

5 Oxidized crystalline silicon surfaces for silicon heterojunction solar cells 117
5.1 Motivation 118
5.2 Theoretical evaluation of the concept 119
5.2.1 Electrical behaviour: tunneling through a thin insulator layer 119
5.2.1.1 Introduction to tunneling 119
5.2.1.2 Tunneling model for the current 120
5.2.1.3 Implementation in AFORS-HET: the tunnel membrane 124
5.2.1.4 Influence of barrier parameters on transport properties 125
5.2.1.5 Limitations of the model 130
5.2.2 Optical behaviour 132
5.2.3 Short summary of preliminary results 134
5.3 Growth of ultra-thin oxide layers 134
5.3.1 Choice of the growth technique 134
5.3.2 Experimental details: revisiting *c*-Si surface preparation 135
5.3.2.1 Smoothing and water oxidation: brief state of the art 136

5.3.2.2 Preparation of *a*-Si:H/silicon oxide/*c*-Si heterojunctions 139
5.4 Experimental evaluation of the concept 140
5.4.1 Passivation quality 140
5.4.1.1 Density of states of oxidized *c*-Si surfaces 140
5.4.1.2 Emitter passivation quality 142
5.4.2 Equilibrium band diagram 144
5.5 Solar cells with oxide passivation layers 146
5.5.1 Cell performance 146
5.5.2 Device spectral response 149
5.6 Discussion 150
5.7 Chapter conclusion 151

Conclusion **152**

A Appendix A: Details on the analytical band bending calculation **157**
A.1 The (n)*a*-Si:H/(p)*c*-Si heterojunction case 157
A.2 Exponential DOS in *a*-Si:H 159

B Appendix B: Details on tunneling current calculation **161**
B.1 Tunneling probability 161
B.2 Supply function *N* 162
B.3 AFORS-HET configuration 163

Bibliography **182**

Acknowledgements **183**

Publications of the author **185**

Curriculum vitæ **187**

List of symbols and abbreviations

α_{np}	Absorption coefficient
α_{par}	'Parasitic' absorption coefficient
χ_{c-Si}, $\chi_{a-Si:H}$	*c*-Si, *a*-Si:H electron affinity
ΔE_c, ΔE_v	Conduction and valence band offset
Δn, Δp	Excess electron, hole concentration
Δn_0	Steady-state excess carrier concentration
Δn_ω	Complex amplitude of the modulated excess carrier concentration
Δp_{int}	Interface excess carrier density
ΔWF	Work function difference between TCO and *a*-Si:H
δ	Tunnel enhancement factor
δ^{c-Si}, $\delta^{a-Si:H}$	Bulk Fermi level position in *c*-Si, *a*-Si:H
Δ_{dip}	Interface dipoles potential drop
δ_{tun}, δ_{res}	Resonant and tunneling components of the tunnel factor
ϵ_0	Vacuum permittivity
ϵ_r	Relative dielectric constant
η	Power conversion efficiency

γ	Light incident angle
λ	Wavelength
$\mathscr{T}$	Tunnel barrier transparency
$\mathscr{T}_{\text{tun}}$, $\mathscr{T}_{\text{res}}$	Resonant and tunneling component of the tunnel barrier transparency
μ_n, μ_p	Electron, hole mobility
ω	Lock-in amplifier modulation frequency
ϕ	Phase shift
$\rho(x)$	Charge density
$\rho_{\text{trap}}(x,t)$	Charge density related to traps
σ_n, σ_p	Trap capture cross sections for electrons, holes
τ_i	Lifetime associated to recombination process i
τ_{bulk}	Effective bulk lifetime
$\tau_{\text{eff,PL}}$	Effective carrier lifetime deduced from photoluminescence measurements
$\tau_{\text{eff},d}$	Effective lifetime derivative
τ_{eff}	Effective lifetime
τ_{int} (or τ_{surf})	Interface (surface) carrier lifetime
θ	Heavyside's function
$\varphi_{c-Si,\text{ill}}$	Band bending in c-Si under illumination
φ_{c-Si}	Equilibrium band bending in c-Si
φ_{bp}^{X}	Branch point energy
ξ_{int}	Interface electric field
A	Absorbance
A_{ph}	Pinholes relative area
b	Ratio between electron and hole mobility values

B_{rad}	Radiative recombination coefficient
c	Speed of light in vacuum
C_{ox}	Mica capacitance
d	Electrode interspacing
$D(E_t)$	Monovalent defect distribution
D^+	Positively charged dangling bond level (no electron)
D^-	Negatively charged dangling bond level (2 electrons)
D^0	Neutral dangling bond level (one electron)
$d_{(i)a-Si:H}$	Thickness of the (i)a-Si:H buffer layer
$d_{a-Si:H}$	a-Si:H layer thickness
$D_{\text{it}}(E)$	Distribution of surface states
D_{max}	Maximum of the defect distribution
d_{ox}	Tunnel barrier thickness
E	Energy
E_a	Activation energy
E_c, E_v	Conduction, valence band edge
E_F	Fermi level
E_g^{c-Si}, $E_g^{a-Si:H}$	c-Si, a-Si:H band gap energies
E_t	Single defect energy level
$E_{\text{DB,max}}$	Maximum defect density position
E_{max}	Maximum energy for the tunneling regime
E_{min}	Minimum conduction band edge energy for tunneling
$E_{F,\text{int}}$	Interface Fermi level energy
$E_{F,n}$, $E_{F,p}$	Electron and hole quasi Fermi levels
E_{i1}, E_{i2}	Energy of level i

$EQE(\lambda)$, $IQE(\lambda)$	External, internal quantum efficiency at wavelength λ
$F(\lambda)$	External photon flux distribution
$f(E, E_F(x))$	Occupation function at the energy E and position x
$F_0(\lambda)$	Incident photon flux distribution
F^e_{depl}	Depletion term for the charge in c-Si
F^h_{inv}	Inversion term for the charge in c-Si
FF	Fill factor
G	Conductance
$G(\lambda)$	Generation rate
G_0	Generation rate steady state component
G_ω	Generation rate modulated component amplitude
G_{norm}	Normalized conductance
h	Planck's constant
J_0	Dark saturation current density
j_n, j_p	Electron, hole drift diffusion current density
$J_{e,\text{tun}}$	Tunneling electron current density
J_{sc}	Short circuit current density
k	Momentun quantum number
k_1, k_2, K	Wavevectors
k_B	Boltzmann's constant
l	Electrode length
L_D^{c-Si}, $L_D^{a-Si:H}$	Screening Debye length in c-Si and a-Si:H
m_1, m_2	light and heavy holes effective masses
M_e, M_h	Electron and hole tunneling effective masses in $\mathrm{SiO_2}$
n	Diode ideality factor

n, p	Electron, hole concentration
$N(E_F)$	Density of states in *a*-Si:H at Fermi level
N_0	Pre-exponential factor for band tail density of states
n_0, p_0	Equilibrium electron, hole concentration
N_A, N_D	Acceptor, donor dopant concentration
N_c, N_v	Conduction, valence band effective density of states
$N_d(E)$, $N_a(E)$ and $N(E)$	Donor, acceptor and total density of states distribution in *a*-Si:H band gap
n_i	Intrinsic carrier density
N_S	Supply function
$N_{(i)a-Si:H}$	Density of states in *a*-Si:H
$N_{DB}(E)$	Dangling bond defect distribution
P_s, N_s	Hole, electron sheet density
P_s(300K)	Hole sheet density at 300 K
$P_s(x)$	Hole sheet density between the interface ($x = 0$) and the position x
P_{ill}	Illumination power
p_{i1}, p_{i2}	Hole concentration in level i
q	Elementary charge (positive)
Q_g	Gate charge
$Q_{-d_{a-Si:H}}$	*a*-Si:H surface charge
$Q_{a-Si:H}$	Charge in *a*-Si:H
Q_{c-Si}	Charge in *c*-Si
Q_{fix}	Fixed charge
Q_{int}	Charge in interface states
Q_{ox}	Oxide charge
Q_{SCR}	Charge in the space charge region

R	Reflectance
R_{bulk}	Total bulk recombination rate
$R_{\text{int}}(\Delta p_{\text{int}})$	Recombination rate at interface defects
S	Surface recombination velocity
T_c, T_v	Conduction, valence band tail characteristic temperature
T_{eq} (and T^*)	Equilibrium temperature
U	Correlation energy
u	Normalized electrostatic potential
U_D	Dember voltage
U_{DB}	Recombination rate through dangling bonds
U_{max}	Maximum surface photovoltage signal
U_{SPV}	Surface photovoltage signal
$V(x)$	Electrostatic potential at x
$V_d^{a-Si:H}$	Potential drop in *a*-Si:H
V_d^{c-Si}	Potential drop in *c*-Si
V_g	Voltage applied to the MIS structure
V_{bi}	Built-in voltage
V_{oc}	Open circuit voltage
V_{ox}	Potential drop across the mica foil
$v_{th,n}$, $v_{th,p}$	Electron, hole thermal velocities
$WF_{a-Si:H}$	*a*-Si:H work function
WF_{TCO}	Transparent conductive oxide work function
x	Distance from illuminated surface or referred to the *a*-Si:H/*c*-Si interface
$\mathrm{H_2}$	Molecular hydrogen
$\mathrm{N_2}$	Molecular nitrogen

B_2H_6	Diborane
HF	Hydrofluoric acid
InGaAs	Indium Gallium Arsenide
NH_4F	Ammonium fluoride
PH_3	Phosphine
SiH_4	Silane
SiO_2	Silicon dioxide
Si	Silicon
a-Si:H	Hydrogenated amorphous silicon
c-Si	Crystalline silicon
AC	Alternative current
AFORS-HET	Automat FOR Silicon HETerojunction
Al	Aluminium
AM	Air mass
AS	Admittance spectroscopy
BP	Branch point
C-V	Capacitance-Voltage
CB, VB	Conduction band, valence band
CdTe	Cadmium Telluride
CIGS	Copper Indium Gallium Selenide
CNL	Charge neutrality level
CS	Capacitance spectroscopy
DB	Dangling bond
DC	Direct current
DI	Deionized (water)

DOS	Density of states
DPM	Defect pool model
ECR	Electron cyclotron resonance
EQ	Equilibrium
FiT	Feed-in Tariff
FZ	Float-zone grown
H	Hydrogen
HIT	Heterojunction with intrinsic thin layer
IP	Internal Photoemission
ITO	Indium tin oxide
IV	Current-Voltage
MIS	Metal-Insulator-Semiconductor
MPL	Modulated photoluminescence
PC	Planar conductance
PCD	Photo-conductance decay
PECVD	Plasma enhanced chemical vapor deposition
PL	Photoluminescence
PS	Photoyield spectroscopy
PV	Photovoltaic
RCA	Radio Corporation of America (cleaning procedure)
RF	Radio frequency
SC	Standard cleaning
SCR	Space charge region
SE	Spectral ellipsometry
SPV	Surface photovoltage

SR	Spectral response
SRH	Shockley-Read-Hall
TCO	Transparent conductive oxide
TLM	Transmission line measurement
UHV-OP	Ultra high vacuum oxygen plasma
VD-SPV	Voltage dependent surface photovoltage
VFP	Voltage filling pulse method
WB	Weak bond
ZnO:Al	Aluminium-doped zinc oxide

Introduction

General context

Photovoltaic (PV) solar cells convert light into electricity. They collect the energy from the Sun and make it usable without emission of green-house gases during operation. The solar energy received on the Earth is tremendous with respect to what humans consume. For these reasons, PV can be considered as an environmentally neutral source of energy [Schiermeier 08] which can take a significant share in the global energy production and consumption. The challenge lies in the ability to create devices that convert the Sun-light into electrical power efficiently enough while their cost remains compatible with the market laws.

Over the past years, the PV market has grown very fast mainly thanks to Feed-in Tariff (FiT) schemes organised by more than 40 countries. Such schemes are necessary to bring the PV electricity to grid parity (i.e. the point where photovoltaic electricity price equals the price on the existing grid) [EPIA 11a]. Recently, in most countries the subventions have been dramatically reduced or even cut off; a stabilization or a even a decrease of PV panels sales is expected in the next years [EPIA 12] and the cost per Watt-peak has already dropped by 50 % since January, 2010 [Sologico 12]. These new conditions (less FiT schemes, lower prices) cast doubt upon the evolution of the market. The technology is now in a maturation phase which, according to estimations, should bring it to grid parity between 2017 and 2019 in southern Europe countries (Spain, Italy, France) and Germany [EPIA 11b].
This will become reality if policies keep accompanying the PV sector in a sustainable way. Nevertheless, the technology has also a role to play. Indeed, to reach grid parity, the PV energy cost (€/Watt) has to be lowered. Two strategies can be set up in this direction: to reduce the production cost (including raw materials and manufacturing) and/or to increase the power conversion efficiency. In addition, the improvement of the conversion efficiency has the

advantage to increase the energetic intensity (W/m^2).

Since the first modern solar cell concept realized about 40 years ago, silicon has been dominating the PV market: its abundance and non-toxicity, and the technological maturity inherited from micro-electronics make silicon a candidate of choice for large scale PV applications. Despite the newly emerging technologies (CIGS, CdTe, concentrated PV, ...) silicon had 82 % market share in 2010. Is is forseen that in 2020 silicon (crystalline and amorphous) will contribute to 70 % of the PV market [EPIA 11a].
Among silicon based solar cells, wafer based technologies have been at the first rank in terms of conversion efficiency and market development. However they combine a few drawbacks. They are based on high temperature processes (dopant diffusion, thermal oxidation) which increase the energy payback time and the production cost. They also use a large amount of expensive material since high temperature steps forbid any use of thin wafers because of high breakage percentage. Therefore, silicon heterojunction solar cells, which are processed at low temperature ($\leq 200\ ^{\circ}C$) have attracted much interest in the past decades.

From conventional *c*-Si wafer based to silicon heterojunction solar cells

In a simplified view, standard crystalline silicon (*c*-Si) wafer based solar cells are made of a p-doped *c*-Si wafer which is strongly n-doped at the front surface; metal contacts finalize the device and allow for extraction of photo-generated charge carriers separated by the p-n junction.
In the 1970s, another type of *c*-Si wafer based devices emerged, namely Metal-Insulator-Semiconductor (MIS) solar cells [Green 74]. Here the photo-generated minority carriers are extracted by tunneling through a thin insulator (silicon oxide) layer. The p-n junction is replaced by the MIS contact and the built-in voltage results from the work function difference between the *c*-Si wafer and the metal. The silicon oxide is used to decrease the defect density and hence the recombination of charge carriers at the interface.
Halfway between these two designs, the amorphous silicon/crystalline silicon (*a*-Si:H/*c*-Si) heterojunction solar cells were first introduced by Hamakawa [Hamakawa 83] and Okuda [Okuda 83]. Ten years later, Sanyo already reached high power conversion efficiencies of more than 18 % [Tanaka 92]. The standard cell structure is made of a *c*-Si wafer (n or p type) on top of which a nanometre-thin doped *a*-Si:H emitter layer (p or n type) is deposited. The heterojunction combines the insulation of the absorber region from the highly recombination-active metal contacts with efficient charge carrier extraction. Indeed, contrary to the MIS structure, photo-generated carriers do not have to tunnel since the *a*-Si:H band gap remains low compared to silicon oxide. Nonetheless, the band gap energy is higher than in *c*-Si so that the built-in voltage is increased, favouring an efficient separation of charge carriers. To some extent, the doped *a*-Si:H layer works simultanously as an efficient passivating layer and as a

contact whose work function can be controlled through doping.
a-Si:H/*c*-Si solar cells are entirely processed at low temperature (≤ 200 ˚C). A power conversion efficiency of up to 23.7 % has been reached recently [Kinoshita 11] on thin wafers (≤ 100 μm instead of 300...500 μm for standard wafers), and several research groups around the world published performances above 20 % [Ribeyron 11, Descoeudres 11, Hernandez 11, Munoz 11].

This work

This thesis is devoted to the study of silicon heterojunction solar cells and focuses on the interface between the doped *a*-Si:H emitter and the *c*-Si absorber. It has been carried out in the frame of a joint PhD program between the Institute for Electrical Engineering of Paris (Laboratoire du Génie Électrique de Paris, LGEP and the Silicon-Photovoltaics department at the Helmholtz Centre Berlin (Helmholtz Zentrum Berlin, HZB). The preparation of samples was done at HZB whereas most of the characterizations were performed at LGEP. Modeling could be done in both places.

This work has benefited from a European project on the development of silicon heterojunction solar cells (HETSI, from 2008 to 2011) and from diverse collaborations between several research institutes: University of Toronto (Prof. Kherani's group, Canada), LPICM (École Polytechnique, France), CEA-INES (Chambéry, France).

Chapter 1 introduces the main concepts useful to the understanding of this work: basics on crystalline and amorphous silicon are presented, before addressing the characteristics of the interface between these two materials.
In Chapter 2, the tools that have been used to carry out this project are presented: samples preparation, characterization tools and numerical device simulator.
Then, three chapters are devoted to presenting the novelties of this work. The points addressed in these chapters are listed below:

- Development of an analytical model to calculate the band bending in *c*-Si as a function of heterojunction parameters: band offsets, thickness of buffer and emitter layers, Fermi level position, contact work function, etc. (Chapters 3 and 4).
- Determination of the band offsets between *a*-Si:H and *c*-Si from a comparison between electrical measurements and analytical calculations (Chapter 3).
- Presentation of a method to understand the role played by the buffer layer relying on complementary measurements of the band bending and the effective lifetime (Chapter 4).
- The positive impact of a high density of states in the (p)*a*-Si:H emitter layer (Chapter 4).

- Development of a new heterojunction interface for high efficiency solar cells: oxidized silicon surfaces are used as a building block for *a*-Si:H/*c*-Si solar cells (Chapter 5).

These three chapters are themselves divided in three parts: presentation of theoretical findings, experimental studies and discussion of results.
Finally, the thesis is summarized in a conclusion part where a few perspectives for further works are also given.

1

Basics of the amorphous silicon/crystalline silicon heterojunction

Amorphous silicon/crystalline silicon heterojunction based solar cells have received a lot of interest over the past decade, particularly in the frame of the European project HETSI running from 2008 until 2011. Publications on different aspects of the silicon heterojunction solar cell, ranging from the understanding of fundamental physics phenomena to the device optimization, have dramatically increased. Several PhD theses have been carried out on the topic: among many others, works of Wilfried Favre (LGEP - France) [Favre 11], Tim Schulze [Schulze 11a] and Caspar Leendertz (HZB - Germany) [Leendertz 11a], Sara Olibet (EPFL - Switzerland) and Jan-Willem Schüttauf (Utrecht University, Holland) are of particular interest. As a conclusion to the HETSI project, a book dedicated to the state of the art of silicon heterojunction solar cells, written by most of the protagonists involved in the project, has been released [van Sark 12]. This chapter aims at presenting fundamental concepts required for the understanding of this manuscript. The reader may refer to cited works for more detailed information.

1.1 Materials properties

1.1.1 Mono-crystalline silicon for photovoltaic applications

1.1.1.1 Basic properties

Silicon has been intensively studied in the field of microelectronics. Its abundance, accessibility and non-toxicity have contributed to its large scale application. In its crystalline phase, covalently bound tetravalent silicon atoms are organised in a diamond-like lattice structure. Crystalline silicon (*c*-Si) is a semiconductor and has a band gap of 1.124 eV at 300 K. This corresponds almost to the maximum of the spectral irradiance of the light provided by the sun on Earth: therefore silicon is a good candidate for light absorption. However this band gap is indirect, which lowers the absorption coefficient, and forces to have relatively thick wafers (typically 200-300 μm). *c*-Si can be easily doped by inserting foreign atoms like boron (p-type doping) or phosphorous and arsenic (n-type doping).

Despite its high bulk crystallinity, silicon is not free of defects. Doping atoms create defects close to the band edges that are not critical for the material properties. However traces of foreign atoms like iron can dramatically increase the recombination of charge carriers [Istratov 99]. Another type of defects in (p)*c*-Si originates from boron-oxygen complexes, especially in Czochralski silicon [Bothe 05]. In the present thesis, these defects do not have much influence on results and discussions as high quality float-zone wafers with bulk effective carrier lifetime of 10 ms or equivalent are used. The recombination of charge carriers is then mostly dominated by the interfaces, as shall be discussed later. Historical reasons have brought boron doped (p-type doped) silicon to dominate the photovoltaic (PV) market. The better mobility of electrons is also an argument to favour p-type *c*-Si, as minority carrier extraction has to be optimized at first. Yet phosphorous n-type *c*-Si is less defective (no boron-oxygen complex), thus offering higher quality *c*-Si wafers. Indeed, for most metallic impurities, the capture cross section for holes is lower than that of electrons, which favours n-type *c*-Si where holes are minority carriers. Table 1.1 summarizes the most important parameters of intrinsic crystalline silicon at room temperature (300 K).

Table 1.1: Material parameters for intrinsic crystalline silicon at 300*K.*

Parameter	Value	Symbol	Reference
Band gap energy	1.124 eV	E_g^{c-Si}	[Alex 96]
Electron affinity	4.05 eV	χ_{c-Si}	[Sze 07]
Relative dielectric constant	11.9	ϵ_r	[Sze 07]
Conduction band effective density of states	2.86×10^{19} cm^{-3}	N_c	[Green 90]
Valence band effective density of states	3.1×10^{19} cm^{-3}	N_v	[Green 90]
Electron mobility	1430 cm^2 V^{-1} s^{-1}	μ_n	[Green 90]
Hole mobility	480 cm^2 V^{-1} s^{-1}	μ_p	[Green 90]
Intrinsic carrier density	1.08×10^{10} cm^{-3}	n_i	[Green 90]

1.1.1.2 Charge generation and recombination mechanisms in *c*-Si

Light absorption and photogeneration: Absorption of light can induce the generation of electrons and holes in *c*-Si. Electrons are excited from the valence band to the conduction band provided the photon energy is greater than the band gap energy. Because of the indirect band gap of *c*-Si, the absorption process also involves a phonon[1]. The wavelength dependent free carrier generation rate $G(\lambda)$ is defined as the number of electron-hole pairs generated per second, and can be calculated using the absorption coefficient α_{np} linked to the creation of electron-hole pairs:

$$G(\lambda, x) = \alpha_{np} F_0(\lambda) e^{-(\alpha_{np}+\alpha_{par})x}, \tag{1.1}$$

where $F_0(\lambda)$ is the incident photon flux transmitted in *c*-Si. F_0 is related to the external photon flux $F(\lambda)$ with the expression $F_0 = F(1-R)$ where R is the reflectance of the sample. α_{par} accounts for 'parasitic' absorption mechanisms from which no electron-hole pair is created and x is the distance from the illuminated surface. α_{np} and α_{par} depend a priori on the wavelength. *c*-Si has only a relatively low amount of gap defects and, even doped, its free carrier concentration remains low enough to assume that parasitic absorption mechanisms like free carrier absorption and sub-band gap absorption are negligible. As a consequence, the absorption coefficient, given by Green and Keevers in [Green 95], corresponds to α_{np}, such that the total generation rate G is given by:

$$G(x) = \int_{\text{spectrum}} \alpha_{np} F_0(\lambda) e^{-\alpha_{np} x} d\lambda. \tag{1.2}$$

[1]Absorption can also occur without involving a phonon, where the band gap is direct (3.4 eV)

Once light has been absorbed and free carriers with densities n for electrons and p for holes have been generated, it is convenient to define Δn and Δp, the so-called electron and hole excess concentrations:

$$\Delta n = n - n_0, \tag{1.3}$$

$$\text{and } \Delta p = p - p_0, \tag{1.4}$$

where n_0 and p_0 are the equilibrium carrier concentrations. In quasi-neutral regions, $\Delta n = \Delta p$.

Recombination processes: The recombination of free carriers in *c*-Si can occur through several phenomena, that are introduced in the following:

- **Radiative recombination**: the radiative recombination process can be thought of as the inverse of the generation mechanism. An electron in the conduction band looses its energy by the emission of a photon (and emission of a phonon to respect the momentum conservation law), and annihilates with a hole in the valence band. The radiative recombination rate reads:

  $$R_{\text{rad}} = B_{\text{rad}} \left(np - n_0 p_0 \right). \tag{1.5}$$

  The radiative recombination coefficient B_{rad} amounts to 4.733×10^{-15} cm^3 s^{-1} [Trupke 03].

- **Auger recombination**: Auger recombination occurs occasionally when two electrons (or two holes) collide. One is excited to a higher energy level while the other one looses its energy to recombine with a hole (or an electron) in the valence (conduction) band. Various parametrization have been proposed, one of the most recent being that of Kerr and Cuevas [Kerr 02]:

  $$R_{\text{Aug}} = np \left(1.8 \times 10^{-24} n_0^{0.65} + 6 \times 10^{-25} p_0^{0.65} + 3 \times 10^{-27} \Delta n^{0.8} \right). \tag{1.6}$$

  Auger recombination is a non-radiative recombination process. As it requires the interaction of three particles (two electrons and one hole or two holes and one electron), it is more likely to happen at high excess carrier densities (doped layers, high injection level).

- **Shockley-Read-Hall recombination**: another non-radiative recombination process is due to the presence of defects (or traps) in the band gap. Considering first a single defect at the energy E_t in the band gap, the Shockley-Read-Hall (SRH) recombination is described by four processes schematically shown in Fig. 1.1: capture of an electron

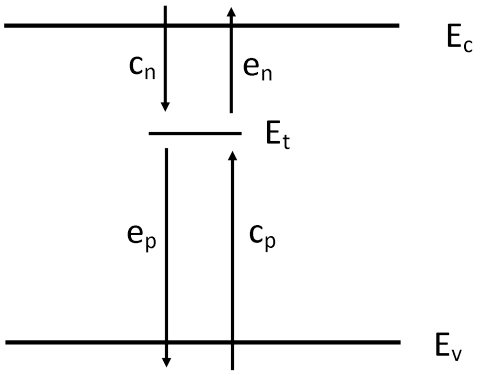

Figure 1.1: Shockley-Read-Hall recombination processes between a trap level at E_t and the conduction and valence band edges E_c and E_v.

from the conduction band into the trap (c_n), emission of an electron from the trap to the conduction band (e_n), and the same transitions for holes between the trap and the valence band (c_p and e_p)[Shockley 52]. The SRH statistics assumes that a trap can accommodate only one hole or one electron. If the trap density is N_t, the recombination rate through the traps is:

$$R_{\mathrm{SRH}}(E_t) = N_t \frac{np - n_i^2}{\frac{n+N_c e^{-\frac{E_c-E_t}{k_B T}}}{v_{th,p}\sigma_p(E_t)} + \frac{p+N_v e^{\frac{E_v-E_t}{k_B T}}}{v_{th,n}\sigma_n(E_t)}} \tag{1.7}$$

$$= N_t \frac{c_n c_p (np - n_i^2)}{c_n n + c_p p + e_n(E_t) + e_p(E_t)}, \tag{1.8}$$

with $c_n = \sigma_n v_{th,n}$, $c_p = \sigma_p v_{th,p}$, $e_n(E_t) = c_n N_c e^{-\frac{E_c-E_t}{k_B T}}$ and $e_p(E_t) = c_p N_v e^{\frac{E_v-E_t}{k_B T}}$. n_i is the intrinsic carrier density and $n_i^2 = N_c N_v e^{-\frac{E_g^{c-Si}}{k_B T}}$, N_c and N_v are the effective conduction and valence band density of states, E_c and E_v are the conduction and valence band edges, $v_{th,n}$ and $v_{th,p}$ are the thermal velocities for electrons and holes (about 10^7 cm s^{-1} in *c*-Si) and $\sigma_n(E_t)$ and $\sigma_p(E_t)$ are the trap capture cross sections for electrons and holes. In the case of a distribution $D(E_t)$ of traps in the band gap, the recombination rate is given by:

$$R_{\mathrm{SRH}} = \int_{E_v}^{E_c} D(E_t) \frac{np - n_i^2}{\frac{n+N_c e^{-\frac{E_c-E_t}{k_B T}}}{v_{th,p}\sigma_p(E_t)} + \frac{p+N_v e^{\frac{E_v-E_t}{k_B T}}}{v_{th,n}\sigma_n(E_t)}} dE_t. \tag{1.9}$$

The total recombination rate in the bulk R_{bulk} is given by:

$$R_{\text{bulk}} = R_{\text{rad}} + R_{\text{Aug}} + R_{\text{SRH}}. \tag{1.10}$$

It is convenient to use the minority charge carrier lifetimes to characterize the carrier recombination dynamics. For each recombination process, a lifetime τ_i is defined as

$$\tau_i = \frac{\Delta p}{R_i} \text{ where } i = \text{rad, Aug, SRH.} \tag{1.11}$$

Here Δp is used under the assumption that investigations are performed on (n)*c*-Si wafers, so that holes are minority carriers [2].

Finally, an effective bulk lifetime τ_{bulk} can be defined:

$$\tau_{\text{bulk}} = \frac{\Delta p}{R_{\text{bulk}}} \tag{1.12}$$

$$\text{with } \frac{1}{\tau_{\text{bulk}}} = \frac{1}{\tau_{\text{rad}}} + \frac{1}{\tau_{\text{Aug}}} + \frac{1}{\tau_{\text{SRH}}}. \tag{1.13}$$

1.1.2 Hydrogenated amorphous silicon

1.1.2.1 Basic properties

The amorphous state of silicon exhibits similar features as its crystalline form. X-ray or neutron diffraction leads to the establishment of the pair correlation function, which gives a picture of the distance between one atom and its neighbours. It has been shown that the first neighbour atom is roughly at the same distance in *a*-Si:H as in *c*-Si. This suggests that the short range order is preserved, which, from a tight-binding perspective, leads to a similar band structure [Street 91]. However, the bond length for higher order neighbours, involving bond angles, have a wider distribution: the long range order is not preserved and the random nature of the network determines the material properties. In such a non-periodic structure, the electrons are scattered from one Bloch state to another so that the uncertainty on the momentum k is of the same order of magnitude as k itself: thus k is not a 'good' quantum number and the bands cannot be described by a $E(\vec{k})$ dispersion relationship. Yet a density of states can still be defined.

It has been shown that disorder in the periodic lattice generates exponential band tails [Souk-

[2] It has however already been mentioned that $\Delta n = \Delta p$ in quasi neutral regions

oulis 84]. Band tail states are localized states and progressively merge into the delocalized band states; the energy points between extended and localized states in the valence and conduction bands are called the 'mobility edges' and are used to define the mobility band gap [Wronski 89]. The valence and conduction band tails are determined by their respective characteristic temperatures T_v and T_c [3]. T_v is related to the topological disorder and is typically in the range 500 K - 1000 K. T_c is related to the thermal agitation in the network and is usually close to 400 K [Aljishi 90].

Moreover in the amorphous network some bonds are not formed, leaving unsaturated or dangling bonds, which create deep defects in the band gap. If the network is composed only of silicon atoms, the density of defects in the gap is so high that *a*-Si is not suitable for electronic and photovoltaic applications. However dangling bonds can be passivated by hydrogen which reduces the density of states by several orders of magnitude: doping is then possible [Spear 75]. *a*-Si:H can be doped with the same dopant elements as *c*-Si, which makes it a good candidate to realize p-n junctions. However the doping efficiency is very low such that a very high concentration of dopant atoms is required [Street 91].

1.1.2.2 Bulk defects and recombination in *a*-Si:H

The same generation and recombination mechanisms as in *c*-Si occur in *a*-Si:H, but their relative role is changed because of the high density of defects. Auger recombination is rather weak and has not been much studied in amorphous semiconductors [Street 91]. Radiative recombination does not only occur between the conduction and valence bands, but also between states in the band tails [Street 91]. However, most of the excess charge carriers recombine non-radiatively through defects in the band gap. Band tail defects can reasonably be treated by the SRH statistics presented earlier. On the contrary, dangling bonds possess three charge states: they can carry no electron (positively charged: energy level D^+), one electron (neutral: energy level D^0), or two electrons (negatively charged: energy level D^-). The levels D^+ and D^0 are located at the same energy; however, D^- is shifted by a correlation energy U with respect to the others due to the Coulomb interaction. In this context, the SRH statistics (assuming only two charge states) is not applicable anymore. Instead, the amphoteric nature of dangling bonds is described using the correlated electrons statistics [Okamoto 77, Vaillant 86, Street 75]. This statistics results from the principle of detailed balance stating that each charge state must be in equilibrium with the band states. Transitions from each charge states (D^+, D^0 and D^-) to the bands are written like in the SRH statistics. The recombination rate U_{DB} through a dangling bond distribution $N_{DB}(E)$ can be written as:

$$U_{DB} = \int_{E_v}^{E_c} A(E) N_{DB}(E) dE, \tag{1.14}$$

[3] $k_B T_v$ and $k_B T_c$ are also called the Urbach energies, where k_B is Boltzmann's constant.

where $N_{DB}(E)$ is the dangling bond distribution. $A(E)$ includes the occupation functions of the three states and defect parameters such as the capture cross sections. The equations are explicitly given in [Li 08]. Similarly to other recombination processes, a charge carrier lifetime associated with the recombination through dangling bonds can be defined (see Eq. 1.11).

The defect distribution in *a*-Si:H is described by the defect pool model (DPM) introduced in the nineties by Powell and Dean [Powell 93, Powell 96]. This model describes the equilibration of dangling bonds (DB) from the pool of weak bonds (WB) in the valence band tail. This process depends on several parameters imposed on the *a*-Si:H material: temperature, hydrogen content, doping (position of the Fermi level). It results from the competition between the chemical reactions:

$$\mathrm{WB} \rightleftharpoons 2\,\mathrm{DB}$$
$$\mathrm{WB} + 2\,\mathrm{Si{-}H} \rightleftharpoons \mathrm{DB} + (\mathrm{Si{-}H} + \mathrm{DB})$$
$$\mathrm{WB} + 2\,\mathrm{Si{-}H} \rightleftharpoons (\mathrm{Si{-}H} + \mathrm{Si{-}H}) + 2\,\mathrm{DB}$$

The breaking of weak bonds requires energy to give two DBs. The energy barrier associated with the process dictates the dynamics of *a*-Si:H equilibration. At high deposition or annealing temperature, *a*-Si:H equilibrates quasi-immediately, whereas at lower deposition temperature the material remains in a metastable state. A critical equilibrium temperature T_{eq} [4] was defined by Meaudre [Meaudre 91]: under 180˚C, the dangling bond concentration is assumed not to evolve during a relevant investigation time (days, weeks), whereas during processing above 180 ˚C it equilibrates very rapidly.

The defect distribution is directly related to the occupation function of amphoteric defects [Vaillant 86], such that it depends on the position of the Fermi level. Doping the material thus leads to a modification of the defect distribution in the gap. Typical distributions calculated using the equations of Powell and Dean [Powell 93, Powell 96] are shown in Fig. 1.2. For undoped *a*-Si:H ((i)*a*-Si:H) [5], a rather low and broad distribution (maximum density is about 10^{16} cm^{-3} eV^{-1}) centred at mid-gap results from the DPM, with equivalent contribution of D^-, D^0 and D^+ states. For (p)*a*-Si:H a distribution of D^+ states dominates in the upper half of the gap, with a maximum density of about 10^{19} cm^{-3} eV^{-1}, whereas for (n)*a*-Si:H a distribution of D^- states in the lower half of the gap with a maximum density of about 10^{19} cm^{-3} eV^{-1} eclipses the other contributions [6].

[4] T_{eq} defined by Meaudre [Meaudre 91] corresponds to T^* introduced later in the defect pool model [Powell 93].

[5] In (i)*a*-Si:H, the Fermi level is not at mid-gap because the valence band tail extends deeper in the band gap than the conduction band tail; to reach the electrical neutrality, the Fermi level shifts toward the conduction band edge.

[6] The exact values of the deep defect concentration depend on the position of the Fermi level.

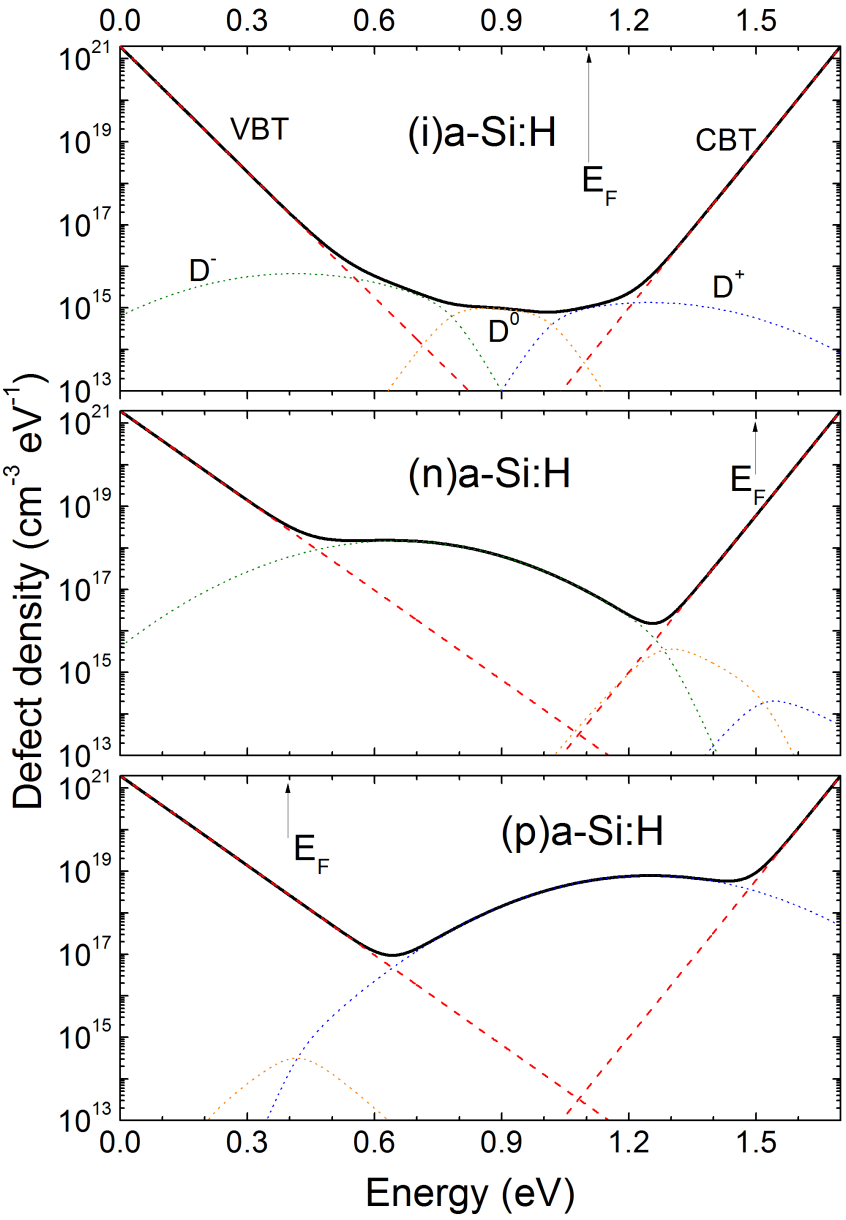

Figure 1.2: Defect distribution in intrinsic, n-doped and p-doped a-Si:H calculated from the defect pool model; equations and material parameters can be found in [Powell 96]. VBT/ CBT: Valence/ Conduction Band Tail.

1.2 The amorphous silicon/crystalline silicon interface

Amorphous silicon and crystalline silicon forming the silicon heterojunction have now been presented. The interface between them has particular features that are introduced in the following sections.

1.2.1 Band offsets

A key feature of the interface is the alignment of the valence and conduction band edges between *a*-Si:H and *c*-Si. Because both materials do not have the same band gap energies – 1.124 eV for *c*-Si and around 1.75 eV for *a*-Si:H – the question of how the valence and conduction bands align arises. Fig. 1.3 presents the different types of heterostructures formed by a wide band gap material and a low band gap material [Sze 07]. It can be intuitively perceived how important the band alignment is, especially for transport properties. For example, for the sketched broken-gap heterojunction, electrons would easily go from the low to wide band gap material (right to left), while the holes would face a very high barrier and be blocked; in that case, electrons and holes would be easily separated. The 'separation power' is less pronounced for a staggered heterojunction and is suppressed for a straddling heterojunction. This discussion was presented without considering the equilibration of the Fermi level (band bending, see later in section 1.2.3), but should nevertheless be kept in mind.

1.2.1.1 Experimental determination of band offsets

The precise knowledge of band offsets at the *a*-Si:H/*c*-Si heterojunction is of prime importance for the prediction of the device performance; indeed it is one of the main input parameter in simulation softwares or analytical calculations. The optimization of the device partly relies on the band offsets. Therefore a considerable work has been done to measure them. The particular case of the *a*-Si:H/*c*-Si heterojunction has been classified in various publications

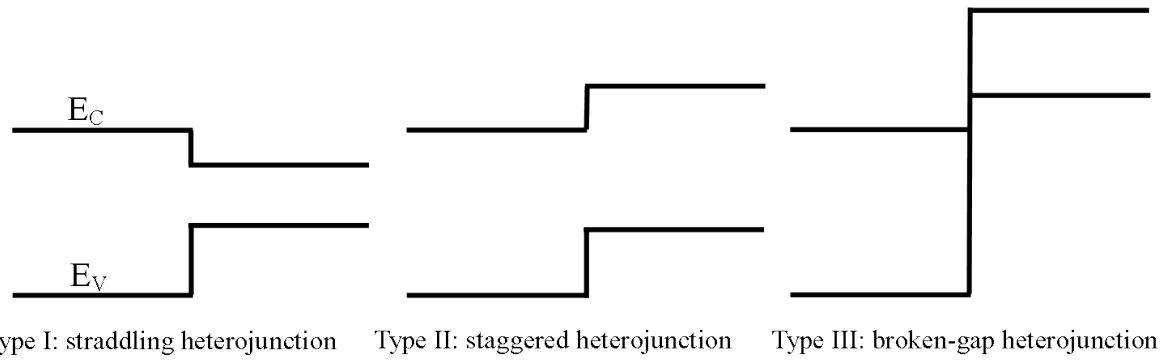

Figure 1.3: Classification of heterojunctions [Sze 07].

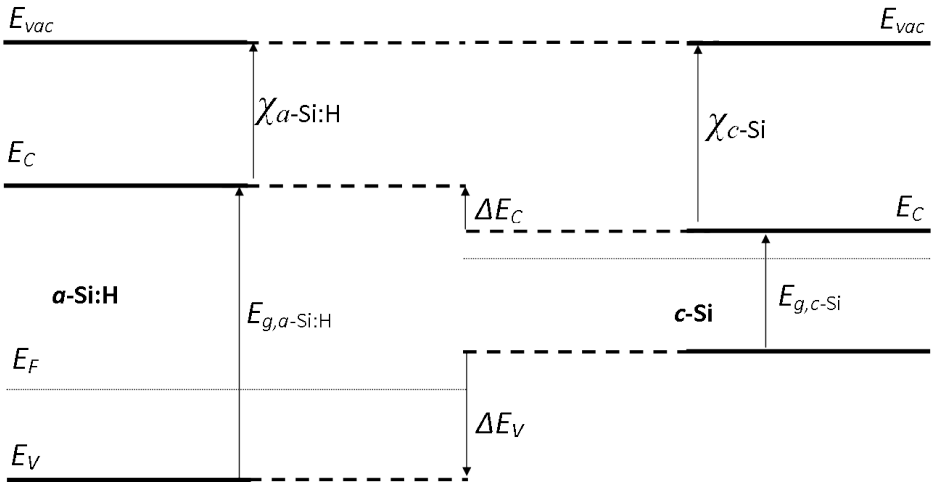

Figure 1.4: Vacuum level alignment at the a-Si:H/ c-Si interface, in the frame of Anderson's theory [Anderson 62]. Fermi level equilibration occurs by charge transfer when the materials are in contact.

as types I or II, with a large advantage to type I in terms of number of publications of band offsets measurements. Table 1.2, updated from [van Sark 12], gives some band offsets values deduced from experimental measurements (the techniques are also given in the table) that can be found in the literature. It can be observed that those values are widely spread. Several explanations can be invoqued to understand such differences. On one hand, samples deposition processes and conditions differ from one institute to another; the materials and the complete structures do not have exactly the same properties. For instance the hydrogen content and the doping density influence the *a*-Si:H band gap, which can have a direct impact on the band offsets [Schulze 11b]. On the other hand, measurement methods such as photoemission or capacitance measurements require strong assumptions which can be inaccurate for *a*-Si:H/*c*-Si heterojunctions and lead to wrong interpretations. For example, some techniques are based on optical processes but optical and electrical *a*-Si:H band gaps are known to be different; doubts have been expressed regarding the reliability of optical measurements to explain electrical behaviours [Wronski 89].

1.2.1.2 Theoretical predictions

The theoretical prediction of band offsets relies on the capability to find a reference energy level that must be the same for each material. Nowadays two major theories are used to predict the band offsets:

- Anderson's rule: vacuum level

  Anderson's rule states that the vacuum level of both materials has to line up at the

Table 1.2: Conduction and valence band offset values, ΔE_c and ΔE_v, deduced from experimental measurements and reported in the literature. X/y structures correspond to the doping type of a-Si:H (X) and c-Si (y). The experimental methods are: IP: Internal Photoemission, SR: Spectral Response, C-V: Capacitance vs Voltage, CS: Capacitance Spectroscopy, IV: Current-Voltage characteristics, VFP: Voltage Filling Pulse method, AS: Admittance Spectroscopy, PS: Photoyield Spectroscopy, PC: Planar Conductance, SE: Spectral Ellipsometry, SPV: Surface Photovoltage.

ΔE_c(eV)	ΔE_v(eV)	Structure	Method	Reference
0.09	0.71	I/n, I/p	IP	[Mimura 87]
0.04...0.8	$-0.1...+0.15$	I/p	IP	[Cuniot 85], [Cuniot 88]
-	0	I/n, I/p	IP	[Lequeux 89]
0.24	-0.06	P/n	IP	[Sakata 04]
0.14	0.63	I/n	IP	[Sakata 09]
0.15...0.175	0.46...0.49	P/n, I/n	SR	[Eschrich 93]
0.06	large	I/n	SR	[Gall 97]
0.20	-	N/p	C-V	[Matsuura 84]
0.14	-	I/p	C-V	[Matsuura 89]
0.45	-	I/p	C-V	[Song 00]
0.01	0.67	N/p	CS	[Essick 96]
0.05	0.58	I/n	CS,VFP	[Essick 89]
0.25	-	I/n	C-V	[Roesch 98]
0.35	-	N/p	CS,IV	[Unold 00]
0.05	-	I/n	AS	[Gall 95]
-	0.44	I/p	PS	[Sebastiani 95]
0.14	0.46	N/p, P/n	PS	[Fuhs 06], [Schmidt 07]
0.15	-	N/p	PC	[Kleider 08]
0.15	-	N/p	PC	[Kleider 08]
0.24...0.32	0.39...0.61	I/n	PS, SPV, SE	[Schulze 11b]

interface. The key parameter is the electron affinity, defined as the energy distance between the bottom of the conduction band and the vacuum level. The band offsets are then determined by the electronic affinity and band gap differences as shown schematically in Fig. 1.4 [Anderson 62]:

$$\Delta E_c = \chi_{c-Si} - \chi_{a-Si:H}, \tag{1.15}$$

$$\text{and } \Delta E_v = E_g^{a-Si:H} - E_g^{c-Si} - \Delta E_c. \tag{1.16}$$

This description suffers from several weaknesses, one of the major being that the electronic affinity is a surface property: its use at the interface between two semiconductors may be criticized. Moreover microscopic dipoles could arise from charge transfer localized at the interface and play a role in the band line-up. More dramatically, Anderson's model fails in describing metal/semiconductor contacts, a particular case of heterojunctions [Sze 07]. As a consequence, the Anderson's rule is an oversimplified theory used to get rapidly a rough estimate of the band offsets.

- The branch point theory

At the surface of a material, the periodicity of its crystalline structure is broken. Interface-induced gap states, stemming from complex solutions of the Schrödinger equation at the surface, tail into the vacuum or the neighbour material [Moench 01]. These defects, originating from the bulk band diagram, are predominantly donor like close to the valence band edge and acceptor like close to the conduction band edge. The branch point (BP), or charge neutrality level (CNL), is defined as the energy point where states go from predominantly donor to acceptor. It is a neutrality point: if the Fermi level coincides with it, interface induced defects host no net charge. Calculations using the augmented plane-wave method made by Tersoff localize the CNL of crystalline silicon

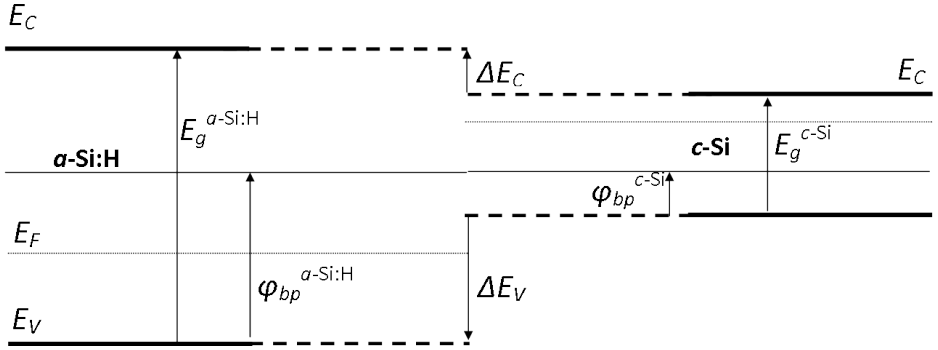

Figure 1.5: Branch points alignment at the a-Si:H/ c-Si interface, in the frame of Bardeen's rule. Fermi level equilibration occurs by charge transfer when the materials are in contact.

at 0.36 eV from the valence band edge [Tersoff 84], whereas Flores placed it at 0.63 eV [Flores 89] on the basis of experimental measurements of barrier heights.

The branch point theory, introduced first by Tejedor and Flores [Tejedor 78], takes the branch point φ_{bp}^{X} in each semiconductor as a reference level (see Fig. 1.5). The band offsets are then calculated by:

$$\Delta E_v = \varphi_{bp}^{a-Si:H} - \varphi_{bp}^{c-Si} + \Delta_{\text{dip}} \tag{1.17}$$

$$\text{and } \Delta E_c = E_g^{a-Si:H} - E_g^{c-Si} - \Delta E_v. \tag{1.18}$$

Δ_{dip} accounts for the presence of interface dipoles, forcing the potential to drop over a few Angströms; this can be represented by an additional contribution to the band offsets.

1.2.2 Interface defects and recombination

The breaking of the crystalline network periodicity at the *c*-Si surface leaves unsaturated bonds. Electronic orbitals participating in no bonding provide available states with energies within the bulk forbidden band gap. The dangling bond density of a perfectly free intrinsic *c*-Si surface (unsaturated dangling bonds, no adsorbed impurities) depends on the surface orientation. On (111) surfaces there is only one dangling bond per surface atom, whereas there are two on (100) surfaces. (111) surfaces are thus less defective than (100) surfaces even if the density of surface atoms is lower in the latter case [Dabrowski 00]: the density of surface dangling bonds amounts to 8.00×10^{14} cm^{-2} for (111) surfaces whereas it reaches 1.39×10^{15} cm^{-2} for (100) surfaces.

Surface dangling bonds act as recombination centres as in the case of dangling bonds in bulk *a*-Si:H and they are expected to be ruled by the same statistics of correlated electrons. However their energy repartition is still not well-known. Namely, do surface dangling bonds obey the defect pool model, meaning that their distribution would depend on the surface position of the Fermi level like in the defect pool model? Or do they rather stay around mid-gap? Numerical models built by Leendertz, Olibet and Steingrube addressed this remaining open question [Leendertz 10b, Olibet 07, Steingrube 10]. It is out of the frame of this work to enter in this discussion. An integrated interface defect density over the band gap (thus in cm^{-2}) will describe the *a*-Si:H/*c*-Si interface defect density. The interface (or surface) carrier lifetime τ_{int} (or τ_{surf}) is expressed as:

$$\tau_{\text{int}} = \frac{\Delta p_{\text{int}}}{R_{\text{int}}(\Delta p_{\text{int}})}, \tag{1.19}$$

where Δp_{int} is the interface excess carrier density and $R_{\text{int}}(\Delta p_{\text{int}})$ is the recombination rate at interface defects calculated similarly to Eq. 1.9 in the case of SRH statistics or as in Eq. 1.14 when accounting for the amphoteric nature of dangling bonds. Using an effective bulk minority carrier density, the notion of interface lifetime leads to the definition of an effective lifetime τ_{eff} including both bulk and surface recombination processes [Brody 03]:

$$\frac{1}{\tau_{\text{eff}}} = \frac{1}{\tau_{\text{int}}} + \frac{1}{\tau_{\text{bulk}}}. \tag{1.20}$$

Obviously, when the bulk lifetime is very high compared to the interface or surface lifetime, the latter limits the effective lifetime. Thus, for the case of high power conversion efficiency solar cells fabricated on high quality float-zone *c*-Si wafers, it is convenient to speak about *the* lifetime of a sample, keeping in mind that the bulk-limited lifetime is considered much larger than the interface-limited lifetime.

It is also useful to define the surface recombination velocity S:

$$S = \frac{U}{\Delta p_{\text{surf}}}. \tag{1.21}$$

In an *a*-Si:H/*c*-Si heterojunction, the *c*-Si surface is passivated by hydrogenated amorphous silicon. The *c*-Si surface dangling bonds are re-bound to Si atoms or form H-Si bonds. This considerably reduces the interface dangling bond density down to around 10^{11} cm^{-2} [Leendertz 11b], leaving about only one unsaturated bond every 10000 interface atoms. The recombination of charge carriers at the interface is thus expected to be drastically reduced. However the presence of *a*-Si:H covering the *c*-Si surface brings a remarkable difference with respect to a free *c*-Si surface in vacuum. Indeed, bulk defects in the *a*-Si:H band gap energy constitute available states for charge carriers coming from *c*-Si. It has been recently proposed that electrons and holes may tunnel from delocalized *c*-Si states into *a*-Si:H localized states, and then recombine [Boehme 06, Schulze 10a, Schulze 11a]. Thus the interface defect density seen by the charges does not come only from unsaturated *c*-Si surface dangling bonds; an additional contribution from a tunneling-assisted recombination process through defects in bulk *a*-Si:H seems to be possible.

In order to reduce interface recombination, Sanyo Electric Co. has added an intrinsic amorphous silicon buffer layer between the doped *a*-Si:H layers (emitter or back surface field) and the *c*-Si absorber. Interestingly, a remarkable improvement of the effective carrier lifetime was observed [Taguchi 00] due to a lower defect density in (i)*a*-Si:H than in p-doped or n-doped *a*-Si:H (see Fig. 1.2). Nonetheless, (i)*a*-Si:H remains amorphous silicon and its defect density is consequently ruled by the defect pool model. In particular, the Fermi level position determines the bulk defect density. When (p)*a*-Si:H is deposited on an (i)*a*-Si:H/(n)*c*-Si structure,

the doped *a*-Si:H layer pushes the Fermi level in (i)*a*-Si:H towards the valence band (see Fig. 1.7). At thermodynamic equilibrium the density of defects in (i)*a*-Si:H increases ((i)*a*-Si:H becomes 'more (p)-like') and the carrier lifetime decreases. This has been shown experimentally [de Wolf 09, Schulze 11c]. Because the conduction band offset is smaller than the valence band offset, and because the Fermi level position in (i)*a*-Si:H is closer to the conduction than to the valence band, this effect is less critical for (n)*a*-Si:H layers deposited on (p)*c*-Si.

1.2.3 Band bending in *c*-Si and inversion layer

1.2.3.1 Origin of the band bending in *c*-Si

When *a*-Si:H and *c*-Si are brought in contact, it is thermodynamically required that the Fermi level in both materials aligns, leading to a constant chemical potential in the structure. This is accomplished by charge transfer from one material to the other. When the equilibrium is reached, electrons are in excess on one side of the junction, and are lacking with respect to the density in the bulk on the other side. As a result, in a region close to the interface, the valence and conduction bands depart from their bulk equilibrium position (with respect to the Fermi level); the energy difference between the interface and bulk band edges is called band bending.

Fundamental definitions are presented in Fig. 1.6. The band bending at the investigated *c*-Si surface is defined as:

$$\varphi_{c-Si} = q\,(V_b - V_s) = E_{c,s} - E_{c,b}, \tag{1.22}$$

where q is the elementary charge, V_s and V_b are the surface and bulk electrostatic potential, $E_{c,s}$ and $E_{c,b}$ the surface and bulk conduction band edge, respectively.

In the case of crystalline silicon, the local charge density originates from free carriers. Free electrons and holes diffuse to reach the thermodynamic equilibrium. On the contrary, amorphous silicon has only a small amount of free carriers due to its higher band gap energy and the difficulty to dope it. Most of the charge density is hosted in the large amount of defects in the band gap, the occupation of which compensates most of the charge that builds up in *c*-Si.

Typical band diagrams of both (n)*a*-Si:H/(p)*c*-Si and (p)*a*-Si:H/(n)*c*-Si are shown in Fig. 1.7. They schematically display what has been discussed so far: band offsets, bulk and interface defects and band bending.

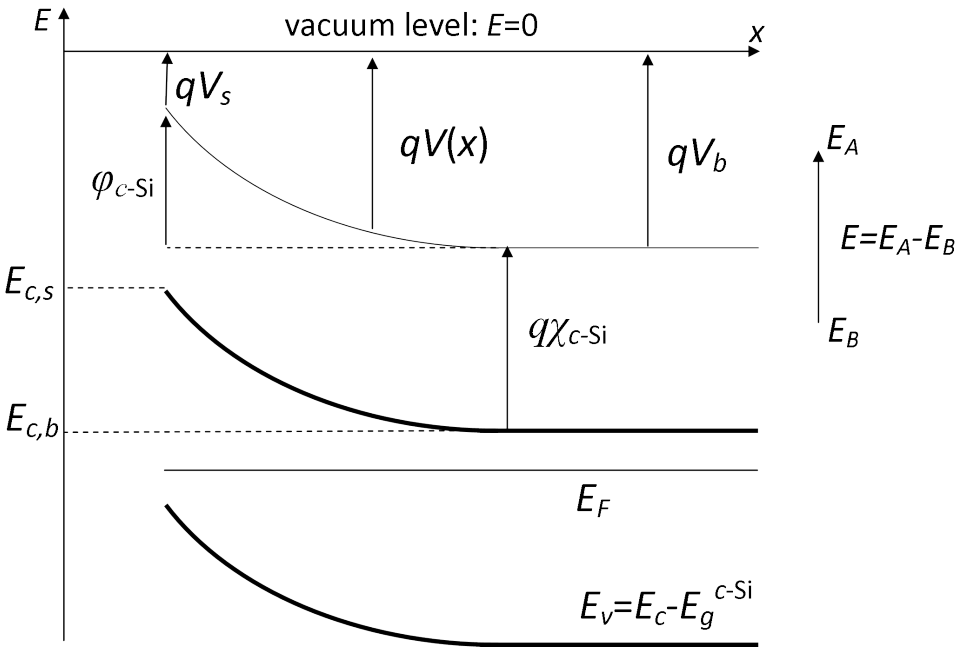

Figure 1.6: Definition of the band bending in c-Si and convention used throughout this work. $V(x)$ is the electrostatic potential at x, χ_{c-Si} is the electron affinity of c-Si, E_c and E_v are the conduction and valence band edge energies, E_F is the Fermi level, s denotes 'surface' whereas b refers to 'bulk'. q is the elementary charge.

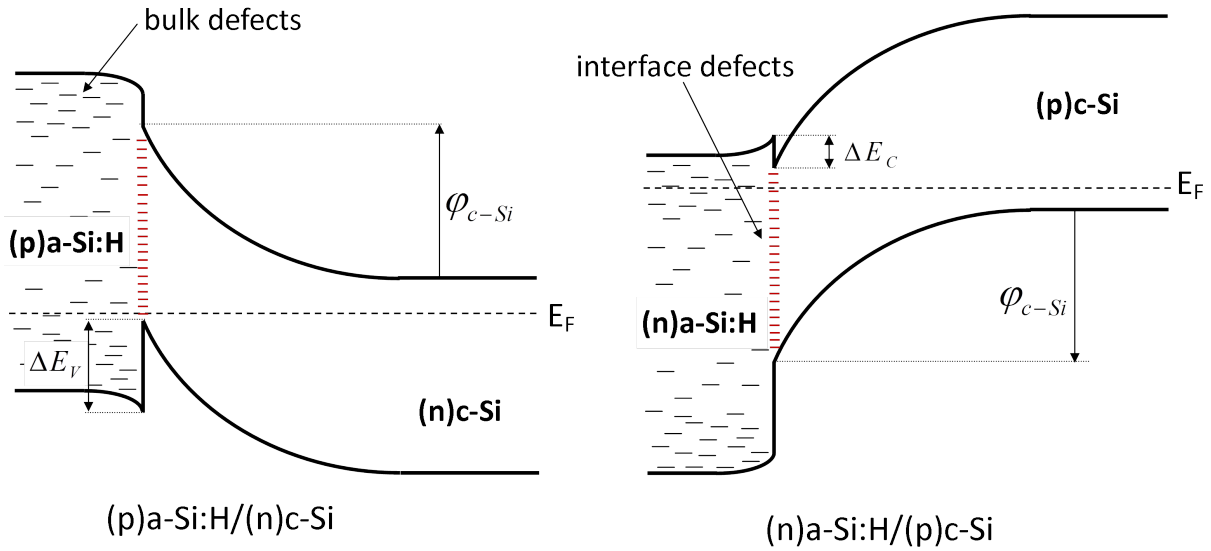

Figure 1.7: Band diagrams of (n)a-Si:H/(p)c-Si and (p)a-Si:H/(n)c-Si heterojunctions.

1.2.3.2 Inversion layer: the (p)*c*-Si/(n)*c*-Si induced diode

When (p)*a*-Si:H and (n)*c*-Si are brought in contact, the energy difference between the Fermi levels of the two materials (not yet in contact) is so important that a huge amount of electrons transfer from (n)*c*-Si to (p)*a*-Si:H when forming the heterocontact. In *c*-Si, it leaves an interface region where holes are majority carriers: a p-induced *c*-Si region appears and the *c*-Si surface is inverted. On the other side, in (p)*a*-Si:H, only a small band bending is necessary to discharge defects counterbalancing the positive charge in *c*-Si.

Measurements of the planar conductance on an *a*-Si:H/*c*-Si heterostructure proved the existence of a strongly inverted region [Favre 10]. Conductive Probe Atomic Force Microscopy measurements performed on a section of a heterojunction also revealed the existence of a high conductive channel located at the interface between *a*-Si:H and *c*-Si [Maslova 10].

The inversion layer reflects the high band bending in *c*-Si: if the wafer is n-doped, then a strong p-doped effective region is located closed to the interface. The heterojunction can actually be seen as a (p)*a*-Si:H/(p-effective)*c*-Si/(n)*c*-Si junction. The inversion channel is dependent on the materials and interface parameters, like the band offsets, the built-in potential across the junction, the defect density in bulk *a*-Si:H, the interface defect density, etc. A detailed analysis will be presented later in this thesis.

1.3 Summary and conclusions

By way of summary, now that the main characteristics of the *a*-Si:H/*c*-Si interface have been presented, it is worth looking briefly at their influence on solar cell performance.
Stangl showed from numerical studies that the valence band offsets window giving the maximum output efficiency for (p)*a*-Si:H/(n)*c*-Si is rather narrow and centred around 0.45 meV [Stangl 01]. Outside this range, two different solar cell parameters are negatively influenced. When the valence band offset is too small, the open circuit voltage (see section 2.2.3.1 for definition) does not benefit from the heterojunction and remains at low values. On the other side, when the valence band offset is too high, hole current is seriously reduced, which degrades the fill factor and ultimately the short circuit current.
The presence of interface defects has its biggest impact on the open circuit voltage [Stangl 03]. Schmidt showed that interface defect densities higher than 10^{11} cm^{-2} seriously deteriorate cell performance [Schmidt 06]. The reduction of the defect density is thus a major objective towards the improvement of device efficiency. To this end, the Japanese company Sanyo developed the HIT concept (for Heterojunction with Intrinsic Thin layer) [Taguchi 00], where a thin intrinsic *a*-Si:H layer hosting a low defect concentration is used as a buffer layer between doped *a*-Si:H and *c*-Si.
The band bending in *c*-Si depends on several structure parameters, such as doping on both sides of the junction, band offsets, etc. A detailed study will be presented later. However it

is already worth saying that a weak band bending leads to low open circuit voltage [Centurioni 03, Varache 12c].
Obviously, the three interface properties presented so far, namely band offsets, interface defects and band bending, are not independent of each other. Intuitively, as heterojunctions have been introduced partly to increase the open circuit potential of crystalline silicon homojunctions, band offsets and band bending are linked. It will be shown later that the higher the valence band offset, the higher the built-in voltage and the band bending in *c*-Si. Band bending in *c*-Si creates an inversion layer at the interface meaning that only one type of carrier is present, which limits the recombination (this is called field effect passivation) [Leendertz 10a]. Experimentally, varying the *a*-Si:H deposition parameters may reduce the interface defect density on one side, but also increase considerably the band gap and thus the band offsets on the other side; the advantage gained by the lowering of the interface defect density may be lost by the carrier transport resistance due to high band offsets. Following the same idea, thick (i)*a*-Si:H layer passivates well the *c*-Si surface; yet, integration of thick (i)*a*-Si:H layers in the device is not reasonable, as charge transport would be seriously hindered, as well as the band bending in *c*-Si.

In this chapter the main notions required for the understanding of this manuscript have been introduced. The reader is referred to cited works for more detailed discussions. Band offsets, interface defects and band bending constitute the main fingerprints of the *a*-Si:H/*c*-Si heterocontact. A large amount of work has already been done on the understanding of this structure, and led to significant power conversion efficiency improvement. However there are topics which are still being discussed. In particular there is a need for accurate electrical measurements of the band offsets. A deep understanding of the dependence of the band bending on relevant heterojunction parameters could help to optimize solar cells. Regarding interface passivation, new insights can be brought by new interfaces. These three aspects will be addressed after introducing the experimental and modeling tools used for the investigation of the amorphous silicon/crystalline silicon heterojunction.

2

Samples preparation & characterization and modeling tools

In order to investigate the amorphous silicon/crystalline silicon hetero-contact, experimental and theoretical studies have been carried out. In this chapter, the preparation of *a*-Si:H/*c*-Si heterojunctions is presented: cleaning of *c*-Si wafers, *a*-Si:H deposition technique, formation of electrical contacts. Then, the experimental methods to probe the band bending in *c*-Si and *a*-Si:H/*c*-Si interface defects are introduced. Standard solar cell characterization tools are briefly described. Finally, basics of the numerical simulation software AFORS-HET are given.

2.1 Amorphous silicon/crystalline silicon heterojunction preparation

As presented in section 1.2, the interface between *a*-Si:H and *c*-Si is a complex system, where interface defects, band line-up and charge transfers play interconnected roles. The device fabrication requires particular care to obtain abrupt junctions and avoid contaminations. The preparation process is here shortly described.

2.1.1 Preparation of the *c*-Si surface

Most investigations presented in this manuscript will deal with (n)*c*-Si wafer based samples; (p)*c*-Si based samples are also studied in some particular cases. Float-Zone (FZ) silicon wafers are used, with a diameter of 4 inches and a resistivity in the range 1...5 Ohm cm. Both sides are polished. The key constituent of most samples studied in this work is a *c*-Si wafer covered by a nanometre thin *a*-Si:H layer. The first step in the fabrication process is the *c*-Si surface preparation. Indeed, as-received wafers may have adsorbed impurities (metal atoms, organic complexes) at their surfaces due to sawing, transport and storage and a detrimental native oxide grows rapidly at *c*-Si surfaces stored in air. In order to clean the surface and make it as smooth as possible, a procedure to get H-passivated surfaces has been developed in the 1960s by Kern [Gale 07], while working at the Radio Corporation of America (RCA) in the field of semiconductors manufacturing. The so-called RCA-process is based on a sequence of oxidation steps that encapsulate contaminants in a SiO_2 matrix, and etching steps that remove the oxide layers. The standard procedure is schematically presented in Fig. 2.1. For the experiments carried out in the present work, samples were cleaned and stored after the last RCA step and before the final etching. The latter was accomplished just before loading the samples into the deposition chamber to prevent any native oxidation or contamination between cleaning and deposition.

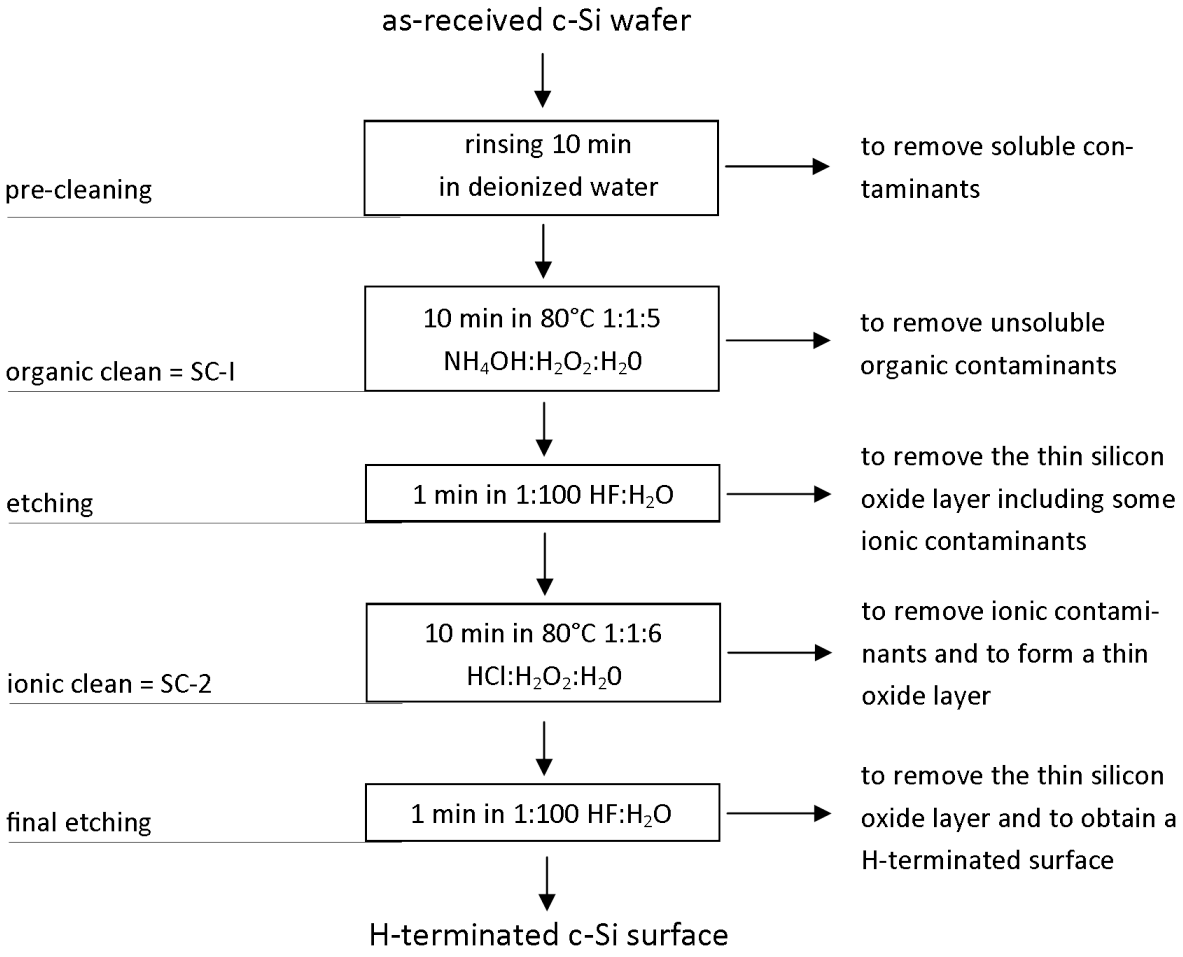

Figure 2.1: Standard RCA wafer cleaning procedure [Gale 07]. SC is used for Standard Cleaning.

2.1.2 *a*-Si:H deposition

Hydrogenated amorphous silicon films are deposited on cleaned H-terminated *c*-Si surfaces by plasma enhanced chemical vapor deposition (PECVD). The technique is based on the decomposition of precursor gases by a RF source. The resulting plasma is in contact [1] with the silicon substrate where Si atoms and $\mathrm{Si-H}$ complexes are adsorbed. Precursor gases used are silane ($\mathrm{SiH_4}$) diluted in hydrogen ($\mathrm{H_2}$) for intrinsic films. To obtain p-doped *a*-Si:H, diborane ($\mathrm{B_2H_6}$) is added to the gas mixture, whereas phosphine ($\mathrm{PH_3}$ is introduced in the chamber when n-doped *a*-Si:H is required. Samples realized at the HZB in the frame of this thesis were processed in a six-chamber cluster tool including three parallel-plate PECVD chambers, two load-locks and a hydrogen passivation chamber. Standard parameters used at HZB for the deposition are summarized in Table 2.1.

[1] In special configurations such as ECR (Electron Cyclotron Resonance) [Sasaki 01] or Saddle Field [Bahardoust 10] the plasma may not be in direct contact with the substrate.

Table 2.1: Deposition parameters used in a RF-PECVD system during the deposition of a-Si:H films at HZB.

Layer	(i)*a*-Si:H	(n)*a*-Si:H	(p)*a*-Si:H
Role	Buffer layer	Back surface field	Emitter
Substrate temperature (°C)	200	130	190
RF frequency (MHz)	13.6	60	60
Silane flow rate (sccm)	10	10	10
Doping (ppm) (gas)	none	2000 (PH_3)	2000 (B_2H_6)
Deposition pressure (mbar)	0.5	0.5	0.5
Layer thickness (nm)	5	10	20

In addition, samples from different institutes were characterized: LPICM (Ecole Polytechnique, France), INES (CEA, France), University of Toronto (Canada). Similar conditions and processes were used to make samples. Samples from LPICM and INES were deposited in standard RF-PECVD systems and those from the University of Toronto were prepared in a saddle-field PECVD chamber. This last deposition method, still under development, separates the plasma from the substrate, which limits the impact of highly energetic particles, while it increases the mean free path of electrons: the precursor gases decomposition is then enhanced [Bahardoust 10].

In all cases the deposition operates at low temperature, typically lower than 200°C, which prevents any damage of the *c*-Si wafer. In addition, the deposition remains at a low energetic budget.

2.1.3 Formation of electrical contacts

To complete the solar cell structure, a transparent conductive oxide (TCO) is deposited on the front side of the structure. 80 nm of aluminium-doped zinc oxide (ZnO:Al) was sputtered in a reactive DC sputtering process under ultra-high vacuum from a metallic zinc target containing 1 weight-% Al under argon and oxygen atmosphere. Aluminium contacts of thickness around 1 µm were deposited on both sides: the back side is fully metalized, whereas a grid-structured mask is used for the front side. During the final step, 1 cm^2 cells were defined by photolithographic mesa etching.

In Fig. 2.2, the standard cell structure prepared at HZB resulting from the standard steps presented up to now is shown.

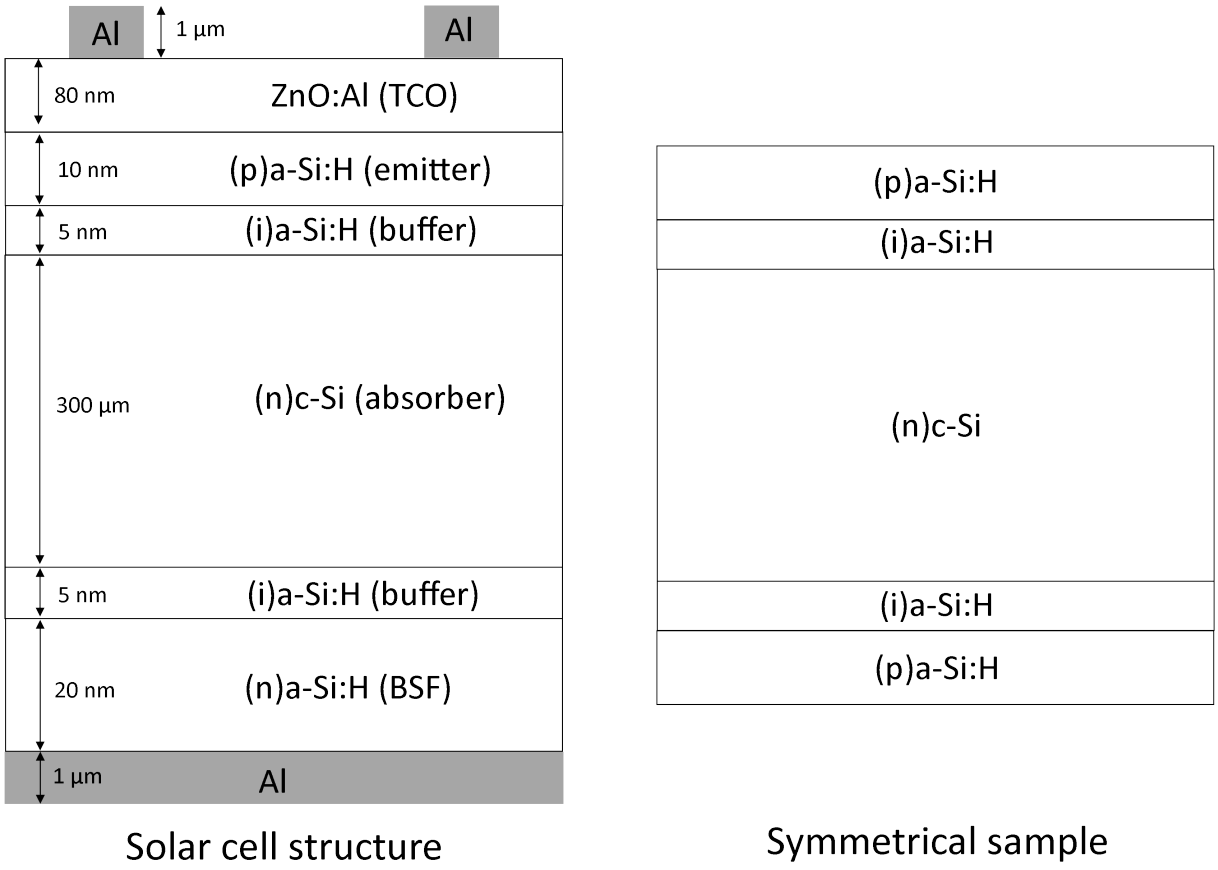

Figure 2.2: Complete solar cell structure as processed at HZB and standard symmetrical sample structure for lifetime measurements (Photo-conductance decay and photoluminescence; see below). BSF stands for Back Surface Field.

2.2 Characterization techniques

As presented in Chapter 1, the *a*-Si:H/*c*-Si heterojunction is the building block of silicon heterojunction solar cells. It is thus of particular interest to study and finely understand the properties and the behaviour of the *a*-Si:H/*c*-Si heterojunction: band line-up, recombination, etc., and to correlate these features with solar cells performance. To this aim, some experiments have been developed; characterization methods used to extract information on band bending (surface photo-voltage, planar conductance) and on interface defects (voltage dependent surface photo-voltage, photo-conductance decay, modulated photo-luminescence) are now briefly described. In the end, tools to assess the solar cells performance are presented.

2.2.1 Band bending measurement

Due to charge equilibration at the *c*-Si surface a band bending builds up in a region (the space charge region; SCR) close to its surface (see section 1.2.3). This is particularly true

for free surfaces [2] (right after oxide removal for instance), oxidized surfaces or *a*-Si:H/*c*-Si heterocontacts. For free or oxidized surfaces the measurement of the band bending gives access to the surface charge. In *a*-Si:H/*c*-Si heterojunctions, the band bending attests the presence of a rectifying p-n junction (see Chapter 4).

2.2.1.1 Surface photo-voltage: SPV

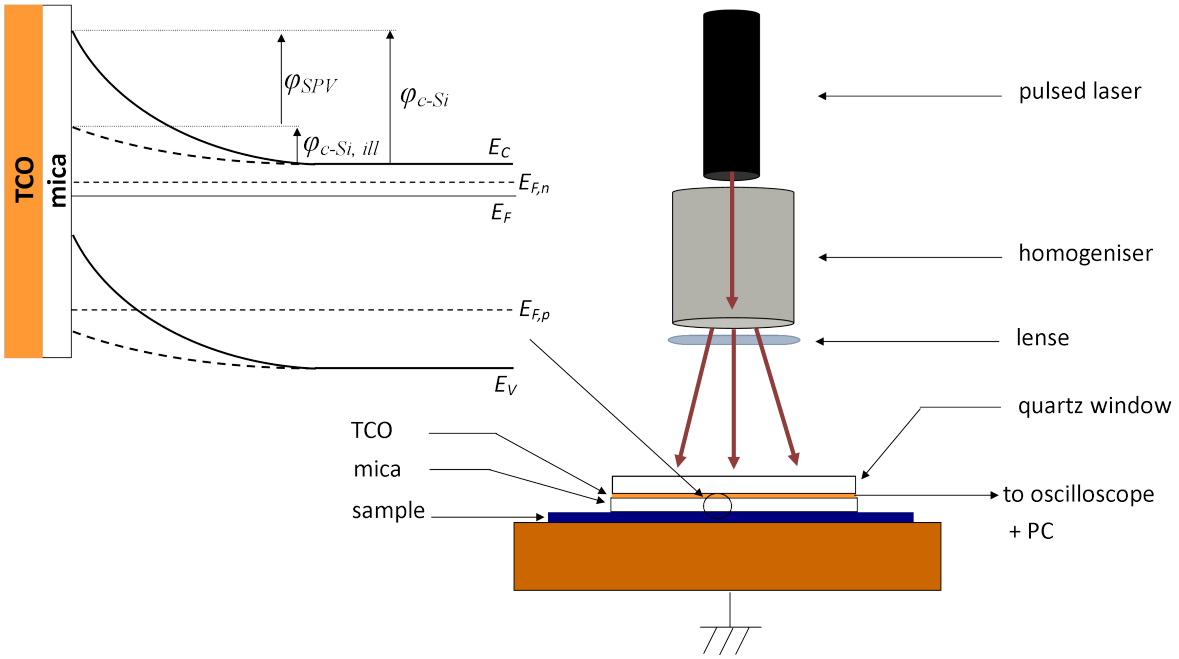

Figure 2.3: Schematic view of the surface photo-voltage experimental setup. A sketch of the band diagram at the surface of the sample is also shown.

Introduction: The surface photo-voltage measurement technique (SPV) is used to measure the surface band bending. Different measurement setups have been elaborated [Kronik 99]. A configuration using a metal-insulator-semiconductor (MIS) contact was developed at HZB by Heilig [Heilig 74]. The basic principle relies on the measurement of the surface potential difference before and after a short light impulse. If the injection of free carriers is high enough with respect to the surface charge, the conduction and valence bands flatten at the surface right after the excitation. The surface potential is modified by an amount equal to the dark band bending. A schematic view of the experimental setup is shown in Fig. 2.3. The MIS structure is made of a transparent conductive oxide (TCO) layer deposited on a quartz window with a diameter of 1 cm; a typically 20 µm thick mica foil is used to insulate the semiconductor sample from the TCO. The back side of the sample is contacted through two spikes; it is either grounded or a voltage up to 1000 V can be applied. The sample is illuminated through the

[2] Even on H-terminated surfaces, a surface density of states, thus surface charge, remains.

quartz window by a pulsed laser (160 ns) at a wavelength of 905 nm (above the band gap of *c*-Si, but below the band gap of *a*-Si:H and SiO_2). An homogeniser and a system of lenses make the laser beam as homogeneous as possible on the active area. The SPV signal, U_{SPV}, is recorded in the TCO over time thanks to an oscilloscope through a fast impedance converter. The pulse signal and a typical time-resolved (also called 'transient') SPV measurement can be seen in Fig. 2.4. At the beginning of the pulse, a high density of excess carriers is generated: U_{SPV} increases rapidly from zero. During the laser pulse U_{SPV} still increases, but more slowly as a competition between generation and recombination takes place. Once the laser turns off, carriers recombine and U_{SPV} decreases. In the frame of this work, the dependence of the SPV signal on time will not be discussed. The interpretation of transient measurements as a tool for the determination of the surface limited excess carrier lifetime can be found in Caspar Leenderzt's thesis [Leendertz 11a] and in [Korte 09]. The SPV signal maximum is denoted as U_{SPV} in this thesis (U_{max} in Fig. 2.4).

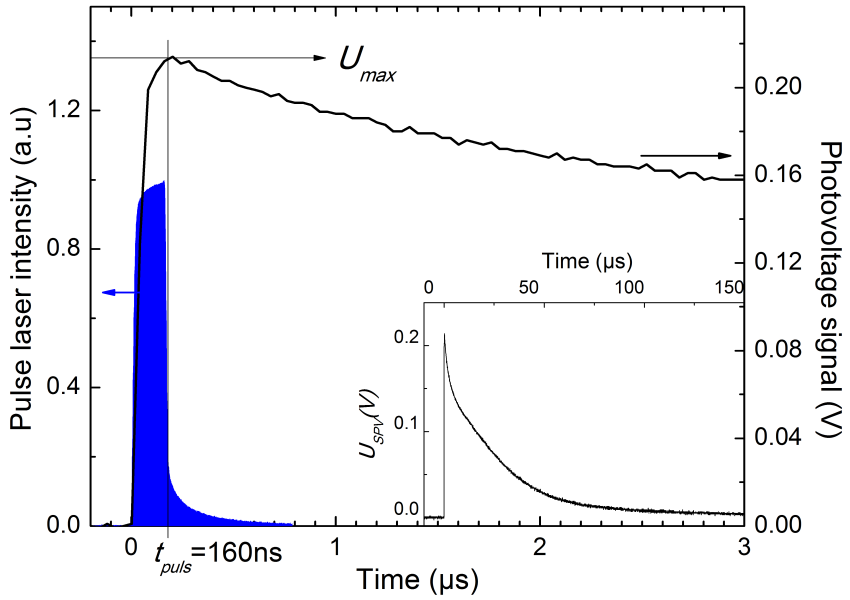

Figure 2.4: SPV setup laser pulse signal (blue) and time resolved surface photo-voltage measurement (full transient in the inset). The end of the laser pulse corresponds to the maximum SPV signal.

Calculation of the band bending in *c*-Si: The measurement of the surface photo-voltage U_{SPV} does not give direct access to the dark band bending in *c*-Si (φ_{c-Si}). Two major points have to be considered. First, the conduction and valence bands become flat at the interface only for low dark band bending and/or high laser intensity[3]. If the band bending in *c*-Si is high, more excess carriers are needed to counterbalance the SCR charge; higher injection

[3]In the case of strong pinning of E_F at the surface due to a high surface defect density, the bands could not be flattened. This case is not taken into account in the following analysis.

levels can be achieved using higher laser power. In most cases, a residual band bending remains at the end of the laser pulse. The determination of φ_{c-Si} has to take it into account. Secondly, electrons and holes generated in the sample drift-diffuse in opposite directions with different mobility values. This leads to an inhomogeneous repartition of electrons and holes in the sample, and gives rise to an additional voltage drop, called Dember voltage, that has to be accounted for.

The approximation that no surface defects are charged or discharged during the short laser pulse and the measurement is made, such that the calculation of φ_{c-Si} results from the charge conservation in the space charge region before and after the light excitation:

$$Q_{SCR}\left(\Delta n = 0, \Delta pn = 0, \varphi_{c-Si}\right) = Q_{SCR}\left(\Delta n, \Delta p, \varphi_{c-Si,\mathrm{ill}}\right), \tag{2.1}$$

where Q_{SCR} denotes the charge in the space charge region and is given by [Frankl 67]:

$$Q_{SCR}\left(\Delta n, \Delta p, \varphi\right) = \mathrm{sign}\left(\varphi\right)\sqrt{2\frac{\epsilon_0\epsilon_r}{q^2}}\cdot F\left(\Delta n, \Delta p, \varphi\right), \tag{2.2}$$

with

$$F\left(\Delta n, \Delta p, \varphi\right) = \sqrt{\varphi\left(N_A - N_D\right) + k_B T\left(\left(p_0 + \Delta p\right)\left(e^{\frac{\varphi}{k_B T}} - 1\right) + \left(n_0 + \Delta n\right)\left(e^{-\frac{\varphi}{k_B T}} - 1\right)\right)}. \tag{2.3}$$

Δn and Δp are the electron and hole excess carrier densities, respectively. $\varphi_{c-Si,\mathrm{ill}}$ is the remaining band bending in c-Si under illumination (see Fig. 2.3). ϵ_0 and ϵ_r are respectively the vacuum permittivity and the relative dielectric constant of c-Si: $\epsilon_0 = 8.854 \times 10^{-12}$ C V^{-1} m^{-1} and $\epsilon_r = 11.9$. N_A and N_D are the acceptor and donor dopant concentrations, k_B is Boltzmann's constant, T the temperature, p_0 and n_0 the equilibrium bulk hole and electron concentrations.

Assuming $\Delta n = \Delta p$, Eqs. 2.2 and 2.1 lead to the expression for φ_{c-Si} [Heilig 74]:

$$\varphi_{c-Si} = -k_B T \ln\left(a - \text{sign}\left(\varphi_{SPV}\right)\sqrt{a^2+2b^2}\right) \tag{2.4}$$

with

$$a = \frac{1}{c}\left(\left(\frac{1}{\lambda}-\lambda\right)\frac{\varphi_{SPV}}{k_B T}+\frac{2\Delta n}{n_i}\right)$$

$$b = \frac{1}{c}\left(\lambda-\left(\lambda+\frac{\Delta n}{n_i}\right)\exp\left(-\frac{\varphi_{SPV}}{k_B T}\right)\right)$$

$$c = 2\left(\left(\frac{1}{\lambda}+\frac{\Delta n}{n_i}\right)\exp\left(-\frac{\varphi_{SPV}}{k_B T}\right)-\frac{1}{\lambda}\right)$$

$$\lambda = \frac{n_i}{n_0},$$

$\varphi_{SPV} = \varphi_{c-Si} - \varphi_{c-Si,\text{ill}}$ (see Fig. 2.3).

n_i is the intrinsic carrier density in c-Si. The oscilloscope measures the photo-voltage $U_{SPV} = \frac{\varphi_{SPV}}{q} + U_D$ where U_D is the Dember voltage given by:

$$U_D = \frac{k_B T}{q}\frac{b-1}{b+1}\ln\left(1+\Delta n\frac{b+1}{n_0 b+p_0}\right), \tag{2.5}$$

where $b = \frac{\mu_n}{\mu_p}$ is the ratio between electron and hole mobility values [Wuerfel 95].

The measurement of U_{SPV}, together with the calculation of U_D from Eq. 2.5, gives φ_{c-Si} from Eq. 2.4 provided that the excess carrier density Δn is known. In order to calibrate the setup and find Δn, a method was developed by Heilig [Heilig 74]: for a p-type wafer, the Dember voltage and the photo-voltage have opposite signs such that a minimum of the SPV signal as a function of Δn can be calculated and measured by changing the laser power. From the additional relationship coming from the minimization of U_{SPV}, Δn can be estimated. The procedure has been done recently by Caspar Leendertz during this work, and Δn was estimated at $2\times10^{17}\text{cm}^{-3}$ [Leendertz 11a]. Errors on Δn values were not estimated though. An estimation of the laser flux by a photodiode led to an excess carrier density slightly lower, around $6\times10^{16}\text{cm}^{-3}$. In both cases variations between samples with different surface properties (parasitic absorption in front layers, difference in reflectivity, etc.) may lead to variations of Δn.

Limits of the SPV technique for band bending measurements: In order to point out the limits of the SPV technique as a measurement method of the band bending, φ_{c-Si} at a (n)c-Si wafer surface was calculated as a function of the measured SPV signal and plotted in Fig. 2.5.

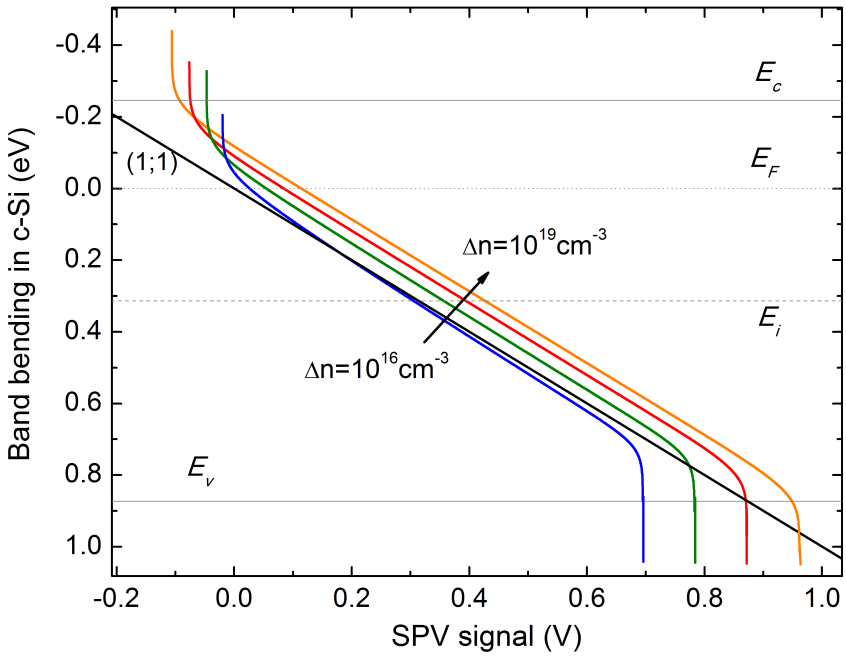

Figure 2.5: Band bending in (n)c-Si φ_{c-Si} upon the measured SPV signal U_{SPV} as calculated in Eq. 2.4 for different excess carrier densities Δn. For information, the bulk conduction and valence band edges, as well as the Fermi and intrinsic levels are shown.

For low excess carrier density, the Dember voltage is low enough so that the measured SPV voltage is the actual band bending. This is true as long as the band bending is weak enough so that the bands flatten during the laser pulse, typically between 0.1 eV and 0.6 eV. For increasing excess carrier density, the Dember voltage plays a significant role: $\varphi_{c-Si}(U_{SPV})$ curves deviate from the $\varphi_{c-Si} = U_{SPV}$ straight line (black in Fig. 2.5). Therefore it is important that the measured sample has an unpassivated rear side with a high recombination velocity such that the excess carrier density is null on the rear side (assumption made to derive the Dember voltage in Eq. 2.5).

At higher injection levels (higher Δn), the bands can be flatten for band bending values exceeding 0.6 eV, typically up to 0.85 eV for $\Delta n = 10^{19}$ cm^{-3}. For a particular Δn, and at high band bending, the $\varphi_{c-Si}(U_{SPV})$ curve diverges. This is because when the band bending increases, the charge in the SCR becomes greater than Δn. $\varphi_{c-Si,\Delta n}$ is defined as the maximum dark band bending in *c*-Si which can be reduced to 0 after a laser pulse corresponding to an excess carrier density Δn: for any φ_{c-Si} greater than $\varphi_{c-Si,\Delta n}$ the SPV signal will saturate as the change of surface voltage will be the same. Thus a slight error on the measurement of U_{SPV} leads to a large uncertainty on φ_{c-Si}.

Moreover, for highly inverted surfaces, the classical calculation of the SCR charge in Eq. 2.2 based on Boltzmann statistics may not be accurate anymore, as the surface (or interface) Fermi level may get very close to or even lie in the band; a treatment based on Fermi-Dirac statistics would give a better accuracy. Confinement in the quantum well formed by the band curvature on one side, and by the mica barrier (or *a*-Si:H in the case of heterojunction) on

the other side is not excluded a priori. In this case, the density of states in *c*-Si could be very different to that used above to write Eq. 2.2 (see section 3.1.7).
As a consequence, the SPV method as such is not suitable for measuring high band bending, 'high' being related to (i) the excess carrier density the laser can generate and (ii) the reliability of Boltzmann's approximation. In this study, the SPV characterization technique will not be used for the determination of φ_{c-Si} in (p)*a*-Si:H/(n)*c*-Si structures because they yield a high band bending (usually above 800 meV, see Chapter 4). However it will be very useful for characterizing free and oxidized surfaces.

2.2.1.2 Planar conductance: focus on the rectifying *a*-Si:H/*c*-Si heterojunction

The planar conductance technique consists in measuring, as a function of sample temperature, current-voltage characteristics between two coplanar electrodes of length l, separated by a distance d and deposited on a rectifying heterojunction (see Fig. 2.6). The current-voltage characteristics are in most cases linear in the typical measurement range (between −1 V and 1 V). The conductance G is extracted from the slope of current-voltage characteristics, and is normalized with the ratio d/l:

$$G_{\text{norm}} = G\frac{d}{l}. \tag{2.6}$$

This measurement technique has been developed at LGEP [Kleider 08]. The sample configuration for a (p)*a*-Si:H/(n)*c*-Si heterojunction is shown in Fig. 2.6.

Provided that a high concentration of carriers is present at the interface (in the inversion layer), three conduction paths for the current are present: (1) through the *a*-Si:H layer, (2) through the highly conductive interface channel and (3) through the bulk wafer. It has been shown on both (p)*a*-Si:H/(n)*c*-Si and (n)*a*-Si:H/(p)*c*-Si structures that paths (1) and (3) are negligible compared to path (2) if the *a*-Si:H layer is highly doped, so that the inversion layer forms (see Fig. 2.7) [Kleider 08, Favre 10]. Indeed, measurements of the conductance of the same *a*-Si:H layer deposited on glass (path (1), "*a*-Si:H/glass" in Fig. 2.7) give values several orders of magnitude less than those measured on the heterojunction (sum of the three paths, "*a*-Si:H/*c*-Si" in Fig. 2.7). Similarly, measurement on an etched heterojunction – *a*-Si:H remains only below the metallic contacts, such that the *c*-Si surface is free between them – (path (3), "*a*-Si:H/*c*-Si, etched" in Fig. 2.7) proved that, whatever the applied voltage, one diode is reverse biased so that the current is very low. Fig. 2.7 presents results on (n)*a*-Si:H/(p)*c*-Si structures; similar data on (p)*a*-Si:H/(n)*c*-Si structures can be found in [Favre 10]. Thus, the measurement of the planar conductance on a heterojunction gives direct access to the interface channel conductance.

Electrodes with different gaps between them were deposited to allow for transmission line

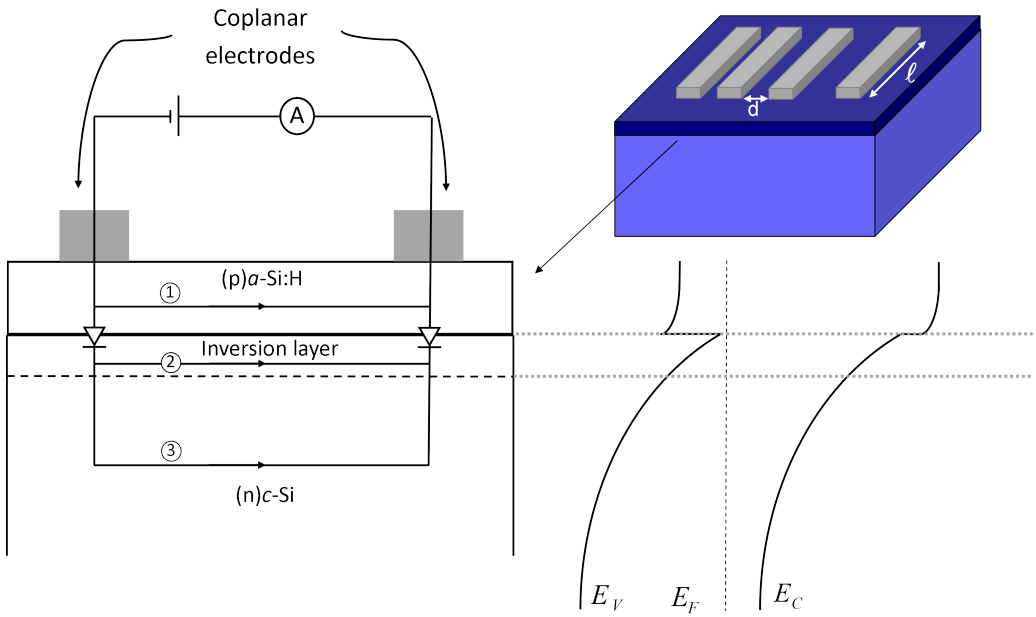

Figure 2.6: Sample configuration for planar conductance measurements (top right). Three possible conduction paths are shown (left), as well as the 1D band diagram (bottom right).

measurements (TLM) in order to test the ohmic behaviour of the channel. The contact geometry was such that the length of the electrodes l was larger than the spacing d between them (see Fig. 2.6), typically by a factor of ten. In that way, field lines sticking out of the $l \times d$ rectangle can be neglected. Planar conductance measurements were performed under vacuum (typically 10^{-6} mbar), in a liquid nitrogen cooled cryostat.

In *a*-Si:H/*c*-Si heterostructures, the measurement of a high interfacial conductance has been attributed to an inversion layer in *c*-Si at the interface; the conductance G is directly related to the minority carrier density at the interface and thus to the band bending in *c*-Si. The detailed analysis of $G(T)$ measurements was partly developed in the frame of this work: in Chapter 3, planar conductance data are used to extract the built-in voltage and the band offsets at the *a*-Si:H/*c*-Si interface, and in Chapter 4 the planar conductance technique is presented as a method to directly measure the band bending.

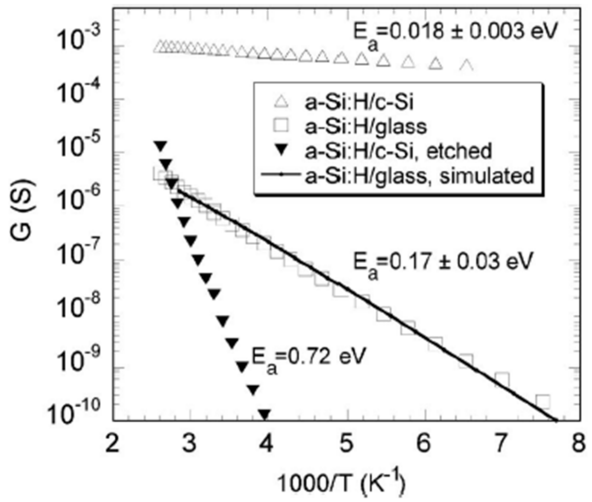

Figure 2.7: Temperature dependence of the measured conductance of a-Si:H/ glass and a-Si:H/ c-Si structures before and after etching. Reproduced from [Kleider 08] with permission.

2.2.2 Interface defect probing

The critical role played by *a*-Si:H/*c*-Si interface defects has been introduced in section 1.2.2. Several characterization techniques have been developed to investigate the recombination at *c*-Si surfaces or interfaces with other materials. A few of them are presented in the following.

2.2.2.1 Voltage dependent surface photo-voltage

The SPV setup presented in section 2.2.1.1 also allows to estimate the density of surface states, as reported by Lam [Lam 71]. The experimental method and the analytical analysis are similar to the one used for capacitance-voltage measurements. A bias voltage V_g is applied to the MIS structure; if V_{ox} is the potential drop across the mica foil (playing the role of insulator), Q_g the gate charge, Q_{SCR} the charge in the space charge region and Q_{int} the charge in surface states:

$$dV_g = dV_{ox} + \frac{1}{q} d\varphi_{c-Si}, \tag{2.7}$$

$$dQ_g + dQ_{SCR} + dQ_{\text{int}} = 0. \tag{2.8}$$

The mica capacitance is given by

$$C_{ox} = \frac{dQ_g}{dV_{ox}}, \tag{2.9}$$

and the density of surface states at a given surface potential $D_{\text{it}}(\varphi_{c-Si})$ reads

$$D_{\text{it}} = -\frac{dQ_{\text{int}}}{d\varphi_{c-Si}}. \tag{2.10}$$

As a result, D_{it} is extracted from the measurement of φ_{c-Si} versus V_g:

$$D_{\text{it}} = C_{ox}\left(\frac{dV_g}{d\varphi_{c-Si}} - \frac{1}{q}\right) + \frac{dQ_{SCR}(\varphi_{c-Si})}{d\varphi_{c-Si}}. \tag{2.11}$$

$\frac{dV_g}{d\varphi_{c-Si}}$ can be numerically determined by the local slope of the measured $V_g(\varphi_{c-Si})$ curve; $\frac{dQ_{SCR}(\varphi_{c-Si})}{d\varphi_{c-Si}}$ can be calculated analytically from Eq. 2.2, with $\Delta n = \Delta p = 0$. C_{ox} is measured at the beginning of the experiment.

It is not possible to measure D_{it} on *a*-Si:H/*c*-Si structures because the high fixed charge in *a*-Si:H 'pins' the Fermi level: the interface Fermi level position cannot be changed by applying voltages in the range of what is available on the setup used here. However, measurements of the density of surface states with the voltage dependent SPV (VD-SPV) method work well for free or oxidized surfaces, where the surface charge is low.

2.2.2.2 Photo-conductance decay

Principle of the Sinton lifetime tester: The photo-conductance decay (PCD) technique has been developed and commercialized by Sinton Consulting [Sinton 96b]. In this work the WCT-100 version of the lifetime tester was used (see a schematic view of the system in Fig. 2.8).

This contactless characterization technique relies on a change of the wafer conductance after a photo flash excitation [Sinton 96a, Cuevas 96]. The wafer, placed near the coil of an oscillator circuit, is illuminated with filtered infrared light in order to have homogeneous absorption in the thickness of the wafer. The generated excess charge carriers cause a variation of the conductance of the sample and generated Foucault's currents modify the coil inductance which can be detected via an external voltage measurement by a fast external circuit. The variation of the conductance ΔG reads: $\Delta G = q(\mu_e \Delta n + \mu_h \Delta p) d_{c-Si}$ where Δn and Δp are the average values of the excess electron and hole densities in the wafer. They are assumed identical, such that $\Delta G = q(\mu_e + \mu_h) d_{c-Si} \Delta n$. As ΔG is proportional to the excess carrier density Δn, the latter can be recorded over very short time steps. The effective excess carrier lifetime is given by $\tau_{\text{eff}}(\Delta n(t)) = -\Delta n(t)\left(\frac{d\Delta n(t)}{dt}\right)^{-1}$ [Nagel 99]. The result of the measurement is thus a $\tau_{\text{eff}}(\Delta n(t))$ data set.

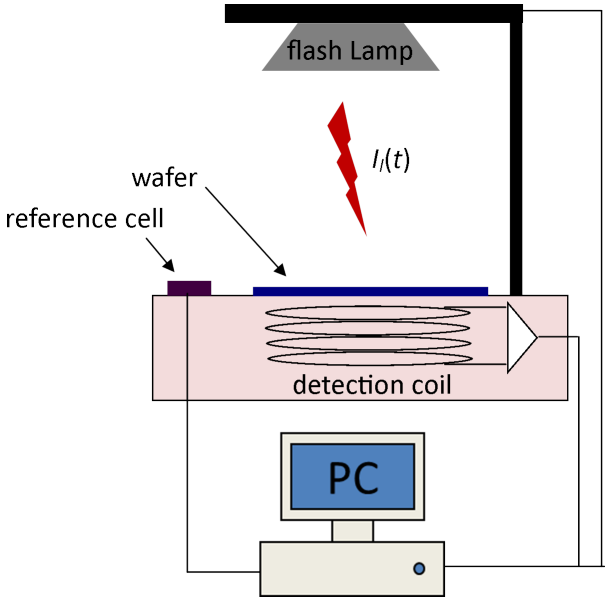

Figure 2.8: Photo-conductance decay measurement setup similar to the WCT-100 proposed by Sinton Consulting.

PCD is sensitive to recombinations everywhere in the sample; therefore, if one wants to investigate one surface, the opposite one has to be very well passivated such that the investigated surface is the limiting one [4]. This is usually done by deposition of a thick (i)*a*-Si:H layer on the *c*-Si wafer. Alternatively, symmetrical structures as presented in Fig. 2.2 can be used.

PCD data analysis: Usually, the lifetime value at a particular injection level Δn is used as a reference parameter for the material quality. The effective lifetime at $\Delta n = 10^{15}\text{cm}^{-3}$ is commonly reported. Alternatively, the injection level corresponding to one sun illumination might be used as a reference value. However, more information can be extracted from $\tau_{\text{eff}}(\Delta n(t))$ data sets. Indeed, it has been reported that a reduction of the interface defect density improves the minority carriers lifetime at high injection levels, whereas field effect increase the passivation for lower Δn. Detailed analysis of PCD measurements have been reported [Garin 05, Olibet 07, Steingrube 10, Leendertz 10a]. They all provide fitting tools for the extraction of interface parameters from PCD measurements. In the frame of this work, the model developed by Leendertz and co-workers is used to fit PCD data [Leendertz 10b, Leendertz 11a]. It models both recombination through interface dangling bond defects and field effect passivation. The band bending in *c*-Si is made injection dependent by considering Fermi-level dependent *a*-Si:H defect charge. The fit is run over two free parameters, namely the interface defect density D_{it} and a surface fixed charge Q_{fix}.

[4] The bulk *c*-Si should also be of high quality, so that τ_{bulk} can be taken as infinite in Eq. 1.20, at least below the Auger limit.

2.2.2.3 Modulated Photo-luminescence

The photo-conductance decay method has the drawback of requiring rather large free surfaces (full 2 inch wafer or quarter of 4 inch wafer minimum). It is for example not suitable for measurements on partly metallized samples. In order to track the passivation properties of the sample during its processing, or during other measurements where contacts are needed, a photo-luminescence (PL) setup has been developed at LGEP. Silicon, because of its indirect band gap, is not an efficient photo-luminescent material. Still, once free electrons and holes have been generated in the bands, the photon flux emitted by the sample is proportional to the radiative recombination rate given in Eq. 1.5 determined by the free carrier concentrations n and p. As n and p are mostly determined by recombination at interfaces, it is possible to estimate the interface recombination by measuring the emitted photon flux.
The technique has already been applied, in the steady-state regime, to investigate the passivation quality of silicon wafers [Trupke 04, Tardon 04]. However, Brüggemann demonstrated that, used in the modulated regime, the photo-luminescence technique gives direct access to the minority carrier lifetime [Brueggemann 06].

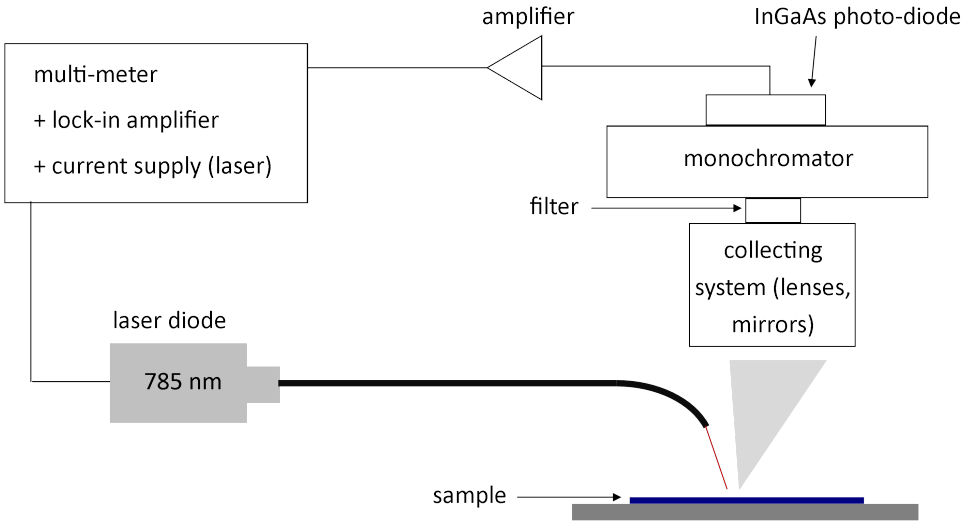

Figure 2.9: Design of the PL setup at LGEP. A filter is used to cut off the laser light reflection. The sample holder can be automatically translated to map the sample.

In this work, only the modulated photo-luminescence (MPL) will be used to characterize wafer surfaces. The PL setup used at LGEP has been developed by Favre [Favre 11], and a schematic view of the technique is shown in Fig. 2.9.
Electron-hole pairs are generated in the sample by illumination from a laser diode ($\lambda = 785$ nm, which corresponds to a photon energy of 1.58 eV, between the c-Si and the a-Si:H band gap). Then, radiative recombination processes lead to a photon emission at different energies close to the c-Si band gap. Those photons can be collected through an optical system with

mirrors and lenses which also focuses the luminescence signal onto a monochromator. An InGaAs photodiode converts the photon flux into a voltage, which is amplified and measured by a multimeter. The laser flux can be modulated by a lock-in amplifier at a frequency ω; the corresponding generation rate reads:

$$G(t) = G_0 + G_\omega e^{i\omega t}, \tag{2.12}$$

where G_0 is the steady-state component of the generation rate, and G_ω is the amplitude of the modulated component.
As a consequence, the PL signal is also periodic with the same frequency and with a phase shift ϕ with respect to the excitation, such that the excess carrier density can be written:

$$\Delta n(t) = \Delta n_0 + \Delta n_\omega e^{i\omega t}, \tag{2.13}$$

where Δn_0 is the steady-state excess carrier concentration. $\Delta n_\omega = \|\Delta n_\omega\| e^{i\phi}$ is the complex amplitude of the modulated excess carrier concentration. Δn_0 and Δn_ω are assumed uniform over the thickness of the sample.

Considering no external electric field, the continuity equation reads:

$$\frac{\mathrm{d}\Delta n(t)}{\mathrm{d}t} = G(t) - R(t), \tag{2.14}$$

where $R(t)$ is the recombination rate. Replacing G and R from Eqs. 2.12, 2.13 and 1.11 in Eq. 2.14 leads to:

$$\frac{\mathrm{d}\Delta n(t)}{\mathrm{d}t} = G_0 + G_\omega e^{i\omega t} - \frac{\Delta n_0 + \Delta n_\omega e^{i\omega t}}{\tau_{\mathrm{eff,PL}}}. \tag{2.15}$$

After the separation of the real and the imaginary parts of Δn [Brueggemann 06]:

$$\|\Delta n_\omega\| = \frac{\tau_{\mathrm{eff,PL}} G_\omega}{\sqrt{1 + \left(\omega \tau_{\mathrm{eff,PL}}\right)^2}} \tag{2.16}$$

$$\text{and } \phi = -\arctan\left(\omega \tau_{\mathrm{eff,PL}}\right). \tag{2.17}$$

Consequently, $\tau_{\mathrm{eff,PL}}$ can be deduced from measurements of $\|\Delta n_\omega\|$ and ϕ at different frequencies (in the setup at LGEP, typically 18 frequencies between 10 Hz and 10 kHz are used).

2.2.2.4 First measurement examples and comparison

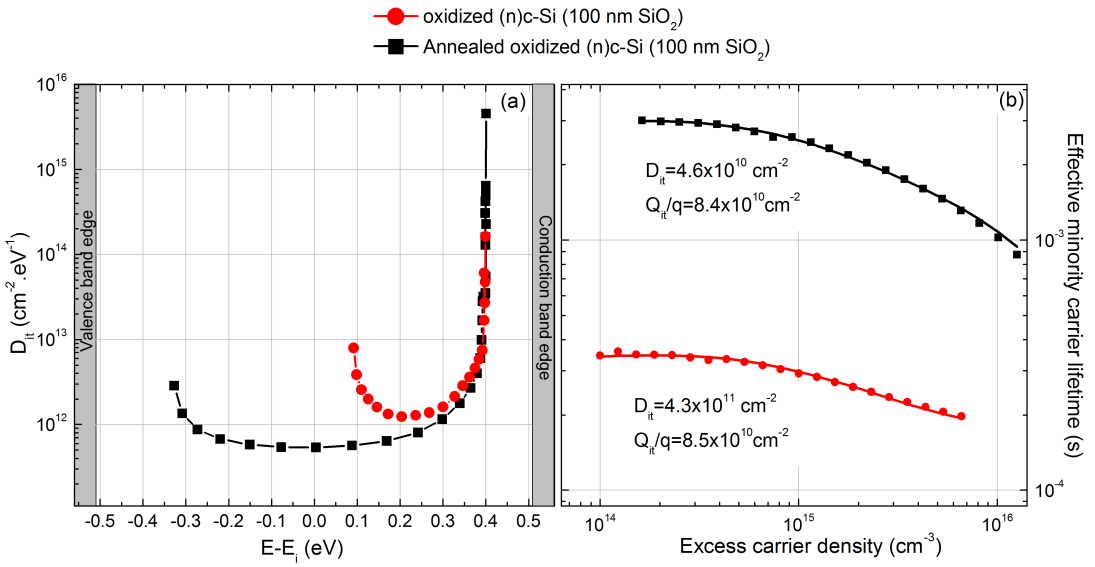

Figure 2.10: (a): Interface defect density in c-Si band gap deduced from VD-SPV measurements for two identical thermally oxidized (n)c-Si wafers; one (black squares) was annealed in forming gas.(b): For the same samples, photo conductance decay data (symbols) and fits (solid line).

VD-SPV versus PCD: In Fig. 2.10(a) typical measurements of the interface defect density measured with the VD-SPV technique on two thermally oxidized (n)*c*-Si wafers [5] are presented. One sample is measured as oxidized (red circles), the second one was annealed in forming gas [6] at 420 ˚C during 60 minutes before the measurement (black squares). The density of states is measured within a part of the *c*-Si band gap, around the equilibrium surface Fermi level position where the density of states has its minimum. For comparison, photo-conductance decay measurements of the effective lifetime as a function of the excess carrier density are shown. The fitting curves and resulting interface properties are also indicated.
Both measurements give similar trends: while the defect density decreases after annealing (SPV), the effective lifetime increases (PCD). However a comparison of D_{it} values from SPV (in $\mathrm{cm}^{-2}\ \mathrm{eV}^{-1}$) and PCD (in cm^{-2}) would require to measure the defect distribution in the full band gap with VD-SPV. This is impossible unless much higher bias voltages are applied. Moreover the knowledge of (or an assumption on) defect capture cross sections is required to fit PCD data, whereas the determination of D_{it} with the SPV technique does not require knowledge on the recombination properties of the defects. In summary, both techniques can be used separately to probe the passivation quality of a set of samples. A detailed comparison between the two techniques could give insight on the capture cross sections of interface defects.

[5] Resulting in a 100 nm SiO_2 passivation layer
[6] Forming gas is a mixture of 10% H_2 in N_2

VD-SPV versus CV: VD-SPV measurements of D_{it} are not often reported in the literature; capacitance voltage measurements are more frequently used to probe interface defects. Thus, for comparison, Fig. 2.11 presents measurements of D_{it} at the SiO_2/*c*-Si interface of a thermally oxidized (p)*c*-Si wafer, after annealing in forming gas during 60 minutes at 420 ˚C. VD-SPV and quasi static capacitance-voltage (CV) techniques were employed. No details on capacitance measurement techniques will be given here and the reader is referred to e.g. [Sze 07, Pun 00].

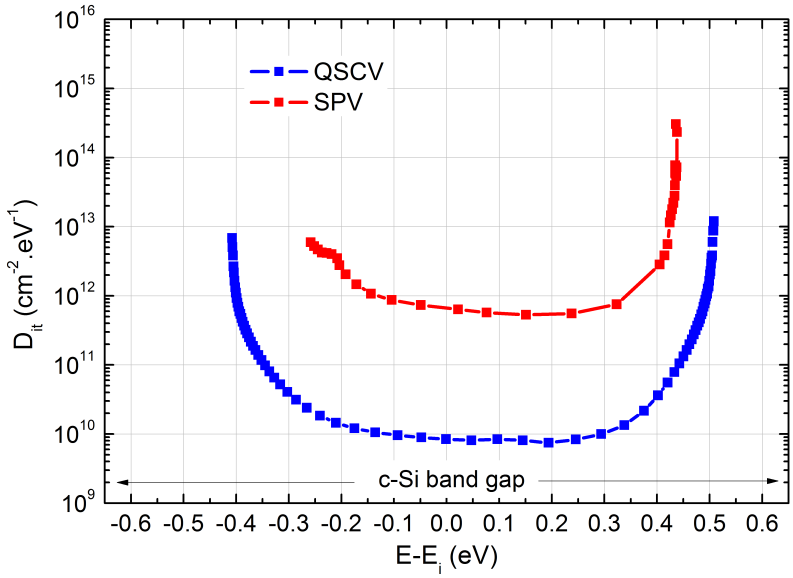

Figure 2.11: Measurement of D_{it} of an oxidized and forming gas annealed (p)c-Si wafer (100 nm SiO_2) with VD-SPV and quasi-static CV.

CV measurements systematically lead to wider distributions and lower defect densities, typically between 1 and 2 orders of magnitude lower. This difference is attributed to systematic measurement errors of the SPV method due to charge and discharge of defects which violates the assumption of charge conservation as used in deriving Eq. 2.1 [Kliefoth 03]. Indeed the SPV technique is based on large signals: during and after the laser pulse, quasi Fermi levels sweep across the whole band gap, probing thus defects over a wide energy range in the band gap. On the contrary, CV works with small amplitudes (10-20 mV), thus probing defects around the Fermi level only. Here again, a comparison between the defect density values extracted using CV and SPV measurements may lead to biased trends. However CV measurements are not possible for samples where a high leakage current deteriorates the sensitivity of the technique. In such conditions, the VD-SPV technique is the relevant one to use and qualitative changes between similar samples can be discussed.

PCD versus PL: In order to compare PCD and MPL data, it is necessary to know at which excess carrier density MPL lifetimes are measured. To this end, the excess carrier density is calculated from the steady-state equation:

$$\tau_{\text{eff}} = \frac{\Delta p}{G} \tag{2.18}$$

$$\text{with } G = \frac{(1 - R(785\text{nm}))(1 - e^{\alpha_{np}(785\text{nm})d})F}{d} \tag{2.19}$$

where R(785nm) and α_{np}(785nm) are the reflectance and absorption coefficient at the laser wavelength 785 nm, d is the thickness of the wafer (300 µm) and F is the incident photon flux. MPL measurements were performed at four laser powers, resulting in photon fluxes equal to 8×10^{16}, 1.2×10^{17}, 1.6×10^{17} and 2×10^{17} cm^{-2} s^{-1} [7]. As outlined by several authors, the lifetime measured with small signal techniques (Microwave PCD [Deb 62, Mada 79], MPL) is not the effective lifetime as defined in Eq. 1.13, but its derivative $\tau_{\text{eff},d}$ with respect to the excess carrier density, such that [Brendel 95, Schuurmans 04, Hahneiser 99, Schmidt 99]:

$$\frac{1}{\tau_{\text{eff}}} = \frac{1}{\Delta p} \int_0^{\Delta p} \frac{dp}{\tau_{\text{eff},d}(p)}. \tag{2.20}$$

In Fig. 2.12 the excess carrier lifetime of two (p)a-Si:H/(n)c-Si samples with different interfaces[8] is plotted against the excess carrier concentration; measurements with PCD and MPL techniques are shown. Lifetimes extracted by fitting the magnitude or the phase of the MPL signal give very similar results. However, as expected from the difference between small signal and steady-state measurements, there is a strong discrepancy between PCD and MPL data. Yet the trends are the same in terms of lifetime evolution for two different samples on one hand, and in terms of excess carrier density dependency on the other hand. This makes the MPL technique suitable for tracking the passivation quality of a series of samples. A method to extract the effective lifetime from its measured derivative has been proposed by Schuurmans [Schuurmans 04]; it relies on the measurement and integration of the lifetime derivative for a wide range of incident flux. This is not done here because the measurements would take too much time. In addition, the PL signal is too low for weak excitations, and the laser power limits the possibility to go to high injection levels.

[7] The photon fluxes are known from calibration with a photodiode

[8] The high lifetime sample has an (i)a-Si:H buffer layer, whereas the low lifetime sample has an oxidized interface

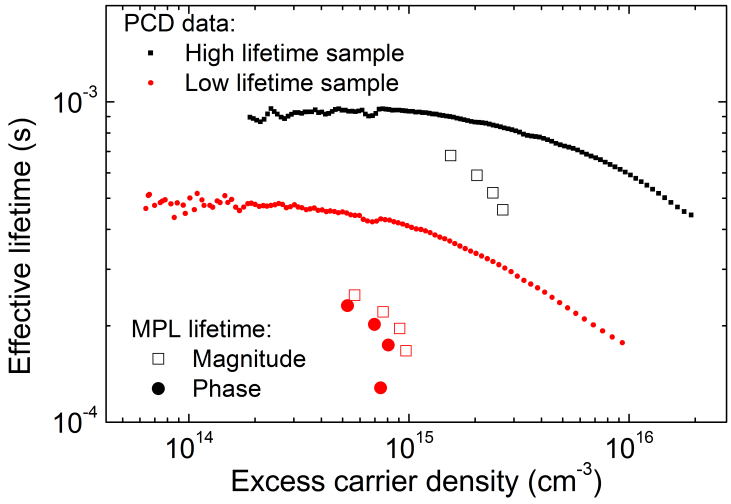

Figure 2.12: Measurement of the minority carrier lifetime versus excess carrier density with PCD and MPL for two samples with different interface passivation. The MPL lifetime is extracted from a fit of magnitude or phase shift versus frequency curves.

2.2.3 Assessing solar cell performance: current-voltage characteristics and spectral response

2.2.3.1 Current-voltage characteristics

The electrical behaviour of the complete solar cell has to be tested. Current-voltage characteristics (so-called I-V curves) are measured under standard conditions: 25 °C , atmospheric pressure, irradiance corresponding to the so-called AM1.5 solar spectrum (solar spectrum received on the Earth after going through 1.5 times the atmosphere thickness - conditions at temperate latitudes). From the typical I-V curve shown in Fig. 2.13, the short circuit current J_{sc}, the open-circuit voltage V_{oc}, the fill factor FF and the power conversion efficiency η are extracted:

$$J_{sc} = J \text{ at } V = 0 \text{ (mA cm}^{-2}\text{)} \tag{2.21}$$

$$V_{oc} = V \text{ at } J = 0 \text{ (V)} \tag{2.22}$$

$$P_{\max} = \max(|I \times V|) \text{ (W cm}^{-2}\text{)} \tag{2.23}$$

$$FF = 100 \times \frac{P_{\max}}{J_{sc} \times V_{oc}} \text{ (\%)} \tag{2.24}$$

$$\eta = 100 \times \frac{P_{\max}}{P_{\text{ill}}} \text{ (\%)}, \tag{2.25}$$

where $P_{\text{ill}} = 100$ mW cm^{-2} at AM1.5 illumination.

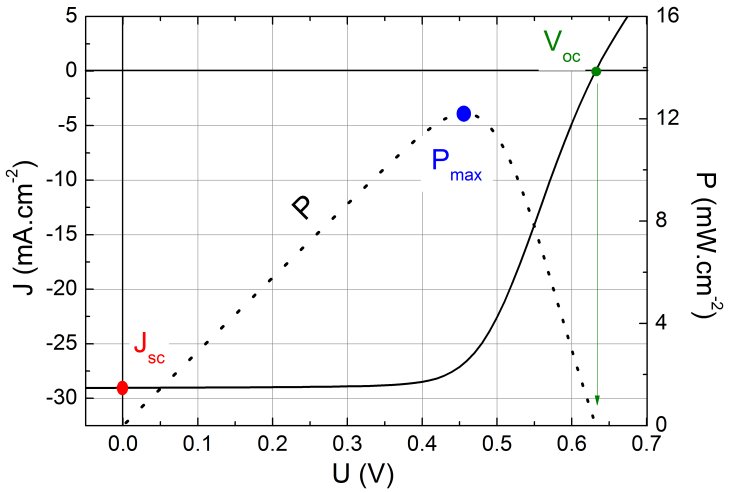

Figure 2.13: Current density (solid line) and power (doted line) versus applied voltage measured on a (p)a-Si:H/(n)c-Si heterojunction solar cell under AM1.5 illumination.

2.2.3.2 Quantum efficiency

The spectral response $SR(\lambda)$ is defined as the short circuit current $J_{sc}(\lambda)$ divided by the illumination power density $P_{\text{ill}}(\lambda)$: $SR(\lambda) = J_{sc}(\lambda)/P_{\text{ill}}(\lambda)$ (in A W^{-1}). It represents the response in terms of generated current to a monochromatic illumination at a wavelength λ. Its normalization with respect to the photon energy leads to the external quantum efficiency ($EQE(\lambda)$), which gives the number (between 0...1) of electrons extracted per *incoming* photon:

$$EQE(\lambda) = SR(\lambda)\frac{hc}{q\lambda} \tag{2.26}$$

where c is the speed of light in vacuum and h Planck's constant: $c = 3.00 \times 10^8$ m s^{-1} and $h = 6.63 \times 10^{-34}$ m^2 kg s^{-1}.

A measurement of the reflectance $R(\lambda)$ of the sample leads to the estimation of the number of electrons extracted per *absorbed* photon, the so-called internal quantum efficiency ($IQE(\lambda)$):

$$IQE(\lambda) = \frac{EQE(\lambda)}{1 - R(\lambda)}. \tag{2.27}$$

The analysis of EQE and IQE data provides information on parasitic absorption and free carrier behaviour (recombination, diffusion) at different depths in the structure, as most of the short wavelength light is absorbed at the front side, whereas the rear side can be probed by low-energy photons only.

The spectral response is usually measured by a lock-in currentmeter using chopped monochro-

matic light from a xenon lamp being decomposed in a grating monochromator. A white bias light equivalent to a 1 sun illumination puts the sample in realistic conditions: recombination processes being dependent on the injection level, it is important to perform the measurement with similar excess carrier densities as in standard working conditions (under one sun illumination).

2.3 Simulation tool: AFORS-HET

2.3.1 Generalities

The device simulation software AFORS-HET (Automate FOR Simulation of HETerostructures) has been developed at HZB since the year 2000 [Froitzheim 03], and is free-on-demand. The software solves Poisson's equation and the continuity equations, based on Maxwell-Boltzmann statistics, in the whole structure. Thermodynamic equilibrium (EQ), DC (steady-state conditions under an external applied voltage or current and/or illumination), AC (weak sinusoidal modulation of an external excitation) and transient (time resolved changes of the system due to a time dependent variation of the excitation) calculation modes are available, which enables the user to simulate the most common measurement methods (current-voltage, capacitance voltage, spectral response, etc). For more details, a complete user guide for AFORS-HET has been recently published [Stangl 12]. In the following, only the main aspects useful in this work will be addressed.

2.3.2 Bulk materials modeling

Within each semiconductor layer composing the structure, Poisson's and the continuity equations for electrons and holes are solved in one dimension for the electrostatic potential $V(x,t)$ and the electron and hole concentrations $n(x,t)$ and $p(x,t)$:

$$\frac{\epsilon_0 \epsilon_r(x)}{q} \frac{\partial V(x,t)}{\partial x^2} = p(x,t) - n(x,t) + N_D(x) - N_A(x) + \sum_{\text{trap}} \rho_{\text{trap}}(x,t) \tag{2.28}$$

$$-\frac{1}{q} \frac{\partial j_n(x,t)}{\partial x} = G(x,t) - R_n(x,t) - \frac{\partial n(x,t)}{\partial t} \tag{2.29}$$

$$+\frac{1}{q} \frac{\partial j_p(x,t)}{\partial x} = G(x,t) - R_p(x,t) - \frac{\partial p(x,t)}{\partial t}. \tag{2.30}$$

ϵ_0 and ϵ_r are the vacuum and relative dielectric constant, N_D and N_A are the ionized donor and acceptor dopant concentrations. G, R_n and R_p are the generation and recombination rates as described in the following. The sum over the traps (trap density $\rho_{\text{trap}}(x,t)$) includes

both donor-like and acceptor-like trap density, occupied according to the Shockley-Read-Hall (SRH) statistics. j_n and j_p are the electron and hole drift diffusion currents resulting from the gradient of the quasi Fermi levels $E_{F,n}$ and $E_{F,p}$:

$$j_n(x,t) = q\mu_n n(x,t)\frac{\partial E_{F,n}(x,t)}{\partial x} \tag{2.31}$$

$$j_p(x,t) = q\mu_p p(x,t)\frac{\partial E_{F,p}(x,t)}{\partial x}, \tag{2.32}$$

where μ_n and μ_p are the electron and hole mobility.

Optical model and generation: A simple optical model based on the Lambert-Beer absorption law is implemented in AFORS-HET. The generation rate $G(x)$ at depth x is given by:

$$G(x) = \int_{\lambda_{\min}}^{\lambda_{\max}} F(\lambda,t)(1-R(\lambda))A(\lambda)\alpha_{np,x}(\lambda)e^{\frac{-\alpha_{np,x}(\lambda)x}{cos(\gamma)}}d\lambda \tag{2.33}$$

where the reflectance R and absorbance A of the illuminated contact can be set by the user. The photon flux F (solar spectrum, monochromatic,...) sets the integration limits $\lambda_{\min}$ and $\lambda_{\max}$. The absorption coefficient $\alpha_{np,x}$ is defined for each layer when creating the layer stack. The incidence angle γ takes into account non-normal incidence (textured wafers for example). A model including coherent and incoherent internal multiple reflections is also accessible in AFORS-HET but won't be used in this study.

Defects and recombination mechanisms: Recombination of excess carriers occurs according to the processes introduced in section 1.1.1.2. Recombination through defects is modelled in the frame of the Shockley-Read-Hall statistics. Several energetic distributions of defects can be defined: single point like defect, constant defect distribution, exponential decay distribution from the conduction or valence band edge and Gaussian distribution. Each defect can be neutral, donor-like or acceptor-like. Two major features of defects in *a*-Si:H cannot be directly simulated in AFORS-HET, namely the amphoteric nature of dangling bonds and the Fermi level dependent defect distribution (defect pool model). The latter point can be circumvented by generating separately the defect density using e.g. the equations given by Powell and Deane [Powell 93, Powell 96], and fit them with Gaussian distributions which can then be defined in AFORS-HET. The former point requires more attention. Indeed, amphoteric defects possess three charge states, meaning that they can behave as donor-like and acceptor-like defects. Simulating a Gaussian distribution of DBs with a statistics of monovalent states forces

the introduction of two Gaussian distributions, each obeying the SRH statistics. Willemen [Willemen 98] studied the validity of this approximation, and found that the SRH statistics can be used if:

- (i) The ratio of the capture cross sections of charged and neutral states is much larger than 1.
- (ii) The correlation energy (see section 1.1.2.2) is positive and much larger than $k_B T$.
- (iii) The defect distribution lies between the quasi Fermi levels of trapped carriers (see [Steingrube 11] for definition).

(i) is satisfied because of the attractive Coulomb interaction and tunneling from more band tail states for charged states than for neutral states [Street 84]. In AFORS-HET the capture cross sections can be set such that the ratio is greater than 1. (ii) was shown in [Northrup 89, Street 91]. (iii) is less straightforward. Steingrube showed that the SRH statistics gives a good approximation of the amphoteric statistics for (i)*a*-Si:H and (p)*a*-Si:H; however discrepancies are observed for (n)*a*-Si:H [Steingrube 11]. In the present study, only (p)*a*-Si:H emitters are considered and the approximation by SRH statistics can thus be applied.

2.3.3 Interface modeling

At the interfaces, charge carrier transport can be treated as in the bulk, following the drift-diffusion equations. However, the possibility of having band discontinuities justifies the implementation of an interface current obeying the thermionic emission theory. In a unified form, the electron and hole currents expressions between semiconductors A and B read:

$$j_n^{TE} = v_{th,n}^A n(x_{\text{int}}^A) e^{-\frac{|\Delta_{E_c}|}{k_B T}\theta(-\Delta E_c)} - v_{th,n}^B n(x_{\text{int}}^B) e^{-\frac{|\Delta_{E_c}|}{k_B T}\theta(\Delta E_c)} \tag{2.34}$$

$$j_p^{TE} = v_{th,p}^A p(x_{\text{int}}^A) e^{-\frac{|\Delta_{E_v}|}{k_B T}\theta(\Delta E_v)} - v_{th,p}^B p(x_{\text{int}}^B) e^{-\frac{|\Delta_{E_v}|}{k_B T}\theta(-\Delta E_v)}, \tag{2.35}$$

where $\Delta E_c = q\chi^B - q\chi^A$ (χ^X is the electron affinity of material X) and $\Delta E_v = E_g^B - E_g^A + q\chi^B - q\chi^A$. θ is Heavyside's function. $v_{th,n}$ and $v_{th,p}$ are the electron and hole thermal velocities in both semiconductors. At the beginning of this work, and in the frame of a close collaboration between LGEP and HZB, a tunneling current through a spike in the conduction or valence band at an abrupt heterojunction has been implemented into AFORS-HET according to Yang's model [Yang 93]. In this work, the thermionic emission current is enhanced by a factor $1+\delta$ accounting for tunneling from one side of the barrier to the other side. Yang's idea will be

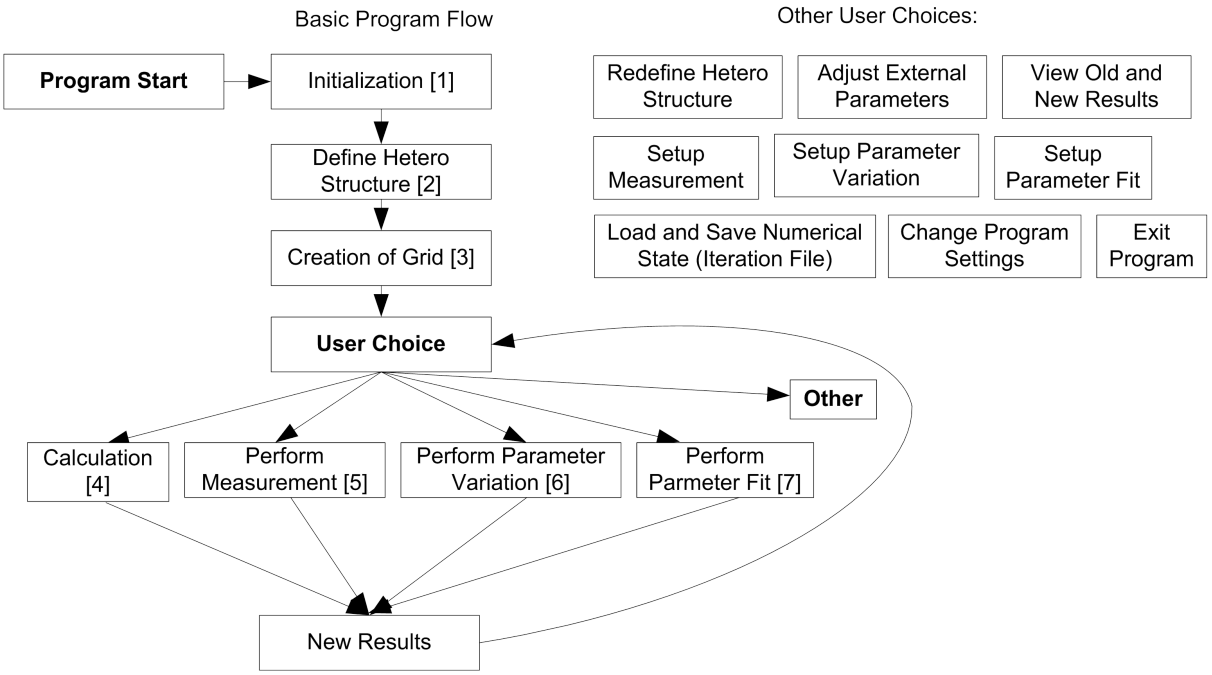

Figure 2.14: AFORS-HET basic program flow [Kriegel 03].

developed further later in this work in order to simulate tunneling through a thin insulator layer at an interface.

2.3.4 AFORS-HET development

In this work, new features will be incorporated in AFORS-HET (see section 5.2.1); thus some basics on the programming are now given.
AFORS-HET has been developed in the integrated development environment Embarcadero Delphi (Borland Software Corporation). Delphi uses its own object oriented programming language based on Pascal. Delphi is recognized by the community to be easy to handle [9] and does not require deep knowledge in computer programming.
AFORS-HET is an event driven program, meaning that there is one thread of execution from beginning to end; the diagram in Fig. 2.14 illustrates the program flow.

More details on the programming features of AFORS-HET can be found in the developer's guide provided with the software [Kriegel 03].

[9] For this reason, it is often compared with Visual Basic.

2.3.5 Standard cell structures for simulations

In the course of this thesis, simulations of silicon heterojunction solar cells shall be presented. If not otherwise specified, the standard cell structure comprises an (n)*a*-Si:H back surface field (back side), an (n)*c*-Si absorber, an (i)*a*-Si:H buffer layer, a (p)*a*-Si:H emitter (front side), and contacts on both sides (see Fig. 2.2). The (n)*c*-Si absorber is standard 300 µm thick *c*-Si, with a donor dopant density of 2×10^{15} cm^{-3}. It is characterized by a single level acceptor-like defect centred at mid-gap with a defect density of 10^9 cm^{-3} and capture cross sections for electrons (σ_n) and holes (σ_p) equal to 10^{-14} cm^{-2}, leading to a bulk minority carrier lifetime of 10 ms at an excess carrier density of 10^{15} cm^{-3}. Band-to-band and Auger recombinations are taken into account according to Kerr's and Cuevas' parametrization [Kerr 02].
For all the *a*-Si:H layers in the cell, the band gap was set to 1.7 eV. The valence and conduction band tail states were modelled by two decaying exponential functions with characteristic temperature T_v and T_c; their capture cross section is set to 7×10^{-16} cm^2 for both holes and electrons. The deep defects, known to be dangling bonds obeying an amphoteric statistics, were modelled by monovalent states ruled by the SRH statistics as explained in section 2.3.2. The deep defect distribution was generated following the defect pool model from standard pool parameters used in [Powell 93, Powell 96] and is replaced by two Gaussian distributions (one donor-like and one acceptor-like); the resulting defects parameters are summarized in Table 2.2. For donor-like defects, the capture cross section is 3×10^{-15} cm^2 for holes and 3×10^{-14} cm^2 for electrons; for acceptor-like defects, the capture cross sections is 3×10^{-14} cm^2 for holes and 3×10^{-15} cm^2 for electrons. In order to counterbalance the charge in band tails and in the Gaussian distributions, the doping density is adjusted to fix the Fermi level position.

The emitter/absorber interface defects were simulated by introducing a 1 nm thick, highly defective (n)*c*-Si layer at the (i)*a*-Si:H/(n)*c*-Si interface. A similar deep defect distribution as in bulk (i)*a*-Si:H was introduced leading to an equivalent 10^{10} cm^{-2} interface defect density. No defects were introduced at the (n)*c*-Si/(n)*a*-Si:H back interface, as it is usually of better quality than the front interface (see for example [de Wolf 09]).

The valence and conduction band offsets between *a*-Si:H and *c*-Si were set to 0.35 eV and 0.23 eV, respectively. Thermionic emission and tunneling through the conduction or valence band spike at the *a*-Si:H/*c*-Si interfaces were taken into account (see section 2.3.3). The front Schottky contact includes reflection by and absorption in ZnO:Al (measured at HZB); if not stated otherwise, its work function is taken equal to the work function of the (p)*a*-Si:H emitter, so that the contact is actually ohmic (flat bands at the interface). The back contact is always taken to be ohmic.

Table 2.2: a-Si:H parameters for layers making the cell structure in AFORS-HET. D/A: Donor/ Acceptor.

Layer	(p)*a*-Si:H	(i)*a*-Si:H	(n)*a*-Si:H
Thickness (nm)	10	3	20
T_c / T_v (K)	700/400	500/400	700/400
$D_{\max}$ (cm^{-3} eV^{-1})	1.19×10^{20}	1.36×10^{16}	1.54×10^{19}
$E_{DB,max}$ (D/A) (eV)	1.05/1.25	0.75/0.95	0.45/0.65
E_F (closest band) (eV)	0.35 (valence)	0.7 (conduction)	0.2 (conduction)
Dopant conc. (cm^{-3})	6.12×10^{19} (acceptor)	5×10^{15} (acceptor)	1.7×10^{19} (donor)

2.4 Chapter conclusion

The preparation of *a*-Si:H/*c*-Si heterostructures and heterojunction solar cells was presented. Crystalline silicon surface conditioning and deposition of amorphous silicon by the plasma enhanced chemical vapor deposition (PECVD) technique constitute the key element for the fabrication of state of the art samples.
The main characterization techniques used to study these structures have been introduced. Surface photo-voltage and planar conductance techniques will be used for investigations on the band diagram of the *a*-Si:H/*c*-Si hetero-contact. Voltage dependent surface photo-voltage, photo-conductance decay and modulated photo-luminescence will serve at probing interface defects. Each method has its specific field of application.
Finally, basics on the simulation tool AFORS-HET were given.

This chapter concludes the introduction of the tools that are now used to investigate the *a*-Si:H/*c*-Si heterojunction. In the following, development, characterization and modeling of *a*-Si:H/*c*-Si interfaces for silicon heterojunction solar cells are presented.

3

Determination of the band offsets at the amorphous silicon/crystalline silicon hetero-contact

This chapter is dedicated to investigations on the band bending in *c*-Si and the determination of band offsets at the *a*-Si:H/*c*-Si interface. It is based on two papers published during the course of this thesis [Varache 12a, Varache 12b]. First, an analytical model for the calculation of the band bending in *c*-Si is presented. The influence on the band bending of *a*-Si:H/*c*-Si heterojunction parameters, such as the band offsets and density of states in *a*-Si:H, is then presented. The band offsets are extracted from a comparison between planar conductance measurements and analytical calculations, and the results are discussed in the frame of the branch point theory for band alignment.

3.1 Analytical calculations of the band bending in *c*-Si

In this section, an analytical calculation of the band bending in *c*-Si, φ_{c-Si}, in an *a*-Si:H/*c*-Si heterojunction at equilibrium is presented. To this purpose, the different charge components of the structure are calculated as a function of φ_{c-Si}: the charge in *c*-Si Q_{c-Si}, the charge in *a*-Si:H $Q_{a-Si:H}$ and the charge in interface defects Q_{int}. In section 3.1.2.1, the charge in *c*-Si is calculated using a classical approach, first; afterwards quantum confinement of holes in a 2-dimensional hole gas at the interface is taken into account. To calculate the charge in *a*-Si:H, it is assumed that the density of states in *a*-Si:H is constant in the band gap. The final determination of φ_{c-Si} results from the overall charge neutrality of the hetero-contact. In the case where Q_{c-Si} is calculated classically, the analytical calculation is compared with numerical simulations using the software AFORS-HET and the influence of the main structure parameters on φ_{c-Si} is studied. In section 3.1.7, the effect of quantum confinement on the determination of φ_{c-Si} is discussed.
Here the calculation for the (p)*a*-Si:H/(n)*c*-Si structure is detailed; the main equations for the reverse (n)*a*-Si:H/(p)*c*-Si structure can be found in Appendix A. At the end of this chapter, results on both structures are presented and discussed.

3.1.1 Equilibrium band diagram

A schematic view of the *a*-Si:H/*c*-Si structure is presented in Fig.3.1.

Without loss of generality, the analysis is developed in the frame of Anderson's theory: the vacuum level, which serves as reference energy level, is introduced. From the analysis of the Fermi level position with respect to the vacuum level on each side of the heterojunction, the valence band offset ΔE_v reads:

$$\Delta E_v = -E_g^{c-Si} + \delta^{c-Si} + qV_d^{c-Si} + \delta^{a-Si:H} + qV_d^{a-Si:H}, \tag{3.1}$$

where $V_d^{c-Si} = V(+\infty) - V(0)$ and $V_d^{a-Si:H} = V(0) - V(-\infty)$ are the potential drops in each material so that the built-in voltage V_{bi} reads $V_{bi} = V(+\infty) - V(-\infty) = V_d^{c-Si} + V_d^{a-Si:H}$. $\delta^{c-Si} = (E_c - E_F)^{c-Si}$ and $\delta^{a-Si:H} = (E_F - E_v)^{a-Si:H}$ are the bulk Fermi level positions referred to the majority carrier band edge in (n)*c*-Si and (p)*a*-Si:H.

Eq. 3.1 can be rewritten in terms of V_{bi}:

$$qV_{bi} = \Delta E_v + E_g^{c-Si} - \delta^{c-Si} - \delta^{a-Si:H}. \tag{3.2}$$

Inversion occurs in n-type semiconductors when the Fermi level at the interface comes closer

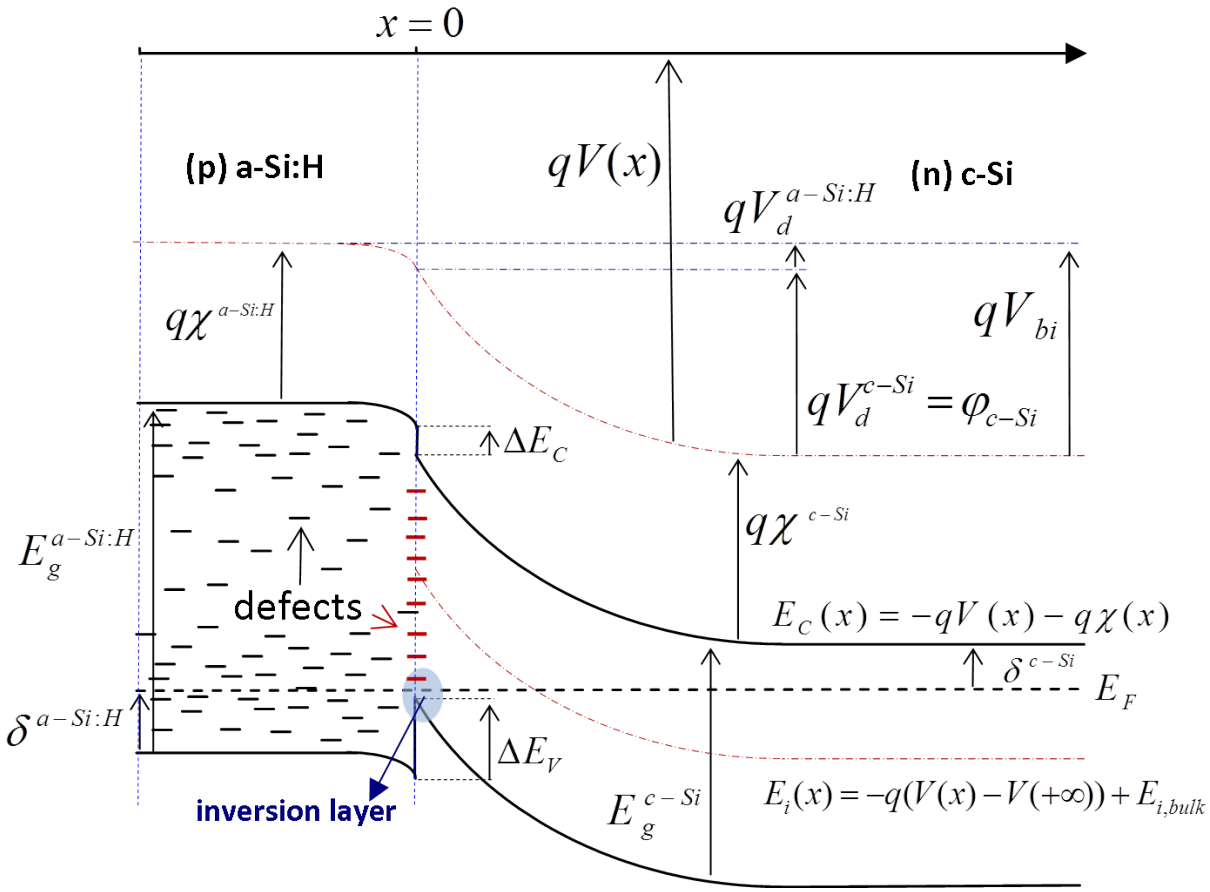

Figure 3.1: Schematic band diagram of a (p)a-Si:H/(n)c-Si heterojunction.

to the valence band edge than it is to the conduction band edge in the bulk:

$$(E_F - E_v)_{\text{int}}^{c-Si} \leq \delta^{c-Si}. \tag{3.3}$$

Considering Eq. 3.1, Eq. 3.3 is equivalent to

$$\Delta E_v \geq \delta^{a-Si:H} - \delta^{c-Si} + qV_d^{a-Si:H}. \tag{3.4}$$

The presence of the inversion layer at the (p)*a*-Si:H/(n)*c*-Si interface is thus converted into a condition on the valence band offset. A lower boundary for ΔE_v can be estimated if one takes $\delta^{a-Si:H} = 0.35$ eV and $\delta^{c-Si} = 0.2$ eV (see later in section 3.2), and if one notices that $qV_d^{a-Si:H}$ is positive: $\Delta E_v \geq 0.15$ eV.

Now, an analytical calculation of the charge components in the structure is developed.

3.1.2 Calculation of the charge components: Q_{c-Si}, $Q_{a-Si:H}$ and Q_{int}

3.1.2.1 Charge in *c*-Si: Q_{c-Si}

The charge in *c*-Si Q_{c-Si} is derived from Poisson's equation. The charge density at a given position $x > 0$ (see Fig. 3.1) reads:

$$\rho(x) = q\left(p(x) - n(x) + N_D - N_A\right) \tag{3.5}$$

$$\text{or } \rho(x) = q\left(p(x) - p_b - (n(x) - n_b)\right), \tag{3.6}$$

where $p(x)$ and $n(x)$ are the hole and electron concentrations at the position x, p_b and n_b are the concentrations in the bulk and N_D and N_A the donor and acceptor dopant concentrations assumed uniform in the *c*-Si wafer. The dimensionless variable

$$u(x) = \frac{E_F - E_i(x)}{k_B T}, \tag{3.7}$$

is introduced, where E_F is the Fermi level (constant through the structure at equilibrium) and E_i is the intrinsic Fermi level position which depends on x via the electrostatic potential $V(x)$: u is related to the electrostatic potential V by $u(x) = C + qV(x)/k_B T$ where C is a constant. T is the temperature and k_B is Boltzmann's constant. The electron density can be written

$$n(x) = n_i e^{u(x)} \tag{3.8}$$

because no quantum effect concerning electrons [1] is expected such that Boltzmann's statistics holds. On the contrary, confinement of holes in the quantum well formed by the valence band offset on the *a*-Si:H side, and by the valence band bending on the *c*-Si side, may occur. Both cases are treated separately later.

Poisson's equation can be rewritten in terms of u:

$$\frac{d^2u(x)}{dx^2} = \frac{1}{2\left(L_D^{c-Si}\right)^2}\left(e^{u(x)} - e^{u_b} - \left(\frac{p(x) - p_b}{n_i}\right)\right). \tag{3.9}$$

L_D^{c-Si} is the intrinsic Debye length defined by $\frac{1}{\left(L_D^{c-Si}\right)^2} = \frac{2q^2 n_i}{\epsilon k_B T}$, where ϵ is the material dielectric

[1] For electrons, there is no quantum well and the Fermi level is far enough from the conduction band edge such that Fermi-Dirac statistics can be approximated by Boltzmann's statistics.

constant [2]. Considering that the electric field in *c*-Si vanishes far from the interface, the integration of Poisson's equation between a position far in the bulk (where $u = u_b$) and a given position x ($u = u(x)$) leads to:

$$\left(\frac{du(x)}{dx}\right)^2 = \frac{1}{\left(L_D^{c-Si}\right)^2}\left[e^u - e^{u_b} - (u-u_b)\,e^{u_b} + \int_x^{+\infty}\frac{du}{dx}\left(\frac{p(x)-p_b}{n_i}\right)dx\right]. \tag{3.10}$$

The quantity $\frac{du}{dx}$ is related to the electric field ξ:

$$\frac{du(x)}{dx} = \frac{q}{k_B T}\frac{dV}{dx} \tag{3.11}$$

$$= -\frac{q}{k_B T}\xi(x), \tag{3.12}$$

such that the application of Gauss' law in *c*-Si leads to Q_{c-Si}:

$$\left(\frac{Q_{c-Si}}{2qn_i L_D^{c-Si}}\right)^2 = F^e_{\text{depl}}(u_s,u_b) + F^h_{\text{inv}}(u_s,u_b). \tag{3.13}$$

The term F^e_{depl} accounts for a depletion of electrons and reads:

$$F^e_{\text{depl}}(u_s,u_b) = e^{u_s} - e^{u_b} - (u_s-u_b)\,e^{u_b}, \tag{3.14}$$

while F^h_{inv} accounts for an excess of holes in the inversion layer:

$$F^h_{\text{inv}}(u_s,u_b) = \int_0^{+\infty}\frac{du}{dx}\left(\frac{p(x)-p_b}{n_i}\right)dx. \tag{3.15}$$

u_s is the value of u at the interface ($x = 0$), such that:

$$\varphi_{c-Si} = k_B T\,(u_b - u_s)\,. \tag{3.16}$$

In the following, the expressions of F^h_{inv} are derived in the classical case (no quantum confinement effect) and in the case where quantum confinement is taken into account.

[2] The material dielectric constant is the product of the relative material dielectric constant and the vacuum permittivity

Classical case: It is first assumed that the charge in the inversion layer derives from a classical treatment where Boltzmann's statistics also holds for holes. In this case, $p(x)$ can also be written in terms of u:

$$p(x) = n_i e^{-u(x)}, \tag{3.17}$$

such that Eq. 3.15 can be integrated after a change of variable ($x \rightarrow u$ and $\frac{du}{dx}dx \rightarrow du$):

$$F^h_{\text{inv}}(u_s, u_b) = \left(e^{-u_s} - e^{-u_b} - e^{-u_b}(u_b - u_s)\right). \tag{3.18}$$

The inversion charge in the classical case is thus given by:

$$Q^2_{c-Si,\text{inv}} = \left(2qn_i L_D^{c-Si}\right)^2 F^h_{\text{inv}}(u_s, u_b). \tag{3.19}$$

Q_{c-Si} can then be expressed in terms of u_s and u_b:

$$Q_{c-Si} = 2qn_i L_D^{c-Si} F(u_s, u_b), \tag{3.20}$$

where

$$F(u, u_b) = \pm\sqrt{2\left[\cosh(u) - \cosh(u_b) - (u - u_b)\sinh(u_b)\right]}, \tag{3.21}$$

the positive sign being taken when $u < u_b$ and the negative sign when $u > u_b$. This is what is found in semiconductor textbooks [Frankl 67, Sze 07].

Thus, the charge in c-Si is determined only by c-Si parameters, like the doping (appearing in u_b) and the band bending in c-Si (appearing in u_s).

Accounting for quantum confinement: In the case of strong band bending, quantum effects are expected to appear in the valence band, such that the classical approach based on fully delocalized states and a parabolic density of states in the valence band can no longer be used. In addition, in case of very strong confinement, the Fermi level may enter in the valence band at the interface so that Boltzmann's statistics can no longer be applied and Fermi-Dirac statistics should be used instead.

In order to account for such effects, an extreme case is considered, where holes are actually

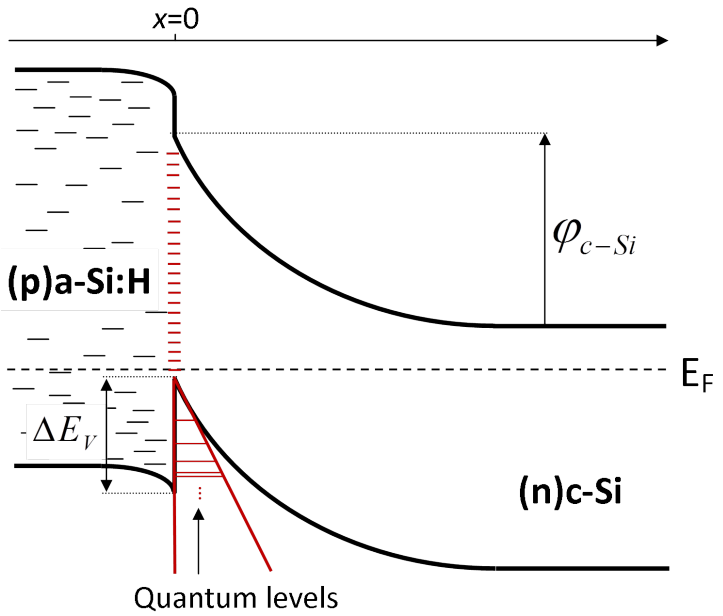

Figure 3.2: Quantum levels in the triangular well formed by the valence band offset and a strong band bending.

confined in an infinite triangular quantum well as drawn in Fig. 3.2. The electric field on the *c*-Si side is assumed constant. In order to evaluate $F^h_{\text{inv}}(u_s, u_b)$ in Eq. 3.15, an assumption is made regarding the electric field appearing through $\frac{du}{dx}$ in the integral; an effective electric field in the inversion layer equal to half the interface field ξ_{int} is taken [Mathieu 09], leading to:

$$F^h_{\text{inv}}(u_s, u_b) \approx -\frac{q\xi_{\text{int}}}{2k_B T}\frac{P_s}{n_i}. \tag{3.22}$$

ξ_{int} can be related to the total charge in *c*-Si through

$$\xi_{\text{int}} = -\frac{Q_{c-Si}}{\epsilon}. \tag{3.23}$$

$P_s = \int_0^{+\infty}(p(x) - p_b)dx$ is the hole sheet density. As p_b is negligible in (n)*c*-Si, $P_s \approx \int_0^{+\infty} p(x)dx$ and P_s results from the filling of quantized levels:

$$P_s = \sum_{i=0}^{+\infty}\left(p_{i1} + p_{i2}\right), \tag{3.24}$$

where indexes 1 and 2 take account of the valence band degeneracy: light and heavy holes with density of states effective masses m_1 and m_2, respectively, give two sets of quantized

levels. For i a positive integer and $j = 1$ or 2, p_{ij} reads [Mathieu 09]:

$$p_{ij} = \frac{m_j}{\pi\hbar^2} k_B T \ln\left(1 + \exp\left(-\frac{E_F - E_{ij}}{k_B T}\right)\right), \tag{3.25}$$

where E_{ij} are quantized level energies referenced at the interface valence band edge in c-Si, such that

$$E_v(0^+) - E_{ij} = \left(\frac{\hbar^2}{2m_j}\right)^{1/3} \left(\frac{3\pi q \xi_{\text{int}}}{2}\left(i + \frac{3}{4}\right)\right)^{2/3}. \tag{3.26}$$

Inserting Eq. 3.22 in Eq. 3.13, the total charge in c-Si is given, in the quantum mechanical case, by

$$Q_{c-Si}^2 = Q_{c-Si,\text{depl}}^2 + qP_s Q_{c-Si}, \tag{3.27}$$

where

$$Q_{c-Si,\text{depl}}^2 = \left(2qn_i L_D^{c-Si}\right)^2 F_{\text{depl}}^e(u_s, u_b). \tag{3.28}$$

Q_{c-Si} being positive in the case of (p)a-Si:H/(n)c-Si heterocontacts, the solution of Eq. 3.27 to consider is:

$$Q_{c-Si} = \frac{qP_s}{2}\left(1 + \sqrt{1 + 4\frac{Q_{c-Si,\text{depl}}^2}{q^2 P_s^2}}\right). \tag{3.29}$$

If $qP_s \gg Q_{c-Si,\text{depl}}$, which is expected to occur at high inversion, the total charge in c-Si is equal to qP_s at the second order:

$$Q_{c-Si} \approx qP_s\left(1 + \frac{Q_{c-Si,\text{depl}}^2}{q^2 P_s^2}\right). \tag{3.30}$$

In the case where quantum confinement effects are taken into account, Q_{c-Si} is no longer a function of c-Si parameters only, because the interface electric field appearing in Eq. 3.26 results from the resolution of the charge neutrality in the structure (see section 3.1.3). However, Q_{c-Si} can still be written as a function of u_s because the interface electric field is a function of

the charge in *a*-Si:H being itself a function of u_s (see section 3.1.2.2).

3.1.2.2 Charge in *a*-Si:H: $Q_{a-Si:H}$

In order to determine the total charge in *a*-Si:H, Poisson's equation has to be solved in *a*-Si:H. Garin *et al.* gave expressions for the total charge in *a*-Si:H in order to analyze effective charge carrier lifetime measurements [Garin 05]. However they did not consider the charge coming from gap defects, which is actually the main contribution to the space charge density. The DOS in *a*-Si:H is commonly described by the defect pool model introduced by Deane and Powell [Powell 93, Powell 96]. It comprises a valence band tail, a conduction band tail, and deep amphoteric dangling bond defects carrying a positive, negative or no charge (see section 1.1.2). For simplicity, only monovalent states (see section 2.3.2) are considered here; the total DOS $N(E)$ is divided into donor and acceptor densities, $N_d(E)$ and $N_a(E)$, respecively, such that $N(E) = N_d(E) + N_a(E)$. Thus, the charge density at $x < 0$ can be written:

$$\rho(x) = q\left(N_D - N_A\right) + q\int_{E_v^{a-Si:H}}^{E_c^{a-Si:H}} \left\{N_d(E)\left[1 - f(E, E_F(x))\right] - N_a(E) f(E, E_F(x))\right\} dE, \tag{3.31}$$

where $f(E, E_F(x))$ is the occupation function at the energy level E within the *a*-Si:H band gap $E_g^{a-Si:H}$, the latter being delimited by the valence and conduction band mobility edges, $E_v^{a-Si:H}$ and $E_c^{a-Si:H}$, respectively. The position of the Fermi level is referenced to the valence band edge which varies according to the band bending. N_D and N_A are the donor-like and acceptor-like dopant concentrations, respectively. The *a*-Si:H bulk Fermi level position that determines the charge neutrality in *a*-Si:H is introduced; it is denoted $E_F(-\infty)$ since this position would be reached very far from the interface in an infinite *a*-Si:H layer. Adding the term $\rho(-\infty) = q\left(N_D - N_A\right) + q\int_{E_v^{a-Si:H}}^{E_c^{a-Si:H}} \left\{N_d(E)\left[1 - f(E, E_F(-\infty))\right] - N_a(E) f(E, E_F(-\infty))\right\} dE = 0$ [3] to Eq. 3.31, the charge density can thus be written

$$\rho(x) = -q\int_{E_v^{a-Si:H}}^{E_c^{a-Si:H}} N(E)\left[f\left(E, E_F(x)\right) - f\left(E, E_F(-\infty)\right)\right] dE. \tag{3.32}$$

Remarkably the doping density does not appear in the expression of ρ. [4]
No analytical solution for $\rho(x)$ is found if one considers the DOS predicted by the defect pool model. However, variations of the charge in *a*-Si:H caused by a weak bending of the bands mainly depend on the DOS at the Fermi level. Therefore the DOS is approximated by a constant level of defects through the gap: $N(E) = N(E_F)$. The Fermi-Dirac function is

[3] In the neutral region in the bulk ($x = -\infty$), $\rho = 0$.
[4] The doping density comes into play in the determination of the bulk Fermi level position.

approximated by a step function, such that $f(E,E_F)$ equals 1 for $E<E_F$ and 0 for $E>E_F$[5]. Eq. 3.32 simplifies to

$$\rho(x)=q^2N(E_F)\left(V(-\infty)-V(x)\right). \tag{3.33}$$

Then, Poisson's equation,

$$\frac{d^2V(x)}{dx^2}+\frac{\rho(x)}{\epsilon}=\frac{d^2V(x)}{dx^2}+\frac{q^2N(E_F)}{\epsilon}\left(V(-\infty)-V(x)\right)=0, \tag{3.34}$$

is solved in the *a*-Si:H layer. The *a*-Si:H layer is not taken semi-infinite anymore (as in Fig. 3.1); instead, its thickness $d_{a-Si:H}$ is introduced, such that *a*-Si:H occupies the domain between $x=-d_{a-Si:H}$ and $x=0$. Taking an electric field equal to zero at the *a*-Si:H surface (more on that in Chapter 4), the resolution of Eq. 3.34 leads to the expression for the potential $V(x)$ at any x between $x=-d_{a-Si:H}$ and $x=0$:

$$V(x)-V(-\infty)=\frac{V(0)-V(-\infty)}{\cosh\left(d_{a-Si:H}/L_D^{a-Si:H}\right)}\cosh\left(\frac{x+d_{a-Si:H}}{L_D^{a-Si:H}}\right). \tag{3.35}$$

$L_D^{a-Si:H}$ is the Debye length in *a*-Si:H and is defined by:

$$L_D^{a-Si:H}=\sqrt{\frac{\epsilon}{q^2N(E_F)}}. \tag{3.36}$$

Finally, the total charge in *a*-Si:H is obtained by the integration of $\rho(x)$:

$$\begin{aligned}Q_{a-Si:H}&=\int_{-d_{a-Si:H}}^{0}\rho(x)dx\\&=-\frac{\epsilon}{L_D^{a-Si:H}}\left(V(0)-V(-\infty)\right)\tanh\left(\frac{d_{a-Si:H}}{L_D^{a-Si:H}}\right).\end{aligned} \tag{3.37}$$

For thicknesses much greater than the Debye length $L_D^{a-Si:H}$, the charge in *a*-Si:H simplifies

[5]This approximation holds as long as $E_v(x)-E_F\gg k_BT$ for x between $-\infty$ and 0.

to:

$$Q_{a-Si:H} = -\frac{\epsilon}{L_D^{a-Si:H}} \left(V(0) - V(-\infty)\right). \tag{3.38}$$

The quantity $V(0) - V(-\infty)$ [6] appearing in the expression of $Q_{a-Si:H}$ (Eqs. 3.37 and 3.38) can be rewritten (see Fig. 3.1):

$$V(0) - V(-\infty) = V_d^{a-Si:H} = V_{bi} - V_d^{c-Si} \tag{3.39}$$

$$= V_{bi} - \frac{k_B T}{q}(u_b - u_s). \tag{3.40}$$

Thus, $Q_{a-Si:H}$ is also expressed as a function of u_s and structure parameters like $N(E_F)$ and V_{bi}.

3.1.2.3 Charge in interface defects: Q_{int}

Because defects might be present at the interface between *c*-Si and *a*-Si:H, the charge they carry must be taken into account as well. A distribution $N_{DB}(E)$ of correlated dangling bonds is considered. The interface charge is thus due to the balance between positively charged and negatively charged defects, and is given by:

$$Q_{\text{int}} = q \int_{E_v^{c-Si}}^{E_c^{c-Si}} N_{DB}(E) \left[f_0^+(E, E_{F,\text{int}}) - f_0^-(E, E_{F,\text{int}}) \right] dE, \tag{3.41}$$

with

$$f_0^+(E, E_{F,\text{int}}) = \frac{1}{1 + 2\exp\left(\frac{E_i - E}{k_B T} + u_s\right) + \exp\left(\frac{2(E_i - E) - U}{k_B T} + u_s\right)} \tag{3.42}$$

and

$$f_0^-(E, E_{F,\text{int}}) = \exp\left(\frac{2(E_i - E) - U}{k_B T} + u_S\right) f_0^+(E, E_{F,\text{int}}), \tag{3.43}$$

[6] For thin *a*-Si:H layers, $V(0) - V(-\infty)$ does not correspond to the potential drop in *a*-Si:H, and V_{bi} does not correspond to the built-in voltage in the considered structure. Eq. 3.35 taken for $x = -d_{a-Si:H}$ gives the difference between $V(0) - V(-\infty)$ and the actual potential drop in *a*-Si:H $V(0) - V(-d_{a-Si:H})$.

where U is the correlation energy [Vaillant 86]. $E_{F,\text{int}}$ is determined from φ_{c-Si} or equivalently u_s:

$$E_{F,\text{int}} - E_v^{c-Si}(0^+) = E_g^{c-Si} - \varphi_{c-Si} - \delta^{c-Si} \tag{3.44}$$

$$= E_g^{c-Si} - k_B T\,(u_b - u_s) - \delta^{c-Si}. \tag{3.45}$$

In (p)a-Si:H/(n)c-Si heterojunctions, $E_{F,\text{int}}$ is expected to be close to the interface valence band edge due to the high band bending. As a consequence, most of the interface defects are empty: Q_{int} gives thus a *positive* contribution to the total charge, and tends to screen the charge in the c-Si space charge region.
In the case of a Gaussian defect distribution, the integration in Eq. 3.41 is made numerically because there is no analytical solution. However, for a single trap of density N_{DB} located at E_t, Eq. 3.41 becomes:

$$Q_{\text{int}} = qN_{DB}\left(f_0^+(E_t, E_{F,\text{int}}) - f_0^-(E_t, E_{F,\text{int}})\right). \tag{3.46}$$

3.1.3 Solution of the charge neutrality equation

All the charges appearing in the structure can now be expressed in function of material parameters (like u_b, $N(E_F)$, etc.), V_{bi} and the normalized surface potential u_s. V_{bi} is itself determined by the valence band offset and the position of the Fermi level in both materials (see Eq. 3.2).
Finally, the charge neutrality equation reads:

$$Q_{a-Si:H} + Q_{\text{int}} + Q_{c-Si} = 0. \tag{3.47}$$

It can be solved numerically for u_s, so that for each set of parameters, the band bending can be calculated with Eq. 3.16. The equations were implemented in a Matlab method which allows the user to study rapidly the influence of all parameters on φ_{c-Si}.

The determination of the band bending is illustrated in Fig. 3.3. For each graph the charge in c-Si is calculated from the classical solution given by Eq. 3.20 and is plotted versus the band bending in c-Si. The absolute value of the charge in a-Si:H is calculated from Eq. 3.38. In Fig. 3.3(c) the charge in interface defects calculated from Eq. 3.46 is added to the charge in a-Si:H. In Fig. 3.3(a) and (b) it can be clearly seen that, as $N(E_F)$ or V_{bi} decreases, both the band bending in c-Si and the absolute value of the charge in a-Si:H decrease. Indeed, at fixed

V_{bi}, the band bending in *a*-Si:H has to increase to maintain the charge if $N(E_F)$ decreases. That decreases the band bending in *c*-Si, because the sum of both band bending equals the constant V_{bi}. Thus, the charge in *c*-Si decreases and from the charge neutrality $|Q_{a-Si:H}|$ decreases too.
If $N(E_F)$ is fixed, a decrease of V_{bi} implies a decrease of band bending both in *c*-Si and *a*-Si:H. Then, charge neutrality implies that charges in both sides drop (in absolute value).
Fig. 3.3(c) shows that interface defects play a role only when the charge they carry becomes of the order of that in *a*-Si:H. As expected from section 3.1.2.3, they are detrimental to φ_{c-Si}. Without interface defects, $Q_{a-Si:H}/q$ is about 2×10^{12} cm^{-2} for the set of parameters used in the calculations. The charge in interface defects starts having a visible effect on the band bending for N_{DB} above 10^{11} cm^{-2} (dotted line in Fig. 3.3(c)).[7] For $N_{DB} = 10^{12}$ cm^{-2}, the drop in φ_{c-Si} compared to the ideal case ($N_{DB} = 0$) is only 20 meV.

In Fig. 3.3(a), the depletion and inversion contributions to the total charge in *c*-Si determined from Eqs. 3.14 and 3.19 are shown. The depletion charge is almost constant in the band bending range explored here; it contributes significantly to the total charge for band bending values lower than 0.75 eV and dominates the total charge for band bending values lower than 0.70 eV. For a band bending higher than 0.75 eV, the total charge can be well approximated by the inversion layer charge.

[7] This is slightly dependent on the interface distribution. No detailed study of the influence of the interface defect distribution is shown here.

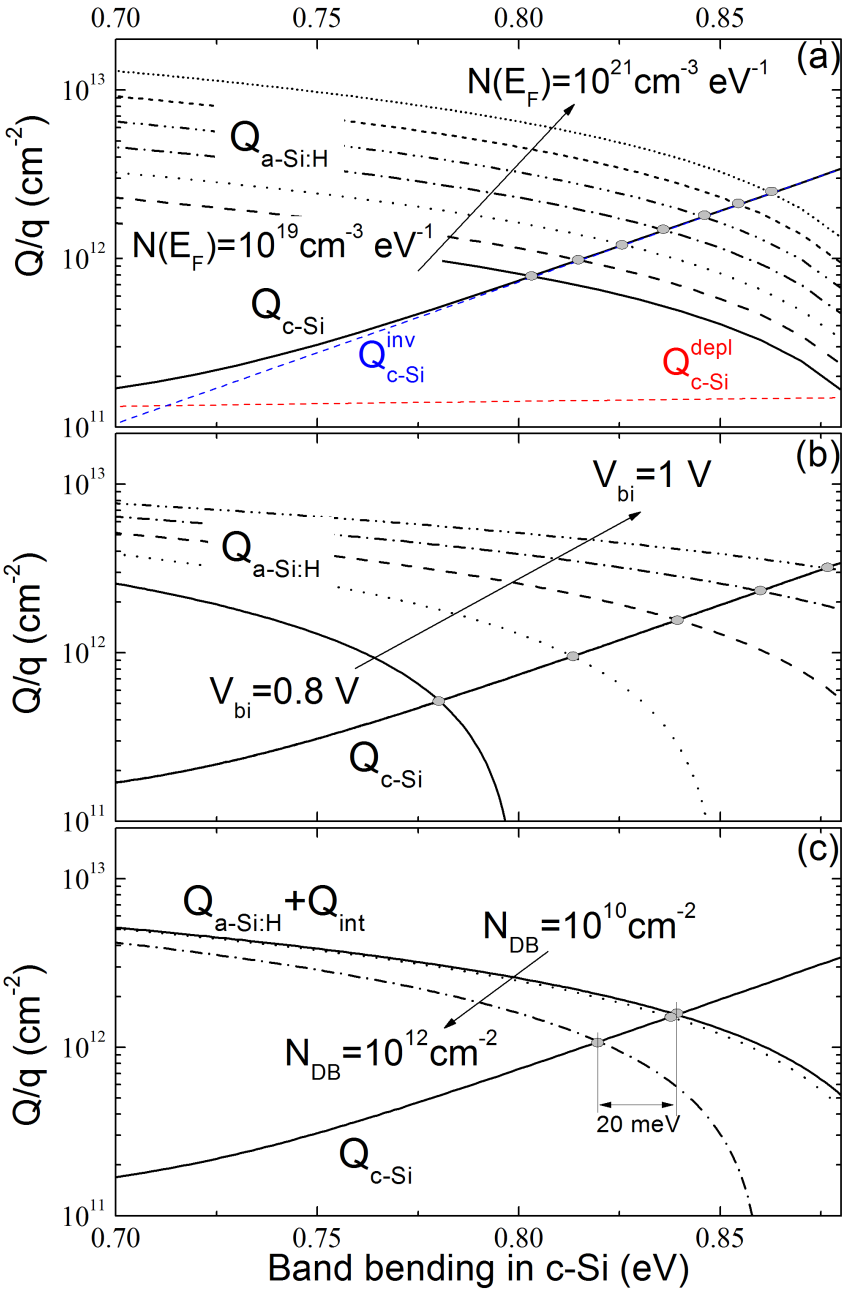

Figure 3.3: Absolute values of the charge in c-Si (Eq. 3.20), in a-Si:H (Eq. 3.38) and in interface defects (Eq. 3.46) as a function of the band bending in c-Si. The intersection of the curves, marked by grey points, gives the charge neutrality in the structure, thus the band bending solution in the structure. Standard parameters used for the calculations are: $N_d = 2 \times 10^{15}$ cm^{-3}, $N(E_F) = 10^{20}$ cm^{-3} eV^{-1}, $V_{bi} = 0.9$ eV. The a-Si:H thickness is considered as infinite. In (a), $N(E_F)$ varies from 10^{19} cm^{-3} eV^{-1} up to 10^{21} cm^{-3} eV^{-1}. In (b), V_{bi} varies from 0.8 V to 1 V every 0.05 V. In (c), a single level a-Si:H/c-Si interface defect at mid-gap is considered, with density $N_{DB} = 10^{10}$, 10^{11} and 10^{12} cm^{-2}.

3.1.4 Validation with AFORS-HET

In order to study the suitability of the approximations made to derive the analytical model, it is necessary to perform numerical simulations for comparison; this is accomplished with the simulation software AFORS-HET introduced in section 2.3. The validation of the analytical model proceeds in several steps. First, a constant DOS $N(E) = N(E_F) = 10^{20}$ cm^{-3} eV^{-1} was introduced in order to test whether the replacement of the Fermi-Dirac occupation function by a step function was relevant. Secondly, since the Fermi level in doped *a*-Si:H lies in the band tail, a single exponential DOS, $N(E) = N_0 \exp((E - E_v)/k_B T_v)$ accounting for the (p)*a*-Si:H valence band tail was introduced. Finally a realistic DOS was introduced: it consists in two exponential distributions of monovalent states for the band tails along with a deep defect distribution of dangling bonds (DBs) calculated using the defect pool model.
Moreover, in AFORS-HET two types of boundary conditions at the surface of *a*-Si:H ($x = -d_{a-Si:H}$) can be chosen: insulator-like conditions, where the surface electric field is set to zero (no surface charge), so that the bands are flat at the surface, or Schottky contact-like conditions, where the surface carrier concentrations are set to their equilibrium bulk values (ohmic-like contact). Although the insulator-like condition is the more realistic description of the samples[8] (see Fig. 2.6), both boundary conditions are studied in the following to illustrate the important role played by this interface.

At room temperature (300 K), the following parameters have been first taken for (p)*a*-Si:H thin films: $N(E_F) = 10^{20}$ cm^{-3} eV^{-1}, $(E_F - E_v)^{a-Si:H} = 0.35$ eV, $E_g^{a-Si:H} = 1.75$ eV, characteristic temperature of the band tail parameter $T_v = 700$ K, and a valence band offset $\Delta E_v = 0.4$ eV. These are typical values that are in agreement with spectral ellipsometry, UV-photoyield spectroscopy and dark conductivity measurements [Schulze 11b, Aljishi 90, Favre 10].

In Fig. 3.4 the band bending in *c*-Si is plotted against the thickness of (p)*a*-Si:H: both analytical calculation (thick green solid line) and AFORS-HET simulation (thin lines + symbols) results are shown.
First it can be noticed that the analytical and numerical simulations in the case of a constant DOS give exactly the same results (green solid line versus orange triangles), suggesting that the approximation of a step function for the occupation function is valid.
Secondly, numerical simulations with the three DOS described above lead to these conclusions: (i) deep Gaussian defects play no role in the band bending calculation because the maximum of the distribution is too far from the Fermi level position, (ii) the replacement of an exponential band tail by a constant DOS does not change the band bending for large thicknesses (above 5 nm in this case) and for thinner (p)*a*-Si:H layers (down to 1 nm), the deviation is only 20 meV. Thus, it can be reasonably concluded that the approximations made to calculate the charge in (p)*a*-Si:H are valid for this problem.

[8] If e.g. adsorbates are present on the surface of the sample, the electric field may not be 0 and the band are not flat at the interface: see Chapter 4

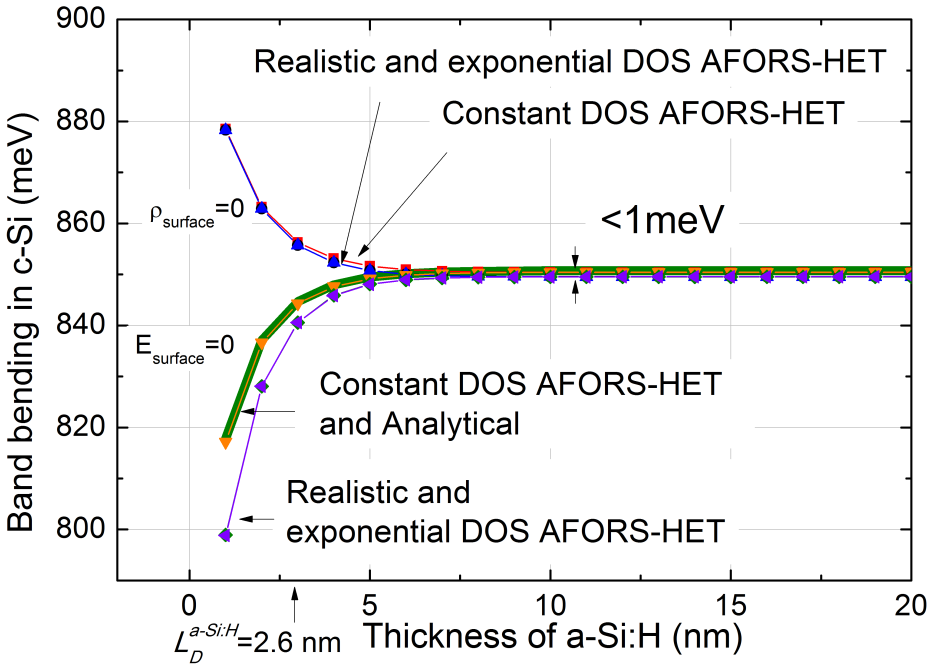

Figure 3.4: Influence of the thickness of the amorphous layer on the band bending in c-Si and comparison of analytical calculations with the heterojunction simulator AFORS-HET. The thick, green, solid curve is for analytical results. Thin line+symbols curves are for numerical simulations. The Debye length in a-Si:H is indicated: $L_D^{a-Si:H} = 2.6$ *nm for* $N(E_F) = 10^{20}$ cm^{-3} eV^{-1}. *For numerical results,* $\rho_{surface} = 0$ *stands for ohmic-like contacts, whereas* $E_{surface} = 0$ *stands for insulator-like contacts (no surface charge).*

In cases of very thin layers, the flat band regime in *a*-Si:H is not reached; the boundary condition at the *a*-Si:H surface has thus a large impact on the band profile in this layer. More precisely, the position of the Fermi level at the *a*-Si:H surface – fixed by the overall charge neutrality in the case of insulator-like boundary condition or imposed by the choice of the contact (metal, TCO) work function in the case of Schottky-like condition – determines the total potential drop over the structure. This impact could be exploited to engineer the best contact at the top *a*-Si:H surface: this will be discussed in Chapter 4. For large thicknesses, the analytical model based on a constant DOS approximation in *a*-Si:H is in very good agreement with AFORS-HET calculations, whatever the DOS model taken (it should be recalled here that the analytical calculations were performed using an insulator-like condition at the *a*-Si:H/air interface): the discrepancies remain below 1 meV.

It can also be observed in Fig. 3.4 that the results become thickness independent when the amorphous silicon layer reaches thicknesses above a few times the characteristic Debye length ($L_D^{a-Si:H} = 2.6$ nm for $N(E_F) = 10^{20}$ cm^{-3} eV^{-1}). Then, the flat band regime is reached in *a*-Si:H far from the *a*-Si:H/*c*-Si interface and one can ignore what happens at the top *a*-Si:H surface for the determination of the band bending in *c*-Si since the two interfaces do not influence each other. For very thin *a*-Si:H layers the analysis of the band bending at the *a*-Si:H/*c*-Si heterojunction depends on the top *a*-Si:H surface conditions.

The high defect density in highly doped thin *a*-Si:H layers, $N(E_F) \geq 5 \times 10^{18}$ cm^{-3} eV^{-1} [Korte 06b], leads to very low values of the Debye length, $L_D^{a-Si:H} \leq 10$ nm. Since the samples that will be used in this study have thicknesses above 20 nm, it is justified to consider an infinite *a*-Si:H thickness in the calculations.

3.1.5 Hole sheet density: band bending and temperature dependence

3.1.5.1 Hole sheet density and band bending

The hole sheet density is defined as

$$P_s(T) = \int_0^{+\infty} \left(p(x,T) - p_b(T)\right) dx, \tag{3.48}$$

where p_b is the hole concentration in bulk *c*-Si. Using the variable $u(x)$, P_s can be written:

$$P_s(T) = \int_{u_s(T)}^{u_b(T)} n_i(T) \left(e^{-u} - e^{-u_b(T)}\right) \left(\frac{du}{dx}\right)^{-1} du. \tag{3.49}$$

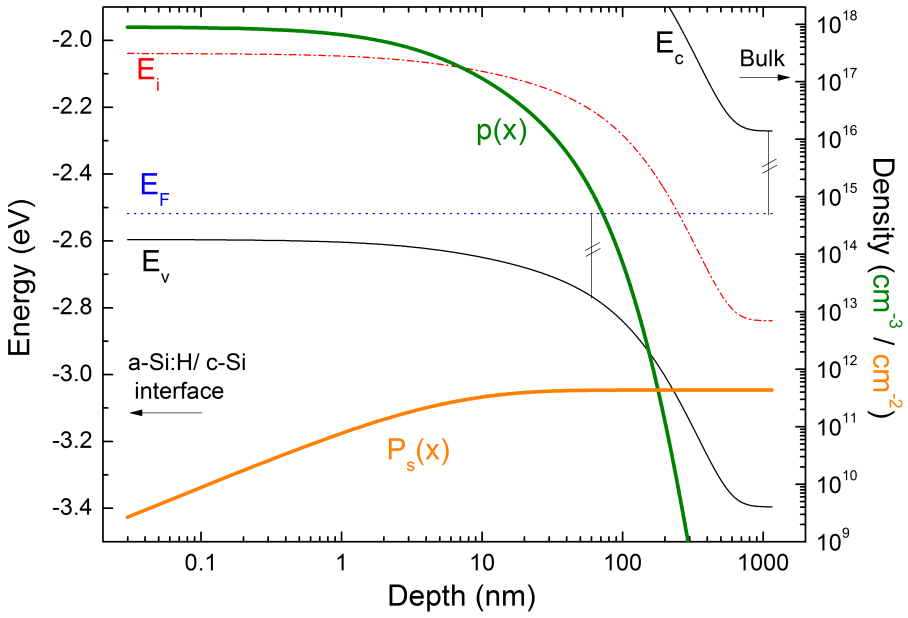

Figure 3.5: Valence and conduction band edges E_v and E_c, intrinsic Fermi level E_i and Fermi level E_F in c-Si close to the (p)a-Si:H/ (n)c-Si interface; the band bending in c-Si was arbitrarily set to 800 meV. The hole concentration $p(x)$ and the hole sheet density $P_s(x)$ between the interface ($x = 0$) and the position x are shown. The inversion layer ends at the position x when $(E_F - E_v)(x) = (E_c - E_F)_{bulk}$.

Because holes are minority carriers in the bulk of (n)*c*-Si, the major contribution to P_s comes from the inversion layer close to the interface. In Fig. 3.5 the band diagram of *c*-Si calculated analytically [9]is presented for a band bending of 800 meV. It can be seen that the inversion layer extends only over a few tens of nanometres; for depths where the space charge region goes from inversion to depletion, $p(x)$ decreases dramatically. As a result, $P_s(x)$, defined as the hole sheet density between the interface ($x = 0$) and the position x, $P_s(x) = \int_0^x \left(p(x,T) - p_b(T)\right) dx$, tends to a constant about 20 nm after the interface.

From Eq. 3.49, the band bending φ_{c-Si} and characteristics of the *c*-Si layer (doping, band gap, etc.) determines the hole sheet density P_s through the quantities u_s, u_b and n_i. Provided φ_{c-Si} is known, P_s is independent of the contacting material (*a*-Si:H for silicon heterojunctions, metal for Schottky barriers, etc.). This is illustrated in Fig. 3.6, where P_s is plotted versus the band bending for the standard properties of *c*-Si used in this thesis. This figure will not be used to extract the band offsets but can help to extract φ_{c-Si} if one can measure P_s (see section 3.2 for details on measurements of P_s): this will be done later in section 4.4.

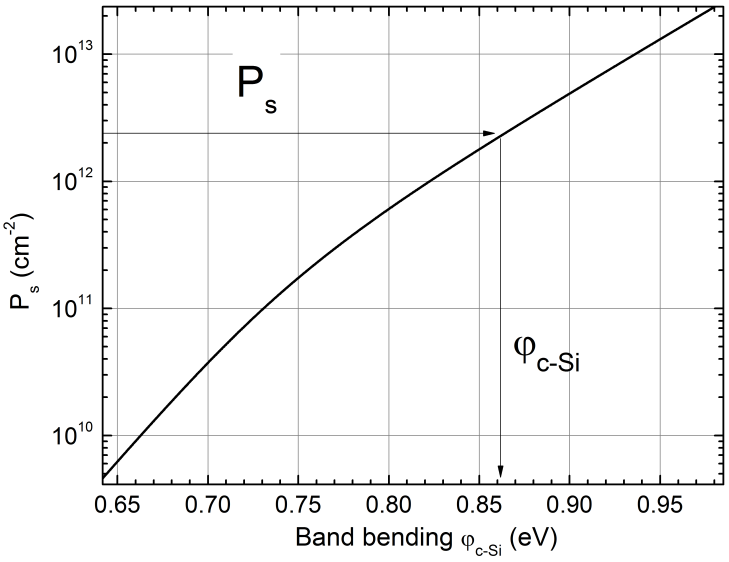

Figure 3.6: Hole sheet density P_s versus the equilibrium band bending in c-Si φ_{c-Si}, and typical extraction of band bending values from experimentally determined P_s data (see section 3.2 for details on measurements of P_s).

Table 3.1: Description of the various possibilities for the dependence of the band offsets upon temperature. "Fixed" means that the level is taken constant with respect to the vacuum level. "Closest Band" for the Fermi level column refers to conduction band (CB) for (n)a-Si:H and valence band (VB) for (p)a-Si:H.

Cases	*a*-Si:H			*c*-Si	
	VB	CB	Fermi level E_F	VB	CB
A0	Fixed	Follows gap variations	Follows closest band	Fixed	Follows gap variations
B0	Fixed	Follows gap variations	Follows closest band	Follows gap variations	Fixed
C0	Follows gap variations	Fixed	Follows closest band	Fixed	Follows gap variations
D0	Follows gap variations	Fixed	Follows closest band	Follow gap variations	Fixed
AW	Fixed	Follows gap variations	Fixed	Fixed	Follows gap variations
BW	Fixed	Follows gap variations	Fixed	Follows gap variations	Fixed
CW	Follows gap variations	Fixed	Fixed	Fixed	Follows gap variations
DW	Follows gap variations	Fixed	Fixed	Follow gap variations	Fixed

3.1.5.2 Hole sheet density and temperature dependence

From the calculation of the band bending in section 3.1.3, the hole sheet density can be calculated from Eq. 3.49 as a function of structure parameters and can be compared with values experimentally deduced from temperature dependent planar conductance measurements. In this calculation, the temperature dependence of u_s is considered, taking into account the temperature dependences (i) of the gap of crystalline silicon, $E_g^{c-Si}(T) = E_g^{c-Si}(0) - \alpha \frac{T^2}{T+\beta}$ with $\alpha = (4.9 \pm 0.2) \times 10^{-4}$ eV K^{-1}, $\beta = (655 \pm 40)$ K and $E_g^{c-Si}(0) = 1.1692$ eV [Alex 96], (ii) of the gap of amorphous silicon, $E_g^{a-Si:H}(T) = E_g^{a-Si:H}(0) - 2.25 \times 10^{-4} T$ [Wronski 92], and (iii) of the effective density of states in the valence and conduction bands in *c*-Si, $N_v(T) = (T/300)^{1.85} \times 3 \times 10^{19}$ cm^{-3}, and $N_c(T) = (T/300)^{1.58} \times 2.86 \times 10^{19}$ cm^{-3} [Green 90].
The band offsets ΔE_c and ΔE_v are de facto temperature dependent through the variations of the gaps with temperature. However, whether this dependence is related to the movement of the conduction or the valence band edge with temperature is not well known. The evolution of the Fermi level position in *a*-Si:H is also not clearly established, as it depends on the evolution of the defect distribution with temperature inside the gap. In order to make the analysis as

[9] The calculation results from the numerical integration of Eq. 3.10 in the classical case to get the depth x as a function of u, which directly gives the electrostatic potential V versus x, the band diagram, and the carrier densities.

general as possible, eight extreme cases are considered, that are summarized in Table 3.1.

3.1.6 Dependence of P_s on key parameters

The analytical approach has been chosen in particular to be able to study the influence of parameters on the band bending and on the planar conductance in a very efficient and rapid way. Calculations of the dependence of the Arrhenius plot of P_s on several key parameters for the case A0 are presented in Fig. 3.7.

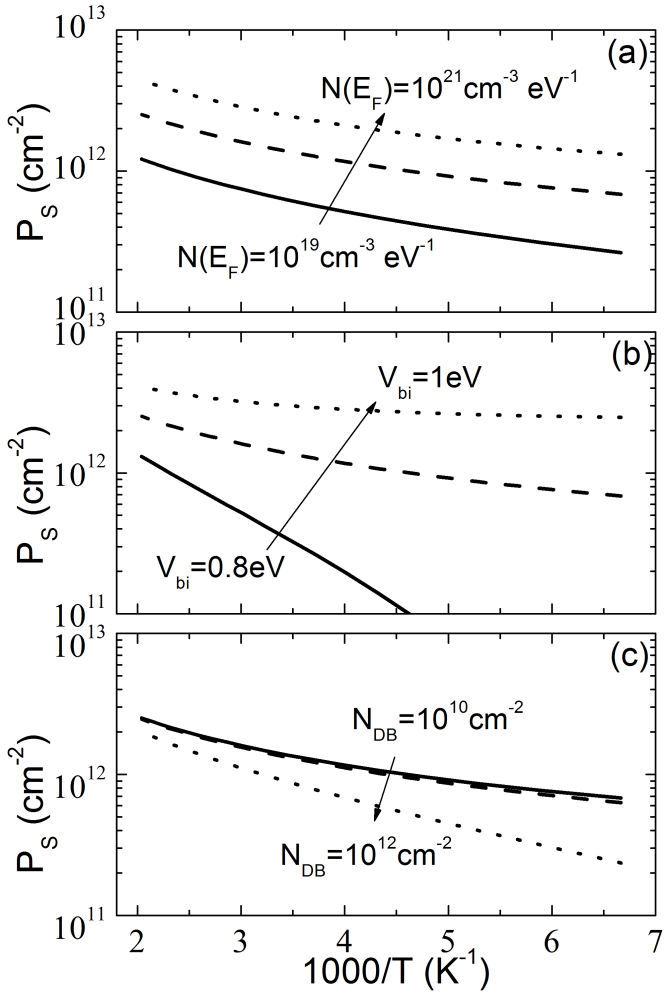

Figure 3.7: Arrhenius plots of the hole sheet density P_s calculated analytically – study of the influence of parameters. Unless otherwise specified, the parameters used for the calculations are the same as in Fig. 3.3. No interface defects are taken into account for plots (a) and (b). Curves in (c) are calculated using a single level dangling bond defect centred at mid-gap, of density N_{DB}. Case A0 in Table 3.1 is used for band offsets temperature dependence.

On a general basis, at a given temperature, a decrease of P_s is equivalent to a decrease of the total charge and of the band bending in *c*-Si; using the charge neutrality statement, the absolute value of the charge in *a*-Si:H also decreases.
If the defect density in *a*-Si:H is decreased while the other parameters are kept constant (Fig. 3.7(a)) the band bending in *a*-Si:H has to increase to discharge more defects in order to attempt to maintain the charge on both sides. Since the total potential drop V_{bi} has been kept constant, this forces the band bending in *c*-Si and P_s to decrease. It must be noticed that the charge in *a*-Si:H cannot be completely maintained and decreases too. The argumentation is corroborated by Fig. 3.3(a), where one can clearly see that a decrease of $N(E_F)$ is responsible for both a decrease of the band bending and the charge in *a*-Si:H.
A decrease of V_{bi} is shared between $V_d^{a-Si:H}$ and V_d^{c-Si}, implying that P_s also decreases (Fig. 3.3(b)).
It is worth emphasizing that changes in the bulk defect density have mainly the effect to shift the curves to higher or lower values with no significant change in the temperature dependence. However, changes in V_{bi} are mainly reflected in changes of the slope, as all the curves converge at high temperature. This property will be used later to extract the band offsets from comparison between measurements and calculations.

A key point in *a*-Si:H/*c*-Si heterojunctions is the passivation of the interface, that is the number of interface defects and their influence on device characteristics. The calculation developed previously includes the charge resulting from these defects (see Eq. 3.41). In Fig. 3.7(c) Arrhenius plots of P_s for several interface state densities are presented; the effect of charged interface defects can be dramatic if their density is sufficiently high, because they screen the charge in the amorphous layer, yielding a lower band bending in *c*-Si. In Fig. 3.8 the dependence of the hole sheet density P_s on the interface defect density is displayed for various values of the DOS in *a*-Si:H. The higher is the density of defects in *a*-Si:H, the weaker is the influence of interface defects. Indeed, the charge present in the interface defects has an impact on the structure only if it can compete with the charge stored in *a*-Si:H bulk defects, as shown in Fig. 3.3(c). Over a wide range of *a*-Si:H bulk defect densities, the interface defects have an influence only for densities around or higher than 10^{12} cm^{-2}. From simulations on the (n)*a*-Si:H/(p)*c*-Si structure, Schmidt showed that interface defects degrade the device performance (power conversion efficiency below 15%) only if their density is higher than 2×10^{11} cm^{-2} [Schmidt 06]. The experimental data presented further in this work were obtained on interfaces that are building blocks of high efficiency solar cells (power conversion efficiencies between 15% and 21% were obtained) for which the density of interface defects should not exceed a few 10^{11} cm^{-2}. Photoconductance decay experiments performed on (p)*a*-Si:H/(i)*a*-Si:H/(n)*c*-Si structures by Leendertz and co-authors showed even lower interface defect densities – around 10^{10} cm^{-2} – attributed to the better passivation capability of the (i)*a*-Si:H layer [Leendertz 10a]. As a consequence, defects at such high quality interfaces play a minor role on the band bending (see dashed domains in Fig. 3.8). Moreover, the planar conductance technique is a static measurement method, involving no response of defects.

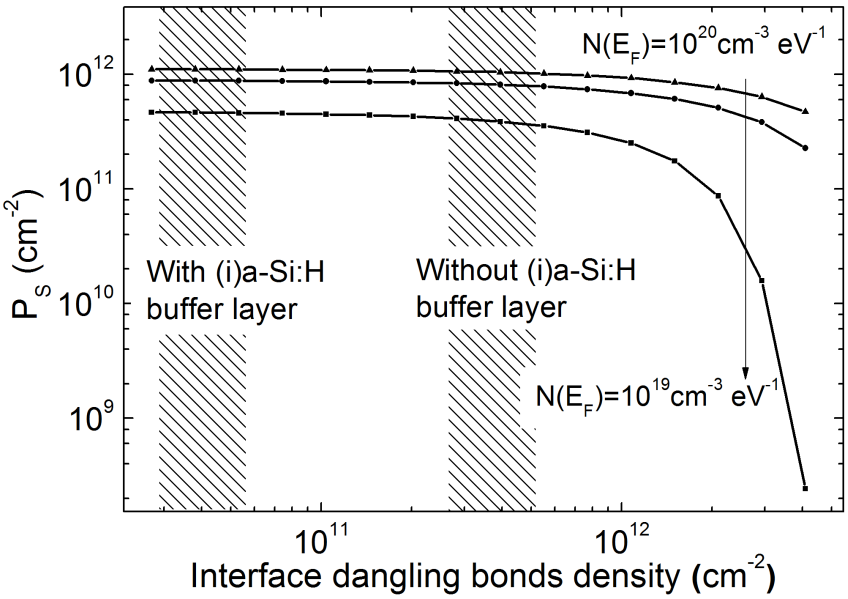

Figure 3.8: Dependence of the hole sheet density on the interface defect density, for several bulk defect concentrations. V_{bi} is set at 0.9 eV. Interface defects are described by a single dangling bond defect level, of density N_{DB}, centred at mid-gap. Typical interface defect densities measured using the photo-conductance decay (and a fit tool) are shown (dashed areas) [Leendertz 11b].

Other methods relying on dynamic processes (surface photo-voltage, capacitance-voltage) are much more sensitive to defects present in a lower concentration.

3.1.7 Quantum confinement at the *a*-Si:H/*c*-Si interface

So far, only classical calculations of the band bending have been presented; equations accounting for quantum confinement have been given in section 3.1.2.1. It should be recalled here that, although the determination of the band bending is made – self consistently – as in the classical case, the calculation of P_s in the quantum case is not derived from Eq. 3.49 but is obtained from Eq. 3.24. In the quantum mechanical case, it is not possible to calculate, as in Fig. 3.3, the charge in *c*-Si as a function of the band bending. Q_{c-Si} now depends on the interface electric field, which can be known only from the charge neutrality statement.
However the calculation of P_s from the sum of hole densities filling quantized states can be illustrated; this is done in Fig. 3.9. Two sets of levels corresponding to the heavy and light hole masses discretize the energy in the quantum well. Levels i with energies greater (in absolute value) than 250 meV give no more contribution to P_s ($\sum p_{i,1}$ and $\sum p_{i,2}$ tend to a constant for $i \geq 4$). In the classical case, the Fermi level stays rather far from the valence band edge at $x = 0^+$ with respect to $k_B T$; in the quantum mechanical case both levels are almost superimposed. However, the energy distance between the Fermi level and the first quantized level is roughly equal to the distance between the classical valence band edge and the Fermi

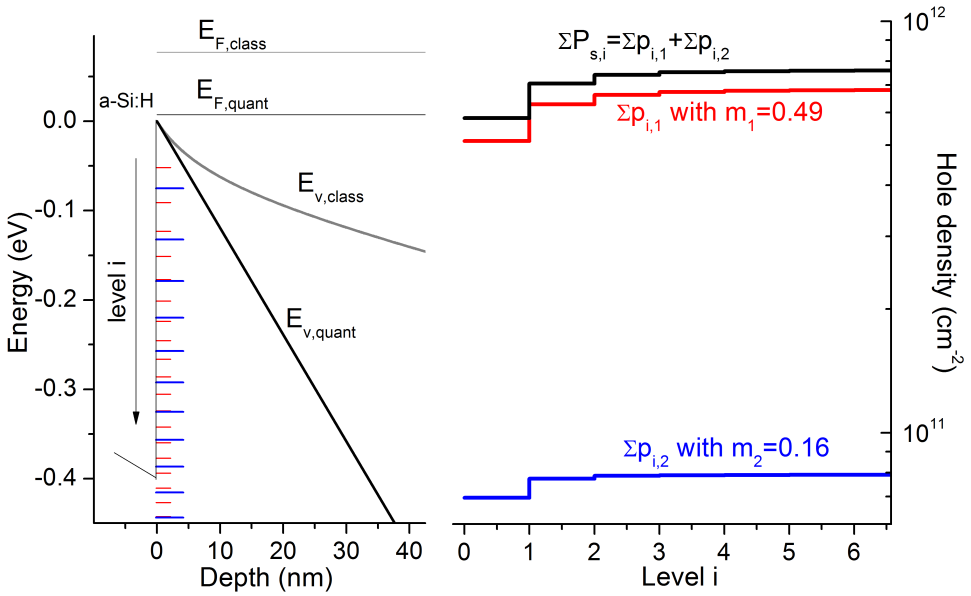

Figure 3.9: Left: Valence band edge and Fermi level in c-Si at the a-Si:H/c-Si interface, in classical (grey) and quantum mechanical (black) cases. Quantized levels are indicated for both masses. Red: $m_1 = 0.49$; Blue: $m_2 = 0.16$. Right: sum of p_{ij}, for both masses m_j, as level number increases, to obtain P_s.

level.

To go further in the comparison between classical and quantum mechanical cases, both the band bending and P_s calculated in both cases are plotted against V_{bi} in Fig. 3.10. It is remarkable that the band bending is higher in the quantum mechanical case than in the classical case, while it is the opposite for P_s. At low built-in voltage values, both calculations tend to the same band bending value, as the depletion charge contribution becomes more and more important with respect to the inversion layer charge. P_s is lower in the quantum mechanical case. This result is consistent with data from the literature regarding inverted MOS structures [Kevkic 10].

Regarding the temperature dependence, Arrhenius plots of P_s calculated with or without quantum confinement are shown in Fig. 3.11. It must be emphasized that the classical and quantum mechanical calculations give similar activation energies for a given V_{bi}. This is consistent with the remark that the spacing between the Fermi level and the first available states is the same in both cases (see Fig. 3.9).

It will be shown later that the activation energy is used to extract V_{bi} from comparison with experimental data. As a consequence, confinement effects as taken into account here have negligible influence for the band offset extraction. Moreover, for simplicity a perfect infinite triangular potential well was considered. This leads to an enhanced confinement effect compared to the actual situation for two reasons. First, the potential can be considered linear

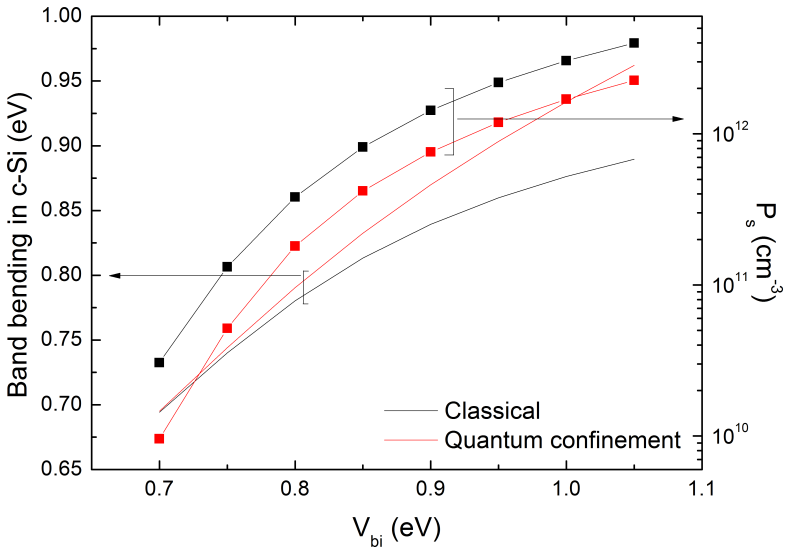

Figure 3.10: Band bending in c-Si and hole sheet density P_s calculated in classical and quantum confinement cases versus the built-in voltage V_{bi}.

only over a small distance from the interface compared to the width of the depletion region. Due to the curvature of the band, the well is expected to open as one goes away from the interface, thus reducing quantum confinement (see Fig. 3.9). Secondly, the approximation of an infinitely high wall on the valence band offset side could also lead to a reduction of the confinement because wavefunctions can tail in *a*-Si:H if the wall has a finite height. This would even be enhanced by the presence of defects in (p)*a*-Si:H which create available energy states. Wavefunctions in the well are thus more delocalized and less confined than assumed. A full quantum mechanical calculation accounting for the realistic structure is expected to give results between the classical and the approximated quantum mechanical cases presented here [10].

In summary, the impact of quantum mechanics on the derivation of band offsets is expected to be weak, and the classical calculations will be retained in the following.

[10] The approximation of taking an effective field in Eq. 3.22 has been checked in the classical case, and brought no significant deviation to the exact calculation.

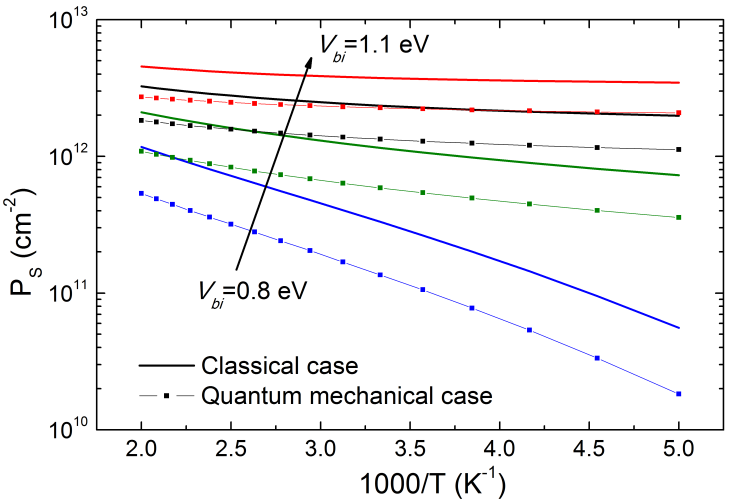

Figure 3.11: Arrhenius plot of the hole sheet density P_s calculated in both classical and quantum mechanical cases, for V_{bi} equal to 0.8, 0.9, 1 *and* 1.1 *eV. The a-Si:H bulk DOS at E_F was taken here at* 5×10^{19} cm^{-3} eV^{-1}.

3.2 Experiments and extraction of band offsets

3.2.1 Temperature dependent planar conductance measurement analysis

The planar conductance measurement technique was presented in section 2.2.1.2. It is worth emphasizing that samples studied here were collected from several institutes - Laboratoire de Physique des Interfaces et des Couches Minces (CNRS, France), University of Toronto (Canada), Helmholtz Zentrum Berlin (Germany), INES (CEA, France). Although deposition conditions are slightly different from one institute to the other, the general fabrication scheme is rather similar (see section 2.1). Two types of samples were studied: (p)*a*-Si:H/(n)*c*-Si and (n)*a*-Si:H/(p)*c*-Si.

To compare experimental results and calculations, conductance values G are converted into carrier sheet densities C_s ($C = P$ for holes in the case of an (n)*c*-Si based structure; $C = N$ for electrons in the reverse structure):

$$C_s(T) = G(T)\frac{d}{q l \mu_c(T)}, \tag{3.50}$$

$\mu_c(T)$ being the mobility of the carriers in the strong inversion layer, l the length of the electrodes, and d the inter-electrode spacing (see Fig. 2.6). The carrier mobility in the strong inversion layer is generally different from that in the bulk *c*-Si. Indeed, at the interface, additional scattering mechanisms at interface defects or interface micro-roughness can occur, thus reducing the mobility with respect to its bulk value. Confinement effects may also have

an impact on the carrier mobility in strongly inverted layers [Price 83, Stern 67]. There have been many studies of carrier mobility in strongly inverted silicon MOS structures leading to various models, with different dependence on temperature and sheet carrier density [Vasileska 96, Masaki 91]. Moreover, confinement by an amorphous silicon layer should be weaker than that obtained from silicon oxide, that has a much larger band gap than *a*-Si:H. This was already discussed in section 3.1.7. At present time, there is no definite model to describe the mobility in such a structure. The lack of precise knowledge of the mobility in *a*-Si:H/*c*-Si structures is circumvented by considering the following temperature dependence:

$$\mu_c(T) = \mu_{c,300}\left(\frac{T}{300}\right)^{-\alpha_c}, \tag{3.51}$$

and looking at two extreme cases :

- in case (i), corresponding to *ideal bulk behavior*, $\mu_{e,300} = 1500$ cm^2 V^{-1} s^{-1}, $\alpha_e = 2.4$, $\mu_{h,300} = 480$ cm^2 V^{-1} s^{-1} and $\alpha_h = 2.2$.
- in case (ii), corresponding to *strongly interface limited behavior*, $\mu_{e,300} = 500$ cm^2 V^{-1} s^{-1}, $\mu_{h,300} = 160$ cm^2 V^{-1} s^{-1} and $\alpha_h = \alpha_e = 0$.

According to the amount of data found in literature, the mobility in *a*-Si:H/*c*-Si structures, in the explored temperature range, should be framed by these two extreme cases [Jacoboni 77]. These two extreme cases are taken to evaluate the relative error in the determination of band offsets.

G values are converted into P_s for one particular sample in Fig. 3.12; in Fig. 3.12(a) the conductance as measured is plotted versus $1000/T$. Using Eq. 3.50, values of the hole sheet density P_s are calculated from G values and are plotted in Fig. 3.12(b), for both mobility cases.

In Fig. 3.13 Arrhenius plots of the carrier sheet densities calculated in case (i) for all the samples that are studied in the following are presented (see Table 3.2). Noticeable variations in terms of activation energy and position of the curves along the y-axis result from the different *a*-Si:H and interface properties (doping, hydrogen content, bulk defects, etc) coming from the different conditions in which the samples were prepared.
It has already been stated in section 1.2.2 that an undoped amorphous silicon layer is often used to passivate the *a*-Si:H/*c*-Si interface and to achieve higher performance. From Fig. 3.13, (p)*a*-Si:H/(i)*a*-Si:H/(n)*c*-Si structures show lower hole sheet densities than samples with no (i)*a*-Si:H layer. Because of the presence of an electric field at the interface, a significant potential drop occurs in the (i)*a*-Si:H layer. This additional band bending in the *a*-Si:H side adds only a negligible charge because (i)*a*-Si:H has a low defect density [Stutzmann 89]. The

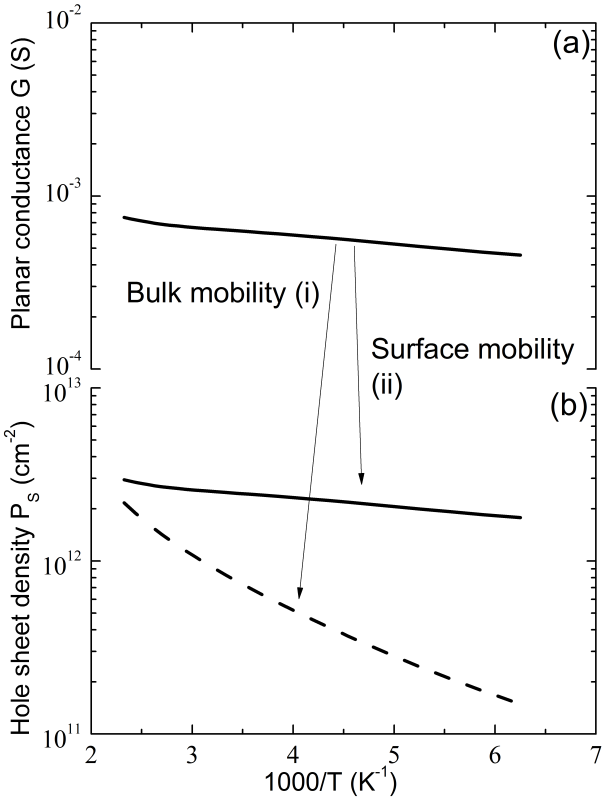

*Figure 3.12: (a) Arrhenius plot of the measured conductance, G, for sample N5: (*20 *nm) (p)a-Si:H/(n) c-Si; the length of the electrodes and the spacing between them were* 10 *mm and* 1 *mm, respectively; b) Arrhenius plots of the hole sheet density P_s extracted from the above conductance under the assumption of two mobility cases (case (i) = bulk mobility; case (ii) = interface-limited mobility).*

built-in potential being fixed by the (p)*a*-Si:H and (n)*c*-Si layers, the structure adjusts itself by reducing the band bending in *c*-Si.
Measurements on samples with an (i)*a*-Si:H buffer layer are shown for completeness. The quantitative analytical description of such a three layer system will be presented later in Chapter 4; for the purpose of determining the band offsets between crystalline silicon and amorphous silicon, it is more straightforward to use a two-layer system rather than a three-layer system, and investigations will thus concentrate on samples without additional buffer passivation layer.

3.2.2 Qualitative analysis: temperature dependence of band offsets

The issue of the possible temperature dependence of the band offsets is first addressed. The following argumentation is based on a qualitative comparison between experimental data and analytical calculations on both (p)*a*-Si:H/(n)*c*-Si and (n)*a*-Si:H/(p)*c*-Si structures because it can be reasonably assumed that the behaviour of band offsets with temperature is the same on both kinds of samples. For the eight possible cases detailed in Table 3.1, the Arrhenius plots

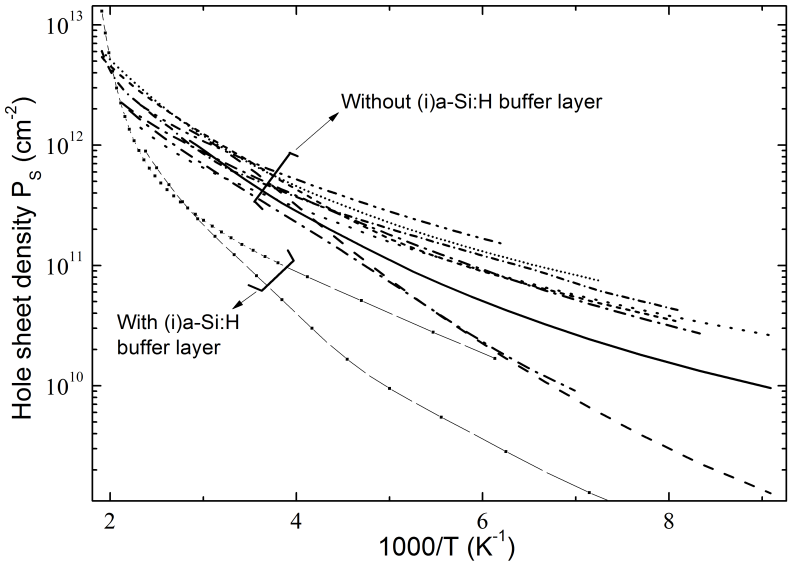

Figure 3.13: Arrhenius plots of the hole sheet density P_s extracted from the conductance measurements of all samples analyzed in this study, with the mobility of the bulk material (case (i)).

of the sheet carrier concentrations are shown in Fig. 3.14. Experimental planar conductance data of one sample from each type are also indicated (grey areas to account for the lack of accuracy on mobility values).

It can be observed that the experimental temperature dependence of the sheet carrier concentration exhibits a linear or slightly convex behaviour in an Arrhenius plot (see also Figs. 3.12 and 3.13). Thus, cases that yield an opposite (concave) curvature for the calculated curves can be eliminated. The comparison being made simultaneously on (p)*a*-Si:H/(n)*c*-Si structures and on (n)*a*-Si:H/(p)*c*-Si structures, only two cases remain that can fit the experimental results particularly well: case A0, where the conduction band edge shifts with temperature in both *a*-Si:H and *c*-Si while the valence band edge is fixed, and case D0, where the conduction band edge is fixed while the valence band edge shifts with temperature in both *a*-Si:H and *c*-Si. It is worth mentioning that the band structures of amorphous and crystalline silicon are similar as far as the valence and conduction bands are concerned: p and s states constitute respectively the valence and conduction band edges in both materials [Street 91]. It is thus expected that they behave in the same way with respect to temperature variations, which is in agreement with the two cases selected above.
To go a step further, and in order to choose the most suitable case between A0 and D0, it should be first remarked that Mönch reported that the electronic affinity of GaAs increases with temperature as the gap shrinks. He came to the same conclusion for Si(111)–7x7 surfaces from works of Bachmann [Moench 81, Bachmann 68]. For *a*-Si:H temperature dependent internal photoemission measurements performed by Wronski also tend to prove that it is the conduction band edge that shifts with temperature, while the valence band edge is fixed [Wronski 92]. This is also consistent with Aljishi's work, who showed that the conduction

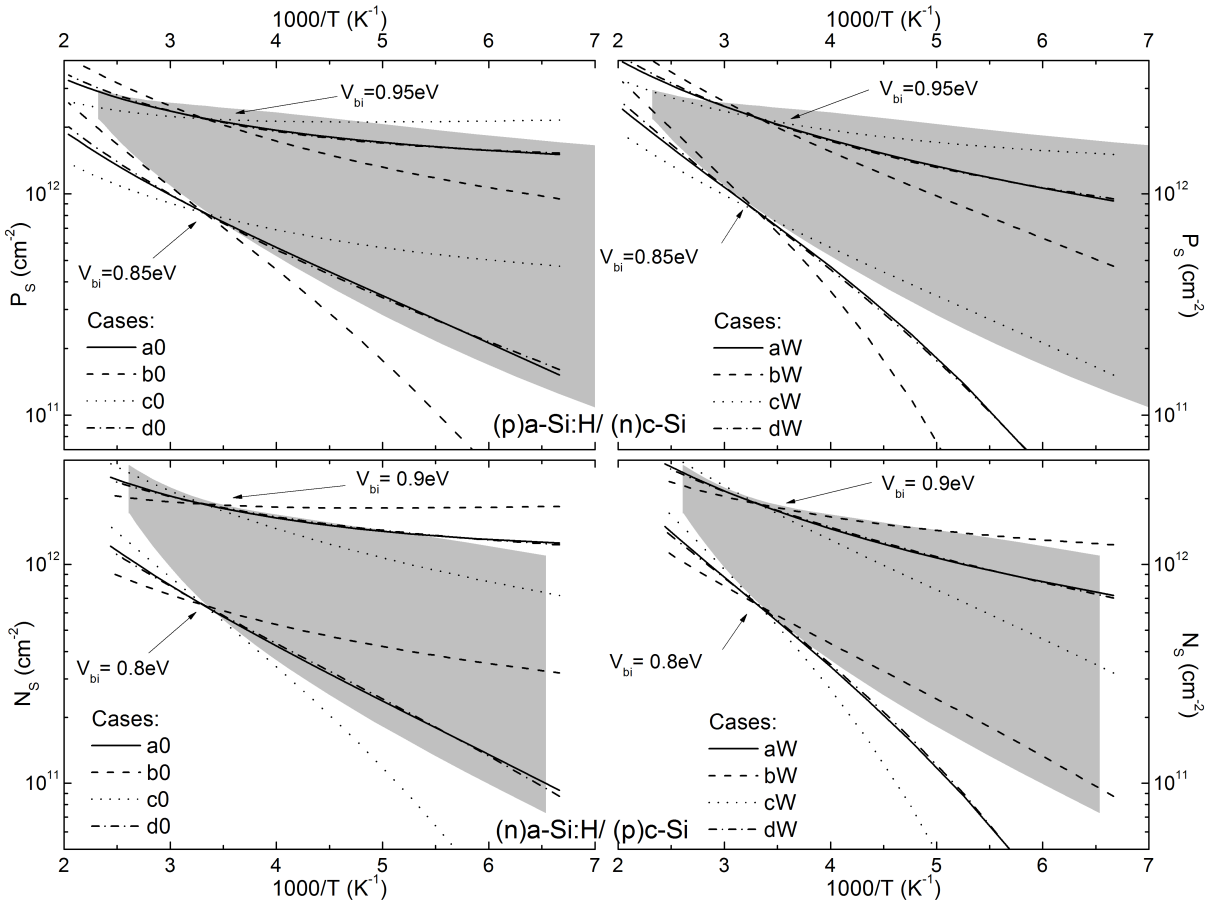

Figure 3.14: Arrhenius plots of the hole (top) and electron (bottom) sheet density calculated for the eight cases of Table 3.1, and for two values of the built-in potential, in both (p)a-Si:H/(n)c-Si (top) and (n)a-Si:H/(p)c-Si (bottom) structures. The constant density of states at E_F is 10^{20} cm^{-3} eV^{-1}. The range of typical experimental data are shown by the grey areas, which account for the uncertainty on the mobility value.

band tail dips strongly with temperature, while the valence band tail shows a much weaker temperature dependence [Aljishi 90]. As the mobility edges, that are the relevant quantities in the context of the present electrical measurements, depend on the tail slopes, the same trend is to be expected for the band offsets.

For those reasons, it is concluded that only case A0 should be retained: in both materials, the decrease of the band gap energy with increasing temperature is attributed to an increase of the electron affinity and the Fermi level stays at the same distance from the closest (majority carrier) band. The valence band offset is thus independent of temperature, while a temperature dependence of the conduction band offset results from different temperature dependences of the gaps of *a*-Si:H and *c*-Si.

3.2.3 Quantitative analysis: extraction of band offsets

In early studies a value of the conduction band offset of 0.15 eV was determined from planar conductance data obtained on (n)*a*-Si:H/(p)*c*-Si structures [Kleider 08]. However, there was no discussion on the possible temperature dependence of the band offset, nor on the influence of the DOS in *a*-Si:H on the band offset determination. Moreover, while some conductance and conductive-probe atomic force microscopy measurements also revealed the existence of an interface channel conductance in (p)*a*-Si:H/(n)*c*-Si structures [Maslova 10], the determination of the valence band offset from these measurements has not been performed yet. The analytical calculations presented above and temperature dependent planar conductance measurements are now used to extract the band offsets.

In section 3.1.6 the influence of various parameters on $P_s(T)$ curves was examined; the built-in potential across the junction has a particularly strong impact on the calculations. It is itself fully determined by the position of the Fermi level position in both materials and the valence band offset (see Eq. 3.2). While the doping determines unambiguously the Fermi level position in *c*-Si, the Fermi level position in *a*-Si:H depends on both the dopant concentration and the defect distribution. This is why additional temperature dependent conductance measurements were performed on *a*-Si:H layers deposited on glass. The activation energy at high temperature ($T \geq 350$ K) was extracted from an exponential fit. In this temperature region, the contribution of transport in delocalized states should be predominant over hopping; the activation energy is thus identified with the Fermi level position in *a*-Si:H. The error in the determination of the Fermi level position was estimated at 0.03 eV [11].

As observed in Fig. 3.7, the *a*-Si:H DOS plays also a significant role for the determination of P_s. Yet the DOS in very thin doped *a*-Si:H layers is not universal and depends on deposition parameters (substrate temperature, pressure, RF power, etc.) and doping. This is why it is very important to test the impact of the DOS in *a*-Si:H on the extraction of band offsets. The influence of the DOS in *a*-Si:H and of the built-in potential on Arrhenius plots of the hole sheet density are decoupled: the first one affects mainly the amplitude, while the latter has an impact on the slope (see Fig. 3.7). This means that, for a coherent use of the model, fits must account for variations of $N(E_F)$ as well as V_{bi}. Therefore the sheet carrier density $P_s(T)$ was calculated for different values of $N(E_F)$ and V_{bi}.
Both calculated and measured curves are fitted by an exponential law around 300 K, $P_s(T) = P_s(300\text{K}) \exp\left[E_a\left(1 - T/300\right)/\left(k_B T\right)\right]$, E_a being the activation energy and P_s(300K) the value of the hole sheet density at 300 K. In this way, any $P_s(T)$ curve calculated for given values of $N(E_F)$ and V_{bi} can be represented by the set (E_a,P_s(300K)). For the simulations, the DOS at the Fermi level in *a*-Si:H was varied between 10^{18} cm^{-3} eV^{-1} and 10^{21} cm^{-3} eV^{-1} while V_{bi} was varied between 0.7 and 1.1 V.

[11] This estimation of the error includes uncertainties on temperature and inaccuracy of the fitting procedure

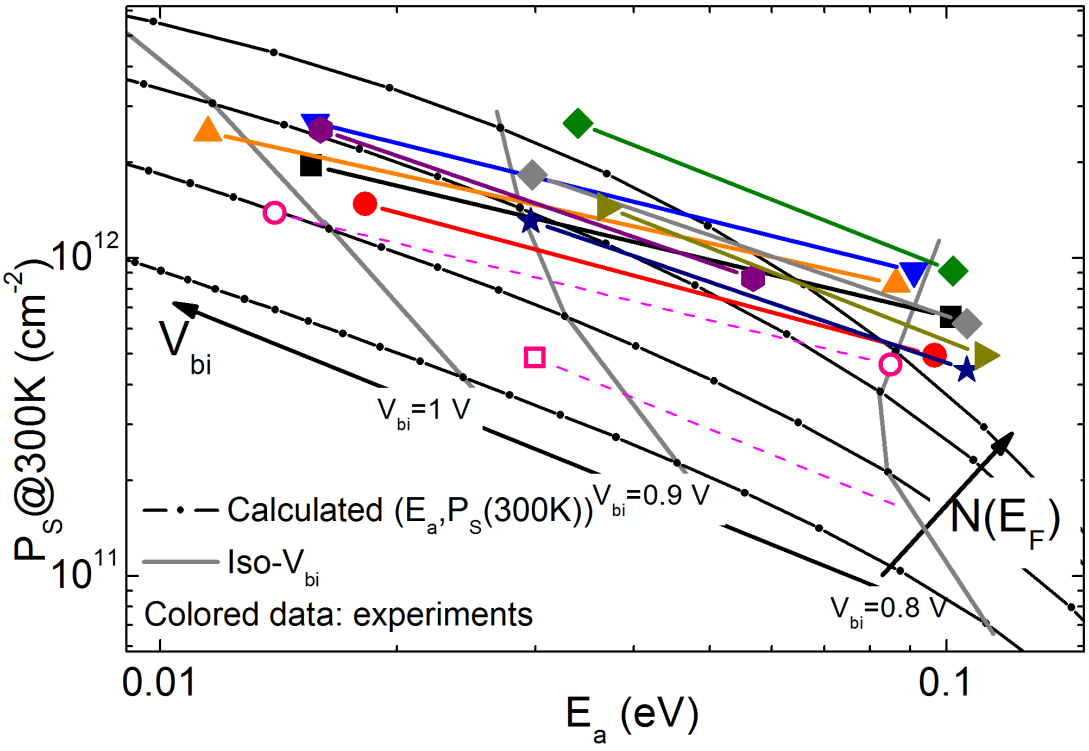

Figure 3.15: Extraction of the built-in potential V_{bi} from comparison between experimental results (pair of symbols joined by a line) and analytical calculations (black solid lines with dots). The activation energy E_a was calculated from the temperature dependence of P_s around room temperature. Each curve is for one density of states ($N(E_F) = 10^{18} \ldots 10^{21}$ cm^{-3} eV^{-1} from bottom to top). The built-in potential varies along each curve as indicated, increasing when E_a decreases or P_s increases. The "iso-built-in potential" curves (grey) are guidelines for the eyes. Each experimental measurement is represented by two symbols connected with a line to account for the uncertainty on the carrier mobility in the strong inversion layer; measurements represented with open pink open symbols were on structures with an (i)a-Si:H buffer layer and are not analyzed here.

One can summarize the results of the study by plotting the values of the sheet carrier concentration at 300 K as a function of the activation energy, as presented in Fig. 3.15. Each point (E_a,P_s(300K)) in Fig. 3.15 is representative of a $P_s(T)$ curve calculated from a pair of parameters ($N(E_F)$,V_{bi}). The experimental results obtained on various samples are also indicated in this figure. Each sample is represented by a line delimited by two points corresponding to the values extracted for the two extreme cases of carrier mobility in the strong inversion region (see section 3.2). This defines the range of uncertainty, other errors coming from the conductance measurement itself are negligible. Then, one can easily read the corresponding built-in potential that fits to the experimental measurements. The band offsets at 300 K are then deduced from Eq. 3.2 using the known values of the Fermi level position in *a*-Si:H and *c*-Si, $\delta^{a-Si:H}$ and δ^{c-Si} [12]. Results for both (p)*a*-Si:H/(n)*c*-Si and (n)*a*-Si:H/(p)*c*-Si structures

Table 3.2: Determination of the band offsets from the extracted values of V_{bi}.

(p)a-Si:H/(n)c-Si			
sample	V_{bi} (meV)	$(E_F - E_v)^{a-Si:H}$ (meV)	valence band offset (meV)
N1	845 ± 35	360 ± 30	329 ± 65
N2	910 ± 70	390 ± 30	422 ± 100
N3	885 ± 95	380 ± 30	385 ± 125
N4	900 ± 100	370 ± 30	391 ± 130
N5	930 ± 120	310 ± 30	360 ± 150
N6	825 ± 55	370 ± 30	316 ± 85
N7	845 ± 60	350 ± 30	318 ± 90
N8	895 ± 80	350 ± 30	370 ± 110
N9	845 ± 55	350 ± 30	318 ± 85
(n)a-Si:H/(p)c-Si			
sample	V_{bi} (meV)	$(E_c - E_F)^{a-Si:H}$ (meV)	conduction band offset (meV)
P1	855 ± 85	260 ± 30	264 ± 115
P2	875 ± 95	170 ± 30	194 ± 125
P3	835 ± 55	170 ± 30	154 ± 85
P4	805 ± 55	130 ± 30	84 ± 85

are summarized in Table 3.2.

Values for the valence band offset range between 0.32 eV and 0.42 eV, with a mean value at 0.36 eV. The standard deviation accounting for measurement errors is 0.04 eV. Considering that the samples investigated here were processed in different institutes, this interval is astonishingly narrow compared to what is found in the literature (see Table 1.2). Moreover, band offset values measured here are in quite good agreement with latest data from photoelectron spectroscopy [Schulze 11b]. Although the P_s curves calculated with two extreme mobilities in Fig. 3.12 look rather different, the uncertainty on the determination of the band offset remains low in most cases, because the valence band offset has the strongest impact on P_s.

The same analysis of planar conductance data has been performed on samples having the reverse structure (n)a-Si:H/(p)c-Si (see Fig. A.1 in the Appendix A). The extracted conduction band offset values, presented in Table 3.2, range from 84 meV to 264 meV. The corresponding mean value is 0.15 eV, the standard deviation is 0.07 eV. For these samples, the band gap energy of the (n)a-Si:H layer was measured by ellipsometry and was found at 1.68 ± 0.02 eV. It was thus possible to deduce the valence band offset from the knowledge of the band gap energy and from the conduction band offset extracted from the analysis of N_s curves using: $E_g^{a-Si:H} = \Delta E_c + \Delta E_v + E_g^{c-Si}$. The deduced values for the valence band offsets in these (n)a-Si:H/(p)c-Si heterostructures are: 292 ± 135, 362 ± 145, 402 ± 105, and 472 ± 105 meV for

[12] For both n-doped and p-doped wafers, $\delta^{c-Si} = 0.25$ eV

samples P1, P2, P3 and P4, respectively, with an average value of 382 meV, in good agreement with that found on (p)*a*-Si:H/(n)*c*-Si heterostructures. However, it should be emphasized that planar conductance measurements on (n)*a*-Si:H/(p)*c*-Si heterostructures are directly related to the *conduction band* offset; care has to be taken in deducing the *valence band* offset, as the optical band gap determined by spectral ellipsometry may be different from the mobility band gap, and it can be prone to large errors on very thin *a*-Si:H layers. The same remark holds when deducing the conduction band offset from planar conductance measurements performed on (n)*a*-Si:H/(p)*c*-Si heterostructures.

A comment on the values of the defect density $N(E_F)$ concludes this section. Values read off from Fig. 3.15 lie mostly between 10^{20} and 10^{21} cm^{-3} eV^{-1}, while the Fermi level position is about 0.35 eV above the valence band edge. This is in rather good agreement with photoelectron spectroscopy measurements of the density of states in the band gap of ultra-thin *a*-Si:H layers using the Constant Final State Yield Spectroscopy mode [Korte 06a], as can be seen in Fig. 3.16. It can be noticed that the valence band tail deviates from the exponential behaviour close to the valence band edge: the factor $N_{v,0}$ usually used in the analytical expression for the exponential valence band tail, $N_v(E) = N_{v,0} \exp\left(\frac{E_v - E_F}{k_B T}\right)$, has no real physical meaning and can strongly differ from the value of the density of states at the valence band edge.

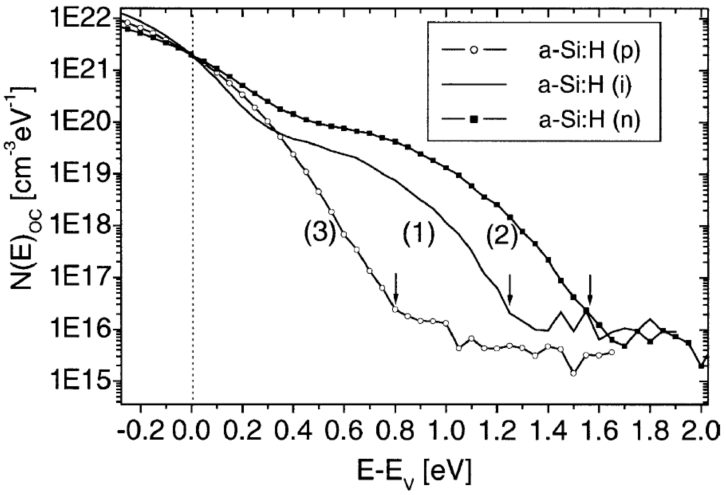

Figure 3.16: Gap state density distribution $N_{OC}(E)$ derived from Constant Final State Yield Spectroscopy of (1) (i)a-Si:H non doped, (2) (n)a-Si:H n-doped with 2×10^4 ppm PH_3, and (3) (p)a-Si:H p-doped with 10^4 ppm B_2H_6. PECVD-deposition at 180 °C, film thickness 10 nm. The arrows mark the position of the Fermi level. Reproduced with permission from [Schmidt 04].

3.3 Comparison with modern band line-up theories

A comparison between temperature dependent planar conductance measurements and analytical calculations led to an estimation of the valence and conduction band offsets. Results can now be discussed in terms of the branch point theory introduced in section 1.2.1.2. A review on interface dipoles at the *a*-Si:H/*c*-Si interface is first presented, before discussing on the position of the branch point in *a*-Si:H.

3.3.1 Review on dipoles at the *a*-Si:H/*c*-Si interface

The presence of dipoles localized at the interface forces the potential to drop over a few angströms; this can be represented by an additional contribution to the band offsets, appearing in the term Δ_{dip} in Eq. 1.18. Dipoles at interfaces are divided in two groups: intrinsic and extrinsic dipoles. Intrinsic dipoles take their origin in the difference between the electronegativities of the species constituting the two adjacent materials. In the case of the *a*-Si:H/*c*-Si heterojunction, this contribution can be neglected because silicon is the main material on both sides.
Extrinsic dipoles stem from foreign atoms present at the interface or defects. H is known to form bonds with Si atoms at the *a*-Si:H/*c*-Si interface, and is used to passivate Si dangling bonds. A $\mathrm{Si}-\mathrm{H}$ dipole is averaged to 0 on the *a*-Si:H side because H is also present on this side of the junction such that $\mathrm{Si}-\mathrm{H}$ dipoles are randomly distributed. However, seen from the crystalline part containing no hydrogen, $\mathrm{Si}-\mathrm{H}$ bonds at the interface all point in the same direction, leading to a finite dipole Δ_{Si-H}. Mönch estimated the potential drop due to $\mathrm{Si}-\mathrm{H}$ dipoles at a *c*-Si surface fully covered with H [Moench 01]. His reasoning was recently applied by Korte to *a*-Si:H/*c*-Si structures; it was shown that for a fully H-covered *a*-Si:H/*c*-Si(111) interface, $\Delta_{Si-H}^{100\%} = 0.09$ eV [Korte 11a]. Accounting for the fact that around 10% of the interface atoms form bonds with H, that yields $\Delta_{Si-H}^{10\%} = 9$ meV.
A similar source of dipoles lies in interface dangling bonds. Due to their amphoteric nature, they can either be empty (D^+, charged +), singly occupied (D^0, charged 0) or doubly occupied (D^-, charged −). Reported estimations for the corresponding dipoles were: $\Delta_{D^+} = 0$ eV, $\Delta_{D^0} = 1$ meV and $\Delta_{D^-} = 2$ meV, for (111) interfaces occupied with 10^{12} cm^{-2} dangling bonds [Korte 11a]. In the case of the (p)*a*-Si:H/(n)*c*-Si structure, it is a good approximation to set the dangling bond dipole contribution to zero, as the Fermi level at the interface is close to the valence band, thus leaving most of the defects empty. On the contrary, it can be assumed that for the (n)*a*-Si:H/(p)*c*-Si structure most of the defects are doubly occupied; one must then account for the additional term Δ_{D^-} in Eq. 1.18.
It is interesting to notice that it is theoretically imaginable to change the charge states of the defects by injecting charges either under illumination or DC bias, thus making dipole contributions injection dependent. As a consequence, band offsets would be also injection dependent. However, from the above values, the predicted variations are very small, smaller than 2 meV, and therefore the injection dependence of the band offset seems to be too low to

be perceived with any method cited previously.

As a conclusion, dipole effects originating from H atoms or from dangling bonds at the interface only bring a negligible contribution to the band offsets. Besides, due to the chemical cleaning of the *c*-Si wafer surface prior to *a*-Si:H deposition it is unlikely that other dipoles bring a significant contribution without seriously affecting the passivation quality of the interface.

3.3.2 The branch point in *a*-Si:H

The branch point concept was introduced earlier in this dissertation (see 1.2.1.2). It was recently proposed, on the basis of experimental determination of the valence band offset between (i)*a*-Si:H and *c*-Si, that the states defining the branch point are actually realized in the bulk of an amorphous material [Korte 11b]. This is consistent with investigations on (i)*a*-Si:H/(p)*c*-Si interfaces by De Wolf and co-workers who recently argued that bulk and interface defects obey the same kinetics [Wolf 12]; the branch point, even if defined by a combination of interface and bulk defects, should be in a large part dominated by bulk defects. The predominantly used and accepted description of the defect distribution in *a*-Si:H relies on the defect pool model (see section 1.1.2): the main idea that serves in the present context is that the defect distribution is dependent on the Fermi level position at the equilibration temperature – and thus on the doping – of the layer. Owing to this concept, several hypotheses can be formulated.

In the first (hypothesis (i)) the branch point is indeed determined by the defect density present in the bulk *a*-Si:H layer. Since any doping would enter the calculation of the neutrality point, the branch point would be nothing else but the bulk Fermi level. Then, a strong evolution of the branch point in *a*-Si:H with the doping of the layers would be expected, and consequently a strong variation of the band offsets. Thus, valence band offsets in (p)*a*-Si:H/(n)*c*-Si structures should be very different from that in (n)*a*-Si:H/(p)*c*-Si structures.

In the second (hypothesis (ii)), one can refine the first hypothesis by considering that only states close to the interface determine the branch point energy. Due to the band bending in *a*-Si:H caused by the charge equilibration between the two materials forming the heterocontact, the position of the Fermi level (referenced to the local valence band edge) at the interface is not at the same position as in the bulk. As a consequence, the defect distribution itself is different at the interface and in the bulk: the branch point could then be the neutrality point of the defect density close to the interface. However, it can be checked from Fig. 3.3 that the band bending in *a*-Si:H does not exceed 100 meV [13], meaning that the difference between the bulk Fermi level and the interface neutrality point will remain small. A strong dependence of the band offsets upon doping would still be observed.

[13] The band bending in *a*-Si:H is calculated from: $V_d^{a-Si:H} = V_{bi} - V_d^{a-Si}$.

Thirdly, (hypothesis (iii)) one could rightly postulate that doping is extrinsic to the material. Thus, the defect distribution to be considered would be the one of the same material (same band gap, same band tails) without doping. Independently from the doping type, the branch point would then lie at the undoped Fermi level position, which is around 0.7…0.9 eV below the conduction band edge. Variations of the branch point energy would then be attributed to variations in the band gap and band tail parameters.

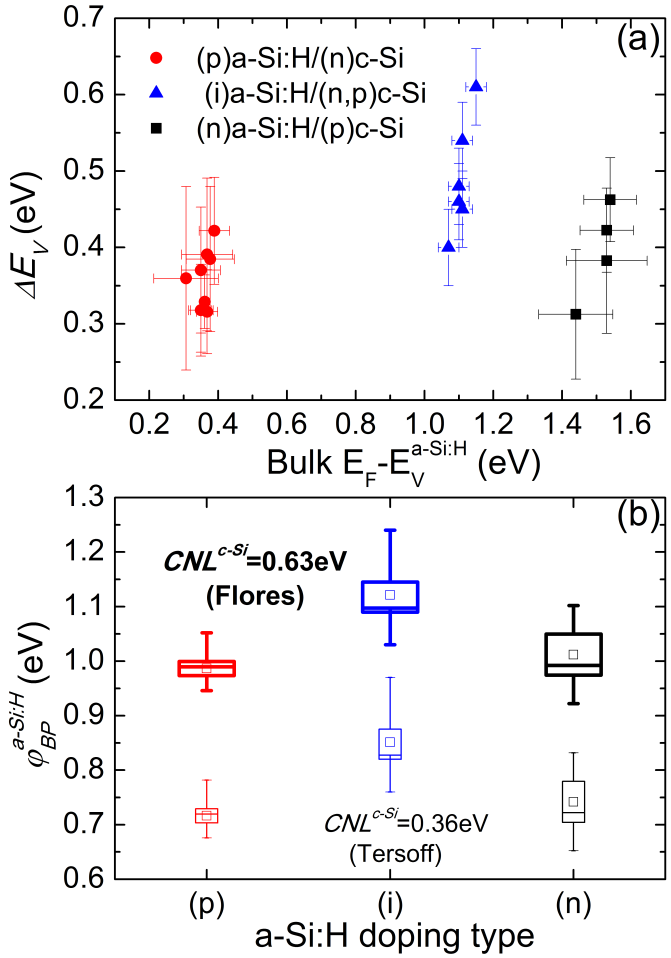

Figure 3.17: (a) Valence band offset versus bulk Fermi level position for the three sets of samples. Samples with doped a-Si:H layers were investigated in this study whereas data for samples with (i)a-Si:H layers are extracted from [Schulze 11b]. (b) Mean value (small inner square), median (horizontal segment), standard errors (big outer box) and min. and max. values (vertical segment) of the branch point energy referenced to the valence band edge, calculated from Eq. 1.18 with Tersoff's (lower values) and Flores' (upper values) c-Si branch point.

In order to check these hypotheses, the dependence of the measured valence band offsets upon the bulk Fermi level position is plotted in Fig. 3.17(a). (p)*a*-Si:H/(n)*c*-Si and (n)*a*-Si:H/(p)*c*-Si samples were measured in the frame of this study (see Table 3.2), whereas samples

with an (i)*a*-Si:H layer were characterized in previous investigations [Schulze 11b, Korte 11b]. No trend is observed: all samples have a valence band offset between 0.3 and 0.6 eV, while the bulk Fermi position increases from 0.3 to 1.6 eV. This eliminates hypotheses (i) and (ii). In Fig. 3.17(b) the mean value, the standard error and the minimum and maximum values of the branch point energy referenced to the valence band edge ($\varphi_{bp}^{a-Si:H}$) are shown for each type of samples. This is done from experimental values of ΔE_v and Eq. 1.18; the branch point in *c*-Si is taken at 0.36 eV (Tersoff's value [Tersoff 84]) and 0.63 eV (Flores' value [Flores 89]). No dipole term is considered, as was argued earlier. The three mean values are almost at the same level, and the small discrepancies can be attributed to variations of the band gaps and band tail parameters between the three types of layers. Interestingly, the branch point in *a*-Si:H calculated with Flores' value for the CNL in *c*-Si lies around 1.05 eV, which is roughly the expected position of the Fermi level in undoped *a*-Si:H, thus tending to support hypothesis (iii).

3.4 Chapter conclusion

In this chapter, an electrical measurement of the band offsets at the *a*-Si:H/*c*-Si interface has been presented. It is based on the comparison of temperature planar conductance measurements and newly developed analytical calculations of the band bending in *c*-Si. Estimations of the band offsets – $\Delta E_v = 0.36$ eV and $\Delta E_c = 0.15$ eV – are in good agreement with recently published data. In addition, it has been argued that the valence band offset does not vary with temperature, whereas the conduction band offset does. Remarkably, the measured valence band offsets have the same values on (n)*a*-Si:H/(p)*c*-Si and (p)*a*-Si:H/(n)*c*-Si suggesting that the branch point in *a*-Si:H is not directly linked to the doping-dependent *a*-Si:H bulk defect distribution.

4

Simulation-based guidelines to open-circuit voltage maximization in *a*-Si:H/*c*-Si solar cells

In chapter 3, a study on the band bending in *c*-Si was used to extract the band offsets at the *a*-Si:H/*c*-Si interface. In order to avoid the consideration of the *a*-Si:H surface, the analysis of planar conductance measurements was made on structures with *a*-Si:H layers much thicker than in silicon heterojunction solar cells. In this chapter, structures devoted to be incorporated in solar cells are studied. A special attention is paid to the influence of the equilibrium band bending in *c*-Si (φ_{c-Si}) on cell performance, in particular on the open-circuit voltage. To do so, the finite thickness of the *a*-Si:H layer and the presence of a buffer layer are now taken into account. First, the qualitative relationship between φ_{c-Si} and V_{oc} is established via numerical modeling. Then theoretical and experimental investigations on the dependence of φ_{c-Si} on materials properties (density of states, thickness, doping density, ...) are presented. These results lead to a discussion on a pathway towards the optimization of such solar cells.

4.1 Band bending and open circuit voltage

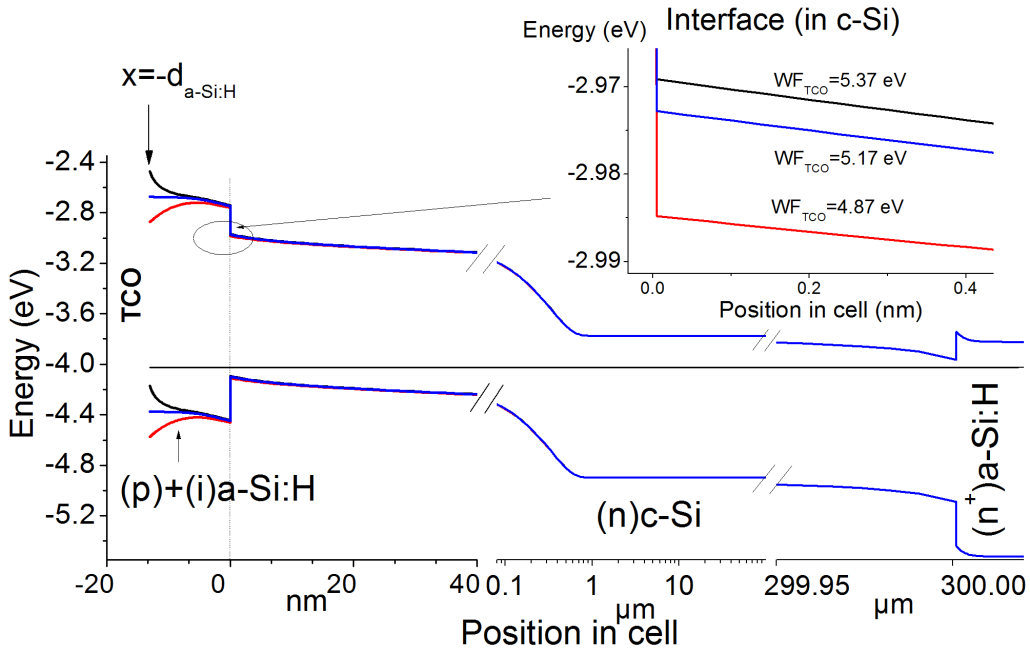

Figure 4.1: Band diagram of a complete TCO/(p)a-Si:H/(i)a-Si:H/(n)c-Si/(n)a-Si:H solar cell calculated with AFORS-HET for three values of the TCO work function: 5.37 *eV (black),* 5.17 *eV (blue) and* 4.97 *eV (red). The inset is a zoom on the (i)a-Si:H/(n)c-Si hetero-interface. The standard structure is described in section 2.3.5.*

In solar cells, the band bending φ_{c-Si} comes from the formation of the p-n junction required to provide an electric field that separates photo-generated charge carriers. The separation of photo-generated electrons and holes leads to the building of the open-circuit voltage across the structure. Therefore, φ_{c-Si} and V_{oc} are expected to be correlated. In order to illustrate theoretically the interdependence between φ_{c-Si} and V_{oc}, simulations of solar cells have been performed with the numerical simulation software AFORS-HET introduced in section 2.3.
The standard *a*-Si:H/*c*-Si cell was presented in section 2.3.5. The thickness of the (p)*a*-Si:H emitter layer is 10 nm; this is too low to assume, like in Chapter 3, that the TCO/*a*-Si:H interface has no impact on φ_{c-Si}. As outlined in [Centurioni 03], a variation of TCO work function (WF_{TCO}) strongly modifies the band diagram in *a*-Si:H, thus the charge in *a*-Si:H. This was also reported by Zhao [Zhao 08]. As a consequence of the overall charge neutrality, the charge in *c*-Si has also to vary, inducing a variation in φ_{c-Si}. The dependence of φ_{c-Si} on the work function of the TCO is illustrated in Fig. 4.1, where the simulated band diagram of the cell is given for three values of WF_{TCO}: 5.37 eV, 5.17 eV and 4.97 eV [1].
φ_{c-Si} is extracted from simulations at equilibrium, while V_{oc} is determined from simulations of I-V curves under AM1.5 illumination. Not only changes in WF_{TCO} can lead to variations

[1] The work function of (p)*a*-Si:H is fixed at 5.17 eV in the simulations.

of φ_{c-Si}. As shown in Chapter 3, band offsets and the DOS in a-Si:H also modulate φ_{c-Si}. However, modifications of parameters of the heterojunction (band offset, doping, etc.) would lead to complicated effects at the a-Si:H/c-Si interface since it also influences charge recombinations and current transport at the interface.
Thus, changing the WF_{TCO} value is technology relevant because in devices the (p)a-Si:H layer is thin enough so that the a-Si:H surface plays a role on the band bending. It is also an easier way to decorrelate the influence of φ_{c-Si} on the cell performance from the impact of other parameters.

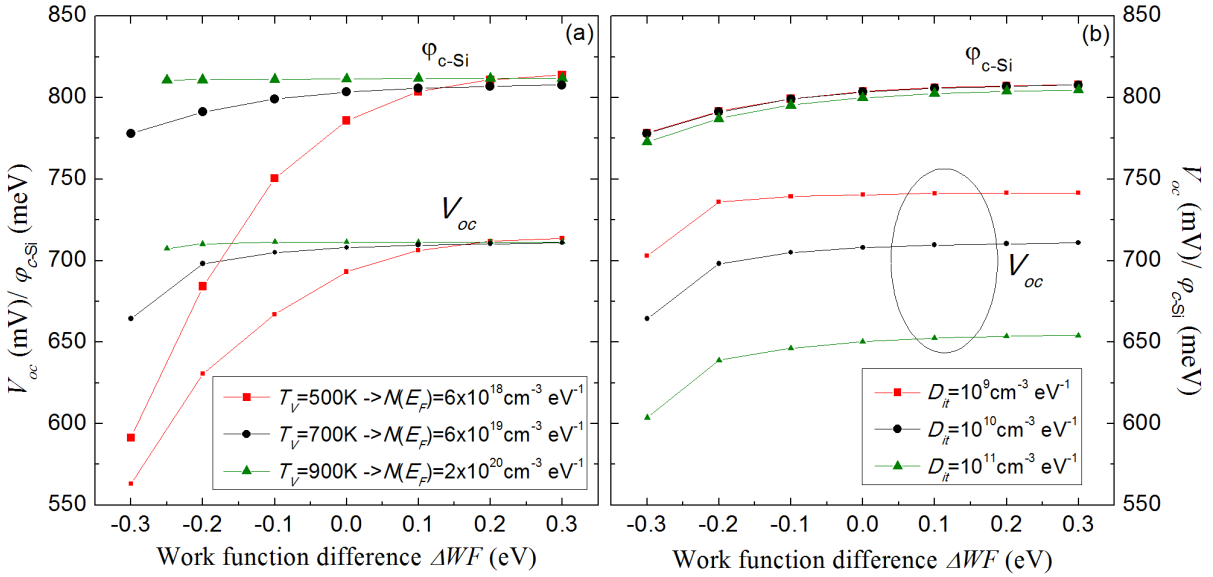

Figure 4.2: Variation of the open circuit voltage V_{oc} and the equilibrium band bending in c-Si (φ_{c-Si}) as a function of $\Delta WF = WF_{TCO} - WF_{a-Si:H}$ [2] for (a) different bulk defect densities in a-Si:H and (b) different interface defect densities (D_{it}) at the a-Si:H/ c-Si hetero-interface.

V_{oc} and φ_{c-Si} extracted from AFORS-HET simulations are plotted in Fig. 4.2 versus $\Delta WF = WF_{TCO} - WF_{a-Si:H}$ for (a) different bulk defect densities in a-Si:H and (b) different interface defect densities. Both V_{oc} and φ_{c-Si} increase when WF_{TCO} increases. In Fig. 4.2(a), V_{oc} and φ_{c-Si} are plotted for three valence band tail parameters leading to three different values of $N(E_F)$. Interestingly, for a fixed value of ΔWF, both V_{oc} and φ_{c-Si} increase when $N(E_F)$ increases. This will be discussed later.
The correlation between V_{oc} and φ_{c-Si} can be explained as follows. V_{oc} gives an indication on how efficiently the photo-generated charges are separated. In a simple one-diode model, it can be expressed as $V_{oc} = \frac{nk_BT}{q} \ln(J_{sc}/J_0 + 1)$ where n is the diode ideality factor and J_0 the dark saturation current[3]. For a given J_{sc}, the lower J_0, the greater is V_{oc}. In a (p)a-Si:H/(n)c-Si heterojunction, the electrons reaching the (p)a-Si:H emitter layer (or more generally, the

[2] The work function in a-Si:H $WF_{a-Si:H}$ is constant and is given by $WF_{a-Si:H} = \chi_{a-Si:H} + (E_c - E_F)^{a-Si:H}$
[3] This estimation of V_{oc} gives an approximation of about 5 % of the measured V_{oc} [Schulze 10b].

amorphous stack consisting of an (i)*a*-Si:H layer and a (p)*a*-Si:H layer) have a higher probability to recombine through gap defects than being repelled backwards to the rear side. Under dark conditions, this recombination current tends to increase the saturation current J_0 and thus to decrease V_{oc}. In order to minimize J_0, electrons have to be repelled *before* they reach the *a*-Si:H layer. This phenomenon is directly related to the value of the band bending in *c*-Si plus the conduction band offset because the barrier seen by the electrons before reaching the *a*-Si:H layer is $\varphi_{c-Si} + \Delta E_c$ (see Fig. 1.7).

Although WF_{TCO} has a huge impact on V_{oc} through φ_{c-Si}, it should not be forgotten that the interface defect density also plays a major role in the device performance. In Fig. 4.2(b) the expected decrease of V_{oc} with the increase of the interface defect density at the *a*-Si:H/*c*-Si interface (D_{it}) is illustrated. It is of particular interest to relate the values and the variations of the V_{oc} in Fig. 4.2(a) and Fig. 4.2(b): although a decrease of the interface defect density leads to an increase of V_{oc} whatever ΔWF, a non-optimized TCO/emitter structure could seriously reduce the cell performance obtainable theoretically for a given D_{it}. In particular, if the reduction of D_{it} is followed by a decrease of the band bending, a trade-off in Fig. 4.2(b) has to be found.
The different variations of V_{oc} with respect to variations of D_{it} (the trend is independent of ΔWF) and $N(E_F)$ (the trend strongly depends on ΔWF) is another illustration of the decoupling between chemical defect passivation and field effect passivation observed in PCD measurements for instance [Leendertz 11b].

In summary, the direct dependence of V_{oc} on φ_{c-Si} has been illustrated. It must be clearly stated that a high V_{oc} implies a high φ_{c-Si}, but the reverse statement is not true because interface recombination has a huge impact on V_{oc} whereas it almost doesn't influence φ_{c-Si}. Thus the question is "how to maximize V_{oc} in relation with the passivation quality and the maximization of φ_{c-Si}?". In the following this question shall be addressed both from the theoretical and experimental points of view.

4.2 Analytical calculations of φ_{c-Si}: influence of thin *a*-Si:H emitter and buffer layers

The analytical calculation presented in the previous chapter considered only one particular case of boundary condition at the *a*-Si:H surface (surface electric field equal to zero) and the analysis of planar conductance measurements was done assuming an infinite (p)*a*-Si:H layer. For this reason, the analytical model is not sufficient to study accurately the dependence of the band bending on solar cell parameters (thickness of the (p)*a*-Si:H layer, property of the contact, etc.), and to investigate how to maximize it. Now, the model is made more complex to describe more precisely the *a*-Si:H/*c*-Si heterojunction present in solar cells. The charge in *c*-Si is given in Eq. 3.20. Modifications only concern the charge in *a*-Si:H and the repartition of potential drops. In particular, the finite thickness of the emitter layer and an interfacial

(i)*a*-Si:H layer are now taken into account.

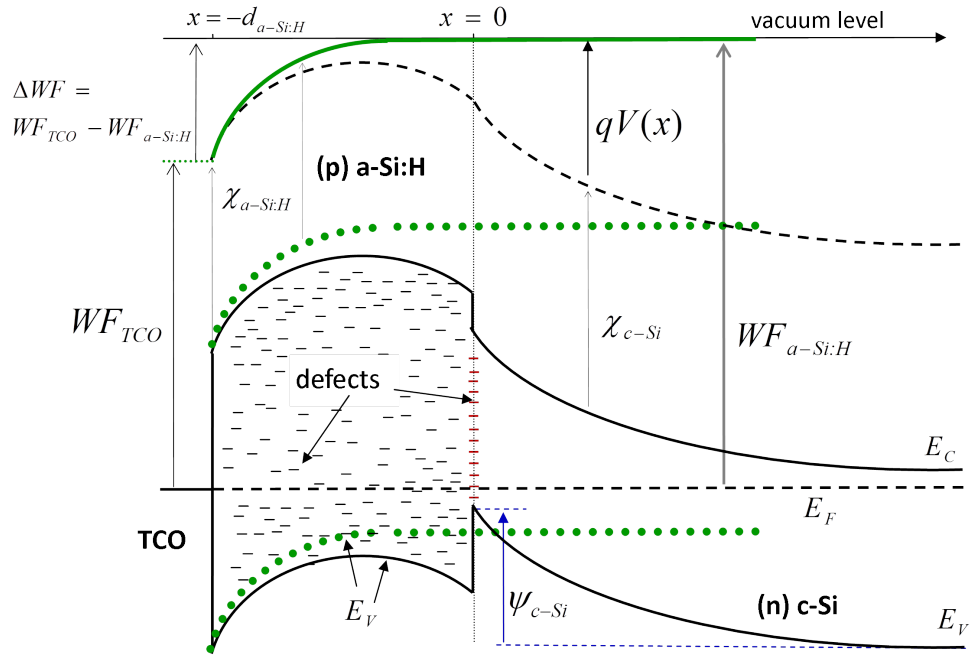

Figure 4.3: Band diagram of a thin a-Si:H layer in contact with a transparent conductive oxide layer (left) and c-Si (right) (black lines) and the same a-Si:H contacted with the same TCO but free of contact on the right side (infinite thickness; green dots). Black dashed and green solid lines are the electrostatic potential in the thin and thick (p)a-Si:H layers and in c-Si (black only), respectively. The electrostatic potential of the thick a-Si:H layer defines the reference for the potential.

Fig. 4.3 shows the band diagram of a (p)*a*-Si:H/(n)*c*-Si heterojunction in contact with a TCO. Parameters like the electron affinities and work functions are presented for each material. The *a*-Si:H/*c*-Si interface is at $x = 0$. From this figure it can already be seen that when the (p)*a*-Si:H layer gets thinner, band curvatures on both side of *a*-Si:H (TCO side and *c*-Si side) overlap such that the *a*-Si:H/*c*-Si interface is influenced by the TCO/*a*-Si:H interface.

4.2.1 Calculation of the charge in a thin *a*-Si:H emitter layer

Specific boundary conditions are imposed by the finite thickness of the *a*-Si:H emitter layer, and have to be addressed more precisely than in Chapter 3. Two types of boundary conditions, already introduced in section 3.1.4, will be considered in the following:

- Neumann conditions if the *a*-Si:H surface is free (i.e. facing the vacuum or air) or covered by an insulator.
- Dirichlet conditions if the *a*-Si:H surface is in contact with a material behaving like a

metal (high density of free carriers, electric field equal to zero).

The amorphous layer is between $x = -d_{a-Si:H}$ and $x = 0$; the surface that will be described by the two types of boundary conditions is located at $x = -d_{a-Si:H}$ (see Fig. 4.3). Like in Chapter 3, a constant DOS is assumed in the *a*-Si:H band gap.

4.2.1.1 Neumann conditions

If the *a*-Si:H layer is uncovered and in contact with air or vacuum, or if an insulator (e.g. SiO_2) is deposited on its surface, the electric field at the surface rules the behaviour of the potential close to the surface. This is the case in many measurement configurations. The boundary condition at $x = -d_{a-Si:H}$ is then given by the surface charge $Q_{-d_{a-Si:H}}$ (or by the charge in the insulator):

$$\xi(-d_{a-Si:H}) = -\left(\frac{dV}{dx}\right)_{x=-d_{a-Si:H}} = \xi_{-d_{a-Si:H}} = Q_{-d_{a-Si:H}}/\epsilon, \tag{4.1}$$

where $\xi_{-d_{a-Si:H}}$ is the electric field. The other boundary condition at $x = 0$ is, like in section 3.1.2.2, given by $V(x=0) - V(-\infty)$, related to φ_{c-Si} through V_{bi} (see Eq. 3.40).

The solution of Eq.3.34 leads to the expression for the potential between $x = -d_{a-Si:H}$ and $x = 0$:

$$V(x) - V(-\infty) = \frac{V(0) - V(-\infty)}{\cosh\left(d_{a-Si:H}/L_D^{a-Si:H}\right)} \cosh\left(\frac{x + d_{a-Si:H}}{L_D^{a-Si:H}}\right) - L_D^{a-Si:H}\xi_{-d_{a-Si:H}} \frac{\sinh\left(x/L_D^{a-Si:H}\right)}{\cosh\left(d_{a-Si:H}/L_D^{a-Si:H}\right)}. \tag{4.2}$$

The total charge in *a*-Si:H is then obtained by the integration of the charge density $\rho(x)$:

$$\begin{aligned} Q_{a-Si:H} &= \int_{-d_{a-Si:H}}^{0} \rho(x)dx \\ &= Q_{-d_{a-Si:H}}\left(\frac{1}{\cosh\left(d_{a-Si:H}/L_D^{a-Si:H}\right)} - 1\right) - \frac{\epsilon}{L_D^{a-Si:H}}\left(V(0) - V(-\infty)\right)\tanh\left(\frac{d_{a-Si:H}}{L_D^{a-Si:H}}\right). \end{aligned} \tag{4.3}$$

Using Neumann boundary conditions at the surface of *a*-Si:H, it is thus possible to obtain an analytical expression for the charge in *a*-Si:H as a function of the surface charge. When $Q_{-d_{a-Si:H}} = 0$ (no surface charge implies a surface electric field equal to zero), the expression of the total charge in a-Si:H is obviously the one found in section 3.1.2.2.

4.2.1.2 Dirichlet conditions

When incorporated in a complete solar cell, the *a*-Si:H layer is covered by a transparent conductive oxide whose electronic behaviour is equivalent to a metal (metal-semiconductor Schottky contact). In this case, the *a*-Si:H layer surface potential is governed by the difference of the work functions; in Fig. 4.3 the difference between the TCO and *a*-Si:H work functions ΔWF is: $\Delta WF = WF_{TCO} - WF_{a-Si:H}$ where $WF_{a-Si:H}$ is the work function of an infinite *a*-Si:H layer. As a consequence, the boundary condition at the *a*-Si:H surface reads:

$$V(-d_{a-Si:H}) - V(-\infty) = \frac{1}{q}(WF_{a-Si:H} - WF_{TCO}) = -\frac{\Delta WF}{q}. \tag{4.4}$$

The solution of Eq. 3.34 gives in this case:

$$V(x) - V(-\infty) = (V(0) - V(-\infty))\frac{\sinh\left(x + d_{a-Si:H}/L_D^{a-Si:H}\right)}{\sinh\left(d_{a-Si:H}/L_D^{a-Si:H}\right)} + \frac{\Delta WF}{q}\frac{\sinh\left(x/L_D^{a-Si:H}\right)}{\sinh\left(d_{a-Si:H}/L_D^{a-Si:H}\right)}, \tag{4.5}$$

which leads to

$$Q_{a-Si:H} = \frac{\epsilon}{L_D^{a-Si:H}}\left[V(0) - V(-\infty) - \frac{\Delta WF}{q}\right]\frac{1-\cosh\left(d_{a-Si:H}/L_D^{a-Si:H}\right)}{\sinh\left(d_{a-Si:H}/L_D^{a-Si:H}\right)}. \tag{4.6}$$

The electric field at $x = -d_{a-Si:H}$ reads from Eq.4.5:

$$\xi(-d_{a-Si:H}) = -\left(V(0) - V(-\infty) + \frac{\Delta WF}{q}\cosh\left(\frac{d_{a-Si:H}}{L_D^{a-Si:H}}\right)\right)\frac{1}{L_D^{a-Si:H}\sinh\left(d_{a-Si:H}/L_D^{a-Si:H}\right)}. \tag{4.7}$$

Thus, Dirichlet conditions lead to an expression of the charge in *a*-Si:H that is a function of the work function difference between *a*-Si:H and the TCO.

4.2.1.3 Charge at the *a*-Si:H surface

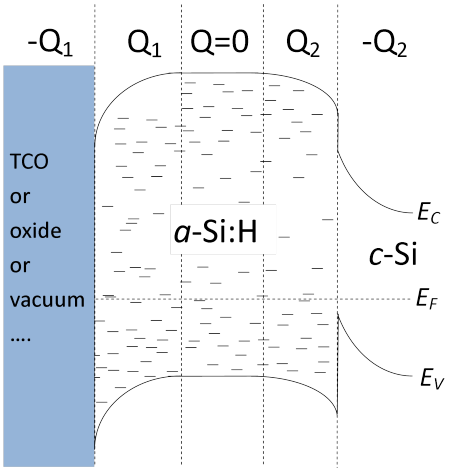

Figure 4.4: Band diagram of a thick a-Si:H layer in contact with c-Si (right). On the left, the a-Si:H surface can be in contact with TCO, metal, oxide, vacuum, etc. Because the a-Si:H surface and the a-Si:H/c-Si interface don't influence each other, the charge neutrality can be written separately at both interface; a neutral zone separates the two regions.

In Fig. 4.4, the band diagram of a (p)*a*-Si:H/*c*-Si is shown, where the *a*-Si:H surface is in contact with any medium cited above: TCO, metal, oxide, vacuum,... In the case of Fig. 4.4, the *a*-Si:H thickness is thick enough so that the flat band regime is reached in *a*-Si:H ($Q = 0$) (case treated in Chapter 3) but it illustrates the fact that the total charge in *a*-Si:H is the sum of the charges in the space charge regions on both side ($Q_{a-Si:H} = Q_1 + Q_2$). Because the *a*-Si:H is thick enough so that both interfaces do not influence each other, the charge neutrality applies independently at both interfaces. On the left side, a surface charge has to be taken into account to compensate the charge in *a*-Si:H. It is given by the electric field at the *a*-Si:H surface. The charge neutrality of the whole structure should take into account this surface charge: $-Q_1 + Q_1 + Q_2 - Q_2 = 0$.

Eq. 4.7 gives the electric field at the surface of *a*-Si:H in the case of a Schottky-like boundary condition (Dirichlet condition). In the case of an insulator-like condition (Neumann condition), the electric field is an input parameter through the surface charge $Q_{-d_{a-Si:H}}$. In both cases, the surface [4]charge (called $-Q_1$ previously) has to be taken into account:

$$Q_{\text{surface}} = \xi_{-d_{a-Si:H}} \times \epsilon. \tag{4.8}$$

In the case of a thick *a*-Si:H layer ($d_{a-Si:H} \gg L_D^{a-Si:H}$), the two interfaces at each side of the *a*-Si:H layer do not influence each other. The total charge on the *a*-Si:H side of the junction

[4]For simplicity, "surface" is used even if it could be an interface (contact with a TCO for example).

can be expressed in the same way as in section 3.1.2.2 when $d_{a-Si:H} \gg L_D^{a-Si:H}$:

$$\lim_{d_{a-Si:H}/L_D^{a-Si:H} \to +\infty} Q_{\text{surface}} + Q_{a-Si:H} = -\frac{\epsilon}{L_D^{a-Si:H}} \left(V(0) - V(-\infty)\right) \tag{4.9}$$

4.2.2 Calculation of the charge in an interfacial *a*-Si:H buffer layer

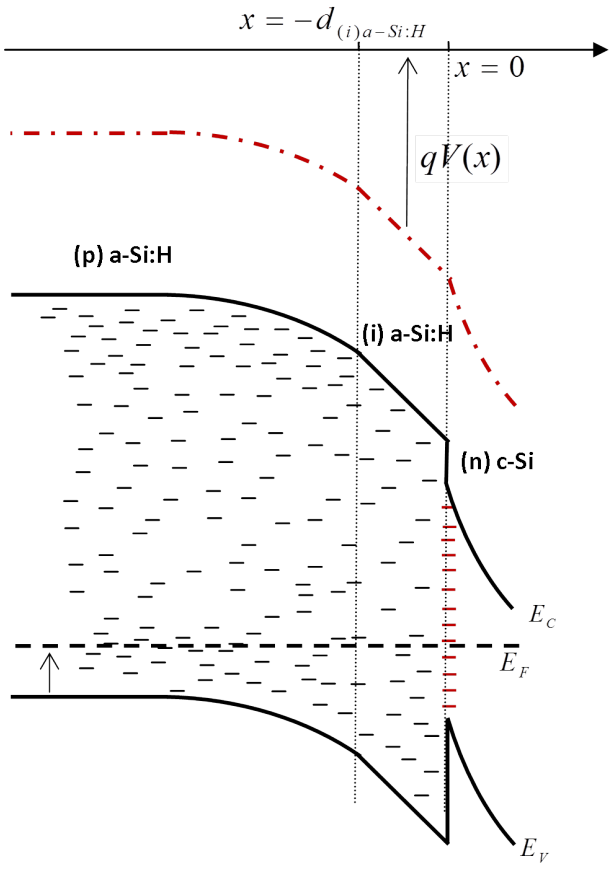

Figure 4.5: Band diagram including a thin (i)a-Si:H layer between the doped a-Si:H layer and the crystalline substrate. The potential is assumed to vary linearly in the (i)a-Si:H.

The effect of the insertion of a thin (i)*a*-Si:H layer between the doped amorphous emitter and the crystalline substrate is now taken into account in the calculation. For simplicity, it is assumed that the electrostatic potential varies linearly over the very small thickness $d_{(i)a-Si:H}$, such that the electric field ξ is constant in the layer. This is a reasonable assumption since the defect density in a (i)*a*-Si:H layer is lower as compared to the one in the adjacent doped amorphous layer. The (constant) electric field in the layer is determined by applying Gauss' law between the *c*-Si bulk (where $\xi(+\infty) = 0$) and the interface, taking into account interface

charged defects (described by the charge Q_{int}):

$$\xi(x=0^-) = \frac{Q_{c-Si} + Q_{\text{int}}}{\epsilon}. \tag{4.10}$$

The band profile in the (i)*a*-Si:H layer is shown in Fig. 4.5 and can be written as:

$$E_F - E_v(x) = E_F - E_v(0^-) + q\xi(0^-)x \text{ for } -d_{(i)a-Si:H} < x < 0. \tag{4.11}$$

The valence band edge $E_v(0^-)$ at the interface on the *a*-Si:H side is related to u_s by (cf Figs. 3.1 and 4.5):

$$E_F - E_v(0^-) = \Delta E_v + E_g^{c-Si} - \left(k_B T(u_b - u_s) + \delta^{c-Si}\right). \tag{4.12}$$

Assuming a constant density of states $N_{(i)a-Si:H}$ through the whole gap, the charge density $\rho(x)$ can be calculated with Eq. 3.33. After the integration of $\rho(x)$ between $x = -d_{(i)a-Si:H}$ and $x = 0$, the charge in (i)*a*-Si:H reads:

$$Q_{(i)a-Si:H} = qN_{(i)a-Si:H}d_{(i)a-Si:H}\left[(E_F - E_v)_{\text{neutral}}^{(i)a-Si:H} - (E_F - E_v(0^-)) - \frac{q}{2}\xi(0^-)d_{(i)a-Si:H}\right] \tag{4.13}$$

where $(E_F - E_v)_{\text{neutral}}^{(i)a-Si:H}$ is the position of the Fermi level referred to the valence band edge that ensures the charge neutrality in (i)*a*-Si:H.
Taking into account the potential drop in (i)*a*-Si:H, the term $V(0) - V(-\infty)$ in Eq. 3.37 should be replaced by $V(-d_{(i)a-Si:H}) - V(-\infty)$ given by:

$$V(-d_{(i)a-Si:H}) - V(-\infty) = V_{bi} - d_{(i)a-Si:H}\xi(0^-) - V_d^{c-Si}. \tag{4.14}$$

The neutrality equation is solved as in the previous chapter to get the value of φ_{c-Si}.

The improved version of the analytical model will be used in the following to study the interplay between the thickness and the density of states in the (p)*a*-Si:H emitter. Later, it will be used to discuss experimental measurements of the band bending in structures with a buffer layer.

4.3 Interplay between thickness and density of states in the (p)*a*-Si:H emitter

4.3.1 Experimental evidence of surface effects

In Chapter 3, the *a*-Si:H layers were all thick enough to consider that the *a*-Si:H/*c*-Si interface was independent of the *a*-Si:H surface. However, in a solar cell the thickness of the emitter layer is drastically reduced to avoid parasitic absorption of light: a too high absorption in the emitter layer reduces the amount of electron-hole pairs generated in the absorber, leading to a decrease of the short circuit current (see section 5.2.2 for an illustration).
The emitter layer thickness being around 10 nm, the *a*-Si:H surface may have an influence on the *a*-Si:H/*c*-Si interface. The planar conductance was measured on such low thickness samples. Fig. 4.6 shows the hole sheet density P_s extracted from planar conductance measurements for the case of an interface limited mobility (see section 3.2). Two samples with the same (p)*a*-Si:H/(n)*c*-Si structure have been measured. Only the thickness of the (p)*a*-Si:H layer differs between the two samples (10 and 30 nm). Experiments were done in this way:

- The sample is loaded in the cryostat.
- Measurements each 10 ˚C from room temperature up to 80 ˚C (red curve).
- Measurements from 80 ˚C down to −120 ˚C.
- Back to room temperature (no measurements), the sample is taken out of the cryostat and left in air for several hours.
- The sample is loaded in the cryostat again, measured from room temperature up to 110 ˚C, annealed 30 minutes at 110 ˚C, and measured down to −120 ˚C (black curve).
- The sample is taken out of the cryostat and left in air for several hours.
- Measurements from room temperature up to 150 ˚C, annealing 30 minutes at 150 ˚C, and measurements down to −120 ˚C (blue curve).

It can be observed that the effect of the annealing is not reversible on the thicker sample whereas for the thinner one each measurement starts from the same point at room temperature. Indeed, when samples are in contact with air, they may adsorb (or absorb in the first layers due to a porosity of the film) some elements like water or $\mathrm{C}-\mathrm{H}$ complexes, creating a surface charge or dipole. Once heated in vacuum, surface contaminants desorbe, changing the surface conditions and the total charge in *a*-Si:H. For the thinner sample, it explains why the measurements before and after the annealing are different. For the thicker sample, the

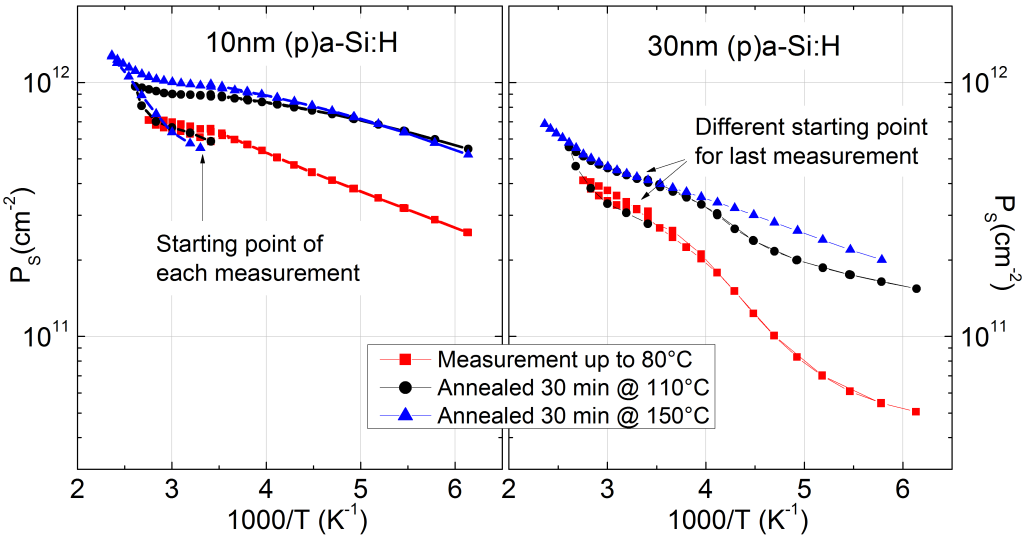

Figure 4.6: Hole sheet density measured by the planar conductance technique for two samples having different emitter thicknesses, before and after annealing at 110 ˚*C and* 150 ˚*C. Between the measurements, the samples were taken out of the cryostat and left in air for several hours.*

a-Si:H surface is expected not to play a role and the annealing seems to modify irreversibly [5]either the (p)*a*-Si:H layer itself or the *a*-Si:H/*c*-Si interface.

This explanation can be illustrated by analytical calculations of P_s versus the *a*-Si:H surface charge as described in section 4.2.1. In Fig. 4.7, P_s is plotted as a function of $Q_{-d_{a-Si:H}}$ for three emitter thicknesses ranging from 10 to 30 nm. For thick emitters, the surface charge has no influence on P_s; however, for thinner emitters the surface charge has an impact on P_s when the surface charge reaches the same order of magnitude as the total charge in *a*-Si:H. A positive surface charge counterbalances the negative charge in *a*-Si:H so that the positive charge in *c*-Si decreases: thus P_s decreases. On the contrary, a negative surface charge increases the total negative charge in *a*-Si:H and P_s increases.
For the sample with the thinnest emitter, changes of the surface state have an impact on the band bending in *c*-Si [6] as the flat band regime is not reached in the *a*-Si:H layer. These results show that the thickness of the emitter layer and the contact at its surface have to be carefully optimized to ensure the highest band bending as possible.

[5]At least the thicker sample does not go back to its initial state after being in air.
[6]The relationship between P_s and the band bending is found in Eq. 3.49 and is detailed later in section 4.4.

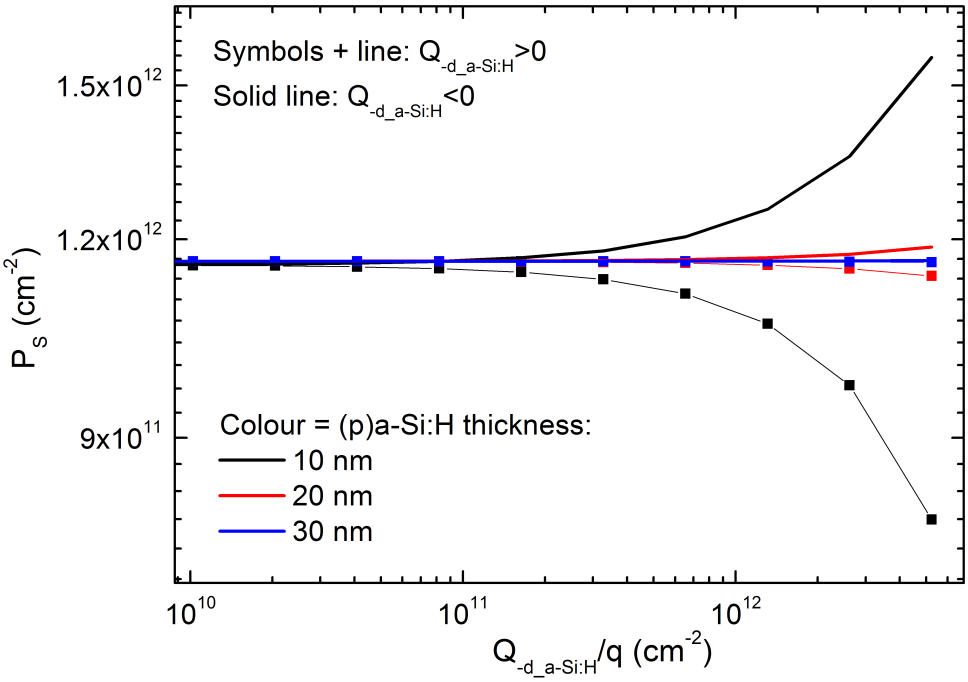

Figure 4.7: Hole sheet density P_s in c-Si versus the a-Si:H surface charge $Q_{-d_{a-Si:H}}$ calculated analytically for three (p)a-Si:H thicknesses. The DOS in (p)a-Si:H is $N(E_F) = 5 \times 10^{20}$ cm^{-3} eV^{-1} and $V_{bi} = 900$ mV.

4.3.2 Emitter density of states/thickness interplay

Planar conductance measurements on samples covered by a metal or a TCO are not possible because an additional highly conductive path would screen out the inversion channel. Therefore, simulations are needed to study structures close to the final solar cells.
The analytical model developed previously was used to calculate φ_{c-Si} for various sets of parameters. Dirichlet boundary conditions were used to simulate a TCO/(p)*a*-Si:H/(n)*c*-Si structure. Neither interface defects nor (i)*a*-Si:H layers were considered here. Variations of φ_{c-Si} as a function of the *a*-Si:H thickness, the (p)*a*-Si:H DOS $N(E_F)$ and the work function difference ΔWF are presented in Fig. 4.8. In these calculations, the bulk Fermi level position E_F in *a*-Si:H is set at 0.35 eV above the valence band edge, the doping density in (n)*c*-Si and the valence band offset ΔE_v are taken equal to 2×10^{15} cm^{-3} and 0.35 eV, respectively. Moreover, ΔWF is modified by changing the work function of the TCO. A set of standard parameters was used as reference (black curves in Fig. 4.8): $N(E_F) = 10^{19}$ cm^{-3} eV^{-1}, $d_{a-Si:H} = 10$ nm, $\Delta WF = 0$ eV.

In Fig. 4.8(a), it can be observed that φ_{c-Si} depends on the (p)*a*-Si:H layer thickness only for $d_{a-Si:H} \leq 10$ nm. In fact, as soon as $d_{a-Si:H}$ is a few times the Debye length in *a*-Si:H, $L_D^{a-Si:H}$, the flat band regime is reached in the *a*-Si:H layer. Then the TCO/(p)*a*-Si:H and (p)*a*-Si:H/(n)*c*-Si interfaces do not influence each other via the electric field: the charge neutrality can be independently stated close to both interfaces. Consequently, φ_{c-Si} stays constant whatever $d_{a-Si:H}$ and ΔWF.

Fig. 4.8(d) shows that φ_{c-Si} increases with $N(E_F)$ except for $\Delta WF = 0.2$ eV, where it decreases slightly for $N(E_F)$ up to 10^{20} cm^{-3} eV^{-1}. This increase is independent of ΔWF for values of $N(E_F)$ above 10^{20} cm^{-3} eV^{-1}. The reason for this is that, for high bulk defect densities, the *a*-Si:H Debye length decreases such that both interfaces are separated for the same reason as in Fig. 4.8(a). Fig. 4.8(c) explicitly shows the dependence of $L_D^{a-Si:H}$ on $N(E_F)$.

Fig. 4.8(b) shows that φ_{c-Si} increases with $N(E_F)$ for low values of ΔWF as already observed in Fig. 4.8(d); however for high ΔWF values, φ_{c-Si} decreases as $N(E_F)$ increases because the 'driving effect' of a favourable ΔWF is lost if $N(E_F)$ increases. Whatever $N(E_F)$, φ_{c-Si} increases with ΔWF, i.e. with increasing work function of the TCO.

Figs. 4.8(a), (b) and (c) illustrate in particular the influence of the TCO work function on φ_{c-Si}. Indeed, increasing WF_{TCO} (and thus increasing ΔWF, $WF_{a-Si:H}$ being constant) moves the valence band edge closer to the Fermi level. More defects are discharged which makes the total (negative) charge increase (in absolute value). In the case of a high DOS ($N(E_F) \geq 5 \times 10^{19}$ cm^{-3} eV^{-1}), WF_{TCO} has no influence on φ_{c-Si} anymore and even a small curvature of the bands creates a high charge. In other words, to reach a given charge value, the higher the defect density in (p)*a*-Si:H, the weaker is the band bending in (p)*a*-Si:H. For a fixed ΔWF, φ_{c-Si} increases with increasing $N(E_F)$ since the built-in voltage remains constant. This is true up to $\Delta WF = 0.1$ eV.

Consequently, (i) for a fixed value of $N(E_F)$, an increase of WF_{TCO} is associated with an increase of φ_{c-Si} except at very high defect density for which modifications in the charge with WF_{TCO} is not significant and φ_{c-Si} keeps the same whatever WF_{TCO}, (ii) for low values of WF_{TCO}, φ_{c-Si} increases with $N(E_F)$ because of a decrease of the band bending in *a*-Si:H. Thus, in almost all cases, higher values of φ_{c-Si} are calculated if highly defective (p)*a*-Si:H layers are used; increasing $N(E_F)$ is a way to reduce the influence of the TCO on the band diagram.
Only for high positive ΔWF (high TCO work function, which is not technologically relevant[7]) the curvature caused by the TCO/*a*-Si:H interface induces an increase of φ_{c-Si}. In this case, it is favourable to have a low $N(E_F)$ in order to couple both interfaces and benefit from the 'driving effect' of the TCO/*a*-Si:H interface.

[7] ΔWF=0.1 eV would mean that the TCO's work function is 5.27 eV; see below for experimental details.

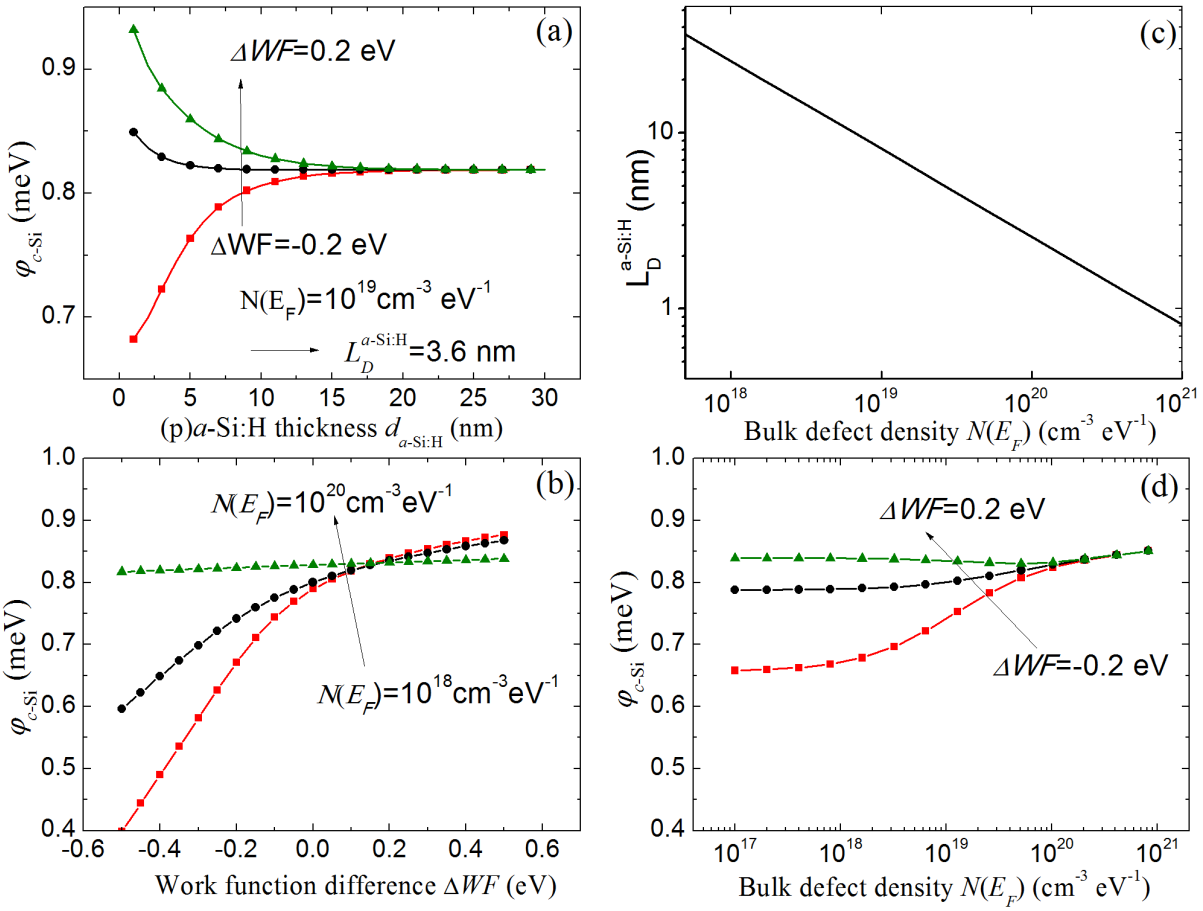

Figure 4.8: (a), (b) and (d): Analytical calculation of the equilibrium band bending in c-Si φ_{c-Si} as a function of the (p)a-Si:H layer thickness (a), the work function difference ΔWF (b) and the a-Si:H bulk defect density at the Fermi level (d). (c): Dependence of the a-Si:H Debye length on $N(E_F)$.

4.3.3 Beneficial high emitter density of states

For most ΔWF values and especially for technologically relevant values of the TCO work function, analytical calculation results show that it is necessary to separate the two interfaces formed by the *a*-Si:H emitter layer to maximize φ_{c-Si}. More precisely, the space charge regions (SCR) in the *a*-Si:H emitter should be separated, which means in other words to have a neutral region in *a*-Si:H (see Fig. 4.4). Zhao showed that the thickness of the emitter should be larger than the sum of the widths of both SCR [Zhao 08]. Here, a slightly different perspective is taken. The analysis presented so far suggests a surprising effect, at least at first glance: if the band bending in *c*-Si increases with the DOS, does that mean that better cell performance is achieved when the (p)*a*-Si:H DOS is increased? Full numerical simulations are needed to extract solar cell characteristics and to answer this question.

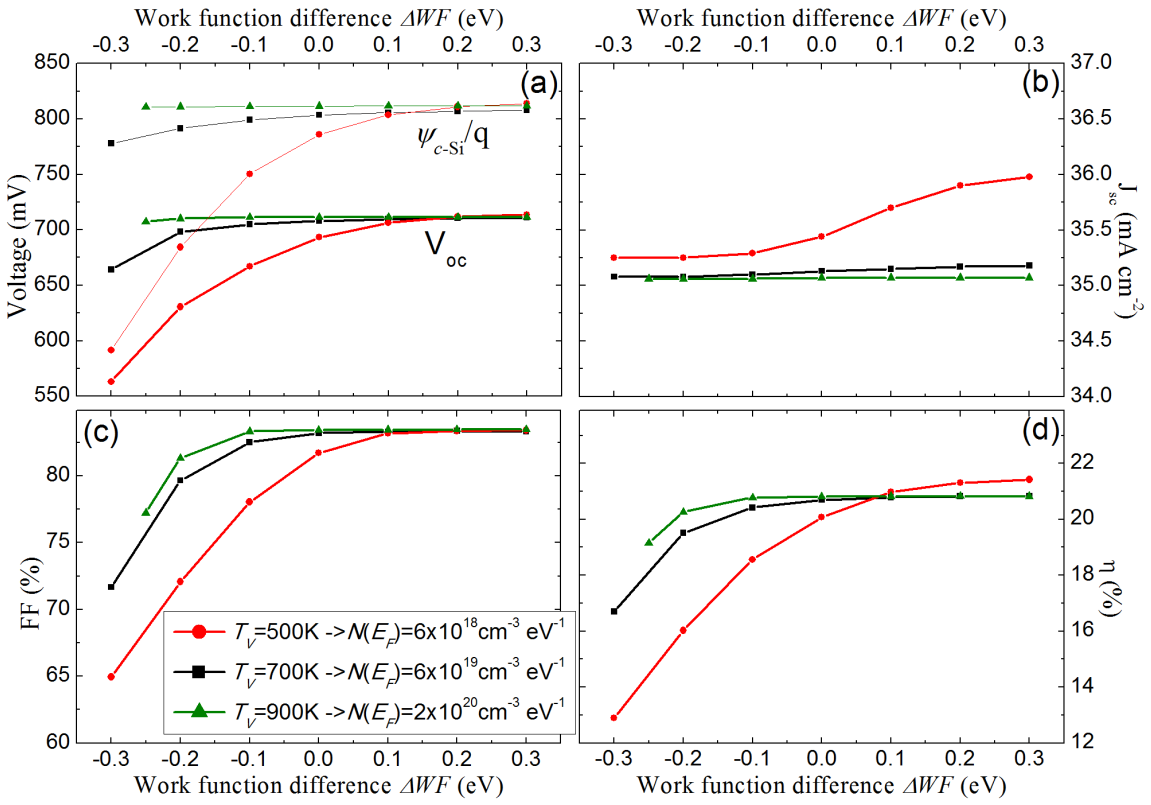

Figure 4.9: Solar cell parameters extracted from I-V simulations under AM1.5 illumination as a function of ΔWF for different values of the density of states at the Fermi level ($N(E_F)$) in the (p)a-Si:H layer.

The same solar cell structures[8] as in section 4.1 were simulated with AFORS-HET; cell parameters were extracted from the I-V curves and are presented in Fig. 4.9. The evolution of V_{oc} with ΔWF, which follows the evolution of φ_{c-Si}, has already been commented earlier. Here the increase of V_{oc} with $N(E_F)$ is emphasized. For the lowest DOS, J_{sc} increases with ΔWF. This is because a low DOS and a high contact work function lead to a strong increase of the electric field in *a*-Si:H such that electrons photo-generated in (p)*a*-Si:H can be extracted to *c*-Si and to the external circuit. FF increases with increasing ΔWF for the same reason and because holes can flow with a lower series resistance towards the contact. Yet it should be noticed that the drop in the FF with decreasing ΔWF is more pronounced for the lowest $N(E_F)$ values. This is related to a higher curvature of the bands in (p)*a*-Si:H forming a Schottky contact at the TCO/(p)*a*-Si:H interface.
In the end, the power conversion efficiency of the cell increases with (i) ΔWF and (ii) $N(E_F)$ except for high values of ΔWF.

One of the usual approaches in the fabrication of *a*-Si:H/*c*-Si heterojunction solar cells is to obtain *a*-Si:H layers with a very low defect density to reduce undesirable recombination. Thus,

[8]Because numerical simulations are performed again, a realistic DOS can be introduced in the *a*-Si:H layers present in the solar cells.

results which show that a possible optimization of the cell consists in having a high defect density in the amorphous emitter, are quite surprising. However, Holman and Jensen [Holman 12, Jensen 00] independently showed that the (p)*a*-Si:H emitter layer can be considered as a 'dead' layer (term used by Zhao [Zhao 08]), because the absorbed light in this layer is not converted into a photo-current; the electric field is too low to separate the photo-generated charges. This is confirmed by the simulations presented in Fig. 4.9 where J_{sc} is constant whatever the electric field in (p)*a*-Si:H (i.e. whatever ΔWF) if $N(E_F)$ is high. In most cases, electron-hole pairs recombine as soon as they have been generated because of the high defect density in *a*-Si:H. In view of this study, the *a*-Si:H emitter should not be necessarily a very low defective layer because a high defect density is necessary to separate the space charge regions in (p)*a*-Si:H. This depends on the property of the TCO/(p)*a*-Si:H contact; thus the optimization of the (p)*a*-Si:H emitter should be performed by considering the properties of the TCO. This process of global optimization of the structure was already suggested by Roedern [Roedern 94].

Nevertheless, it is important to point out the weaknesses of numerical simulations performed with AFORS-HET. First, the model introduced in the software do not take into account the doping efficiency in *a*-Si:H. It would be an illusion to think that the Fermi level can be adjusted in *a*-Si:H whatever the band tail parameter T_v. In particular, for high density of states (high value of T_v), doubts can be expressed regarding the possibility to move E_F towards the valence band edge. On the opposite, it is unrealistic to have a highly doped material with a low defect concentration because dopant atoms bring disorder in the structure and increase T_v [Korte 06a].
Concerning the software itself, it is not yet possible to relate bulk defects with interface recombination. However it is considered that the interfacial (i)*a*-Si:H layer isolates the (p)*a*-Si:H layer from the substrate [9]. In addition, neglecting hopping transport in *a*-Si:H is believed to decrease the hole conduction. The high DOS in *a*-Si:H and the possible formation of a Schottky contact at the TCO/*a*-Si:H interface suggest that hopping could lower the series resistance: the approach presented here certainly underestimates FF and J_{sc}, in particular for high defect densities.

As a conclusion, some hints on experimental features are given. As defined earlier from an experimentally relevant description of (p)*a*-Si:H, (p)*a*-Si:H has a work function of 5.17 eV, which is due to its high band gap and high p-type doping (close to the valence band).
First, for the (p)*a*-Si:H/(n)*c*-Si heterojunctions, a high TCO work function is beneficial. Indium Tin Oxide (ITO) and ZnO:Al are commonly used in this technology. The ITO's work function has been measured between 4.6 and 4.75 eV from electrical properties of ITO/*c*-Si junctions [Balasubramanian 91]; independently, slightly lower values between 4.4 and 4.5 eV were estimated from photo-electron spectroscopy [Park 96]. The work function of ZnO:Al was found between 4.25 and 4.95 eV by Gobeli [Gobeli 62], depending on the considered crystal

[9] The Fermi level position is kept at 0.35 eV from the valence band in bulk (p)*a*-Si:H, so no big change in (i)*a*-Si:H defects equilibration is expected as the band bending changes.

face. Values between 3.7 and 4 eV have been reported after photo-electron spectroscopy measurements [Jiang 03], and values reaching almost 5 eV were measured on oxygen-rich samples using the Kelvin force microscopy [Jaramillo 11]. For some measurement techniques, or in back contacted heterojunction solar cells where no TCO is needed, metal/*a*-Si:H contacts are formed; the same issues as for TCO/*a*-Si:H contacts appear. Thanailakis reported the work functions of metals likely to be used to form contacts with *c*-Si: he found 4.17 eV for aluminium, 4.41 eV for silver, 4.55 for copper, 5.1 eV for gold and 5.3 for platinum [Thanailakis 75, Thanailakis 76] [10]. It means that the best material, from the point of view of the contact, is platinum (this is unfortunately also the most expensive one). However, the calculation of band offsets and band bending at a Schottky junction in the frame of Anderson's model fails [Moench 01]. As a consequence, the work function in TCO may not be a relevant quantity to describe the TCO/*a*-Si:H contact; for example, dipole effects could modify the band offsets and give more favourable contacts than the one introduced in the simulations.
Regarding the advantage to increase the density of states in (p)*a*-Si:H to reduce the band bending in *a*-Si:H, doubts can be expressed on the possibility to dope efficiently the layer if a high concentration of defects counterbalance the charge brought by the dopants.
Last but not least, the thickness of the (p)*a*-Si:H emitter cannot be increased too much, otherwise parasitic absorption may reduce the external current.

4.4 Experiment: variation of the (i)*a*-Si:H thickness and doping in *a*-Si:H/*c*-Si solar cells

The HIT concept introduced by Sanyo has led to noticeable improvements of heterojunction solar cells performance because the (i)*a*-Si:H buffer layer reduces the recombination of charge carriers at the interfaces. However this is no magic bullet: a compromise has to be found concerning the (i)*a*-Si:H layer thickness to obtain a good passivation without increasing parasitic absorption of light and reducing the band bending in *c*-Si. In the following, two series of samples are investigated with the aim to understand the passivation mechanism in *a*-Si:H/*c*-Si solar cells and the role played by the buffer layer on V_{oc}.

First, the thickness of the (i)*a*-Si:H layer was changed. In the frame of a close collaboration between the LGEP and the University of Toronto, a series of symmetrical (p)*a*-Si:H/(i)*a*-Si:H/(n)*c*-Si samples were prepared using the saddle field PECVD technique [Bahardoust 10, Hallio 12]. The (p)*a*-Si:H emitter layer was 20 nm thick, with a constant doping. Values of the (i)*a*-Si:H layer thickness are 0, 4 and 10 nm. Directly after the preparation, PCD was measured in order to estimate the passivation quality of the interfaces. Then, contacts were deposited to perform planar conductance measurements.

In the second series, samples devoted to the study of the back surface field were prepared at

[10] The error on these values was around 0.05 eV

the CEA-INES [Martin De Nicolas 12] for which the buffer layer was slightly n-doped with a varying doping density. (n)*a*-Si:H/(n$^-$)*a*-Si:H stacks were deposited on (p)*c*-Si to study the field effect produced by the stacks. Indeed, the challenge lies in the ability to maintain a field effect while reducing the interface defects, or inversely to maintain a low interface defect density while increasing the field effect. Investigations were carried out on (n)*a*-Si:H/(n$^-$)*a*-Si:H/(p)*c*-Si/(p)*a*-Si:H samples. The (p)*a*-Si:H layer is the same for all samples and is supposed not to limit the effective lifetime. The (n)*a*-Si:H layer doped with 215 sccm PH_3 has also fixed properties, and a thickness of 32 nm. The 6 nm thick (n$^-$)*a*-Si:H layers were prepared with PH_3 flows of 5 and 20 sccm. In addition, a sample with no buffer layer was deposited. The effective lifetime was tracked by MPL (no PCD measurements were possible because of contacts on the device) and the planar conductance was measured between top contacts (on the (n)*a*-Si:H side).

4.4.1 (i)*a*-Si:H thickness variations

The series with different thicknesses of the (i)*a*-Si:H layer is first studied. Results of PCD and planar conductance measurements are presented in Fig. 4.10: Fig. 4.10(a) gives the Arrhenius plot of the normalized conductance *G* (Eq. 2.6) and Fig. 4.10(b) shows the effective carrier lifetime as a function of the excess carrier density.

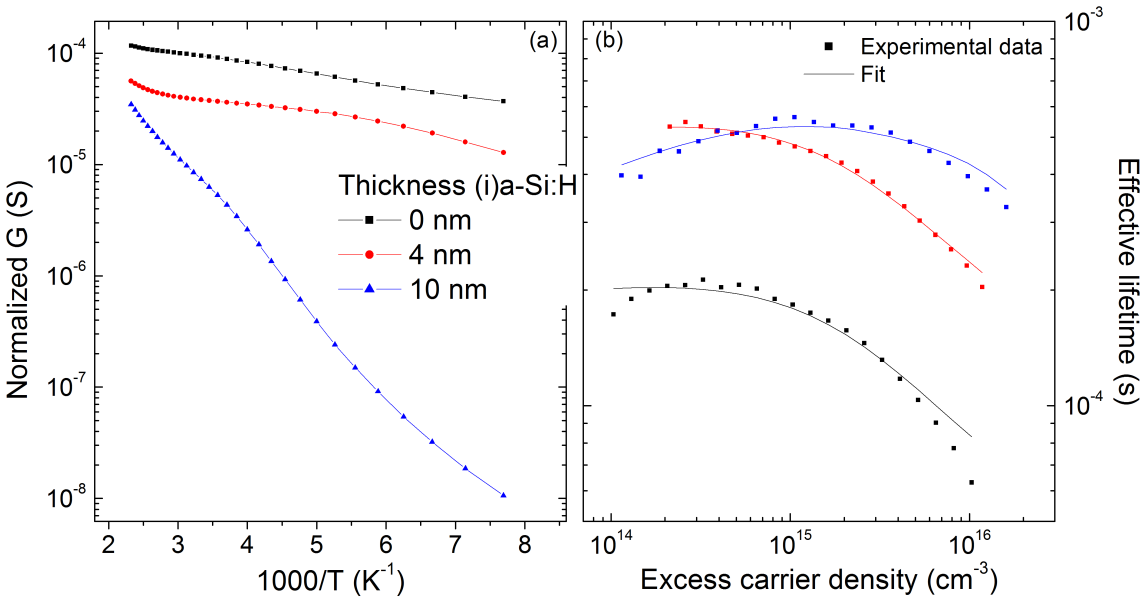

Figure 4.10: (a)Normalized conductance values G versus 1000/*T (Planar conductance) and (b) effective carrier lifetime versus the excess carrier density (PCD) measured on (p)a-Si:H/ (i)a-Si:H/ (n)c-Si structures, with varying thicknesses of the (i)a-Si:H layer.*

G decreases with increasing (i)*a*-Si:H thickness whereas the activation energy increases.

According to PCD measurements, the sample without buffer layer shows a much lower effective lifetime in the whole range of excess carrier densities. At low injection level, the carrier lifetime decreases in the sample with the 10 nm (i)*a*-Si:H layer, which suggests a weaker field effect passivation. This is at first sight consistent with planar conductance measurements.
In order to analyse further these results, the band bending in *c*-Si was extracted from the planar conductance G: from the value of G at 300 K in Fig. 4.10(a), two values of P_s are determined using equations given in section 3.2[11]. Then Fig. 3.6 is used to extract the band bending in *c*-Si from the value of P_s. The use of two extreme values for the mobility in the inversion region yields an uncertainty of about 50 meV on the band bending value. PCD data were fitted to obtain the interface defect density and fixed charge (see section 2.2.2.2).

Results are presented in Fig. 4.11: the band bending decreases from about 850 meV down to 750 meV when the (i)*a*-Si:H layer thickness increases from 0 to 10 nm. The fixed charge Q_{fix} [12] also drops (in absolute values), and the interface defect density D_{it} decreases by about one order of magnitude.

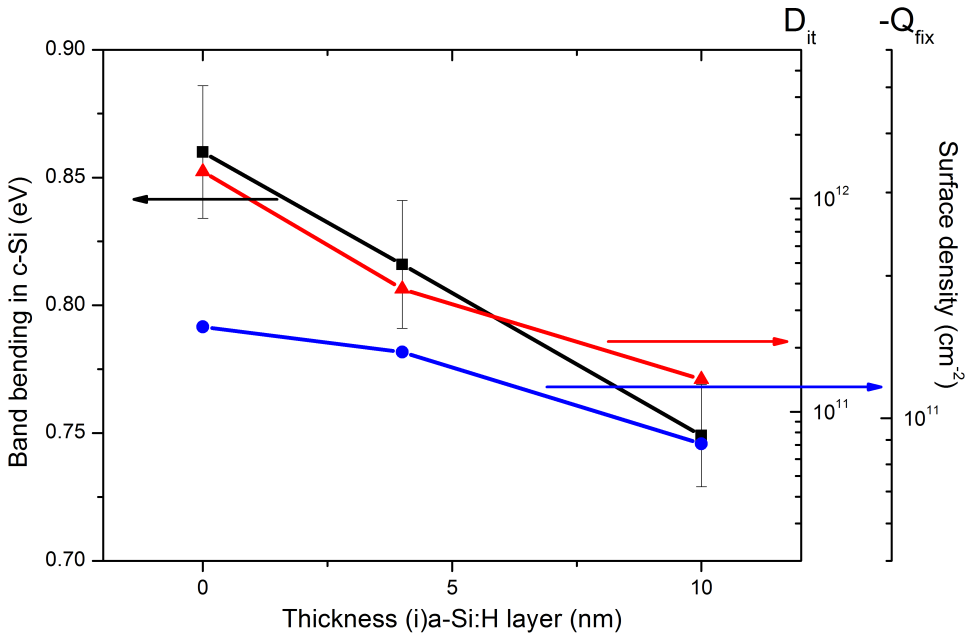

Figure 4.11: Measurement data analysis: measured band bending in c-Si (planar conductance) and fit parameters (interface defects D_{it} and fixed charge Q_{fix}) of PCD data.

These results confirm that a too thick buffer layer reduces drastically the band bending in *c*-Si. A detailed discussion of the results will be given in section 4.4.3.

[11] Two extreme mobility values in the inversion layer are considered.
[12] The fixed charge corresponds to a charge at about 10^{14} cm^{-3} excess carrier density, so that no direct comparison to the band bending at equilibrium is possible.

4.4.2 Buffer layer doping variations

Now, the series with variations of the buffer layer doping is studied. Arrhenius plots of the planar conductance are shown in Fig. 4.12. The effective carrier lifetime measured using the modulated photoluminescence technique is shown in the legend.

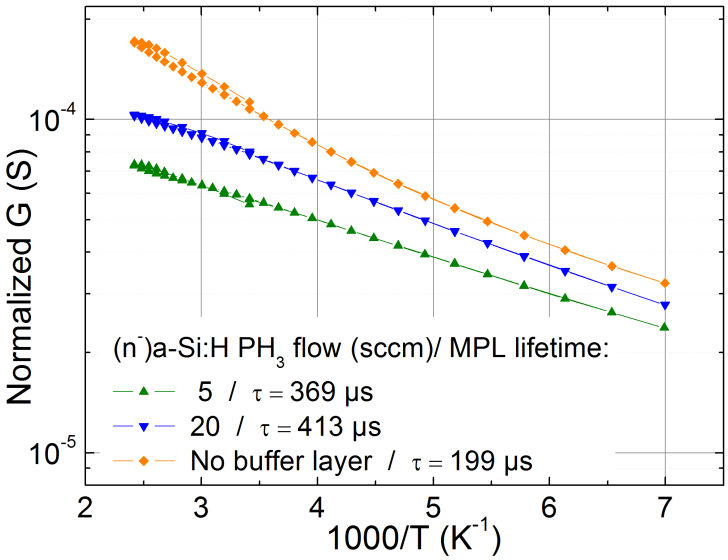

Figure 4.12: Arrhenius plots of the planar conductance measured on (n)a-Si:H/(n^-)a-Si:H/(p)c-Si/(p)a-Si:H samples structures, for three different doping of the buffer layer. The effective lifetime measured using the MPL technique is indicated in the legend for each sample.

The magnitude of the planar conductance increases when the doping of the buffer layer increases; the activation energy also increases as the doping increases. This is in contradiction with curves presented in Chapter 3 (see Fig. 3.7 for exemple) where the activation energy of $P_s(T)$ became usually lower when $P_s(300K)$ increased. A reason for this unexpected behaviour will be given in the discussion.
The effective lifetime deduced from the MPL technique (see the legend of Fig. 4.12) has no monotonic dependence with respect to the doping of the buffer layer. This can be due to the low injection level reached in the PL setup (around or below 10^{15} cm^{-3}) for which the measured lifetime is a combination of chemical passivation and field effects. It enlightens the complexity of the passivation mechanism.

4.4.3 Discussion

In the last sections, measurements of samples were presented where the buffer layer thickness and doping were varied. A discussion of these results follows.

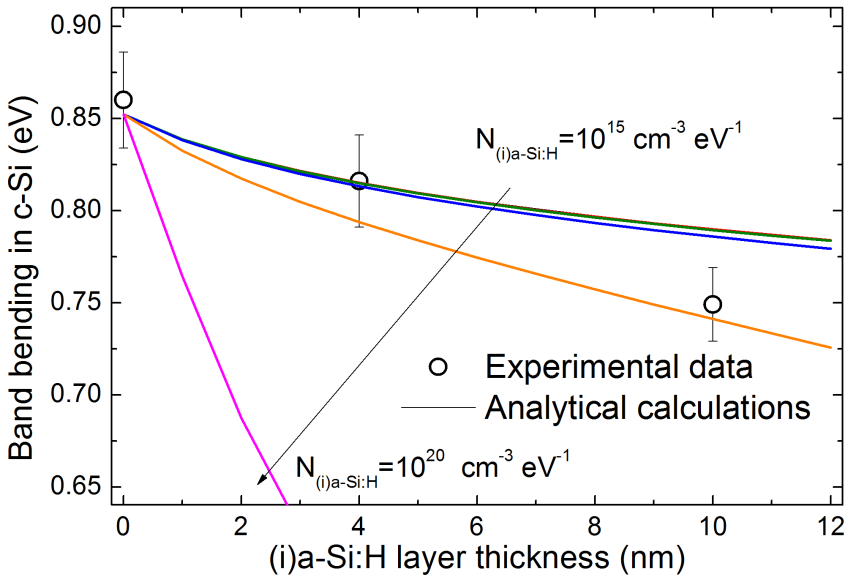

Figure 4.13: Band bending measured with the planar conductance technique for samples with three (i)a-Si:H layer thicknesses and band bending calculated with the analytical model developed previously, for different defect densities in (i)a-Si:H: $N_{(i)a-Si:H} = 10^{15}$, 10^{16}, 10^{17}, 10^{18}, 10^{19} and 10^{20} cm^{-3} eV^{-1}.

(i)*a*-Si:H thickness variations: The analytical model developed to calculate the band bending in *c*-Si as a function of the buffer layer thickness is now used to understand better those experimental results. In Fig. 4.13, band bending values extracted from planar conductance measurements are plotted versus the thickness of the (i)*a*-Si:H buffer layer. In addition, the calculated band bending in *c*-Si (see section 4.2.2) accounting for a thin (i)*a*-Si:H layer is shown in the figure. The sample with no buffer layer was first studied independently to get (p)*a*-Si:H properties: $N(E_F) = 3 \times 10^{20}$ cm^{-3} eV^{-1}, $\Delta E_v = 0.36$ eV, $(E_F - E_v)_{a-Si:H} = 0.34$ eV [13]. Then the thickness of the (i)*a*-Si:H was increased up to 12 nm, with a defect density in (i)*a*-Si:H varying from $N_{(i)a-Si:H} = 1 \times 10^{15}$ cm^{-3} eV^{-1} to $N_{(i)a-Si:H} = 1 \times 10^{20}$ cm^{-3} eV^{-1}.
Both experimental and calculated data coincide for a density of states in (i)*a*-Si:H around 1×10^{19} cm^{-3} eV^{-1}. Although (i)*a*-Si:H is expected to be less defective if one considers the defect pool model, such a high value for $N_{(i)a-Si:H}$ is not surprising because the analytical model makes the rough approximation that the DOS is constant in the whole (i)*a*-Si:H band gap. This approximation was reasonable for doped *a*-Si:H because the Fermi level probes only a small energy region in the band gap (the band bending in (p)*a*-Si:H is less than 100 meV); however, because the Fermi level in (i)*a*-Si:H incorporated in (p)*a*-Si:H/(i)*a*-Si:H/(n)*c*-Si structures can be very far from its equilibrium position[14], a wide range of the defect distribution is covered by E_F. Therefore, $N_{(i)a-Si:H}$ is not the defect density at E_F at equilibrium, but an effective density of states in the gap.

[13] No real fitting procedure – like minimization of the residual – was used; the parameters here may not be unique nor optimized, but it should not alter the qualitative discussion.

[14] E_F is about 1 eV above the valence band edge in the bulk, whereas it is about 0.4 eV above the valence band edge in (p)*a*-Si:H/(i)*a*-Si:H/(n)*c*-Si structures.

In view of this warning, several comments have to be done on effects that could appear when the (i)*a*-Si:H layer thickness increases.
First, it has been assumed that the valence band offset is the same whatever the thickness of the (i)*a*-Si:H; yet, variations of layer properties (doping, hydrogen content) may induce variation of the band gap and thus of the band offsets. Schulze reported variations of 0.2 eV [Schulze 11b] depending on the hydrogen content of the layer. Moreover, it is not obvious that the (p)*a*-Si:H deposited directly on *c*-Si is the same as (p)*a*-Si:H deposited on (i)*a*-Si:H: variations in doping and density of states could explain the observed deviation. No band offsets between (p)*a*-Si:H and (i)*a*-Si:H were introduced in the calculations whereas differences in the band gap can also exist between these two layers. Indeed, an additional valence band offset could have an influence on the band bending in *c*-Si. A negative (p)*a*-Si:H/(i)*a*-Si:H valence band offset – (p)*a*-Si:H valence band edge higher than (i)*a*-Si:H valence band edge at the (p)*a*-Si:H/(i)*a*-Si:H interface – would decrease the effective *a*-Si:H/*c*-Si band offset (and vice versa); a decrease of the effective valence band offset can be easily taken into account in the calculation by decreasing the valence band offset introduced at the (i)*a*-Si:H/(n)*c*-Si interface.

At this point, numerical simulations would be needed to fit the dependence of the band bending on the thickness of the (i)*a*-Si:H layer, as a realistic density of states could be incorporated. Such simulations, that are beyond the scope of this thesis, could help to correlate band bending values measured using the planar conductance technique, the interface defect density and the fixed charge extracted from the PCD measurements. In particular, the role played by the interface defects on the band bending could be precisely taken into account in the simulations, and a comparison with the experimental determination of the band bending could lead to an estimation of their density. Finally, by comparison with PCD data fitting which assumes values for the capture cross sections, these last parameters could be evaluated.

Buffer layer doping variations: The increase of the planar conductance with increasing doping of the buffer layer as shown in Fig. 4.12 (samples with 5 and 20 sccm PH_3 doped buffer layers and with no buffer layer) needs to be clarified. To shed light on this point, the band bending in (p)*c*-Si was calculated taking into account an (i)*a*-Si:H buffer layer in a similar way as in section 4.2.2 [15]. Both the bulk Fermi level position and the density of states in the *a*-Si:H buffer layer were varied; results are plotted in Fig. 4.14. For a fixed density of states, the band bending increases as the bulk Fermi level gets closer to the conduction band edge. Indeed, due to the high band bending in (p)*c*-Si, the Fermi level in the (n)*a*-Si:H/(p)*c*-Si heterojunction is close to the conduction band edge at the interface (on the *a*-Si:H side). Driving the bulk Fermi level [16] closer to the conduction band edge reduces the amount of extra charged states,

[15] The full structure is then (n)*a*-Si:H/ (i or n^-)*a*-Si:H/(p)*c*-Si.

[16] The bulk Fermi level realises the charge neutrality in the same thick layer through a balance between positively and negatively charged defects, and dopants (free carriers being negligible in *a*-Si:H).

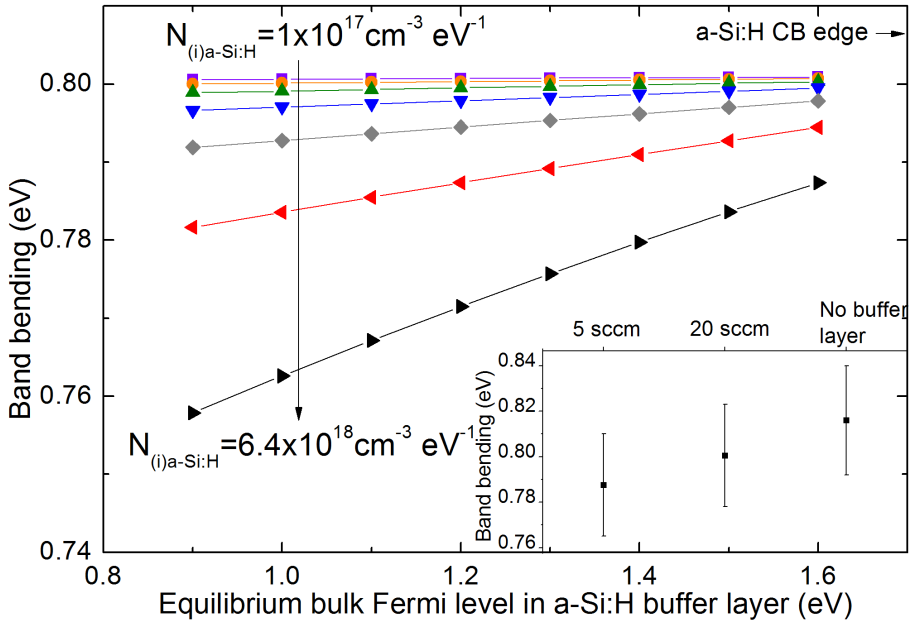

Figure 4.14: Band bending versus the bulk position of the Fermi level (referenced to the valence band edge) in the buffer layer, for several defect densities in the buffer layer $N_{(i)a-Si:H}$. In the inset: experimental values of the band bending extracted from planar conductance measurements presented in Fig. 4.12.

and diminishes (in absolute value) the – negative – charge in the buffer layer. From charge neutrality – on (n)*a*-Si:H/(p)*c*-Si structures, the inversion layer hosts a negative charge – the band bending increases. The same argument holds when the Fermi level position is fixed but the density of states increases: increasing the DOS makes the negative charge in the buffer layer greater, thus the band bending decreases.

Remarkably, the activation energy of G increases while $G(300K)$ increases in Fig. 4.12. In the light of the discussion in section 3.1.6, this can be explained by a change in both the defect density in the buffer layer and in the built-in voltage V_{bi} across the structure. The increase of the defect density can be explained by the addition of dopant atoms in the buffer layer; this is consistent with PCD measurements performed on similar series of sample which showed that the interface defect density increases when the doping of the buffer layer increases [Martin De Nicolas 12]. The change in V_{bi} can be due to a change of the band offset between *a*-Si:H and *c*-Si. A decrease of the conduction band offset would tend to reduce V_{bi} and increase the activation energy. A lowering of the band offset is consistent with the introduction of doping in the buffer layer: doping brings more disorder in the layer and tends to reduce the band gap, thus the band offsets [Chacorn 88].

The band bending values extracted from planar conductance measurements are also presented in the inset of Fig. 4.14. As the doping of the *a*-Si:H buffer layer increases (the Fermi level gets closer to the conduction band edge), the band bending increases from about 790 meV up to 810 meV. This is consistent with the analytical calculations and the above discussion, although no quantitative comparison can be made since the precise influence of doping on the position of the Fermi level has not been established in this study.

Fig. 4.2 indicated that the band bending in *c*-Si should be maximized to increase the V_{oc}; this has to be done without deteriorating the interface passivation. Investigations on two series of samples with different properties of the buffer layer were presented. They suggest that a trade-off has to be found in Fig. 4.2(b) because an increase of the band bending is realized with an increase of the interface defect density when the buffer layer gets thinner or more doped. Two new tools were presented here, namely the planar conductance technique for the extraction of the band bending and the analytical calculation of φ_{c-Si} as a function of structure properties. They can help to understand the dependence of the open-circuit voltage on the buffer layer properties and to optimize the structure.

4.5 Chapter conclusion

This chapter has been driven by the relationship between the open circuit voltage and the equilibrium band bending in *c*-Si; a possibility to increase the V_{oc} and power conversion efficiency of a solar cell is to maximize the band bending in *c*-Si. In order to understand finely how the band bending can be maximized, a comprehensive picture based on a complete analytical model, numerical simulations and experimental results has been built.
The main conclusions are: (i) a high density of states in the emitter layer can be beneficial for solar cell performance and (ii) a trade-off between passivation of interface defects and high band bending in *c*-Si has to be found through the optimization of the buffer layer.
Several heterojunction properties can be experimentally tuned: thickness and doping of the buffer layer, emitter thickness. Others give only a small leeway. First, the contact work function and the density of states in the bulk (p)*a*-Si:H should be optimized together because they play interconnected roles. Then, the degradation of the passivation quality of the (i)*a*-Si:H/(n)*c*-Si interface after the deposition of the (p)*a*-Si:H emitter seems unavoidable [de Wolf 09].
The use of complementary techniques to estimate both passivation quality *and* the band bending in the devices is a useful approach to understand the passivation mechanisms and to optimize silicon heterojunction solar cells.

5

Oxidized crystalline silicon surfaces for silicon heterojunction solar cells

So far, investigations have concerned the widely used *a*-Si:H/*c*-Si heterocontact. This last chapter is devoted to the development of a new type of interfaces. First, the concept of a heterojunction with a silicon oxide as passivation layer is tested theoretically. As a prerequisite to the study of the electrical behaviour of solar cells, a model accounting for a tunnel current is implemented in AFORS-HET. The influence of an oxide layer on the optical behaviour is briefly commented. In order to realize solar cells based on the concept of silicon heterojunctions with silicon oxide as buffer layer, *c*-Si surfaces are oxidized in pure deionized water before receiving *a*-Si:H layers. The passivation quality of the interfaces and the equilibrium band diagram are investigated experimentally. Solar cells with silicon oxide buffer layers are fabricated to evaluate the potential of the concept.

5.1 Motivation

Undoped amorphous silicon used as a passivation layer between the *a*-Si:H emitter and the *c*-Si absorber constitutes the basis of the HIT concept. It is partly responsible for the high power conversion efficiency reached recently on silicon heterojunction solar cells [Kinoshita 11]. However, as discussed previously in section 1.2.2, it has been found that after the deposition of a (p)*a*-Si:H emitter on top of an (i)*a*-Si:H/(n)*c*-Si structure, the effective minority carrier lifetime and thereby the (implied) V_{oc} decrease [de Wolf 09]. An explanation for this phenomenon relies on the creation of defects due to the equilibration of their distribution following a change of the Fermi level position in (i)*a*-Si:H. This is the result of an inefficient decoupling between bulk and interface/buffer layer properties. A better passivating material should be insensitive to the subsequent (p)*a*-Si:H deposition. This would extend the possibilities for the emitter properties; in particular, the advantage of having a highly doped material – increasing thus the built-in voltage – could be realised without generating a high defect concentration in the interfacial layer. Amorphous silicon also has the disadvantage of having a relatively low optical band gap energy: photons from the high energy part of the solar spectrum are absorbed by the emitter/buffer layer stack and do not contribute to the output power, because the photo-generated charge carriers recombine before being separated [Holman 12].
For those reasons, it is of great interest to develop new types of interfaces. Müller already introduced amorphous silicon suboxides deposited by PECVD to replace (i)*a*-Si:H [Mueller 08]. Silicon oxide appears to be a good candidate to replace (i)*a*-Si:H. While it absorbs no light, it offers a good passivation potential as demonstrated for thermally grown oxides [Kerr 02]. Moreover, ultra-thin silicon oxide layers attract more and more interest in the photovoltaic community, especially regarding third generation cell concepts where quantum effects like tunneling or confinement play a major role [Roelver 08]. Thus it is important to incorporate such layers in systems that have already been intensively studied before applying them directly to new concepts.
Silicon oxides are wide band gap materials, which gives rise to the formation of energy barriers hindering charge carrier transport. A detailed study of the current transport in a heterojunction with an insulator as a buffer layer is required to evaluate the potential of the concept.

In the following sections, the concept of an *a*-Si:H/*c*-Si heterojunction with a silicon oxide passivation layer between the emitter and the absorber is studied from both the theoretical and the experimental point of view. A new model accounting for tunneling transport through an insulator barrier at the interface is developed, implemented in AFORS-HET and used to study the transport properties of the heterojunction. Then, experimental investigations on silicon oxide layers grown in pure deionized water lead to the realization of solar cells with new interfaces.

5.2 Theoretical evaluation of the concept

To begin with, two aspects of the *a*-Si:H/*c*-Si solar cell are addressed using numerical simulations, namely current transport at the interface and optical behaviour. A simulation tool is developed to take into account tunneling through an interfacial insulator layer. Optical simulations are performed to look at the impact of the oxide layer on light absorption in *c*-Si.

5.2.1 Electrical behaviour: tunneling through a thin insulator layer

The first concern in the application of a silicon oxide interlayer to silicon heterojunction solar cells deals with electrical conduction. Indeed, as oxide layers have a wide band gap, electrical transport through energy barriers in the conduction and valence bands could be seriously hindered. A possible solution to this problem is to make the layers ultra-thin ($\leq$ 2 nm); charge carriers may then cross the barrier by tunneling, like in the case of metal-insulator-semiconductor devices. A detailed investigation is required to specify the range of parameters (thickness, barrier height, etc.) one can afford for the insulator layer without deteriorating the device performances. The effect of a thin insulator layer on the electrical conduction is investigated after developing a tunnel current model in the software AFORS-HET described in section 2.3.

5.2.1.1 Introduction to tunneling

When a particle (an electron or a hole in the present case) faces a potential barrier, the only classical way it can cross the barrier is to have enough energy to get over the barrier. In contrast to this classical picture, the quantum theory states that, because of the wave-like behaviour of any particle, the probability of the particle to cross the barrier is finite, even if its energy is lower than the barrier height. The tunneling probability depends on many factors such as the mass of the particles, the width and height of the barrier, etc. Considerable work has been done to study tunneling of electrons and holes through a thin silicon oxide layer separating a metal and crystalline silicon: this is the typical MIS structure (Metal-Insulator-Semiconductor). References [Green 74, Shewchun 77, Hezel 97] give an overview of what has been done, especially for the use of MIS structures for photovoltaic conversion. However, to the best knowledge of the author, tunneling through a thin insulator layer sandwiched between two semiconductors has not been much studied [1] although Shewchun treated the topic from a theoretical point of view in [Shewchun 72].

[1] The particular case of a degenerate semiconductor, such as highly doped poly-silicon or Transparent Conductive Oxide, on one side of the oxide is closer to the MIS structure.

5.2.1.2 Tunneling model for the current

The equations which govern the electron current through an energy barrier in the conduction band are now developed. The considered situation is depicted in Fig. 5.1. The current equations are derived from a model first introduced by Yang [Yang 93] to simulate a tunneling current across an abrupt heterojunction. The following approximations are made:

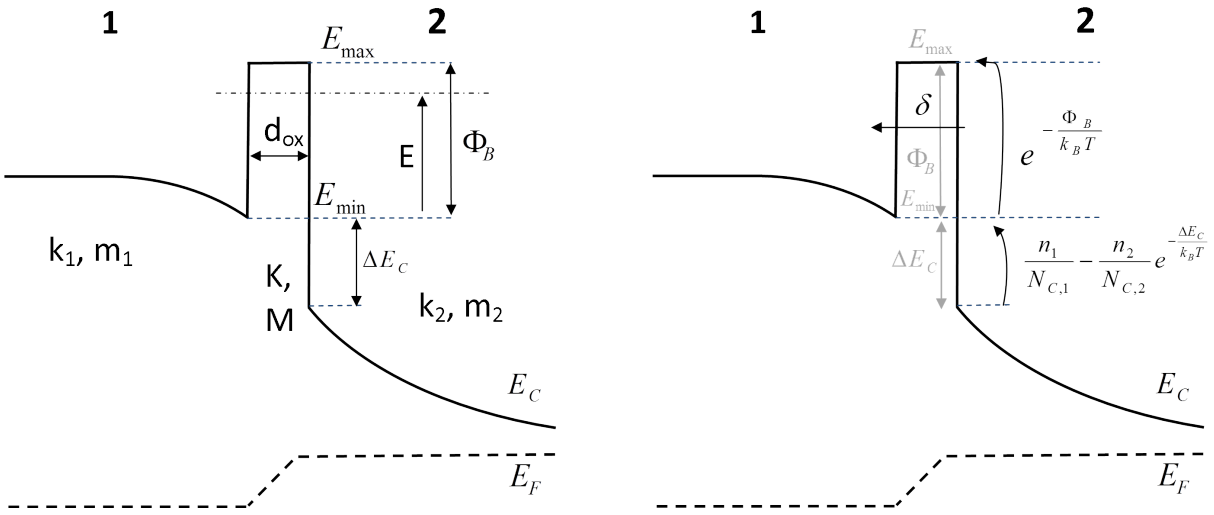

Figure 5.1: Schematic conduction band diagram of a heterojunction including a thin insulator layer. E_F is the electron quasi Fermi level. ΔE_c is the conduction band offset of the heterojunction without any insulator layer. On the right, the terms ruling the current transport through the interface are sketched.

- Effective-mass approximation: the semiconductor band edges are assumed parabolic and can thus be described by a density of state effective mass m^*. m^* is assumed to be the same on both sides of the insulator layer.

- Conservation of parallel momentum: the parallel (to the interface) wavevector is not changed by the tunneling process.

- Square shape: the barrier is assumed to be thin enough to neglect the potential drop across it, such that the barrier has an asymmetrical [2] rectangular shape.

- Maxwell-Boltzmann statistics: the semiconductors are assumed to be non-degenerate, so that the Fermi-Dirac distribution of the charge carrier energies can be approximated by a single exponential term.

[2] Asymmetrical because of band offsets between *a*-Si:H and *c*-Si.

The starting point is the expression for the electron current density known as Tsu-Esaki formula [Tsu 73]:

$$J_{e,\text{tun}} = \frac{4\pi q m^*}{h^3} \int_{E_{\min}}^{+\infty} \mathscr{T}(E) N(E) dE, \tag{5.1}$$

where $E_{\min}$ is the minimum conduction band edge energy allowing for tunneling. The transparency $\mathscr{T}$ of the barrier gives the probability for an electron with an energy E to tunnel through the barrier. Its determination is not straightforward, as it is a purely quantum mechanical quantity that requires the exact knowledge of the barrier profile and particle wavefunctions in the entire structure. A full quantum calculation is possible in the simple case of an asymmetrical rectangular potential barrier. The calculation, based on the plane wave approximation, is detailed in the Appendix B and leads to $\mathscr{T}$ in the case of Fig. 5.1:

$$\mathscr{T} = \mathscr{T}_{\text{tun}} = \frac{4K^2 k_1 k_2}{K^2(k_1+k_2)^2 + (K^2+k_1^2)(K^2+k_2^2)\sinh^2(K d_{\text{ox}})} \text{ for } E \le E_{\max}, \tag{5.2}$$

$$\text{and } \mathscr{T} = \mathscr{T}_{\text{res}} = \frac{4K^2 k_1 k_2}{K^2(k_1+k_2)^2 + (K^2-k_1^2)(K^2-k_2^2)\sin^2(K d_{\text{ox}})} \text{ for } E \ge E_{\max}, \tag{5.3}$$

where the wavevectors in each region read: $k_1 = \sqrt{\frac{2m^*}{\hbar^2}(E - E_{\min})}$, $k_2 = \sqrt{\frac{2m^*}{\hbar^2}(E - E_{\min} + \Delta E_c)}$ and $K = \sqrt{\frac{2M}{\hbar^2}(E_{\max} - E)}$ for $E \le E_{\max}$ and $K = \sqrt{\frac{2M}{\hbar^2}(E - E_{\max})}$ for $E \ge E_{\max}$. M is the electron effective mass in the insulator layer; although such a concept to describe the electronic property of an amorphous insulator or seminconductor is criticized [Franz 56], previous works have shown a good correlation between the experiment and theoretical models relying on this approximation [L.F. Register 99, B. Brar 96]. $E_{\max}$ is the conduction band energy in the barrier, such that $E_{\max} - E_{\min}$ gives the barrier height. ΔE_c is the conduction band offset between the two semiconductors [3] and d_{ox} is the barrier thickness. $\mathscr{T}_{\text{tun}}$ and $\mathscr{T}_{\text{res}}$ refer to the tunneling and resonant regime respectively.

N_S is called the 'supply function': it represents the number of particles likely to tunnel. Using Maxwell-Boltzmann statistics it reads [Gehring 03] (see Appendix B for the derivation):

$$N_S(E) = k_B T \left(e^{-\frac{E - E_{F1}}{k_B T}} - e^{-\frac{E - E_{F2}}{k_B T}} \right), \tag{5.4}$$

where $E_{F,i}$ is the position of the electron quasi Fermi level in material i ($i = 1$ or 2). If both quasi-levels are equal, the structure is in equilibrium, $N_S(E) = 0$ and no current flows. Using

[3] ΔE_c is taken positive here.

the relation between the electron density n_i [4] and the position of the Fermi level with respect to the conduction band edge $E_{c,i}$, $n_i = N_{c,i}\exp\left(\frac{E_{F,i}-E_{c,i}}{k_BT}\right)$, N_S can be rewritten as a function of the electron densities on both sides of the barrier:

$$N_S(E) = k_BT\left(\frac{n_1}{N_{c,1}}e^{-\frac{E-E_{c,1}}{k_BT}} - \frac{n_2}{N_{c,2}}e^{-\frac{E-E_{c,2}}{k_BT}}\right), \tag{5.5}$$

which leads to the new expression for the current:

$$J_{e,\mathrm{tun}} = \frac{4\pi qm^*}{h^3}k_BT\int_{E_{\min}}^{+\infty}\left[\frac{n_1}{N_{c,1}}e^{-\frac{E-E_{c,1}}{k_BT}}\mathscr{T}(E) - \frac{n_2}{N_{c,2}}e^{-\frac{E-E_{c,2}}{k_BT}}\mathscr{T}(E)\right]dE. \tag{5.6}$$

The integral in Eq. 5.6 is calculated as follows:

$$\begin{aligned}\int_{E_{\min}}^{+\infty} e^{-\frac{E-E_{c,i}}{k_BT}}\mathscr{T}(E)dE &= \int_{E_{\min}}^{E_{\max}} e^{-\frac{E-E_{c,i}}{k_BT}}\mathscr{T}_{\mathrm{tun}}(E)dE + \int_{E_{\max}}^{+\infty} e^{-\frac{E-E_{c,i}}{k_BT}}\mathscr{T}_{\mathrm{res}}(E)dE \\ &= k_BT\left\{\int_0^{\frac{\Phi_B}{k_BT}} e^{-u}\mathscr{T}_{\mathrm{tun}}(k_BTu+E_{\min})du\right. \\ &\quad \left. + \int_{\frac{\Phi_B}{k_BT}}^{+\infty} e^{-u}\mathscr{T}_{\mathrm{res}}(k_BTu+E_{\min})du\right\}e^{\frac{E_{c,i}-E_{\min}}{k_BT}} \\ &\text{with } u = \frac{E-E_{\min}}{k_BT}.\end{aligned} \tag{5.7}$$

In the particular case sketched in Fig. 5.1, $E_{\min} = E_{c,1}$. Then, Eqs. 5.6 and 5.7 lead to the final expression for the tunneling current:

$$J_{e,\mathrm{tun}} = \frac{4\pi qm^*}{h^3}(k_BT)^2\delta\left[\frac{n_1}{N_{c,1}} - \frac{n_2}{N_{c,2}}e^{-\frac{\Delta_{Ec}}{k_BT}}\right], \tag{5.8}$$

where

[4] Here n_i is the electron concentration in material i (= 1 or 2) at the interface with the barrier and should not be confused with the intrinsic carrier concentration.

$$\delta = \delta_{\text{tun}} + \delta_{\text{res}} \tag{5.9}$$

$$= \int_0^{\frac{\Phi_B}{k_B T}} e^{-u} \mathscr{T}_{\text{tun}}(k_B T u + E_{\min})\, du + \int_{\frac{\Phi_B}{k_B T}}^{+\infty} e^{-u} \mathscr{T}_{\text{res}}(k_B T u + E_{\min})\, du, \tag{5.10}$$

with $\delta_{\text{tun}} = \int_0^{\frac{\Phi_B}{k_B T}} e^{-u} \mathscr{T}_{\text{tun}}(k_B T u + E_{\min})\, du$ and $\delta_{\text{res}} = \int_{\frac{\Phi_B}{k_B T}}^{+\infty} e^{-u} \mathscr{T}_{\text{res}}(k_B T u + E_{\min})\, du$.

The final equation Eq. 5.8 allows one to easily interpret the considered model (see Fig. 5.1 right). $\frac{n_1}{N_{c,1}} - \frac{n_2}{N_{c,2}} e^{-\frac{\Delta_{E_c}}{k_B T}}$ is exactly the thermionic emission current term across the junction when there is no tunnel barrier: the band offset is the only obstacle for charge carriers. The thermionic emission current is composed of electrons coming from material 1 to material 2 that 'fall down' the energy difference, plus electrons in material 2 having to be excited to the energy corresponding to the band offset to reach material 1. Now the barrier is considered in addition to the band offset: the thermionic emission current is multiplied ('×' and 'and' are equivalent in terms of probability) by a sum ('+' is equivalent to 'or') giving the two possible ways to cross the barrier: δ_{res} represents the path over the barrier whereas δ_{tun} gives the probability to tunnel through the barrier. In δ_{res}, the probability $\mathscr{T}_{\text{res}}$ oscillates between its minimum value $4k_1k_2/(k_1+k_2)^2$ and its maximum 1; no phase shift accompanies the reflection on potential discontinuities for thicknesses such that $Kd = n\pi$ (resonance condition) for n integer and stationary waves are solutions of Schrödinger's equation above the barrier. On the contrary, far from resonances, interferences attenuate the wavefunction. The transmission probability $\mathscr{T}$ is plotted in Fig. 5.2(a) for a barrier height of 3 eV and several thicknesses: for energies below the barrier height, $\mathscr{T}$ grows almost exponentially, whereas for higher energies, oscillations appear. The value of the integral in Eq. 5.10 up to an intermediate energy (abscissa energy), $\delta(E) = \int_0^{\frac{E}{k_B T}} e^{-u} \mathscr{T}_{\text{tun}}(k_B T u + E_{\min})\, du$ for $E \leq \Phi_B$ and $\delta(E) = \delta_{\text{tun}} + \int_{\frac{\Phi_B}{k_B T}}^{E} e^{-u} \mathscr{T}_{\text{res}}(k_B T u + E_{\min})\, du$ for $E \geq \Phi_B$, is shown for increasing energies in Fig. 5.2(b): because of the exponential term e^{-u} in δ_{tun} and δ_{res}, δ saturates after a few tenths of an eV above the minimum energy (= 0 in the figure).

The derivation presented above concerns electrons tunneling through a barrier in the conduction band. A similar expression for the hole tunneling current through a barrier in the valence band can be derived.

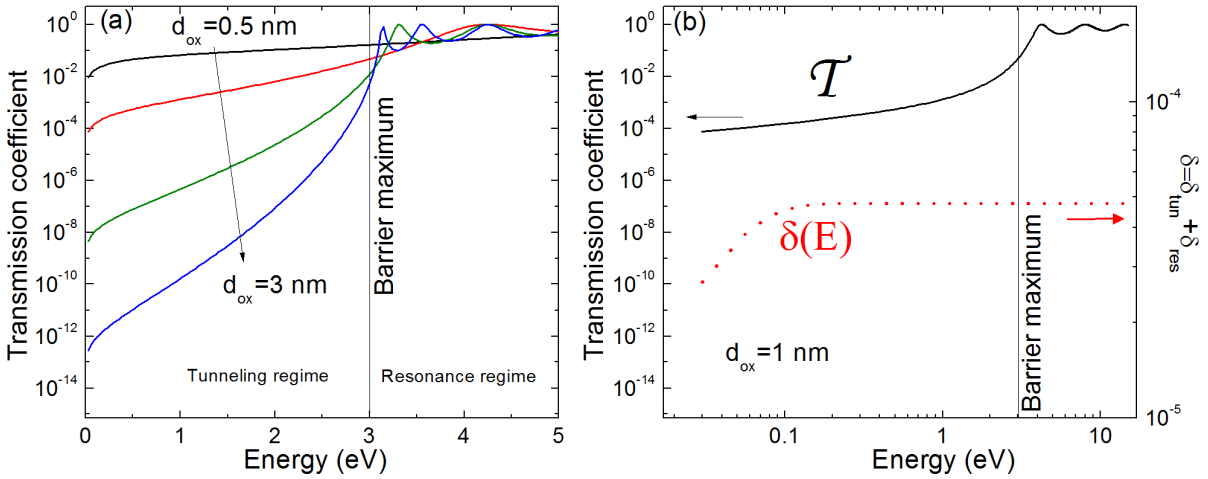

Figure 5.2: (a) Transmission coefficient $\mathcal{T}$ versus the energy for a 3 *eV high barrier; thicknesses are* 0.5, 1, 2 *and* 3 *nm. (b)Transmission (black solid line) and* δ *(integration up to the abscissa energy - red dotted line) versus the energy for a* 1 *nm thick barrier.*

5.2.1.3 Implementation in AFORS-HET: the tunnel membrane

Tunneling is a non-local quantum process: the tunnel current at a given position in the structure depends on properties of the structure far from the point considered, namely on the other side of the barrier. An electron facing a barrier has a finite probability to reappear on the other side without participating to the classical current equations in between. Moreover, far from being a simple perturbation to the system, tunneling through an energy barrier in the structure is expected to drive the behaviour of the whole device if no other conduction path is significant. Those considerations make the implementation of a tunneling current through an insulator layer in a quasi-classical simulation software resource-demanding and unstable. Authors treated the tunnel current as a local generation rate [Gehring 03]. Shen developed a new algorithm to simulate band to band tunneling [Shen 11].

For the 1-D simulation software AFORS-HET, another perspective is taken. The problem caused by the insertion of a real tunneling layer was circumvented by treating a thin insulator layer as a new interface type. No real tunneling layer is inserted. Instead, the interface between the two semiconductors is treated as a *membrane* that alters the carrier transport in the same way as if there were actually a tunneling layer. As outlined in section 2.3, AFORS-HET allows to choose between different interface types: drift-diffusion and thermionic emission (optionally also including tunneling through a spike [Yang 93]). Considering Eq. 5.8, the equations describing the "thermionic emission" current in AFORS-HET were modified to take into account tunneling through a 'virtual' insulator layer. In the Appendix B Fig. B.1 is a screen-shot of the AFORS-HET configuration window showing the options to activate tunneling through a barrier.

5.2.1.4 Influence of barrier parameters on transport properties

The developed and implemented model is now used to check the influence of a thin tunnel layer between *a*-Si:H and *c*-Si on current transport properties and, ultimately, on solar cell performance. Instead of a simple thermionic emission interface, the new interface type 'tunneling through an insulator' is switched on. Many parameters appear in the calculation. First, it will be assumed that the tunnel layer is pure SiO_2 with a band gap energy lying around 9 eV [DiStefano 71]. The precise knowledge of the effective masses is still a challenge: for the electron tunneling effective mass the value of $M_e = 0.3$ reported by König *et al.* [König 07] was used, even if an enhancement of the mass due to the very low thickness is possible [Staedele 03]. Concerning holes, the value of $M_h = 0.33$ has been measured by Vexler on very thin (2 to 3 nm) SiO_2 films [Vexler 05]. The electron affinity is taken equal to 1.0 eV according to Goodman and O'Neill [Goodman 66]. If the band gap in *a*-Si:H is assumed to be 1.7 eV and the electronic affinity 3.9 eV, the resulting barrier heights are 2.9 eV and 4.4 eV for electrons and holes respectively.
To begin with, the dependence of the factor δ on barrier parameters will be studied. Then, simulated dark I-V curves will be discussed. Finally, simulations of illuminated solar cells shall give insight into the relevance of the new solar cell concept presented in this chapter.

Tunneling factor δ: The factor δ as given by Eq.5.10 is the key quantity accounting for tunneling in the structure. It depends on several parameters which are usually not precisely known because they spread over a wide range in the literature or because the studied material differs from what has already been reported (composition, thickness, etc.). Therefore, as future results will depend strongly on δ, the dependence of δ on structure parameters is studied.
In Fig. 5.3, the factor δ is plotted versus (a) the barrier thickness for several barrier heights, (b) the barrier height for several thicknesses, (c) the relative effective mass in the insulator and (d) the relative effective mass in the semiconductors (here Si) for several heights. An increase of the thickness by a few nanometres (Fig. 5.3(a)) or of the barrier height by a few electron-volts (Fig. 5.3(b)) dramatically affects δ which decreases almost exponentially. However for thin and low barriers, δ remains in the range of 0.1.
The effective mass in the insulator plays also a significant role (Fig. 5.3(c)), which is unfortunate if one aims at accurate (predictive) simulations because it has not been precisely determined.
On the contrary, the effective mass in the semiconductors plays only a negligible role (Fig. 5.3(d)): different effective masses in *a*-Si:H and *c*-Si can be well approximated by a unique effective mass.

In the light of those first calculations, a dramatic effect of a pure SiO_2 interlayer of a few nanometres on the heterojunction solar cells performance is expected. However, thin layers

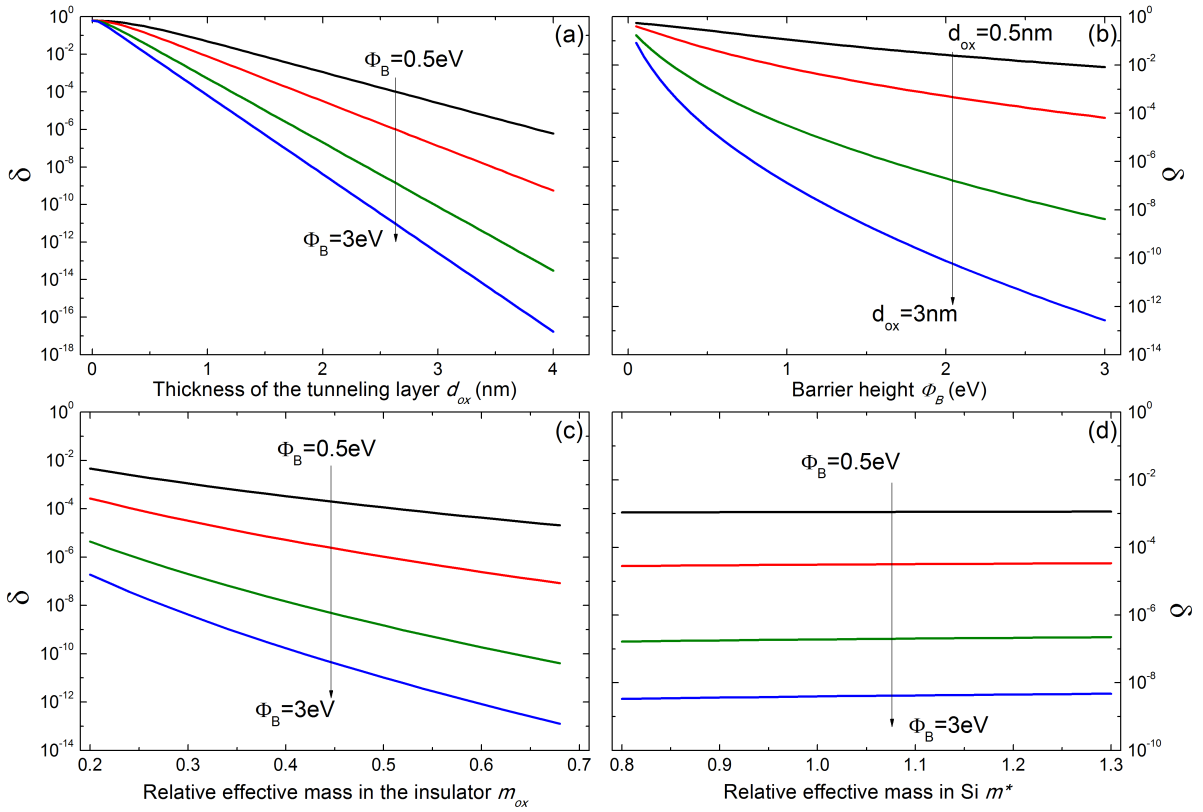

Figure 5.3: Variations of the factor δ accounting for tunneling through a thin insulator layer. The standard parameters are: $d_{ox} = 1\,nm$, $\Phi_B = 3$ eV, $m_{ox} = 0.3$, $m^* = 1$ and $T = 300\,K$. In (a), (c) and (d), Φ_B amounts 0.5, 1, 2 *and* 3 *eV; in (c), d_{ox} is* 0.5, 1, 2 *and* 3 *nm.*

with smaller band gaps (compared to the 9 eV SiO_2 band gap) may maintain a significant current across the interface.

Dark current: The next step consists in simulating dark I-V curves with AFORS-HET for several barrier configurations. The same structure as introduced in section 2.3.5 is considered, except that the (i)*a*-Si:H and (n)*a*-Si:H layers are removed such that the structure metal/(p)*a*-Si:H/barrier/(n)*c*-Si/metal is considered. The barriers in the conduction and valence bands have the same height. The I-V characteristics in the forward regime for several sets of barrier parameters are shown in Fig. 5.4: the thickness is varied from 0 to 1.5 nm (Fig. 5.4(a)), and the tunnel barrier height ranges from 0 to 2 eV (Fig. 5.4(b)).
Three different regions are delimited by the markers A, B and C: in the present case, A is about 0-0.5 V, B is 0.5-1.7 V and C is for voltages greater than 1.7 V. For region A, the current is limited by the space charge in *c*-Si: because the *c*-Si base is strongly inverted at the interface, almost no electrons are present at the interface and the band bending constitutes a high barrier that cannot be crossed by the charge carriers. Therefore there is no difference between the calculated currents. In region B, the bands on both sides of the interface flatten; the current is

now limited by the interface properties, namely the tunnel barrier. In this region, the barrier has a huge impact on the current: between no barrier and a 1.5 nm thick barrier, the current is reduced by 4 orders of magnitude. For thinner barriers, the impact is less important. The same comments hold for variations of the barrier height. In region C, most of the potential drops in the (p)*a*-Si:H layer such that the resistivity of the emitter limits the output current.

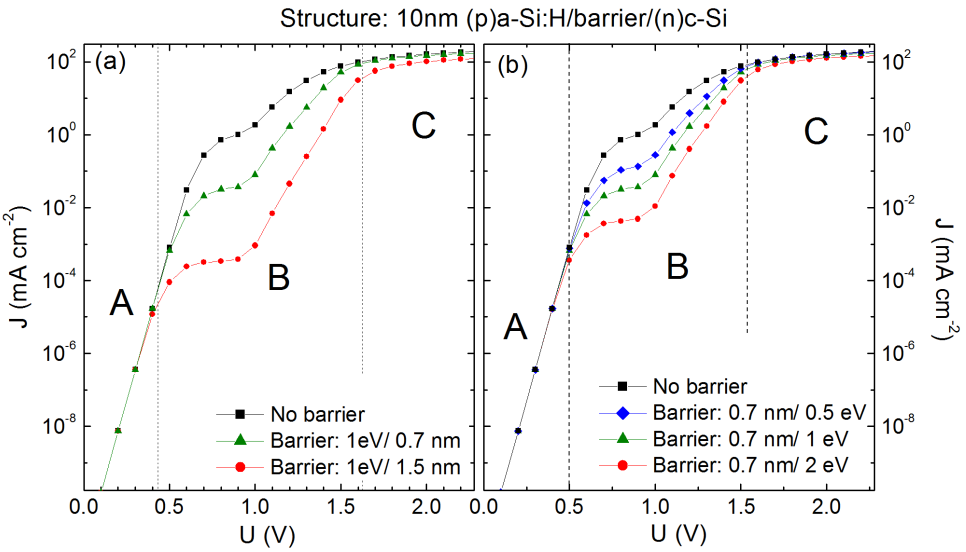

Figure 5.4: Forward I-V curves from simulations of a p-n heterojunction in the dark for different tunnel barriers (the barrier height is the same in the conduction and valence bands): (a) variation of the barrier thickness; (b) variation of the barrier height.

As a V_{oc} value of the order of 700 mV is expected, and because the working point of solar cells lies around 500-600 mV, it is expected that the barrier does have an impact on device performance. In particular, too thick and/or high barriers are expected to strongly limit the extraction of photo-generated charge carriers.

Solar cell simulation: To explore the behaviour of solar cells with an insulator layer between the (p)*a*-Si:H emitter and the (n)*c*-Si absorber, I-V curves of solar cells under AM1.5 illumination were simulated with AFORS-HET. As a basis, the same cell structure as introduced in section 2.3.5 is considered, except that the (i)*a*-Si:H layer is removed. The interface type 'tunneling through a barrier' is used.

In Fig. 5.5 the impact of the barrier height and thickness of the tunnel layer on solar cell performance is shown: for a barrier height of 1 eV, thicknesses up to 0.7 nm have a limited impact on the solar cells, though the fill factor monotonically decreases. Above 1 nm the power conversion efficiency drops dramatically. For a thickness of 0.7 nm, barriers up to 1

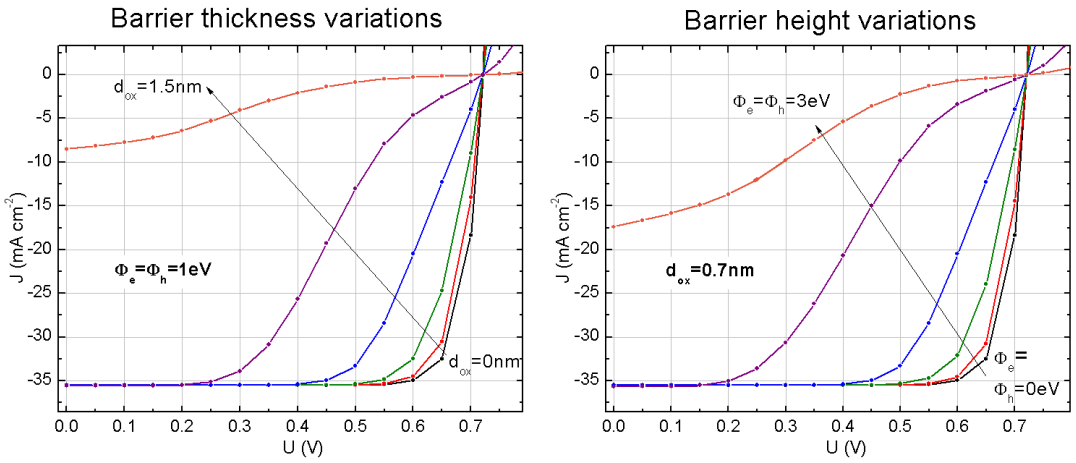

Thickness (nm)	Jsc (mA/cm²)	Voc (mV)	FF (%)	n (%)
0	35.53	720.7	83.6	21.4
0.3	35.51	720.7	80.69	20.65
0.5	35.5	720.7	76.6	19.6
0.7	35.5	720.7	65.04	16.64
1	35.57	720.7	42.08	10.79
1.5	8.503	720.7	21.72	1.331

Barrier (eV)	Jsc (mA/cm²)	Voc (mV)	FF (%)	n (%)
0	35.53	720.7	83.6	21.4
0.2	35.51	720.8	80.83	20.68
0.6	35.5	720.7	76.09	19.47
1	35.5	720.7	65.04	16.64
2	35.68	720.7	35.66	9.171
3	17.41	720.7	23.83	2.99

Figure 5.5: I-V curves from simulations of solar cells under AM1.5 illumination with AFORS-HET. Left: variations of the barrier thickness from 0 *to* 1.5 *nm (the barrier height is* 1 *eV). Right: variations of the barrier height from* 0 *to* 3 *eV (the barrier thickness is* 0.7 *nm).*

eV have a limited impact on the solar cells; above 2 eV, the performance deteriorates much quicker.

The insertion of a tunnel barrier has mostly an impact on the fill factor FF: the barrier increases the series resistance and the recombination of charge carriers. In open-circuit conditions, as no current flows, the voltage V_{oc} remains unchanged. For high or thick barriers, the short-circuit current J_{sc} also drops; this can be understood by looking at the main quantities involved in the charge carrier dynamics extracted from the simulation of solar cells under AM1.5 illumination and short circuit conditions. For both structures with no barrier and with a 0.7 nm thick and 3 eV high barrier, the band diagrams (a), the current densities (b), the carrier concentrations (c) and the recombination and generation rates (d) are shown in Fig. 5.6. The generation of electron-hole pairs is not modified whether there is a tunnel barrier or not. The electron current is also only weakly changed because electrons generated in *c*-Si flow towards the rear side, thus do not encounter the emitter interface. However, the hole current is considerably reduced, because holes have to cross the tunnel barrier in order to be collected. As a result, holes accumulate in the wafer and participate to a large amount at

enhancing the recombination at the interface and in the bulk *c*-Si. Generated carriers are therefore annihilated: the short circuit current and the cell performance decrease.

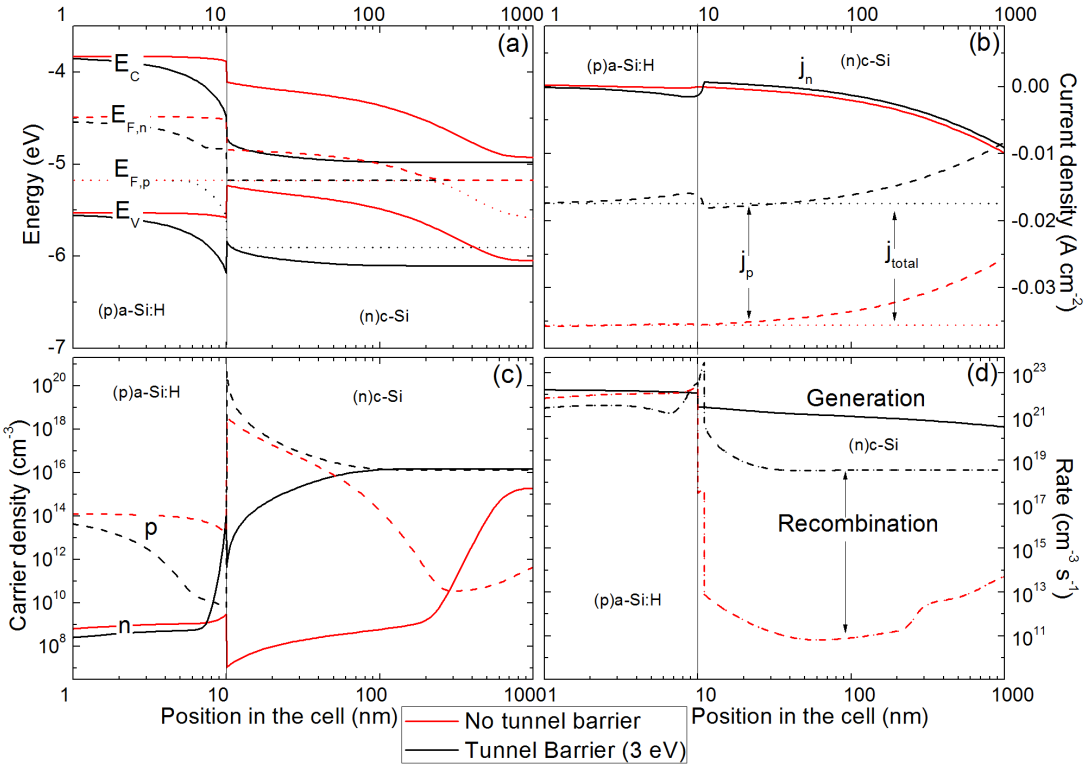

Figure 5.6: Simulations of solar cells under AM1.5 illumination, with and without a tunnel barrier ($\Phi_B = 3$ eV; $d_{ox} = 0.7$ nm), in short circuit conditions. (a) Band diagram including conduction and valence bands, as well as electron and hole quasi Fermi levels. (b) Electron, hole and total current density: $j_n + j_p = j_{total}$. (c) Electron (n) and hole (p) densities. (d) Generation and recombination rates. The quantities are plotted versus the position in the cell, the origin being the surface of the (p)a-Si:H layer. The (p)a-Si:H/SiO_2/(n)c-Si interface is located at $x = 10$nm.

In the range of parameters representative for pure SiO_2 – with an electron and hole barrier height as high as 3 eV and 4 eV respectively – no significant photocurrent can flow. The concept of a heterojunction with a buffer layer having the properties of a "perfect" bulk SiO_2 layer is thus unsuitable to reach power conversion efficiencies at least comparable to the case of a heterojunction without buffer layer.
However, for thicknesses corresponding to only a few monolayers (the $Si-O$ bond length is around 0.16 nm [Devine 87]) and for low band gap energies (resulting in low barrier heights), conduction across the interface seems efficient enough to maintain good cell performance.

5.2.1.5 Limitations of the model

A simple model was proposed to simulate a tunnel barrier between the emitter and the absorber of a heterojunction solar cell. Although it has permitted to carry out a comprehensive study on the effect of such a layer on transport properties, it has some drawbacks. In particular, the model takes into account only one conduction path, namely tunneling from band to band. In reality, many other features should be considered to describe the problem adequately:

- Shape of the barrier: the model assumes that a negligible potential drop takes place across the ultra-thin tunnel barrier. Thus a rectangular barrier is always considered. In reality, a trapezoidal shape (assuming a constant electric field in the barrier) should be taken, which would increase the transmission probability for high energies. Clerc showed that a trapezoidal barrier can be well replaced by a rectangular barrier, provided that the barrier height is reduced by half of the height of the triangular part [Clerc 01]. The present model just assumes a constant barrier height for any voltage, thus a constant factor δ, whereas it should depend on the interface electric field. Thus the barrier height given as a parameter to the computation is the maximum barrier height: the model tends to underestimate the current across the barrier.

- Image force: when a charge faces a dielectric layer, it induces an opposite charge at the surface which acts as if there were the same point charge with opposite charge at the same distance on the other side of the surface (image charge effect). This image charge induces a potential that reduces the barrier height [Rhoderick 88, Fischetti 95]. Kleefstra and Herman gave an expression for the barrier lowering in the case of three dielectrics in contact [Kleefstra 80]. Fig. 5.7 shows (a) the influence of this effect on a 3 eV high and 1 nm thick barrier profile and (b) the barrier height reduction as a function of the thickness of the barrier. A strong reduction of the barrier height for thicknesses below $1-1.5$nm is observed. This contributes to enhance the tunnel current and to reduce the dramatic impact of the insulator layer.

- Defects: another conduction path for the carriers consists in trap-assisted tunneling. Carriers can first tunnel from delocalized states to a trap in the barrier, and then be re-emitted on the other side. Herrmann and Schenk derived expressions to calculate the trap-assisted tunneling current [Herrmann 95]. The model developed in this work does not take this phenomenon into account. However, here again, the trap-assisted tunneling component would add a parallel contribution to the total current: the current simulated with the present model is thus underestimated.

- Pinholes: due to the very low thickness of the oxide layer, pinholes are expected to make a junction between *a*-Si:H and *c*-Si without any oxide in between. AFORS-HET being a 1D simulation program, the only way to take 2D effects into account (in this case, inhomogeneities of the barrier thickness in the interface plane) is to define effective

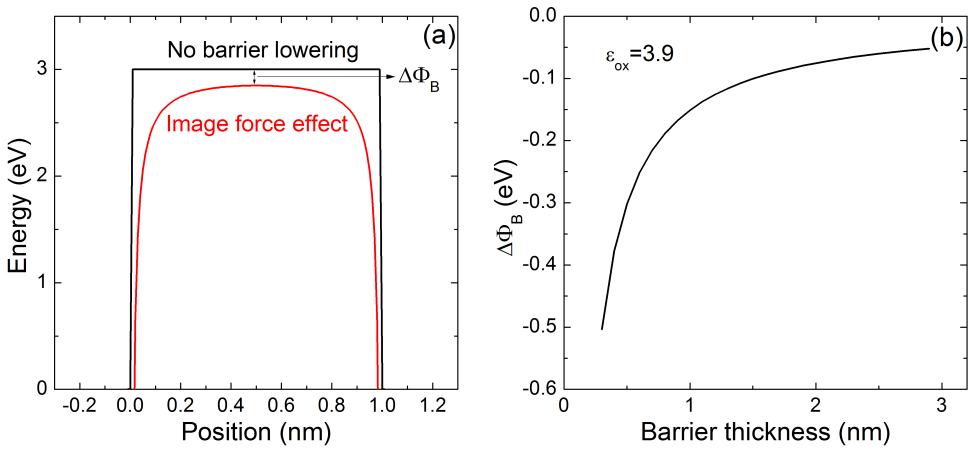

Figure 5.7: (a) Calculation of the barrier profile taking into account image force lowering effects. (b) Dependence of the barrier lowering $\Delta\Phi_B$ defined as the minimum image effect energy with respect to the thickness of the barrier.

quantities. The total current through the interface is actually the sum of the parallel currents: one component (J_{tun}) taking into account tunneling through the oxide layer, the other (J_{TE}) being simply the thermionic emission at the *a*-Si:H/*c*-Si interface such that the total current J reads $J = J_{\text{TE}}(1 - A_{\text{ph}}) + J_{\text{tun}} A_{\text{ph}}$ where A_{ph} is the relative pinhole area (parameter to be introduced in AFORS-HET). This is an oversimplification of the reality as current crowding effect could play a significant role [Vexler 01]. In Fig. 5.8, I-V curves simulated under an AM1.5 illumination are plotted for several relative pinholes areas. Even a small percentage of pin holes makes the current pass more easily; in that way, the range of the barrier parameters which do not limit cell performance is wider.

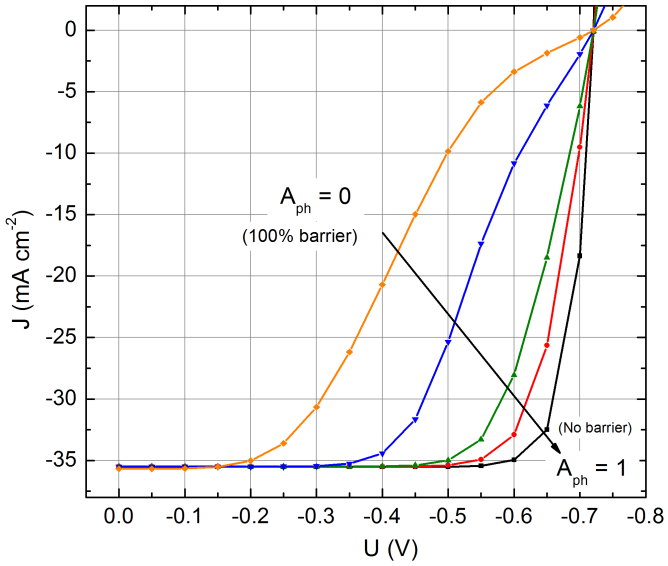

Figure 5.8: Simulations of solar cells under AM1.5 illumination for an insulator thickness of 0.7 *nm, and symmetrical barriers of* 2 *eV. Pin holes relative areas* A_{ph} *are* 0 *(fully covered surface),* 0.01, 0.05, 0.1 *and* 1 *(no insulator layer).*

5.2.2 Optical behaviour

The insertion of an oxide layer between crystalline and amorphous silicon may not only have an impact on charge carrier transport, but also on the absorption of light by the *c*-Si wafer, for instance because of undesired reflection of light at the interface. In order to investigate this effect, optical calculations using the Matlab method developed by Burkhard, Hoke and McGehee [Burkhard 10] were performed. The program calculates the light absorption in each layer composing the sample, as well as the reflection. The calculation is based on the transfer matrix formalism [Pettersson 99, Peumans 03]. The method was used to simulate the optical behaviour of the ZnO:Al (80 nm)/*a*-Si:H (10 nm)/X/*c*-Si (300 µm) planar structure; X is either no layer (called X=none in the following), 2 nm SiO_2 or 5 nm *a*-Si:H. The input optical constants for *c*-Si were taken from Adachi's review [Adachi 99]. Data for zinc oxide and amorphous silicon were measured at HZB. The refractive index for SiO_2 was taken from [Malitson 65].

In Fig. 5.9(a) the absorption in each layer and in (b) the reflection of the different structures for each wavelength are shown. An additional 5 nm thick *a*-Si:H layer plays a detrimental role on the total absorption in the cell. Indeed, it can be observed that the absorption of the incoming light in *c*-Si decreases (especially in the high photon energy range) when the total *a*-Si:H stack thickness goes from 10 to 15 nm. More 'blue' light is absorbed in the *a*-Si:H layers. On the contrary, the addition of a SiO_2 layer has no negative impact on the optical behaviour of the structure; the light absorption in *c*-Si even tends to increase slightly in presence of a SiO_2 buffer layer.

From the integration of the absorption in *c*-Si $a_{c-Si}(\lambda)$ [5] multiplied by the AM1.5 solar spectrum spectral irradiance $\Phi_{\mathrm{AM1.5}}(\lambda)$ (in W cm^{-2} nm^{-1}), the short circuit current linked to the light absorption spectrum can be estimated:

$$J_{sc} = \int_{\lambda_{\min}}^{\max} \Phi_{\mathrm{AM1.5}}(\lambda) a_{c-Si}(\lambda) \frac{q\lambda}{hc} d\lambda. \tag{5.11}$$

For X=none, J_{sc} = 44.7 mA cm^{-2}; for X=5 nm *a*-Si:H, J_{sc} = 42.5 mA cm^{-2}; for X=2 nm SiO_2, J_{sc} = 45.0 mA cm^{-2}. Note that the high J_{sc} values do not take into account shadowing from the metal grid and assume an internal quantum efficiency of 1 for all wavelengths. J_{sc} is reduced by about 5 % when the total *a*-Si:H stack thickness goes from 10 to 15 nm. To a lesser extent, the insertion of 2 nm SiO_2 is accompanied by an increase of J_{sc} of less than 1 %.

Thus, as far as light absorption is concerned, cell performance and particularly the short circuit current are expected not to be degraded by the insertion of a silicon oxide layer.

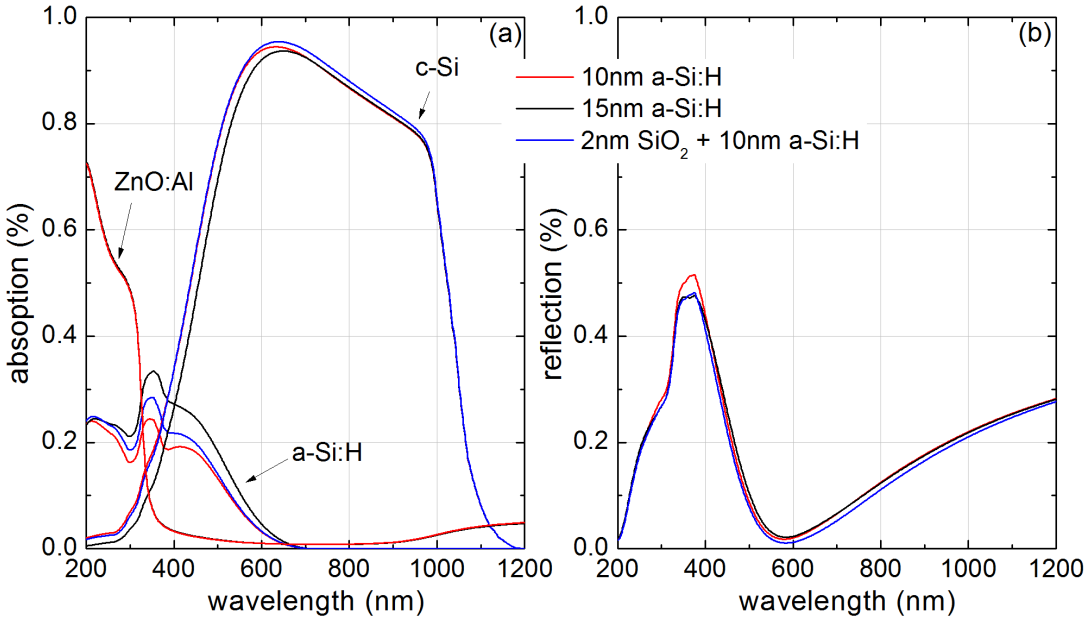

Figure 5.9: Optical simulation of ZnO:Al (80 nm)/a-Si:H (10 nm)/X/c-Si (300 µm) structures where X is none (red), 5 nm (i)a-Si:H (black) and 2 nm SiO_2 (blue): (a) Light absorption in the different layers of the structure. (b) Reflection of the total structure.

[5] Light absorbed in *a*-Si:H is assumed to give no contribution to the ouput current [Holman 12].

5.2.3 Short summary of preliminary results

In the first part of this chapter devoted to investigations on a new type of interfaces, namely oxide buffer layers between *a*-Si:H and *c*-Si, a model accounting for a tunneling current through an insulator layer sandwiched between two semiconductors has been developed and implemented in the simulation software AFORS-HET. Simulations of solar cell structures showed that for thin (≤ 0.7 nm) and low (≤ 1 eV) enough tunnel barriers, cell performance is not dramatically deteriorated. Moreover, several aspects of experimentally feasible buffer layers could not be taken into account and are expected to reduce even more the influence of a tunnel barrier on device efficiencies: tunneling through traps, presence of pinholes, barrier shape modification (electric field and image force lowering).
In addition, optical simulations indicated that a SiO_2 layer between *a*-Si:H/*c*-Si has no impact on light absorption by the *c*-Si absorber and does not reduce the short circuit current, contrary to an (i)*a*-Si:H buffer layer.

In the light of these preliminary results, the concept of a silicon heterojunction with a silicon oxide buffer layer between the emitter and the absorber requires further consideration. The challenge now is to grow or deposit such ultra-thin silicon oxide layers on *c*-Si and reach a good passivation quality.

5.3 Growth of ultra-thin oxide layers

5.3.1 Choice of the growth technique

The growth of ultra-thin high quality silicon oxide layers remains a challenge. The thermal growth results in highly defective first layers, rending this method unsuitable to reach thicknesses around 1 nm [Stathis 93]. Moreover it is highly energy-demanding, increasing the device production cost. The deposition by PECVD techniques leads also to bad quality interfaces [Beck 01]. At HZB, an ultra-high vacuum chamber has been used to oxidize silicon wafers in an atomic oxygen plasma [Stegemann 08]. This method leads to very thin SiO_2 layers, with an abrupt interface and a relatively low interface defect density. Since a dozen of years, an other activity at HZB has concerned the cleaning and preparation of silicon wafers and oxidation by room temperature wet chemical means [Angermann 97].
As a prerequisite step to the application of silicon oxide layers in silicon heterojunctions, the growth method has to be chosen. The interface defect densities D_{it} of samples processed and/or characterized in the frame of this work are presented in Fig. 5.10. The samples constitute a series of oxidized (n)*c*-Si wafers [6] ; ECR-CVD [7], oxygen plasma (UHV-OP), thermal oxidation and wet chemical oxidations (in RCA solutions, pure deionized water or H_2O_2/SO_4)

[6] The wafers may not have the same properties (origin, orientation, etc.) so that an accurate comparison between the samples is hazardous.

[7] Electron Cyclotron Resonance Chemical Vapour Deposition, a remote plasma version of the PECVD.

were used. D_{it} was measured using the VD-SPV technique presented in section 2.2.2.1.
It is clear that each oxidation method gives very different interface properties: the more 'agressive' the deposition/growth technique, the higher is D_{it}. The oxidation in ultra-pure deionized water seems to give one of the best interfaces in terms of low interface defect density. In addition to that, the energetic budget of this oxidation method is very small [8] compared to techniques requiring ultra-high vacuum, high process temperature or post-annealing.

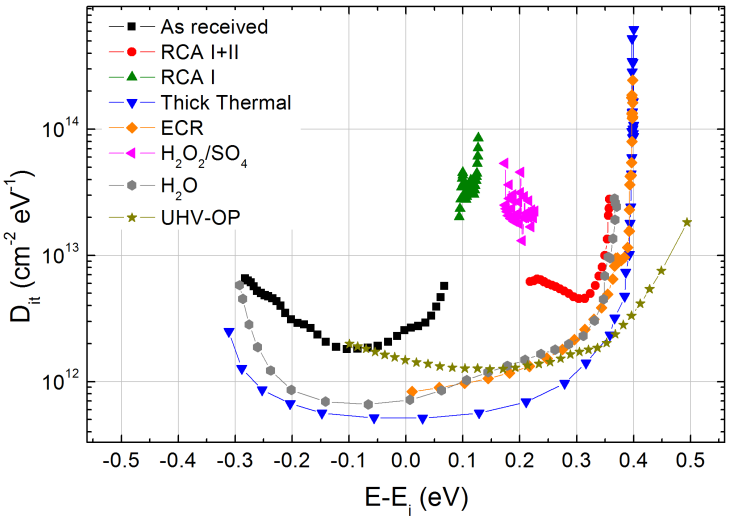

Figure 5.10: Interface defect distribution in the c-Si band gap of (n)c-Si oxidized wafers (methods are indicated in the legend) as measured with the VD-SPV technique.

In the light of the discussion above and based on the know-how acquired by the HZB on wet-chemical surface pre-treatment and chemical oxidation, it has been decided to develop the concept of a heterojunction with a silicon oxide passivation layer grown in hot water. More details on oxidation in ultra pure deionized water are now given.

5.3.2 Experimental details: revisiting *c*-Si surface preparation

The standard sample preparation was introduced in section 2.1. With the intention of developing new interfaces between *a*-Si:H and *c*-Si, specific *c*-Si surface preparations will be used. They are here briefly described. Then, the incorporation of new process steps in the heterojunction cell preparation is presented.

[8] However application in a production line may be complicated because of the long oxidation times (several hours).

5.3.2.1 Smoothing and water oxidation: brief state of the art

The preparation of *c*-Si surfaces aims to reduce the interface defect density. Contamination by impurities has to be avoided. The RCA cleaning results in low defect density H-passivated surfaces. However Angermann showed that the interface defect density of a H-terminated surface is related to its micro-roughness [Angermann 04]: the lower the micro-roughness, the lower is the surface defect density. Thus a smoothing step has been developed in order to reduce the micro-roughness of *c*-Si wafer surfaces and increase further the quality of the *a*-Si:H/*c*-Si interface. The smoothing step consists in an additional oxidation of the wafer surface in a boiling solution of H_2O_2:HSO_4 (1:1) for 10 minutes, followed by an optimized chemical etching: 4.5 minutes in pure NH_4F (40 %, pH=7.8).
In Fig. 5.11, a comparison between surface density of states measured by VD-SPV is presented for both (100) and (111) oriented surfaces of (n)*c*-Si wafers, smoothed or not. For both orientations, smoothing lowers significantly the interface defect density (Fig. 5.11(d)), especially in the lower half of the *c*-Si band gap. The SPV signal without external bias votlage is also lower for smoothed surfaces, which means that the band bending in *c*-Si and thus the surface fixed charge decrease after smoothing (Fig. 5.11(a) and (b)). Fig. 5.11(c) shows that charge and discharge of surface defects, a source of hysteresis, are not significant for the smoothed surfaces.

Directly applied to the preparation of standard *a*-Si:H/*c*-Si solar cells, this additional pretreatment brought significant improvement of cell properties [Angermann 09].

The oxidation of *c*-Si surfaces in ultra-pure deionized water is usually seen as a drawback of *c*-Si surfaces, where poor quality native oxide can rapidly grow. However, performed in a controlled way on cleaned, smoothed and etched surfaces, it can yield oxidized surfaces with a low defect density. Angermann reported values down to 3×10^{11} cm^{-3} eV^{-1} measured with VD-SPV [Angermann 04]. The standard procedure consists in immersing the sample in water at a temperature of 80 °C during a certain time. A schematic view of the experimental setup is shown in Fig. 5.12. Efforts are made to minimize the contamination risks of the surface (work under a laminar flow, use of quartz glass, neutral rinsing, etc.).
Oxidation in hot water results in a relatively low growth rate. After 2 hours in the bath, about 1 nm oxide is formed on (111) surfaces [Angermann 97]. This is encouraging for an application as an ultra-thin buffer layer: in that way, a fine control of the layer thickness seems possible, such that layers with thicknesses lower than 1 nm are realistically achievable.
Tunnel oxide layers prepared in hot water have been successfully used in MIS back contact silicon solar cells [Kliefoth 00]. Since the thickness requirement as found based on simulations in the preceding section is satisfied, this growth technique shall be applied to *a*-Si:H/*c*-Si heterojunction solar cells.

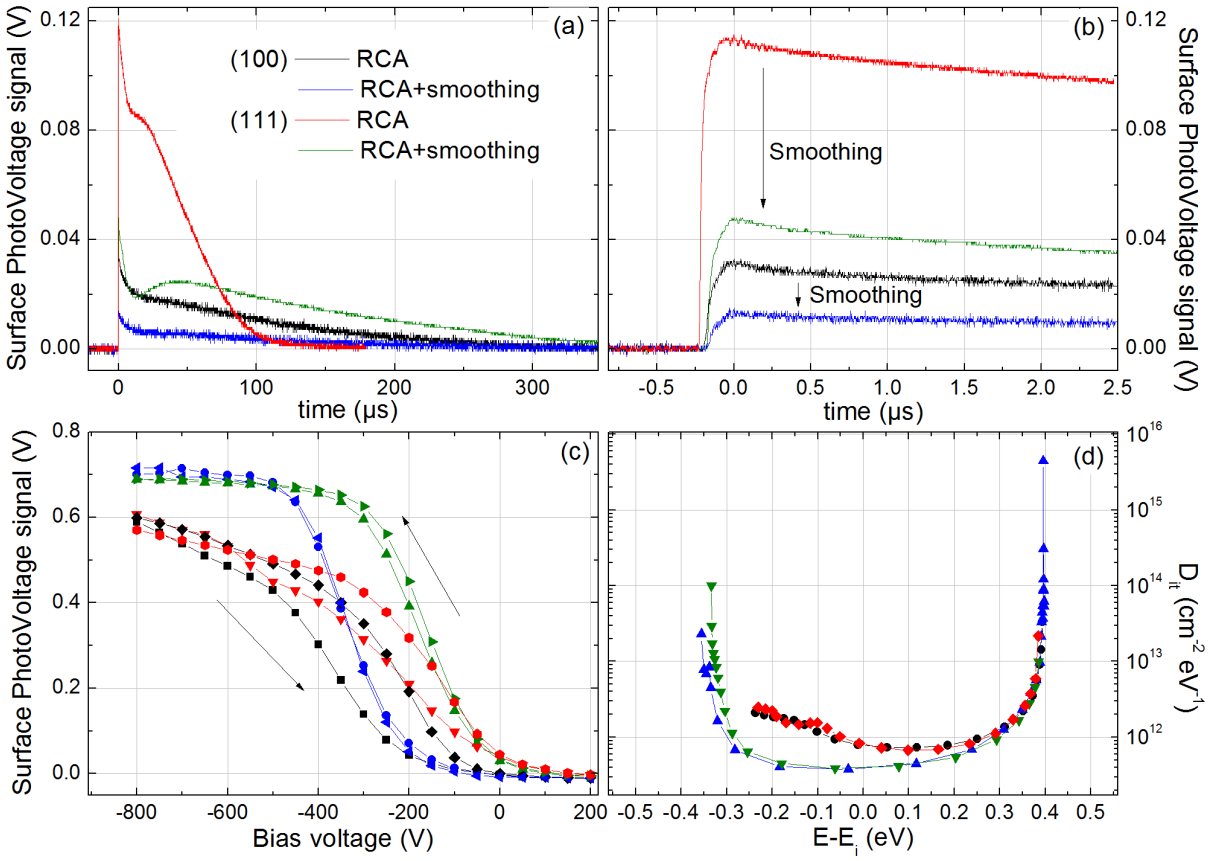

Figure 5.11: Comparison between RCA treatment and RCA+smoothing of (100) and (111) (n)c-Si wafers.(a) and (b): transient SPV signals at 0 *V. (c) SPV signal versus the applied voltage. (d) Interface density of states versus the energy in the c-Si gap.*

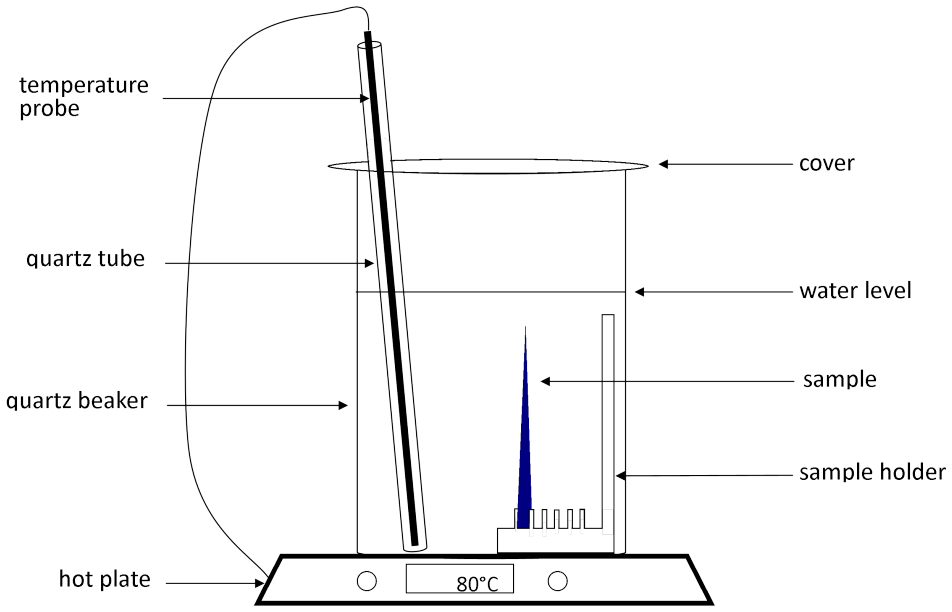

Figure 5.12: Experimental setup for the oxidation. The temperature is maintained at 80°C during the whole oxidation time. The setup is placed in a laminar flow box to avoid contamination of water by impurities in air.

5.3.2.2 Preparation of *a*-Si:H/silicon oxide/*c*-Si heterojunctions

In order to realize heterojunction solar cells, polished wafers were first used. In a further step that won't be treated here, textured wafers should be preferred to polished ones in order to increase light trapping. On textured wafers, pyramids have (111)-oriented surfaces. Therefore, investigations on planar (111) surfaces constitute the best starting point.

The starting point is, as for standard cell processing, the RCA cleaned wafer. After etching in HF, the wafer can either be smoothed and/or oxidized in hot water.
The final etching to remove the oxide layer after smoothing can be done by dipping the sample into HF diluted to 1% in H_2O or in ammonium fluoride, NH_4F.
The samples are rinsed in deionised water at room temperature and dipped in the oxidation bath sketched in Fig. 5.12. Once the oxidation is completed, the samples are dried under a nitrogen blow and stored in a nitrogen box until the next step (*a*-Si:H deposition) or are directly transferred to the PECVD chamber.

The oxidation of the *c*-Si surface complicates the standard cell fabrication process introduced earlier in section 2.1[9]. Indeed, the oxidation procedure forces to oxidize both sides of the silicon wafer as it is dipped entirely in water. As a consequence, the process flow has to be adapted to keep the oxide layer where it is wanted (front side and/or back side) [10].
The four typical process flows that are followed to prepare *a*-Si:H/*c*-Si heterojunction solar cells with different interfaces are shown in Fig. 5.13.
Samples Ox_Ox received an oxidation before any *a*-Si:H deposition. As a result, both front and back interfaces are oxidized: the emitter and the back surface field doped *a*-Si:H layers were deposited after the oxidation without removal of the oxide (no HF dip).
Samples Ox_i received first the *a*-Si:H layers forming the back surface field, and were then oxidized before receiving the emitter (p)*a*-Si:H layer. Thereby, only the front interface is oxidized[11]. This is the typical structure that raises interest in the frame of this study. Indeed an (i)*a*-Si:H layer at the back side causes no parasitic absorption: there is no advantage in replacing it.
Ref_i and Ref_p are reference samples respectively with and without a front (i)*a*-Si:H buffer layer.

[9] The standard cell preparation sequence takes into account that a deposition should not be done at a temperature higher than previous depositions.
[10] A HF dip not well-considered could remove the oxide layer although it should stay.
[11] The (n)*a*-Si:H surface is also oxidized, but a HF dip will remove the oxide on this side before the metallization.

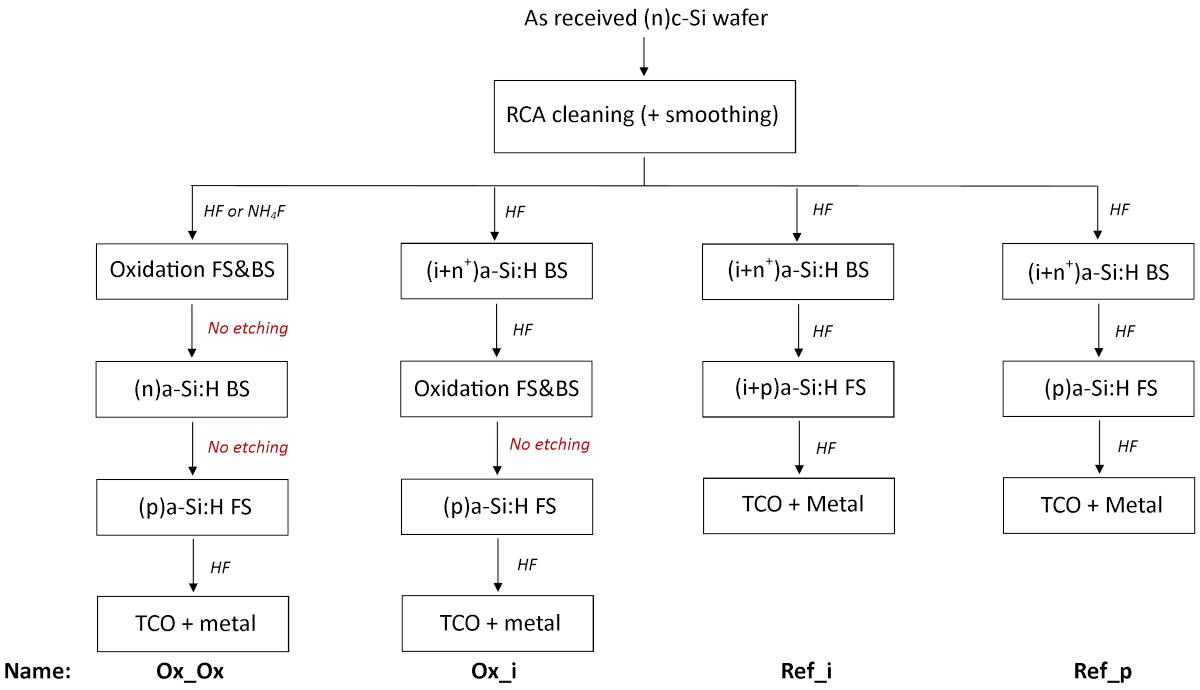

Figure 5.13: Process flow for solar cell preparation. Bs: Back Side (Back Surface Field), FS: Front Side (emitter). HF (NH_4F): etching in hydrofluoric acid (ammonium fluoride). Names for each flow are indicated for reading the experimental results later.

5.4 Experimental evaluation of the concept

The first series of samples are devoted to the study of fundamental aspects of the newly developed heterostructures. The passivation quality and the equilibrium band diagram are now addressed.

5.4.1 Passivation quality

5.4.1.1 Density of states of oxidized *c*-Si surfaces

On the way to fabricate heterojunction solar cells, the first step is to establish the quality of the surface prior to oxidation. Surface preparation is aimed at being part of the full device production line. Therefore, a compromise between surface quality and cost of the process has to be found.
In the following, several surface preparations commonly used are presented: RCA cleaning followed by smoothing or not, final etching with HF or NH_4F. The resulting estimations of the surface defect density are plotted against the energy in the *c*-Si band gap in Fig. 5.14. In (a) and (b), samples were first RCA-cleaned, and then either etched (red) or smoothed and etched (blue) such that in both cases surfaces are H-terminated. In (a), HF was used as final

etching solution, whereas in (b) NH_4F was used. In both (a) and (b), the surface density of states decreases after smoothing (see also Fig. 5.11(d)). Moreover, final etching with NH_4F results in wider and lower defect distribution than HF for both RCA-cleaned and smoother surfaces.
The four samples discussed here were subsequently oxidized during 2 hours in 80 ˚C deionized (DI) water ((c) and (d)). The density of surface states increases in all cases with respect to H-terminated surfaces. While no noticeable difference is seen for HF-etched samples, smoothing seems to provide more suitable surfaces for subsequent oxidation for NH_4F-etched surfaces: in (d), the defect distribution is lower (minimum at 7×10^{11} cm^{-3} eV^{-1}) for the smoothed sample than for the RCA-cleaned one, especially in the lower half of the band gap.

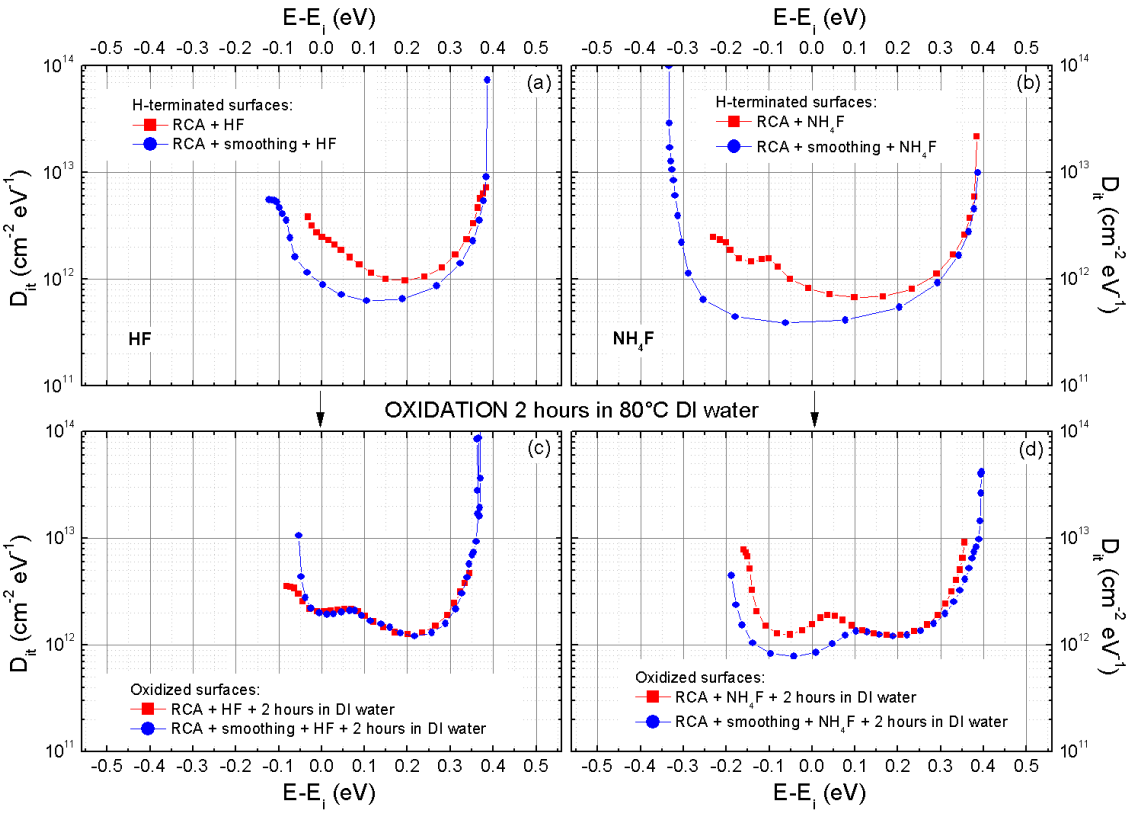

Figure 5.14: Preparation of (111) c-Si surfaces: surface defect density from VD-SPV measurements. Red: surfaces are solely RCA-cleaned. Blue: surfaces are RCA-cleaned and smoothed. (a) and (c): final etching after RCA-cleaning and smoothing uses HF. *(b) and (d): final etching after RCA-cleaning and smoothing uses* NH_4F. *(a) and (b): H-terminated surfaces. (c) and (d): oxidized surfaces (2 hours in* 80 ˚*C deionized (DI) water.*

In the light of these results, smoothed and oxidized surfaces with NH_4F as the last etching

step seem more suitable for incorporation into *a*-Si:H/*c*-Si heterostructures. However, if HF is employed, no advantage is gained by smoothing the surfaces.

5.4.1.2 Emitter passivation quality

The next step consists in investigating the passivation quality of the interfaces through measurements of the effective minority carrier lifetime with the photo-conductance decay technique (see section 2.2.2.2).

As-oxidized wafers result in very low minority carrier lifetimes, as can be seen in Fig. 5.15. However, after the (p)*a*-Si:H deposition, the lifetime increases up to a level equal to or above lifetimes measured on wafers passivated with (p)*a*-Si:H (see below for a detailed comparison). This is attributed to the hydrogen brought by *a*-Si:H deposition which passivates dangling bonds and increases the passivation quality.

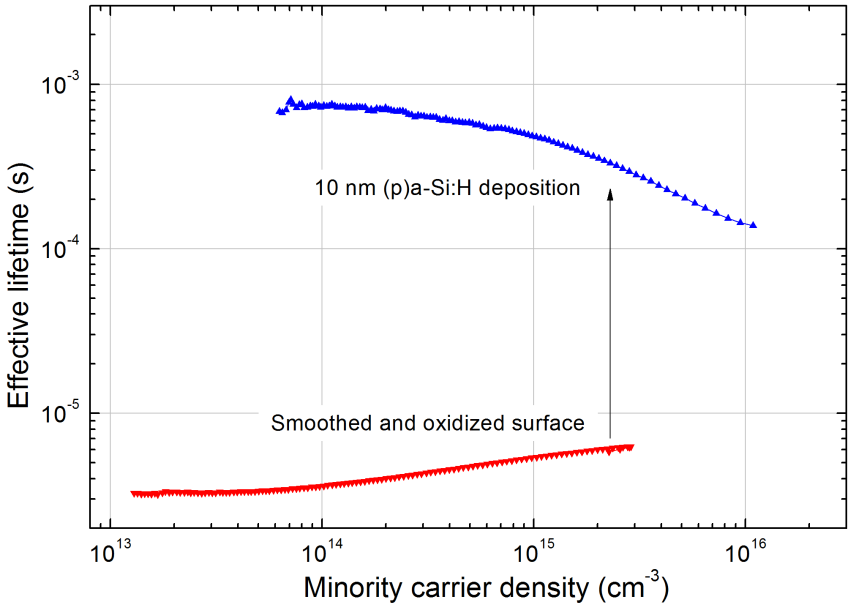

Figure 5.15: Minority carrier effective lifetime versus excess minority carrier density for as-oxidized and symmetrical (p)a-Si:H/ silicon oxide/ (n)c-Si samples.

In order to compare passivation qualities between the different interfaces, symmetrical samples with the emitter structure (p)*a*-Si:H/buffer layer/(n)*c*-Si/buffer layer/(p)*a*-Si:H were prepared. The buffer layer may be: none, (i)*a*-Si:H, silicon oxide. Effective lifetime measurements are shown in Fig. 5.16. In (a) and (b) no buffer layer is present such that 10 nm (p)*a*-Si:H passivates the *c*-Si surface. In (c) and (d), 5 nm (i)*a*-Si:H buffer layers and oxidized surfaces are covered by 10 nm (p)*a*-Si:H. In (a) and (c), only HF etching is used; in (b) and (d), NH_4F is used after smoothing.

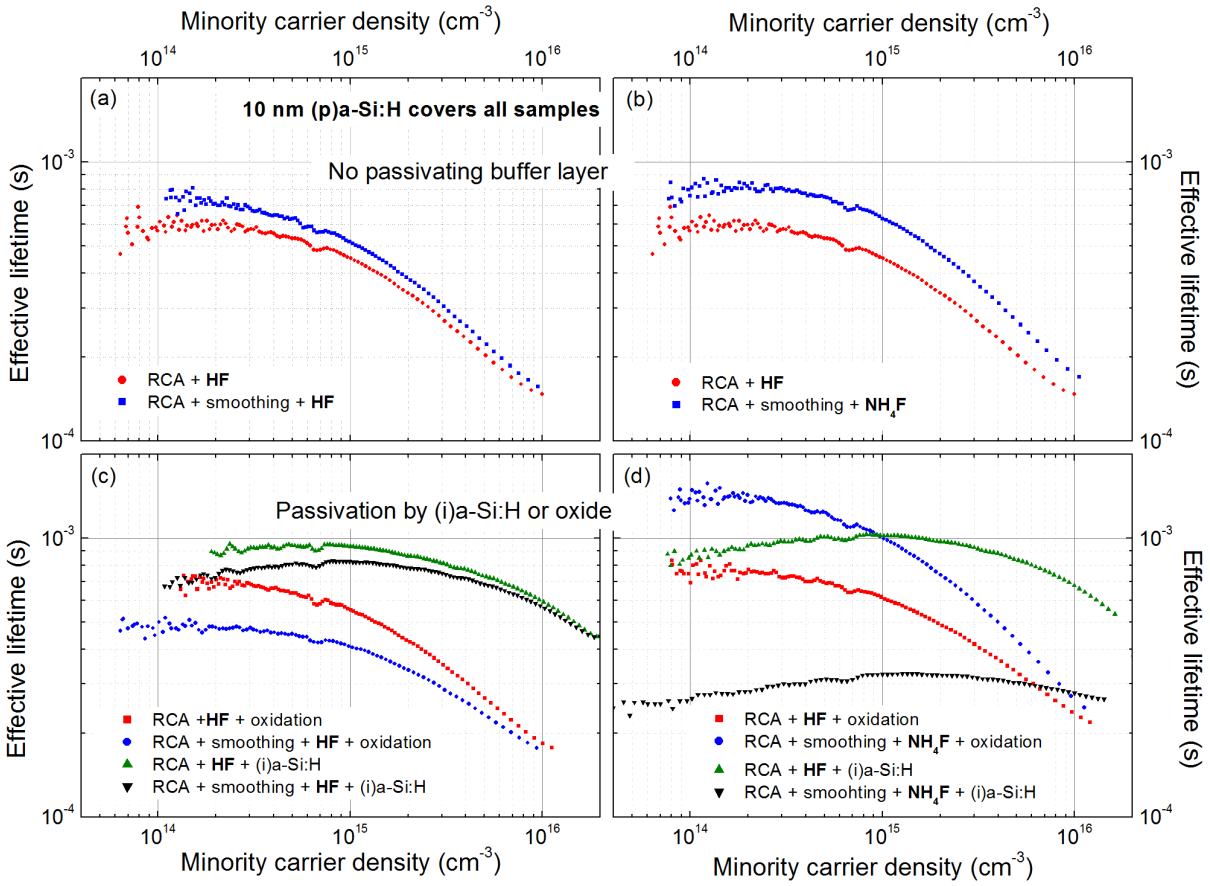

Figure 5.16: Minority carrier effective lifetime versus excess minority carrier density as measured by PCD on symmetrical (p)a-Si:H/ buffer layer/ (n)c-Si structures. Top ((a) and (b)): no buffer layer is inserted. Bottom ((c) and (d)): 5 *nm (i)a-Si:H and oxidized surfaces serve as buffer layers. Left ((a) and (c)):* HF *etching. Right ((b) and (d)):* NH_4F *etching after smoothing.*

Several points should be commented. First, it appears that for surfaces receiving (p)*a*-Si:H without passivating buffer layer ((a) and (b)), smoothing leads to a small increase in the effective lifetime only. This is consistent with the thesis that the interface defects of a pure *a*-Si:H/*c*-Si interface are actually determined by the bulk of the *a*-Si:H layer, the interface defects having no particular feature (see section 1.2.2).
Smoothing the surfaces of samples receiving an (i)*a*-Si:H buffer layer plays a minor role (black and green curves in Fig. 5.16 (c)). However a final etching with NH_4F is detrimental to the *a*-Si:H/*c*-Si interface because NH_4F may remain on the substrate and act as impurity defects (black curve in (d)).
On the contrary, the smoothed and NH_4F-etched oxidized surface samples (blue in (d)) shows a high effective lifetime, comparable to the reference sample with the (i)*a*-Si:H/(p)*a*-Si:H stack (green in (d)).

To extract more information from the photo-conductance decay measurements, lifetime data

Table 5.1: PCD data fit results. The oxidized sample was smoothed and etched with NH_4F *before oxidation (blue curve in Fig. 5.16(d). Samples used as references are reprented by a blue curve in Fig. 5.16(a) (no buffer layer) and a green curve in Fig. 5.16(d) ((i)a-Si:H buffer layer).*

sample	Q_{fix}/q (cm^{-2})	D_{it} ($cm^{-2}\ eV^{-1}$)	implied V_{oc} (mV)
(n)*c*-Si/ (p)*a*-Si:H	-1.15×10^{11}	4.05×10^{10}	662
(n)*c*-Si/ (i)+(p)*a*-Si:H	-6.32×10^{10}	8×10^{9}	697
(n)*c*-Si/ oxide/ (p)*a*-Si:H	-1.52×10^{11}	3.79×10^{10}	675

are fitted (see section 2.2.2.2). The fixed charge and interface defect densities are indicated in table 5.1. As already discussed in section 4.4.3, the introduction of an (i)*a*-Si:H layer lowers the fixed charge in the amorphous stack, which reduces the dark band bending and degrades the field effect passivation. This effect is totally suppressed and even reversed when silicon oxide replaces the (i)*a*-Si:H layer as the (absolute value of) fixed charge increases with comparison to the sample with no buffer layer. This suggests that the oxide layer carries a negative charge which adds up to the (p)*a*-Si:H negative charge and creates a stronger field effect passivation. Although it is more common that silicon oxide carries a positive fixed charge [Aberle 92], authors also reported negative fixed charge values especially for ultra-thin (a few nanometres) oxide layers grown from plasmas [Hernandez 96, Boogaard 09].
Regarding interface defect densities, the (i)*a*-Si:H layer still offers a better chemical passivation with respect to the case with no buffer layer or with an oxidized surface. The oxidized interface is also characterized by a slightly reduced interface defect density with respect to the case with no buffer layer, but still higher than the (i)*a*-Si:H passivated interface.
In summary, the lifetime improvement due to the oxidation steps comes from both a reduction of the interface defect density and an increase of the field effect passivation.

5.4.2 Equilibrium band diagram

The establishment of the equilibrium band diagram can bring new insight on the understanding of the three emitter structures introduced so far: no buffer layer, (i)*a*-Si:H as passivation layer and oxidized *c*-Si surface.
First, the equilibrium band bending of oxidized samples (without any *a*-Si:H layer on top) was measured using the SPV technique: it amounts to about 200 meV. Using Eq. 3.20, the corresponding charge in *c*-Si is $+6.8\times10^{10}\ cm^{-2}$; then, the charge neutrality implies that the oxide carries a negative charge $Q_{ox} = -6.8\times10^{10}\ cm^{-2}$. This is in reasonable agreement with the difference of fixed charge values extracted from the PCD data fitting: the fixed charge is $-3.7\times10^{10}\ cm^{-2}$ lower (values are negative) when there is an oxide layer (see Table 5.1). The fixed charge in the oxide can thus explain the increase in field effect passivation.
In order to determine if this fixed charge has an effect on the (p)*a*-Si:H/(n)*c*-Si equilibrium band diagram, emitter/absorber samples with three different interfaces (no buffer layer, (i)*a*-Si:H and silicon oxide buffer layers) were prepared to perform planar conductance mea-

surements. The equilibrium band bending is extracted from the measurements as explained in Chapter 4. Values are plotted in Fig. 5.17 for the three interfaces.
As outlined in section 4.4.3, an (i)*a*-Si:H buffer layer is responsible for a decrease of the band bending in *c*-Si with respect to the case without buffer layer. This drop is of about 100 meV. In the case of an oxidized surface, a weaker decrease of the band bending is observed; the drop amounts to about 40 meV [12].
Considering that a negative fixed charge has been found in the oxide from both PCD and SPV measurements, it is surprising that the band bending value drops. However, in (p)*a*-Si:H /(n)*c*-Si structures, a band bending of 820 meV creates a charge equal to -1.08×10^{12} cm^{-2} in (p)*a*-Si:H: $Q_{ox} = -6.8 \times 10^{10}$ cm^{-2} is not high enough to play a significant role in the charge neutrality at equilibrium (see also discussions on interface defects influence on the band bending in section 3.1.6). No increase of the band bending could have been expected [13].
Thus, the band bending decrease in the case of a silicon oxide buffer layer may be first attributed to the thickness difference: while the (i)*a*-Si:H layer is 5 nm thick, the oxide layer is expected to be less than 1 nm. The dielectric constant ϵ also differs between silicon oxide and *a*-Si:H: the relative value is 11.9 for *a*-Si:H whereas it is 3.9 for SiO_2. Consequently, the electric field in the oxide layer is a factor $11.9/3.9 \approx 3$ greater than in *c*-Si. If the potential drop in the buffer layer is a linear function of the thickness, a 40 meV drop in the oxide corresponds to a thickness of 0.7 nm[14]. Such a thickness is consistent with published thickness values [Angermann 97] and spectral ellipsometry measurements (not shown here).
The valence band offset may also be influenced, through interface dipoles for instance (see section 3.3.1).

Although temperature dependent measurements have been carried out on those structures, it will not be tried to extract the built-in voltage and the band offsets from these measurements. Indeed, the procedure developed in Chapter 3 should be applied only on emitter/absorber structures without buffer layer, as an additional buffer layer would add too much unknown parameters: band offsets, thickness, defect density.

To summarize first experimental analyses, oxidized *c*-Si surfaces seem to be suitable for application in *a*-Si:H/ *c*-Si heterojunction solar cells: they offer a better passivation quality than (p)*a*-Si:H while maintaining a significant band bending in *c*-Si. Now, solar cells are measured under illumination and their performance are tested.

[12] Although the error ranges slightly overlap, the drop is discussed as if it corresponded to the difference of the band bending mean values, which comes from the approximation that the mobility close to the interface does not vary much between the samples.
[13] This is not in contradiction with PCD data because the charge in *a*-Si:H is likely to depend on the excess carrier density whereas the fixed charge in the oxide stays constant.
[14] A simple cross-product is applied to estimate the 0.7 nm from the 40 meV drop.

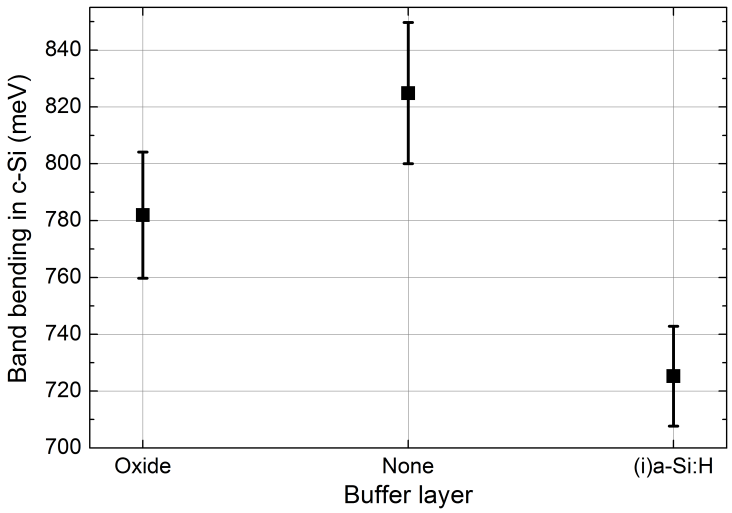

Figure 5.17: Equilibrium band bending in c-Si in (p)a-Si:H/ X/ (n)c-Si structures where X is: none, 5 *nm (i)a-Si:H and silicon oxide. Error bars come from the lack of knowledge on the mobility values.*

5.5 Solar cells with oxide passivation layers

5.5.1 Cell performance

Solar cell structures introduced in Fig. 5.13 were completed with deposition of a TCO and metallization (see section 2.1). Current-voltage characteristics were measured under AM1.5 illumination; cell parameters, i.e. the short-circuit current J_{sc}, the open circuit-voltage V_{oc}, the fill factor FF and the power conversion efficiency η, were extracted and are presented in Fig. 5.18; the tables above the graphs give details on the procedure followed during the fabrication.

First it can be noticed that, as expected, the reference cells with an (i)*a*-Si:H buffer layer have a better open circuit voltage than the cells without any buffer layer: the (i)*a*-Si:H plays its role of reducing interface recombination. Interestingly, cells with oxide on the front side (red) have a better V_{oc} than cells without buffer layer (black), and comparable to the one of cells with (i)*a*-Si:H. Cells with oxide on both sides of the *c*-Si wafer have a lower V_{oc}.
For all samples, the short circuit current lies at the same level within 1 mA cm^{-1}. However, the samples including 5 nm more *a*-Si:H (Ref_i) are in the lower part of the distribution due to a stronger absorption in the thicker amorphous silicon stack. Because flat wafers were used, the short circuit current values are rather low.
The fill factor evolution follows the V_{oc} trend, indicating that it is limited by recombination processes. The lower fill factor for Ref_i is attributed to an increased series resistance caused by the 5 nm thick front (i)*a*-Si:H layer. Surprisingly, the fill factor of cells with oxide buffer layers does not dramatically drop as expected in section 5.2.1.4 from simulations. The globally low fill factor level is attributed to a low conductivity of the zinc oxide.

The resulting power conversion efficiencies are plotted in the bottom right graph. Interestingly, structures with oxide at the front interface offer better performance than the reference cells. Both side oxidized *c*-Si wafers indicate clearly poorer conversion efficiencies than when the oxide is just on the front side. This may have two explanations:

- (i) (i)*a*-Si:H passivates the back interface much better than silicon oxide. This argument is supported by the negative fixed charge in the oxide which is not adapted for the back surface field passivation.
- (ii) The oxidized front side is better passivated if it is oxidized after the deposition of the back surface field (see Fig. 5.13).

An analysis of quantum efficiency measurements should shed light on this point. Smoothing the *c*-Si surface prior to oxidation does not seem to be necessary.

Structure:
(p)a-Si:H/ buffer at front side/ (n)c-Si/ buffer at rear side/ (n^+)a-Si:H

Name	Ox_i	Ox_Ox	S_Ox_i	S_Ox_Ox	Ref_i	Ref_p
c-Si preparation	RCA	RCA	RCA + smoothing	RCA + smoothing	RCA	RCA
Buffer layer at front side	Oxide	Oxide	Oxide	Oxide	(i)a-Si:H	None
Buffer layer at rear side	(i)a-Si:H	Oxide	(i)a-Si:H	Oxide	(i)a-Si:H	(i)a-Si:H

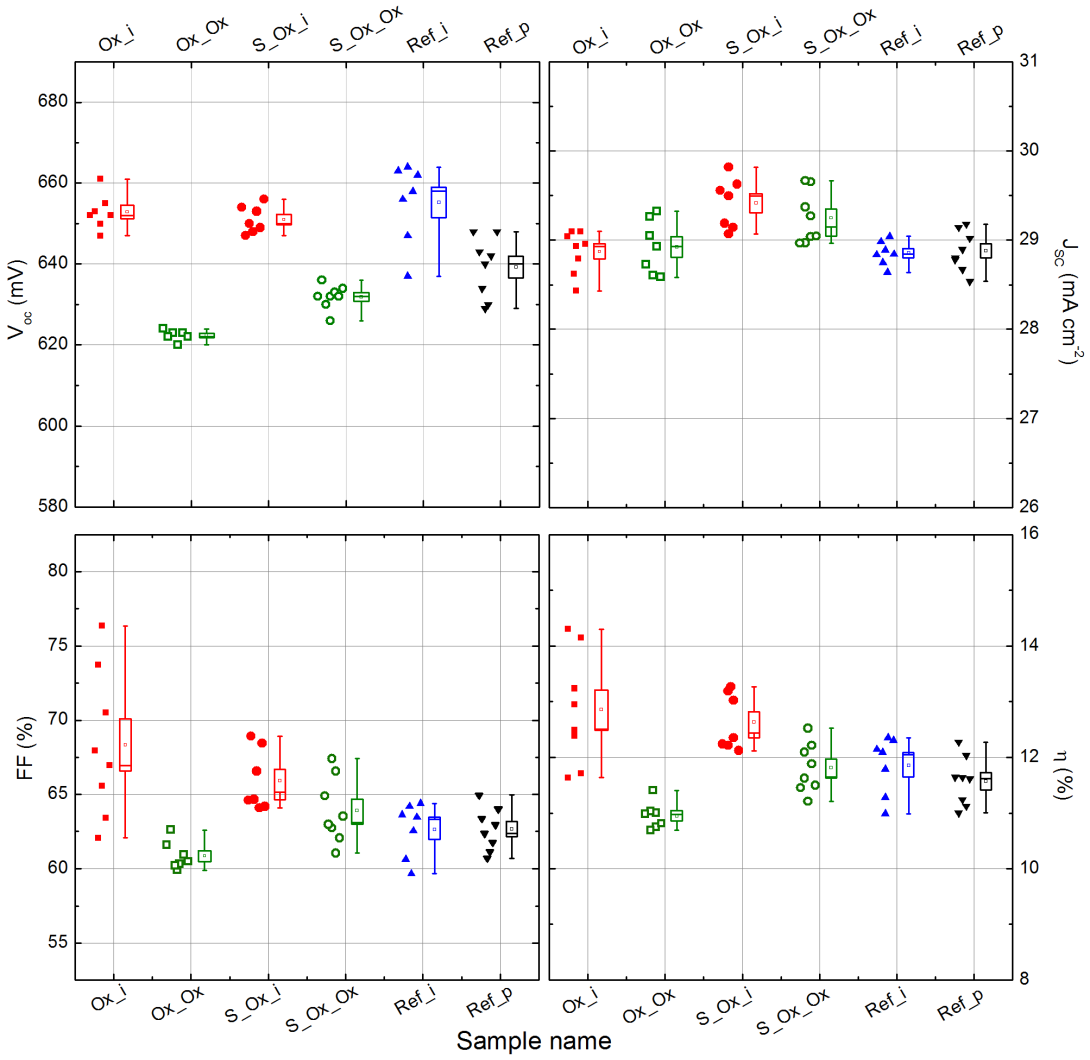

Figure 5.18: Table: name and preparation of c-Si surfaces and structure of each group of 1 cm^2 *solar cells. Graphs: solar cells open circuit voltage, short circuit current, fill factor and power conversion efficiency. Raw data (symbols) and statistical analysis: Outlet=min-max, Large rectangular box=standard error, Small square=mean, Horizontal segment=median.*

5.5.2 Device spectral response

To study in more detail the behaviour of the fabricated solar cells, the external quantum efficiency (EQE) and the reflection (R) were measured; the internal quantum efficiency (IQE) was calculated from those measurements. Results are presented in Fig. 5.19.
First, no difference between the different samples is seen as far as the long wave length response is concerned, suggesting that the back side is not limiting cells performance. However differences appear at shorter wavelength, where most of the light is absorbed close to the interface. The lower IQE for Ref_i is attributed to optical losses due to the thicker *a*-Si:H stack (in total 15 nm instead of 10 nm for other samples). This is strengthened by optical simulations presented earlier in section 5.2.2, and the different behaviour observed in the reflection spectra (reduced reflection around 400 nm). Samples Ref_p and Ox_Ox show the same behaviour. Only Ox_i has an increased response for short wavelengths, which is attributed to a lower recombination as the optical behaviour should be the same for Ox_Ox and Ox_i.
In the light of these results, the poorer performance of solar cells with oxidized surfaces on both the front and back side can be explained by better front interfaces when the oxidation is performed after the deposition of back surface field (BSF). At this point, there is no clear explanation for this phenomenon and only hypotheses can be formulated: when the BSF is first deposited, the etching just before the oxidation may remove impurities deposited on the surface during the BSF processing (transfer to PECVD, etc.). On the contrary, when the oxidation is first done on both sides, no etching is done between the back side and front side depositions: this may be a source of contamination [15].

[15] The (p)*a*-Si:H deposition is not done right after the (n)*a*-Si:H deposition, as the doping type of the chamber has to be changed first.

Name	Ox_i	Ox_Ox	Ref_i	Ref_p
c-Si preparation	RCA	RCA	RCA	RCA
Buffer layer at front side	Oxide	Oxide	(i)a-Si:H	None
Buffer layer at rear side	(i)a-Si:H	Oxide	(i)a-Si:H	(i)a-Si:H

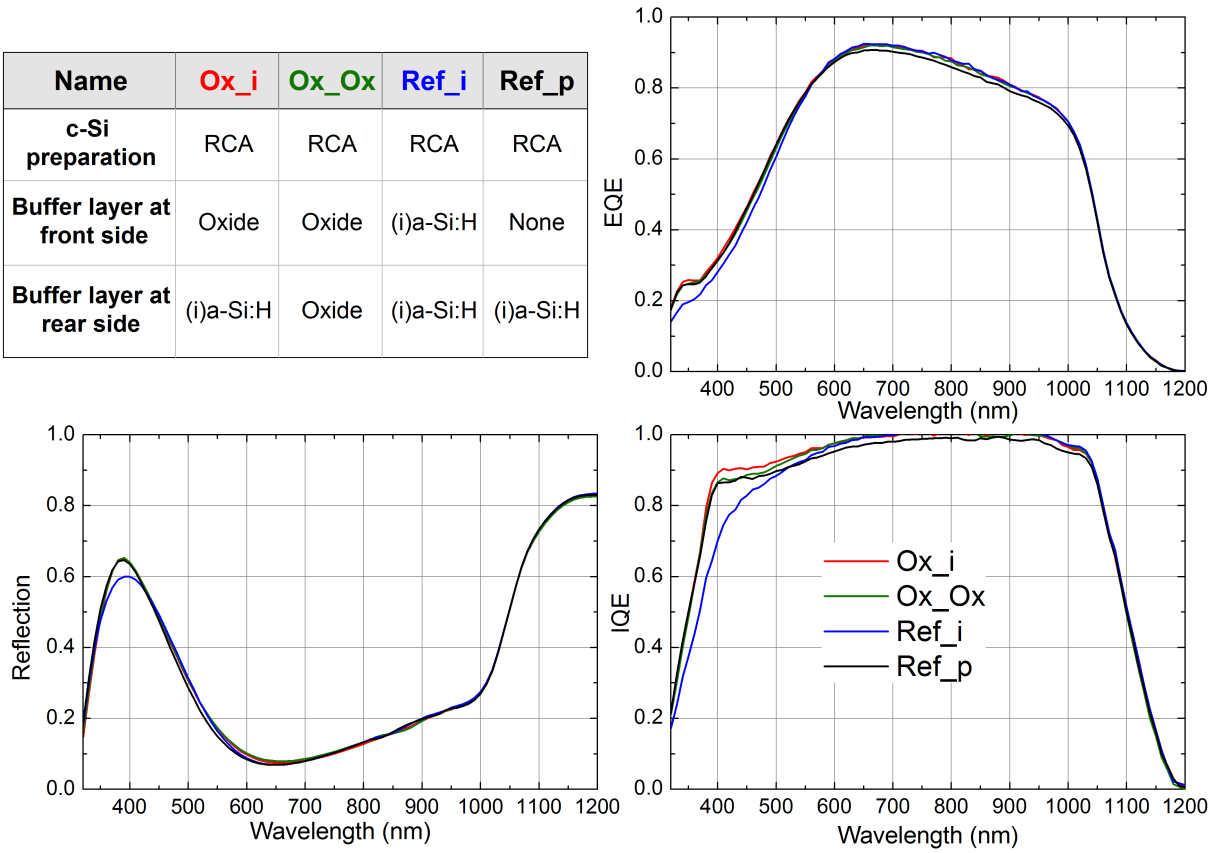

Figure 5.19: External Quantum Efficiency (EQE), Reflection (R) and Internal Quantum Efficiency (IQE) of solar cells with different interface preparations.

5.6 Discussion

Lee recently applied ultra-thin silicon oxide layers to silicon heterojunction solar cells [Lee 12]. The silicon oxide layers were grown using rapid thermal oxidation. The conclusion of the authors was that the band gap of the buffer layer material has to be controlled to allow for tunneling. This is also what is shown in the simulation part of this chapter. In the light of the theoretical analysis presented in section 5.2.1, doubts can be expressed regarding the relevance of using pure and 'thick' (a few nanometres) SiO_2 buffer layers.
As a consequence, to the best knowledge of the author, this study is the first successful report on the application of tunnel silicon oxide as buffer layer for *a*-Si:H/*c*-Si solar cells. The ultra-thin thickness (a few monolayers only) reached by the growth method (oxidation in hot water) employed to passivate the *c*-Si wafers is certainly an advantage.

The passivation study led to the conclusion that the oxide films carry a negative fixed charge responsible for the enhanced field effect passivation. Therefore, open circuit voltages higher than 650 mV were reached on solar cells which were not optimized as far as the TCO is concerned. The negative fixed charge is beneficial for (n)*c*-Si based solar cells as it repeals

the photo-generated electrons toward the back side. However, such an oxide layer would probably act in the reverse direction for (p)*c*-Si based solar cells as it would not repeal the holes. The choice of n-type wafers was thus a relevant choice.

One of the most important finding coming out of this study on solar cells with oxidized *c*-Si surfaces is that the front side is of better quality if the *c*-Si wafer is oxidized after the back surface field has been deposited. This means that, like for H-terminated surfaces, the (p)*a*-Si:H front emitter should be deposited as soon as the *c*-Si surface has been oxidized. As a consequence, the oxide layer cannot be used as a protecting layer that would allow the experimenter to delay the *a*-Si:H deposition after the wafer has been processed (cleaned and oxidized).

So far, a smoothing of the *c*-Si surfaces prior to oxidation has not brought any advantage, suggesting that the state of the *c*-Si surface was not the limiting factor in this study. Post-treatment such as annealing in hydrogen may have more impact on the defect passivation than the pre-treatment. However the smoothing step should be kept as a solution to improve further the sample quality once higher passivation levels are reached.

5.7 Chapter conclusion

This chapter was devoted to the development of a new *a*-Si:H/*c*-Si interface type to be incorporated in silicon heterojunction solar cells: oxidized *c*-Si surfaces as an alternative to (i)*a*-Si:H have been studied from the growth up to the application in complete solar cells.
A model accounting for tunneling through an energy barrier has been developed and implemented in AFORS-HET. From simulations, the typical range of barrier parameters – thickness, height – which are not detrimental for solar cells performance has been established: the thickness should be below 0.7 nm, and the barrier height below 1 eV. This constitutes a lower limit, as many phenomena expecting to increase the interface current could not be considered.
Optical simulations showed that a SiO_2 layer does not degrade cell optical properties, as light absorption in *c*-Si is not reduced.
In the light of these simulation results, a pathway toward the incorporation of ultra-thin silicon oxide in silicon heterojunction solar cells has been set up. The consideration of many growth techniques and the need to find a trade-off between oxide passivation quality, thickness and cost led to regard oxidation in hot water as the most suitable technique.
Investigations on *a*-Si:H/oxide/*c*-Si structures showed an interesting potential for the concept: the passivation quality is enhanced in structures with an oxide buffer layer with respect to structures without buffer layer because of a negative fixed charge brought by the oxide. The band bending in *c*-Si is maintained despite the presence of a thin insulator layer.
Finally, solar cells were fabricated and performances of those whose front surface were oxidized demonstrated better open circuit voltage and power conversion efficiencies than cells without buffer layer.

Conclusion

Summary and conclusions

In this thesis, three interdependent aspects of the *a*-Si:H/*c*-Si heterojunction have been studied: the band offsets between *a*-Si:H and *c*-Si, the band bending in *c*-Si caused by the equilibration of the Fermi level in the structure and the development of a new type of interface aimed at reducing optical absorption in the undoped *a*-Si:H buffer layer while limiting the recombination of charge carriers at the interface.

The valence and conduction band offsets between *a*-Si:H and *c*-Si were extracted from a comparison between temperature dependent planar conductance measurements and analytical calculations of the band bending in *c*-Si. Planar conductance measurements demonstrated a highly conductive interface channel which is due to an inversion layer in *c*-Si.
A model to calculate analytically the band bending in *c*-Si has been developed to relate the carrier density in the inversion channel to the properties of the heterojunction through the band bending in *c*-Si. The channel conductivity is particularly strongly dependent on the band offsets and the density of states in *a*-Si:H (assumed constant in the calculations) close to the Fermi level. The interface defects, whose charge was taken into account in the global charge neutrality statement, play no significant role at their expected densities. The presence of quantum effects in the strongly inverted triangular quantum well were discussed: confinement tends to decrease the carrier sheet density without changing the temperature dependence (activation energy of the exponential decay).
The analysis of temperature dependent planar conductance measurements led to the conclusion that the valence band offset is independent of the temperature whereas the conduction band offset follows the evolution of the band gaps with temperature. On (p)*a*-Si:H/(n)*c*-Si structures, the hole sheet density value at 300 K and activation energy determined exper-

imentally were compared with calculations such that the valence band offset mean value was estimated at 0.36 eV with a standard deviation equal to 0.04 eV. In the same way, the conduction band offset was extracted from the study of (n)*a*-Si:H/(p)*c*-Si structures: the mean value was found to be 0.15 eV, with a standard deviation of 0.07 eV. Considering that the study was realized on series of samples coming from several institutes around the world (HZB, University of Toronto, LPIM-École Polytechnique, CEA-INES), the results stay close to their mean value, in contrast to what is found in the literature. The errors on the measurements come mainly from the not exactly known mobility values at the strongly inverted *c*-Si surface. Because valence band offsets values determined on (n)*a*-Si:H/(p)*c*-Si and on (p)*a*-Si:H/(n)*c*-Si structures are almost the same, it is suggested that the branch point in *a*-Si:H is determined by its intrinsic defect density and stays at the (i)*a*-Si:H Fermi level position.

The analysis of the band bending calculations used to extract the band offsets was done on structures with thick *a*-Si:H layers and without buffer layer. Because the band bending in *c*-Si determines cell performance, in particular the open-circuit voltage, it is also important to study its behaviour in structures closer to the final device: thin emitters contacted with a metal-like material, presence of an ultra-thin insulator-like buffer layer. For this purpose, the analytical model has been improved to take into account different boundary conditions at the *a*-Si:H emitter surface and a potential drop in a buffer layer between the doped *a*-Si:H emitter and (n)*c*-Si.
It has been proven from simulations that, in order to reduce the impact of the *a*-Si:H emitter surface on the band bending in *c*-Si, a high density of states in the emitter can be beneficial to the open circuit-voltage and ultimately to power conversion efficiencies, except for the unrealistic case of high TCO work function.
Two series of samples with varying buffer layer thickness, and with different doping levels, have been studied: the band bending was measured with the planar conductance technique while the effective lifetime was tracked with photo-conductance decay and modulated photo-luminescence measurements. Data were interpreted using the analytical calculations. In all cases, a trade-off between a high band-bending in *c*-Si and a high passivation quality has to be found. This can be done either by optimizing the thickness of the (i)*a*-Si:H buffer layer or by micro-doping it to maintain a sufficient field effect.

The last point addressed in this thesis was the development of a new type of interfaces, namely oxidized crystalline silicon surfaces as a building block for silicon heterojunction solar cells. In order to study the influence of an oxide layer between the *a*-Si:H emitter and the *c*-Si base, a model taking into account a tunneling current through a thin insulator layer has been developed, implemented in the simulation software AFORS-HET and used to study the influence of such a barrier on cells performance: for thicknesses and heights lower than 0.7 nm and 1 eV respectively, the impact of the barrier on the current transport is within what one can afford to reach high efficiencies. Moreover, such an inter-layer has no negative influence on the optical behaviour of the cell.
Samples were prepared using oxidation of *c*-Si wafers in pure de-ionized water at 80 ˚C

after different treatments of the interfaces: standard RCA cleaning, smoothing, etching with hydrofluoric acid (HF) or ammonium fluoride (NH_4F).
Smoothed, NH_4F-etched and oxidized samples show a better charge carrier lifetime than samples with no buffer layer, and close to samples with an (i)*a*-Si:H buffer layer. The improved lifetime is attributed mostly to an increased negative fixed charge brought by the oxide.
Despite all solar cells performance are strongly limited by the fill factor and the open-circuit voltage, it is remarkable that cells with a front oxidized interface have an open-circuit voltage above the cells with no buffer layer, and of the same order of the cells with an (i)*a*-Si:H buffer layer. This promises a great potential for this new silicon heterojunction cell concept.

Perspectives

A comprehensive study on the concept of heterojunction solar cells with silicon oxide buffer layers has been presented. However, several questions, both from the theoretical and experimental points of view, remain open.
Regarding simulations, the implemented tunneling current model is rather simple as it takes only one transport path into consideration. A further improvement should be the implementation of a trap-assisted tunnel transport. The image force effect could also be implemented, as its effect on the barrier shape is dramatic especially for ultra-thin insulator layers. To go beyond the concept studied here, it would be of great interest to implement a tunnel current through an insulator at the contacts with the external circuit. This would allow, for instance, to simulate a thin silicon oxide forming at the early stage of the TCO deposition.
Concerning experiments, more information on the silicon oxide layer formed during the oxidation in hot water is needed. Particularly, knowledge on the stoichiometry of the films is still lacking: is it pure silicon dioxide? Or are silicon sub-oxides dominating? The answer could be given by X-ray photo-electron spectroscopy analyses. Complementary information on the layer thickness would also be given by this technique.
Finally, from the device point of view, it would be relevant to vary the emitter properties in order to find out how this new interface behaves with respect to deposition conditions (temperature, ion bombardment) on one side, and with respect to the Fermi level position imposed by the emitter (defect equilibration?) on the other side.

The method used to determine the band offsets relies on simple equipments (liquid nitrogen cooled cryostat and I-V measurements setup) which makes the technique easily applicable as such in any research laboratory. Other types of heterojunctions could be investigated by the same method: the requirements are only a highly inverted region on one side of the junction (providing the highly conductive channel and the blocking diode) and a low conductivity of the top material. The essential role played by the band offsets on the formation of the highly conductive channel makes this method very accurate. However, even better accuracy could be reached if one could determine the mobility values in the strongly inverted layers. Investigations are currently being carried out to get insight on the mobility values from

measurements on MOS-FET structures where the gate has the structure metal/SiO_2/(p)*a*-Si:H/(n)*c*-Si. This will hopefully make the planar conductance method much more accurate regarding the extraction of band offsets and measurement of band bending.

The theoretical prediction that a high density of states in the *a*-Si:H emitter is beneficial for solar cell performance may be difficult to test experimentally. Indeed, increasing the defect density would decrease the doping efficiency as it would be harder to push the Fermi level towards the valence band edge, thus limiting the built-in voltage potential. It could also be detrimental for the interface passivation if the buffer layer does not properly isolate the absorber from the emitter.

Finally, the complementary measurements of the effective lifetime *and* the band bending in *c*-Si can help to understand the passivation mechanisms and to find a trade-off between the chemical passivation of defects and the electric field necessary to separate the photo-generated charges. Adequate methods have to be used: the planar conductance is suggested to determine the band bending, while photo-conductance decay and/or modulated photo-luminescence can be applied on samples without/with contacts, respectively. This two-measurement method should bring all the information (at the exception of parasitic light absorption, which requires reflection/transmission measurements made on layers deposited on glass for instance) required to study the effect of buffer layer variations (thickness, micro-doping,...) on cell performance.

A

Appendix A: Details on the analytical band bending calculation

A.1 The (n)*a*-Si:H/(p)*c*-Si heterojunction case

For the (n)*a*-Si:H/(p)*c*-Si heterojunction, the built-in potential is:

$$qV_{bi} = q(V(-\infty) - V(+\infty)) = \Delta E_c + E_g^{c-Si} - \delta^{c-Si} - \delta^{a-Si:H}. \tag{A.1}$$

where ΔE_c is the conduction band offset, $\delta^{c-Si} = (E_F - E_v)^{c-Si}$ and $\delta^{a-Si:H} = (E_c - E_F)^{a-Si:H}$.

The charge in *c*-Si is calculated according to Eq. 3.20 without any modification.

The charge in *a*-Si:H reads like Eq. 3.37 (or Eqs. 4.3 and 4.6): only the term $V(-\infty) - V(0)$ has to be modified according to Eq. A.1.

The charge in interface defects has the same expression as in Eq. 3.41.

The charge neutrality is then solved like for the (p)*a*-Si:H/(n)*c*-Si heterojunction.

Appendix A. Appendix A: Details on the analytical band bending calculation

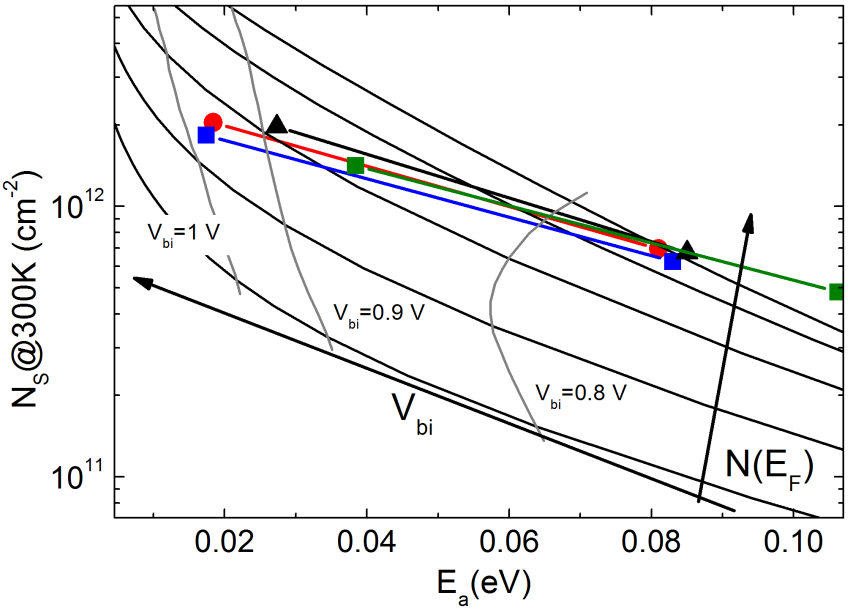

Figure A.1: Extraction of the built-in potential V_{bi} from comparison between experimental results (symbols joined by a line) and analytical calculations (black lines). The activation energy E_a was calculated from the temperature dependence of N_s around room temperature. Each curve is for one density of states ($N(E_F) = 10^{18} \ldots 10^{22}$ cm^{-3} eV^{-1} from bottom to top). The built-in potential varies along each curve as indicated, increasing when E_a decreases or N_s increases. The "iso-built-in potential" curves are guidelines for the eyes. Each experimental data is represented by a segment to account for the uncertainty on the carrier mobility in the strong inversion layer.

The electron sheet density N_s is defined in the same way as P_s:

$$N_s(T) = \int_0^{+\infty} (n(x,T) - n_b(T))\, dx, \tag{A.2}$$

where $n(x,T) = n_i e^{u(x,T)}$ is the electron concentration at x and $n_b(T) = n_i e^{u_b(T)}$ is the electron concentration in the bulk.

Using the variable $u(x)$, P_s can be written as

$$N_s(T) = \int_{u_s(T)}^{u_b(T)} n_i(T) \left(e^u - e^{u_b(T)}\right) \left(\frac{du}{dx}\right)^{-1} du. \tag{A.3}$$

The same analysis as for P_s can be done and lead to the determination of V_{bi} in Fig. A.1.

A.2 Exponential DOS in *a*-Si:H

In doped *a*-Si:H, the Fermi level is expected to lie in the band tails, so that a better approximation of the density of states (DOS) is an exponential decay distribution.
For (p)*a*-Si:H layers considered infinitely thick, an analytical solution can be found provided that the Fermi-Dirac occupation function is approximated by a step function. This is a priori justified because the temperature T remains lower than the valence band tail parameter ($T_v \geq 500$ K).

The DOS can be written as:

$$N(E) = N_0 \exp\left(-\frac{E - E_v}{k_B T_v}\right). \tag{A.4}$$

where N_0 is a pre-exponential factor. Eq. 3.34 can be integrated to give the charge density $\rho(x)$:

$$\rho(x) = qN(E_F) k_B T_v \left(\exp\left(q\frac{V(-\infty) - V(x)}{k_B T_v}\right) - 1\right). \tag{A.5}$$

Finally, the charge in *a*-Si:H takes the expression:

$$Q^2_{a-Si:H} = 2\epsilon qN(E_F) k_B T_v \left[\frac{k_B T_v}{q}\left(\exp\left(q\frac{V(-\infty) - V(0)}{k_B T_v}\right) - 1\right) - (V(-\infty) - V(0))\right]. \tag{A.6}$$

No analytical expression can be found for lower thicknesses, where the *a*-Si:H surface plays a significant role.
Moreover, after a thorough comparison study with the AFORS-HET software, it has been found that the approximation of constant DOS + step occupation function is in better agreement with the numerical calculations than the exponential DOS + step occupation function approximation. This is due to the fact that the band bending in *a*-Si:H remains of the same order of magnitude as $k_B T$ (≈ 25 meV): variations of both the DOS and the occupation function play a role in the calculation of the charge. For that reason the thesis is based on the constant DOS approximation even if it appears rough at first sight.

B

Appendix B: Details on tunneling current calculation

B.1 Tunneling probability

Details on the calculation of the tunneling probability given in section 5.2.1.2 are now given. The derivation can be found in any quantum physics textbook, for instance [Cohen-Tannoudji 73]; it is also detailed in [Clerc 01]. Equations are based on Fig. 5.1. Firstly, the case of an energy greater than the barrier height is considered: $E > E_{\max}$. In the three regions, propagating wavefunctions are solutions of Schrödinger's equation:

$$\Phi_1(x) = Ae^{ik_1} + Be^{-ik_1} \tag{B.1}$$

$$\Phi_{ox}(x) = Ce^{iK} + De^{-iK} \tag{B.2}$$

$$\Phi_2(x) = Ee^{ik_2} + Fe^{-ik_2}, \tag{B.3}$$

with $k_1 = \sqrt{\frac{2m}{\hbar^2}(E - E_{\min})}$, $K = \sqrt{\frac{2M}{\hbar^2}(E - E_{\max})}$ and $k_2 = \sqrt{\frac{2m}{\hbar^2}(E - E_{\min} - \Delta E_c)}$ are the wavevectors in each region. It is assumed that the effective mass is the same in regions 1 and 2: $m_1 = m_2 = m$. The effective mass in the insulator is M. Considering an electron coming from far in region 1 ($x \to -\infty$), F can be taken equal to 0 without loss of generality. Linking

conditions of the wavefunctions and their derivatives at $x = 0$ and $x = d_{ox}$ lead to an expression of A as a function E:

$$A = \frac{1}{2}\frac{k_1 + k_2}{k_1} e^{ik_2 d} \left\{ \cos(K d_{ox}) - i \frac{K^2 + k_1 k_2}{K(k_1 + k_2)} \sin^2(K d_{ox}) \right\} E. \tag{B.4}$$

The transmission of the barrier $\mathscr{T}$ is defined as the ratio between the probability current of the transmitted wave, $J_t = \frac{\hbar k_2}{m} |E|^2$ with the probability current of the incident wave, $J_i = \frac{\hbar k_1}{m} |A|^2$:

$$\mathscr{T} = \frac{J_t}{J_i} = \frac{k_2}{k_1} \frac{|E|^2}{|A|^2}. \tag{B.5}$$

Thus, from Eq. B.4:

$$\mathscr{T} = \frac{4K^2 k_1 k_2}{K^2(k_1 + k_2)^2 + (K^2 - k_1^2)(K^2 - k_2^2)\sin^2(K d_{ox})} \text{ for } E \geq E_{max}. \tag{B.6}$$

For $E < E_{max}$, no propagating wave solution exists inside the barrier (region 2); instead, solutions of Schrödinger's equation have an evanescent wave form, such that K in Eq. B.3 has to be replaced by $-iK$ with $K = \sqrt{\frac{2M}{\hbar^2}(E_{max} - E)}$. The same derivation for $\mathscr{T}$ leads to:

$$\mathscr{T} = \frac{4K^2 k_1 k_2}{K^2(k_1 + k_2)^2 + (K^2 + k_1^2)(K^2 + k_2^2)\sinh^2(K d_{ox})} \text{ for } E \leq E_{max}. \tag{B.7}$$

B.2 Supply function N

As used in the Tsu-Esaki formula, the supply function N reads:

$$N(E_x) = \int_0^{+\infty} \left(f_1(E) - f_2(E) \right) dE_{//}, \tag{B.8}$$

where f_i ($i = 1$ or 2) is the Fermi-Dirac occupation function for electrons in region i. The total energy E is split into the perpendicular (to the interface) component E_x and the parallel component $E_{//}$, such that $E = E_x + E_{//}$.
For $E_{min} - E_F \gg k_B T$, the Fermi-Dirac distribution can be approximated by a Maxwell-Boltzmann distribution: $f_i(E) = \exp\left(\frac{E_{F,i} - E}{k_B T}\right)$.
The integration in Eq. B.8 over the parallel component of the energy (that is assumed to be

unchanged when the electron tunnels) leads to the expression for the supply function:

$$N(E_x) = k_B T \left(e^{-\frac{E_x - E_{F,1}}{k_B T}} - e^{-\frac{E_x - E_{F,2}}{k_B T}} \right). \tag{B.9}$$

For convenience, $E = E_x$ is used in the following.

B.3 AFORS-HET configuration

Fig. B.1 is a screen-shot of the AFORS-HET configuration window showing the options to activate tunneling through a barrier: 'd' is the thickness, 'chi' is the electronic affinity (useful to adjust the conduction band barrier height), 'Eg' is the gap (required to adjust the valence band barrier height), 'me' and 'mh' are the relative electron and hole effective masses inside the barrier.

Appendix B. Appendix B: Details on tunneling current calculation

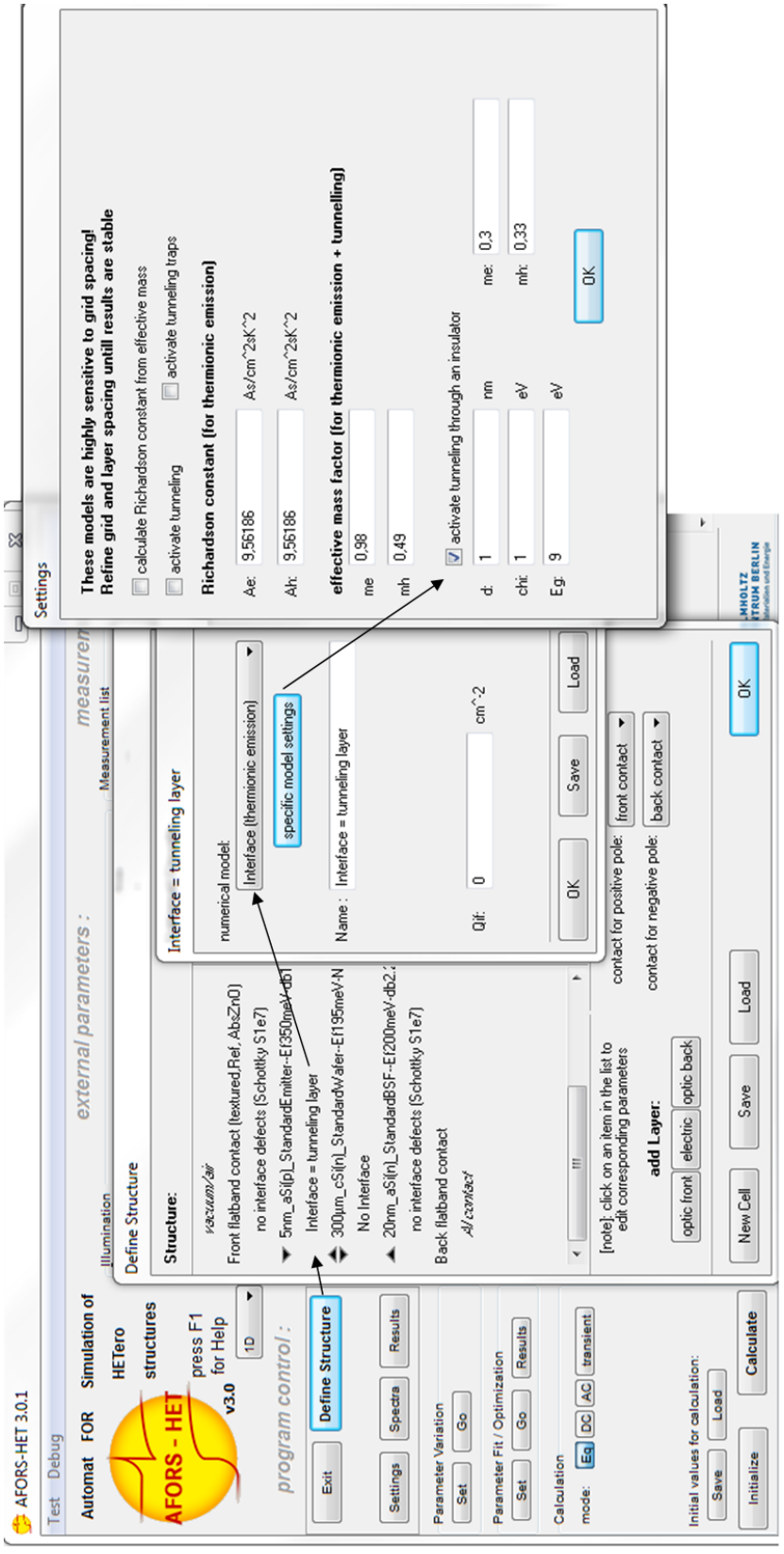

Figure B.1: Configuration of AFORSHET to activate tunneling through a barrier.

Bibliography

[Aberle 92] Armin G. Aberle, Stefan Glunz & Wilhelm Warta. *Impact of illumination level and oxide parameters on Shockley–Read–Hall recombination at the Si-SiO2 interface.* J. App. Phys., vol. 71, no. 9, pages 4422–4431, May 1992.

[Adachi 99] S. Adachi. Optical constants of crystalline and amorphous semiconductors - numerical data and graphical information. Kluwer Academic Publ., Boston, 1999.

[Alex 96] V. Alex, S. Finkbeiner & J. Weber. *Temperature dependence of the indirect energy gap in crystalline silcon.* J. App. Phys., vol. 79, page 6943, 1996.

[Aljishi 90] S. Aljishi, J. D. Cohen, S. Jin & L. Ley. *Band tails in hydrogenated amorphous silicon and silicon-germanium alloys.* Phys. Rev. Lett., vol. 64, pages 2811–4, 1990.

[Anderson 62] R. L. Anderson. *Experiments on Ge-GaAs Heterojunctions.* Solid State Electron., vol. 5, pages 341–51, 1962.

[Angermann 97] H. Angermann, W. Henrion, M. Rebien, J. T. Zettler & A. Roeseler. *Characterization of chemically prepared Si-surfaces by UV-VIS and IR spectroscopic ellipsometry and surface photovoltage.* Surf. Sci., vol. 388, pages 15–23, 1997.

[Angermann 04] H. Angermann, W. Henrion, M. Rebien & A. Roeseler. *Wet-chemical passivation and characterization of silicon interfaces for solar cell applications.* Sol. Energ. Mat. Sol. C., vol. 83, pages 331–46, 2004.

[Angermann 09] H. Angermann, E. Conrad, L. Korte, J. Rappich, T.F. Schulze & M. Schmidt. *Passivation of textured substrates for a-Si:H/c-Si heterojunction solar cells: Effect of wet-chemical smoothing and intrinsic a-Si:H interlayer.* vol. 159-160, pages 219–223, 2009.

[B. Brar 96] G.D. Wilk B. Brar & A.C. Seabaugh. Appl. Phys. Lett., vol. 69, page 2728, 1996.

[Bachmann 68] R. Bachmann. Physik Kondens. Materie, vol. 8, page 31, 1968.

[Bahardoust 10] Barzin Bahardoust, Alongkarn Chutinan, Keith Leong, Adel B. Gougam, Davit Yeghikyan, Tome Kosteski, Nazir P. Kherani & Stefan Zukotynski. *Passivation study of the amorphous-crystalline silicon interface formed using DC saddle-field glow discharge.* Phys. Status Solidi A, vol. 207, pages 539–543, 2010.

[Balasubramanian 91] N. Balasubramanian & A. Subrahmanyam. *Studies on Evaporated Indium Tin Oxide (ITO)/Silicon Junctions and an Estimation of ITO Work Function.* J.Electrochem. Soc., vol. 138, no. 1, pages 322–324, 1991.

[Beck 01] R.B. Beck, A. Jakubowski, L. Lukasiak & M. Korwin-Pawlowski. *Challenges in ultrathin oxide layers formation.* Journal of Telecommunications and Information Technology, pages 27–34, 2001.

[Boehme 06] C. Boehme, J. Behrend, K. v. Maydell, M. Schmidt & K. Lips. *Investigation of hopping transport in n-a-Si:H/c-Si solar cells with pulsed electrically detected magnetic resonance.* J. Non-Cryst. Sol., vol. 352, pages 1113–6, 2006.

[Boogaard 09] A. Boogaard, A.Y. Kovalgin & R.A.M. Wolters. *Net negative charge in low-temperature SiO2 gate dielectrics layers.* Microelectronic Eng., vol. 86, pages 1707–1710, 2009.

[Bothe 05] K. Bothe, R. Sinton & J. Schmidt. *Fundamental boron oxygen related carrier lifetime limit in mono and multicrystalline silicon.* Prog. Photovoltaics, vol. 13, pages 287–296, 2005.

[Brendel 95] R. Brendel. *Note on the interpretation of injection-level-dependent surface recombination velocities.* Appl. Phys. A - Mater., vol. 60, pages 523–524, 1995.

[Brody 03] J. Brody, A. Rohatgi & A. Ristow. *Review and comparison of equations relating bulk lifetime and surface recombination velocity to effective lifetime measured under flash lamp illumination.* Sol. Energ. Mat. Sol. C., vol. 77, pages 293–301, 2003.

[Brueggemann 06] R. Brueggemann & S. Reynolds. *Modulated photoluminescence studies for lifetime determination in amorphous-silicon passivated crystalline-silicon wafers.* J. Non-Cryst. Sol., vol. 352, pages 1888–1891, 2006.

[Burkhard 10] G. F. Burkhard, E. T. Hoke & M. D. McGehee. *Accounting for Interference, Scattering, and Electrode Absorption to Make Accurate Internal Quantum Efficiency Measurements in Organic and Other Thin Solar Cells.* Adv. Mater., vol. 22, page 3293, 2010.

[Centurioni 03] E. Centurioni & D. Iencinella. *Role of front contact work function on amorphous silicon/crystalline silicon heterojunction solar cell performance.* IEEE Electr. Device L., vol. 24, no. 3, pages 177 – 179, mar. 2003.

[Chacorn 88] V. Chacorn & D. Haneman. *Thickness and doping dependence of the optical gap in amorphous hydrogenated silicon films.* Solid State Commun., vol. 65, pages 609–11, 1988.

[Clerc 01] R. Clerc. *Etude des effets quantiques dans les composants CMOS à oxydes de grille ultra minces - modélisation et caractérisation.* PhD thesis, INPG Grenoble, 2001.

[Cohen-Tannoudji 73] C. Cohen-Tannoudji, B. Diu & F. Laloë. Mécanique quantique. Hermann, 1973.

[Cuevas 96] A. Cuevas, R.A. Sinton & M. Stuckings. *Determination of Recombination Parameters in Semiconductors from Photoconductance Measurements.* In Optoelectronic and Microelectronic Materials and Devices Proceedings, 1996.

[Cuniot 85] M. Cuniot & Y. Marfaing. *Study of the band discontinuities at the a-Si:H/c-Si interface by internal photoemission.* J. Non-Cryst. Sol., vol. 77-78, no. Part 2, pages 987–990, December 1985.

[Cuniot 88] M. Cuniot & Y. Marfaing. *Energy-Band Diagram of the a-Si:H/c-Si Interface as Determined by Internal Photoemission.* Philos. Mag. B, vol. 57, pages 291–300, 1988.

[Dabrowski 00] J. Dabrowski & H.J.Muessig. Silicon surfaces and formation of interfaces. World Scientific Publishing Co. Pte. Ltd., 2000.

[de Wolf 09] Stefaan de Wolf & Michio Kondo. *Nature of doped a-Si:H/c-Si interface recombination.* J. App. Phys., vol. 105, no. 10, page 103707, 2009.

[Deb 62] S. Deb & B. R. Nag. *Measurement of Lifetime of Carriers in Semiconductors through Microwave Reflection.* J. App. Phys., vol. 3, page 1604, 1962.

[Descoeudres 11] A. Descoeudres, L. Barraud, P. Bôle Rothen, S. De Wolf, B. Demaurex, J. Geissbuehler, Z.C. Holman, J. Seif, F. Zicarelli & C. Ballif. Technical Digest 21rst International Photovoltaic Science and Engineering Conference (Fukuoka, Japan), vol. 3A-1O-02, pages 3A–1O–02, 2011.

[Devine 87] R. A. B. Devine & J. Arndt. *Si-O bond-length modification in pressure-densified amorphous SiO2.* Phys. Rev. B, vol. 35, pages 9376–9379, Jun 1987.

[DiStefano 71] T. H. DiStefano & D.E. Eastman. *Photoemission Measurements of the Valence Levels of Amorphous SiO2.* Phys. Rev. Lett., vol. 27, pages 1560–1562, Dec 1971.

[EPIA 11a] EPIA. *Solar generation 6: Solar Photovoltaic Electricity Empowering the World.* http://www.epia.org/publications/epiapublications, pages (accessed August, 1rst, 2012), 2011.

[EPIA 11b] EPIA. *Solar photovoltaic: competing in the energy sector.* http://www.epia.org/publications/epiapublications, pages (accessed August, 1rst, 2012), 2011.

[EPIA 12] EPIA. *Global market outlook for photovoltaics until 2016.* http://www.epia.org/publications/epiapublications, pages (accessed September, 18th, 2012), 2012.

[Eschrich 93] H. Eschrich, J. Bruns, L. Elstner & C. Swiatkowski. *The Dependence of a-Si:H/c-Si Solar Cell Generator and Spectral Response Characteristics on Heterojunction Band Discontinuities.* J. Non-Cryst. Sol., vol. 164-166, pages 717–20, 1993.

[Essick 89] J.M. Essick & J.D. Cohen. *Band offsets and deep defect distribution in hydrogenated amorphous silicon-crystalline silicon heterostructures.* Appl. Phys. Lett., vol. 55, pages 1232–4, 1989.

[Essick 96] J.M. Essick, Z. Nobel, Y.M. Li & M.S. Bennett. *Conduction- and valence-band offsets at the hydrogenated amorphous silicon-carbon/crystalline silicon interface via capacitance techniques.* Phys. Rev. B, vol. 54, page 4885, 1996.

[Favre 10] W. Favre, M. Labrune, F. Dadouche, A. S. Gudovskikh, P. Roca i Cabarrocas & J.-P. Kleider. *Study of the interfacial properties of amorphous*

silicon/n-type crystalline silicon heterojunction through static planar conductance measurements. Phys. Status Solidi C, vol. 7, pages 1037–1040, 2010.

[Favre 11] W. Favre. *Silicium de type n pour cellules á hétérojonctions : caractérisations et modélisations.* PhD thesis, Universitè Paris-Sud 11, 2011.

[Fischetti 95] M.V. Fischetti, S.E. Laux & E. Crabb. *Understanding hot-electron transport in silicon devices: is there a shortcut?* J. Appl. Phys., vol. 78, pages 1058–1085, 1995.

[Flores 89] F. Flores, A. Munoz & J.C. Duran. *Semiconductor interface formation: The role of the induced density of interface states.* Appl. Surf. Sci., vol. 41-42, pages 144–150, November 1989.

[Frankl 67] D. R. Frankl. Electrical properties of semiconductor surfaces. Pergamon Press, Oxford, 1967.

[Franz 56] W. Franz. Handbuch der physik. Springer, Berlin, 1956.

[Froitzheim 03] A. M. Froitzheim, M. L. D. Scherff, A. Ulyashin, O. Milch, M. Schmidt, W. R. Fahrner & W. Fuhs. *AFORS-HET: A Computer-program For The Simulation Of Heterojunction Solar Cells To Be Distributed For Public Use.* In K. Kurokawa et al., editeur, Proceedings of the 3rd World Conference on Photovoltaic Energy Conversion, pages 1P–D3–34, Osaka, Japan, 2003.

[Fuhs 06] W. Fuhs, L. Korte & M. Schmidt. *Heterojunctions of hydrogenated amorphous silicon and monocrystalline silicon.* J. Optoelectron. Adv. Mat., vol. 8, pages 1989–95, 2006.

[Gale 07] G. W. Gale, R. J. Small & K.A. Reinhardt. Aqueous cleaning and surface conditioning. William Andrew Publishing, 2007.

[Gall 95] S. Gall, R. Hirschauer & D. Brauenig. *Admittance measurements at a-Si:H/c-Si heterojunction devices.* In Proceedings of the 13th European Photovoltaic Solar Energy Conference, pages 1264–1267, Nice, France, 1995.

[Gall 97] S. Gall, R. Hirschauer, M. Kolter & D. Brauenig. *Spectral characteristics of a-Si:H/c-Si heterostructures.* Sol. Energ. Mat. Sol. C., vol. 49, no. 1-4, pages 157–162, December 1997.

[Garin 05] M. Garin, U. Rau, W. Brendle, I. Martin & R. Alcubilla. *Characterization of a-Si:H/c-Si interfaces by effective-lifetime measurements.* J. Appl. Phys., vol. 98, no. 9, pages 093711–9, November 2005.

[Gehring 03] Andreas Gehring. *Simulation of tunneling in semiconductor devices.* PhD thesis, University of Vienna, Austria, 2003.

[Gobeli 62] G. W. Gobeli & F. G. Allen. *Direct and Indirect Excitation Processes in Photoelectric Emission from Silicon.* Phys. Rev., vol. 127, pages 141–49, 1962.

[Goodman 66] A. M. Goodman & J. J. O'Neill. *Photoemission of Electrons from Metals into Silicon Dioxide.* J. Appl. Phys., vol. 37, page 3580, 1966.

[Green 74] M.A. Green, F.D. King & J. Shewchun. *Minority carrier MIS tunnel diodes and their application to electron- and photo-voltaic energy conversion–I. Theory.* Solid State Electron., vol. 17, no. 6, pages 551–561, June 1974.

[Green 90] M.A. Green. *Intrinsic concentration, effective densities of states, and effective mass in silicon.* J. App. Phys., vol. 67, page 2944, 1990.

[Green 95] Martin A. Green & Mark J. Keevers. *Optical properties of intrinsic silicon at 300 K.* Prog. Photovoltaics, vol. 3, no. 3, pages 189–192, 1995.

[Hahneiser 99] Olaf Hahneiser & Marinus Kunst. *Theoretical and experimental study of charge carrier kinetics in crystalline silicon.* J. Appl. Phys., vol. 85, pages 7741–7754, 1999.

[Hallio 12] B. Hallio, M.F. Salaun, W. Favre, R. Varache, M.E. Gueunier-Farret, J.P. Kleider & N.P. Kherani. *Interface properties of amorphous-crystalline silicon heterojunctions prepared using DC saddle-field PECVD.* J. Non-Cryst. Sol., vol. 358, pages 2227–2231, 2012.

[Hamakawa 83] Y. Hamakawa, K. Fujimoto, K. Okuda, Y. Kashima, S. Nonomura & H. Okamoto. *New types of high efficiency solar cells based on a-Si.* Appl. Phys. Lett., vol. 43, page 644, 1983.

[Heilig 74] K. Heilig. *Determination of Surface Properties by Means of Large Signal Photovoltage Pulses and the Influence of Trapping.* Surf. Sci., vol. 44, pages 421–37, 1974.

[Hernandez 96] M. J. Hernandez, J. Garrido, J. Martinez & J. Piqueras. *Electrical properties of electron cyclotron resonance plasma-deposited silicon dioxide: effect of the oxygen to silane flow ratio.* Semicond. Sci. Tech., vol. 11, pages 422–426, 1996.

[Hernandez 11] J. L. Hernandez, K. Yoshikawa, A. Feltrin, N. Menou, N. Valckx, E. Van Assche, J. Poortmans, D. Adachi, M. Yoshimi, T. Uto, H. Uzu, T. Kuchiyama, C. Allebe, N. Nakanishi, T. Terashita, T. Fujimoto, G. Koizumi & K. Yamamoto. Technical Digest 21rst International Photovoltaic Science and Engineering Conference (Fukuoka, Japan), pages 3A–1O–05, 2011.

[Herrmann 95] M. Herrmann & A. Schenk. *Field and high temperature dependence of the long term charge loss in erasable programmable read only memories: measurements and modeling.* J. App. Phys., vol. 77, pages 4522–4540, 1995.

[Hezel 97] Rudolf Hezel. *Recent progress in MIS solar cells.* Prog. Photovoltaics, vol. 5, no. 2, pages 109–120, 1997.

[Holman 12] Z.C. Holman, A. Descoeudres, L. Barraud, F.Z. Fernandez, J.P. Seif, S. De Wolf & C. Ballif. *Current Losses at the Front of Silicon Heterojunction Solar Cells.* IEEE J. Photovoltaics, vol. 2, no. 1, pages 7 –15, jan. 2012.

[Istratov 99] A.A. Istratov, H. Hieslmair & E.R. Weber. *Iron and its complex in silicon.* Appl. Phys. A - Mater., vol. 69, pages 13–44, 1999.

[Jacoboni 77] C. Jacoboni, C. Canali, G. Ottaviani & A. Quaranta. Solid State Electron., vol. 20, page 77, 1977.

[Jaramillo 11] Rafael Jaramillo & Shriram Ramanathan. *Kelvin force microscopy studies of work function of transparent conducting ZnO:Al electrodes synthesized under varying oxygen pressures.* Sol. Energ. Mat. Sol. C., vol. 95, no. 2, pages 602 – 605, 2011.

[Jensen 00] N. Jensen, U. Rau, R. M. Hausner, S. Uppal, L. Oberbeck, R. B. Bergmann & J. H. Werner. *Recombination mechanisms in amorphous silicon/crystalline silicon heterojunction solar cells.* J. App. Phys., vol. 87, no. 5, pages 2639–2645, March 2000.

[Jiang 03] X. Jiang, F. L. Wong, M. K. Fung & S. T. Lee. *Aluminum-doped zinc oxide films as transparent conductive electrode for organic light-emitting devices.* Appl. Phys. Lett., vol. 83, no. 9, pages 1875–1877, 2003.

[Kerr 02] Mark J. Kerr & Andres Cuevas. *General parameterization of Auger recombination in crystalline silicon.* J. App. Phys., vol. 91, no. 4, pages 2473–2480, February 2002.

[Kevkic 10] T.S. Kevkic & D.M. Petkovic. Proceedings of the 27th International Conference on Microelectronics, pages 115–118, 2010.

[Kinoshita 11] T. Kinoshita, D. Fujishima, A. Yano, A. Ogane, S. Tohoda, K. Matsuyama, Y. Nakamura, N. Tokuoka, H. Kanno, H. Sakata, M. Taguchi & E. Maruyama. *The approachesfor high efficiency HIT solar cell with very thin (<100mm) silicon wafer over 23%.* Proceedings of the 26th European Photovoltaic Solar Energy Conference, pages 871–874, 2011.

[Kleefstra 80] M. Kleefstra & G.C. Herman. J. App. Phys., vol. 51, page 4923, 1980.

[Kleider 08] J. P. Kleider, A. S. Gudovskikh & P. Roca i Cabarrocas. *Determination of the conduction band offset between hydrogenated amorphous silicon and crystalline silicon from surface inversion layer conductance measurements.* Appl. Phys. Lett., vol. 92, no. 16, page 162101, 2008.

[Kliefoth 00] K. Kliefoth, P. Kanschat, W. Fuessel, F.Fenske, H. Angermann, L. Elstner & W. Fuhs. *MIS Back Contact for Crystalline Silicon Solar Cells.* In Proceedings of the 16th European Photovoltaic Solar Energy Conference, pages 1005–8, 2000.

[Kliefoth 03] K. Kliefoth. *Der SPV-Messplatz.* Arbeitsbericht, 2003.

[König 07] D. König, M. Rennau & M. Henker. *Direct tunneling effective mass of electrons determined by intrinsic charge-up process.* Solid State Electron., vol. 51, no. 5, pages 650 – 654, 2007.

[Korte 06a] L. Korte. *Die elektronische Struktur des amorph-kristallinen Silizium-Heterostruktur-Kontakts.* PhD thesis, Philipps-Universität Marburg, 2006.

[Korte 06b] L. Korte, A. Laades & M. Schmidt. *Electronic states in a-Si:H/c-Si heterostructures.* J. Non-Cryst. Sol., vol. 352, pages 1217–20, 2006.

[Korte 09] L. Korte, A. Laades, K. Lauer, R. Stangl, D. Schaffarzik & M. Schmidt. *Surface photovoltage investigation of recombination at the a-Si/c-Si heterojunction.* Thin Solid Films, vol. 517, pages 6396–400, 2009.

[Korte 11a] L. Korte & M. Schmidt. *Doping type and thickness dependence of band offsets at the amorphous/crystalline silicon heterojunction.* J. App. Phys., vol. 109, pages 063714–1–6, 2011.

[Korte 11b] L. Korte, T. F. Schulze, C. Leendertz, M. Schmidt & B. Rech. *Band alignment at amorphous/crystalline silicon hetero-interfaces.* In MRS Symp Proceedings, volume 1321, 2011.

[Kriegel 03] M. Kriegel, T. Geipel & R. Stangl. *AFORS-HET developer's guide.* Rapport technique, HZB, 2003.

[Kronik 99] L. Kronik & Y. Shapira. *Surface Photovoltage Phenomena: Theory, Experiment, and Applications.* Surf. Sci. Rep., vol. 37, pages 5–206, 1999.

[Lam 71] Y. W. Lam. *Surface-State Density and Surface Potential in MIS Capacitors by Surface Photovoltage Measurements.* J. Phys. D Appl. Phys., vol. 4, pages 1370–75, 1971.

[Lee 12] Y. Lee, W. Oh, V. Ai Dao, S. Q. Hussain & J. Yi. *Ultrathin Oxide Passivation Layer by Rapid Thermal Oxidation for the Silicon Heterojunction Solar Cell Applications.* Int. J. Photoenergy, vol. 2012, 2012.

[Leendertz 10a] C. Leendertz, N. Mingirulli, T. F. Schulze, J. P. Kleider, B. Rech & L. Korte. *Physical Insight into Interface Passivation of a-Si:H/c-Si Heterostructures by Analysis of Injection-dependent Lifetime and Band Bending.* In Proceedings of the 25th European Photovoltaic Solar Energy Conference, 6-10 September 2010, Valencia, Spain, pages 1377–1381. WIP Munich, 2010.

[Leendertz 10b] C. Leendertz, R. Stangl, T. F. Schulze, M. Schmidt & L. Korte. *A recombination model for a-Si:H/c-Si heterostructures.* Phys. status solidi C, vol. 7, pages 1005–10, 2010.

[Leendertz 11a] C. Leendertz. *Effizienzlimitierende Rekombinationsprozesse in amorph/kristallinen und polykristallinen Siliziumsolarzellen.* PhD thesis, Technische Universitaet Berlin, 2011.

[Leendertz 11b] C. Leendertz, N. Mingirulli, T. F. Schulze, J. P. Kleider, B. Rech & L. Korte. *Discerning passivation mechanisms at a Si:H/c Si interfaces by means of photoconductance measurements.* Appl. Phys. Lett., vol. 98, page 202108, 2011.

[Lequeux 89] N Lequeux & M Cuniot. *Internal photoemission measurements on a - Si1-xGex : H/c - Si heterojunctions.* J. Non-Cryst. Sol., vol. 114, no. Part 2, pages 555–557, December 1989.

[L.F. Register 99] E. Rosenbaum L.F. Register & K. Yang. Appl. Phys. Lett., vol. 74, page 457, 1999.

[Li 08] Tsu-Tsung Andrew Li, Keith R. McIntosh & Andres Cuevas. *Limitations of a simplified dangling bond recombination model for a-Si:H.* J. Appl. Phys., vol. 104, page 113718, 2008.

[Mada 79] Yoichi Mada. *A nondestructive method for measuring the spatial distribution of minority carrier lifetime in silicon wafers.* Jpn. J. Appl. Phys., vol. 18, pages 2171–2172, 1979.

[Malitson 65] I.H. Malitson. *Interspecimen comparison of the refractive index of fused silica.* J. Opt. Soc. Am., vol. 55, pages 1205–1208, 1965.

[Martin De Nicolas 12] S. Martin De Nicolas. PhD thesis, Université Paris-Sud 11 (CEA-INES), 2012.

[Masaki 91] K. Masaki, K. Taniguchi, C. Hamaguchi & M. Iwase. Jpn. J. Appl. Phys., vol. 30, page 2734, 1991.

[Maslova 10] O. A. Maslova, J. Alvarez, E. V. Gushina, W. Favre, M. E. Gueunier-Farret, A. S. Gudovskikh, A. V. Ankudinov, E. I. Terukov & J.-P. Kleider. *Observation by conductive-probe atomic force microscopy of strongly inverted surface layers at the hydrogenated amorphous silicon/crystalline silicon heterojunctions.* Appl. Phys. Lett., vol. 97, page 252110, 2010.

[Mathieu 09] H. Mathieu & H. Fanet. Physique des semiconducteurs et des composants électroniques. Dunod, 2009.

[Matsuura 84] H. Matsuura, T. Okuno, H. Okushi & K. Tanaka. *Electrical properties of n-amorphous/p-crystalline silicon heterojunctions.* J. Appl. Phys., vol. 55, pages 1012–9, 1984.

[Matsuura 89] H. Matsuura. *Hydrogenated amorp silcon /crystalline silicon heterojunction: properties and applications.* IEEE T. Electron. Dev., vol. 36, pages 2908–2914, 1989.

[Meaudre 91] M. Meaudre, P. Jensen & R. Meaudre. Philos. Mag. B., vol. 63, page 815, 1991.

[Mimura 87] Hidenori Mimura & Yoshinori Hatanaka. *Energy-band discontinuities in a heterojunction of amorphous hydrogenated Si and crystalline Si measured by internal photoemission.* Appl. Phys. Lett., vol. 50, no. 6, page 326, 1987.

[Moench 81] W. Moench, R. Enninghorst & H.J. Clemens. Surf. Sci., vol. 102, page L54, 1981.

[Moench 01] W. Moench. Semiconductor surfaces and interfaces. Springer, 2001.

[Mueller 08] T. Mueller, S. Schwertheim, M. Scherff & W.R. Fahrner. *High quality passivation for heterojunction solar cells by hydrogenated amorphous silicon suboxide films.* Appl. Phys. Lett., vol. 92, page 033504, 2008.

[Munoz 11] D. Munoz, T. Desrues, A. S. Ozanne, N. Nguyen, S. de Vecchi, F. Souche, S.Martin de Nicolàs, C. Denis & P. J. Ribeyron. Proceedings of the 26th European Photovoltaic Solar Energy Conference and Exhibition, page 861, 2011.

[Nagel 99] H. Nagel, C. Berge & A. Aberle. *Generalized analysis of quasi-steady-state and quasi-transient measurements of carrier lifetimes in semiconductors.* J. App. Phys., vol. 86, pages 6218–6221, 1999.

[Northrup 89] J.E. Northrup. *Effective correlation energy of a-Si:H dangling bond calculated with the local-spin-density approximation.* Phys. Rev. B, vol. 40, pages 5875–5878, 1989.

[Okamoto 77] H. Okamoto & Y. Hamakawa. *Electronic behaviors of the gap states in amorphous semiconductors.* Solid State Commun., vol. 24, page 23, 1977.

[Okuda 83] K. Okuda, H. Okamoto & Y. Hamakawa. *Amorphous Si/Polycrystalline Si Stacked Solar Cell Having More Than 12% Conversion Efficiency.* Jpn. J. Appl. Phys., vol. 22, pages L605–7, 1983.

[Olibet 07] S. Olibet, E. Vallat-Sauvain & C. Ballif. *Model for a-Si:H/c-Si interface recombination based on the amphoteric nature of silicon dangling bonds.* Phys. Rev. B, vol. 76, page 35326, 2007.

[Park 96] Y. Park, V. Choong, Y. Gao, B. R. Hsieh & C. W. Tang. *Work function of indium tin oxide transparent conductor measured by photoelectron spectroscopy.* Appl. Phys. Lett., vol. 68, no. 19, pages 2699–2701, 1996.

[Pettersson 99] L.A.A. Pettersson, L.S. Roman & O. Inganas. J. App. Phys., vol. 86, page 487, 1999.

[Peumans 03] P. Peumans, A. Yakimov & S. Forrest. J. App. Phys., vol. 93, page 3693, 2003.

[Powell 93] M. J. Powell & S. C. Deane. *Improved Defect-Pool Model for Charged Defects in Amorphous Silicon.* Phys. Rev. B, vol. 48, pages 10815–27, 1993.

[Powell 96] M. J. Powell & S. C. Deane. *Defect-pool model and the hydrogen density of states in hydrogenated amorphous silicon.* Phys. Rev. B, vol. 53, pages 10121–32, 1996.

[Price 83] P.J. Price & F. Stern. Surf. Sci., vol. 132, page 577, 1983.

[Pun 00] Ooi Chee Pun. *A Quasi-Static Technique for CV Measurement of a MOS Capacitor.* In EEC 2000 Proceedings, 2000.

[Rhoderick 88] E. H. Rhoderick & R. H. Williams. Metal-semiconductor contacts. 1988.

[Ribeyron 11] P.-J. Ribeyron, D. Munoz, J.-P. Kleider, Wilfried Favre, P. Roca i Cabarrocas, M. Labrune, B. Geerligs, A. Weeber, M. Spaeth, C. Olson, N. Dekker, G.J.H.M. van Sark, J.A. Schuetauf, J.K. Rath, R.E.I. Schropp, M. Tucci, S. De Iullis, I. Gordon, B. O'Sullivan, A. Descoeudres, S. De Wolf, C.Ballif, T. Schulze, L. Korte, F. Madon, N. Le Quang, M. Scherff, R. Doll, Y. Zemen & G. Zietek. *European Record Efficiency Amorphous-Crystalline-Silicon Heterojunction Solar Cells: Final Results from the HETSI Project.* In Proceedings of the 26th European Photovoltaic Solar Energy Conference, page 853. WIP, Munic, 2011.

[Roedern 94] B. v. Roedern. In Proceedings of the 12th EU-PVSEC, 1994.

[Roelver 08] R. Roelver, B. Berghoff, D. Buetzner, B. Spangenberg, H. Kurz, M. Schmidt & B. Stegemann. *Si/SiO2 multiple quantum wells for all silicon tandem cells: Conductivity and photocurrent measurements.* Thin Solid Films, vol. 516, pages 6763–6, 2008.

[Roesch 98] M. Roesch, R. Brueggemann & G.H. Bauer. *Influence of interface defects on the current-voltage characteristics of amorphous silicon/crystalline silicon heterojunction solar cells.* In Proceedings of the 2nd World Conference on Phtovoltaic Solar Energy Conversion, pages 964–967, 1998.

[Sakata 04] I. Sakata, M. Yamanaka & R. Shimokawa. *Band Lineup at the Interface Between Boron-Doped P-Type Hydrogenated Amorphous Silicon and Crystalline Silicon Studied by Internal Photoemission.* Jpn. J. Appl. Phys., vol. 43, pages L954–L956, 2004.

[Sakata 09] Isao Sakata, Mitsuyuki Yamanaka & Hitoshi Kawanami. *Characterization of heterojunctions in crystalline-silicon-based solar cells by internal photoemission.* Sol. Energ. Mat. Sol. C., vol. 93, no. 6-7, pages 737–741, June 2009.

[Sasaki 01] Kimihiro Sasaki. *Fundamental properties of ECR plasma CVD and hydrogen-induced low temperature Si epitaxy.* Thin Solid Films, vol. 395, pages 225 – 229, 2001.

[Schiermeier 08] Q. Schiermeier, J. Tollefson, T. Scully, A. Witze & O. Morton. *Energy alternatives: Electricity without carbon.* Nature, vol. 454, page 816, 2008.

[Schmidt 99] J. Schmidt. *Measurement of differential and actual recombination parameters on crystalline silicon wafers.* IEEE T. Electron. Dev., vol. 46, pages 2018–2025, 1999.

[Schmidt 04] M. Schmidt, A. Schoepke, L. Korte, O. Milch & W. Fuhs. *Density Distribution of Gap States in Extremely Thin a-Si:H Layers on Crystalline Silicon Wafers.* J. Non-Cryst. Sol., vol. 338-340, pages 211–4, 2004. Konferenz-Beitrag zur ICAMS-20, Campos de Jordao, Brasilien.

[Schmidt 06] M. Schmidt, H. Angermann, E. Conrad, L. Korte, A. Laades, K. von Maydell, Ch. Schubert & R. Stangl. *Physical and Technological Aspects of a-Si:H/c-Si Hetero-Junction Solar Cells.* In Conference Record of the 4th IEEE World Conference on Photovoltaic Energy Conversion, pages 1433–8, 2006.

[Schmidt 07] M. Schmidt, L. Korte, A. Laades, R. Stangl, Ch. Schubert, H. Angermann, E. Conrad & K.v. Maydell. *Physical aspects of a-Si:H/c-Si heterojunction solar cells.* Thin Solid Films, vol. 515, pages 7475–80, 2007.

[Schulze 10a] T. F. Schulze, H. N. Beushausen, C. Leendertz, A. Dobrich, B. Rech & L. Korte. *Interplay of amorphous silicon disorder and hydrogen content with interface defects in amorphous/crystalline silicon heterojunctions.* Appl. Phys. Lett., vol. 96, no. 25, page 252102, 2010.

[Schulze 10b] T. F. Schulze, L. Korte, E. Conrad, M. Schmidt & B. Rech. *Electrical transport mechanisms in a-Si:H/c-Si heterojunction solar cells.* J. Appl. Phys., vol. 107, page 023711, 2010.

[Schulze 11a] T. Schulze. *Structural, electronic and transport properties of amorphous/crystalline silicon heterojunctions.* PhD thesis, Technische Universitaet Berlin, 2011.

[Schulze 11b] T. F. Schulze, F. Ruske, B. Rech & L. Korte. *Band lineup in amorphous/crystalline silicon heterojunctions and the impact of hydrogen microstructure and topological disorder.* Phys. Rev. B, vol. 18, page 165314, 2011.

[Schulze 11c] T.F. Schulze, C. Leendertz, N. Mingirulli, L. Korte & B. Rech. *Impact of Fermi-level dependent defect equilibration on Voc of amorphous/crystalline silicon heterojunction solar cells.* Energy Procedia, vol. 8, pages

282 – 287, 2011. Proceedings of the SiliconPV 2011 Conference (1st International Conference on Crystalline Silicon Photovoltaics).

[Schuurmans 04] F. M. Schuurmans, A. Schonecker, A. R. Burgers & W. C. Sinke. *Simplified evaluation method for light-biased effective lifetime measurements.* Appl. Phys. Lett., vol. 71, pages 1795–1797, 2004.

[Sebastiani 95] M. Sebastiani, L. Di Gaspare, G. Capellini, C. Bittencourt & F. Evangelisti. *Low-Energy Yield Spectroscopy as a Novel Technique for Determining Band Offsets: Application to the c-Si(100)/a-Si:H Heterostructure.* Phys. Rev. Lett., vol. 75, pages 3352–5, 1995.

[Shen 11] Chen Shen, Li-Tao Yang, Ganesh Samudra & Yee-Chia Yeo. *A new robust non-local algorithm for band-to-band tunneling simulation and its application to Tunnel-FET.* Solid State Electron., vol. 57, no. 1, pages 23 – 30, 2011.

[Shewchun 72] J. Shewchun & V. A. K. Temple. *Theoretical tunneling current characteristics of the SIS (semiconductor-insulator-semiconductor) diode.* J. App. Phys., vol. 43, page 5051, 1972.

[Shewchun 77] J. Shewchun, R. Singh & M. A. Green. *Theory of metal-insulator-semiconductor solar cells.* J. App. Phys., vol. 48, pages 765–770, February 1977.

[Shockley 52] W. Shockley & W. T. Read. *Statistics of the Recombinations of Holes and Electrons.* Phys. Rev., vol. 87, page 835, 1952.

[Sinton 96a] R. A. Sinton & A. Cuevas. *Contactless determination of current-voltage characteristics and minority-carrier lifetimes in semiconductors from quasi-steady-state photoconductance data.* Appl. Phys. Lett., vol. 69, page 2510, 1996.

[Sinton 96b] R.A. Sinton, A. Cuevas & M. Stuckings. *Quasi-steady-state photoconductance, a new method for solar cell material and device characterization.* In Conference Record of the Twenty Fifth IEEE Photovoltaic Specialists Conference, pages 457–460, 1996.

[Sologico 12] Sologico. *Preisbarometer.* www.sologico.com/priceindex/, pages (accessed September, 18th, 2012), 2012.

[Song 00] YJ Song, MR Park, E Guliants & WA Anderson. *Influence of defects and band offsets on carrier transport mechanisms in amorphous silicon/crystalline silicon heterojunction solar cells.* Sol. Energ. Mat. Sol. C., vol. 64, no. 3, pages 225–240, October 2000.

[Soukoulis 84] C. M. Soukoulis, M. H. Cohen & E. N. Economou. *Exponential band tails in random systems.* Phys. Rev. Lett., vol. 53, pages 616–9, 1984.

[Spear 75] W.E. Spear & P.G. Le Comber. *Substitutional doping of amorphous silicon.* Solid State Commun., vol. 88, page 1015, 1975.

[Staedele 03] M. Staedele, F. Sacconi, A. Di Carlo & P. Lugli. *Enhancement of the effective tunnel mass in ultrathin silicon dioxide layers.* J. App. Phys., vol. 93, page 2681, 2003.

[Stangl 01] R. Stangl, A. Froitzheim, L. Elstner & W. Fuhs. *Amorphous/crystalline silicon heterojunction solar cells, a simulation study.* In Proceedings of the 17th European Photovoltaic Solar Energy Conference, page 1383, October 2001.

[Stangl 03] R. Stangl, A. Froitzheim, M. Schmidt & W. Fuhs. *Design Criteria for Amorphous/Crystalline Silicon Heterojunction Solar Cells - a Simulation Study.* In K. Kurokawa et al., editeur, Proceedings of the 3rd World Conference on Photovoltaic Energy Conversion, pages 4P–A8–45, Osaka, Japan, 2003.

[Stangl 12] R. Stangl & C. Leendertz. Physics and technology of amorphous-crystalline heterostructure silicon solar cells, chapitre 13, pages 445 – 458. Springer, 2012.

[Stathis 93] J. H. Stathis, D. A. Buchanan, D. L. Quinlan, A. H. Parsons & D. E. Kotecki. *Interface defects of ultrathin rapid-thermal oxide on silicon.* Appl. Phys. Lett., vol. 62, page 2682, 1993.

[Stegemann 08] B. Stegemann, D. Sixtensson, T. Lussky, A. Schoepke, I. Didschuns, B. Rech & M. Schmidt. *Ultrathin SiO(2) layers on Si(111): preparation, interface gap states, and the influence of passivation.* Nanotechnology, vol. 19, page 424020, 2008.

[Steingrube 10] S. Steingrube, DS Steingrube, R. Brendel & PP Altermatt. *Comprehensive model for interface recombination at a-Si: H/c-Si interfaces based on amphoteric defects.* Phys. status solidi C, vol. 7, no. 2, pages 276–279, 2010.

[Steingrube 11] S. Steingrube. *Recombination models for defects in Silicon solar cells.* PhD thesis, Gottfried Wilhelm Leibniz Universitaet Hannover, 2011.

[Stern 67] F. Stern & W.E. Howard. Phys. Rev., vol. 163, page 816, 1967.

[Street 75] R.A. Street & N.F. Mott. *States in the gap in glassy semiconductors.* Phys. Rev. Lett., vol. 35, page 1293, 1975.

[Street 84] R.A. Street. *Disorder effects on deep trapping in amorphous semiconductors.* Philos. Mag. B., vol. 49, pages L15–L20, 1984.

[Street 91] R. A. Street. Hydrogenated amorphous silicon. Cambridge University Press, 1991.

[Stutzmann 89] M. Stutzmann. *The defect density in amorphous silicon.* Philos. Mag. B, vol. 60, pages 531–46, 1989.

[Sze 07] S. M. Sze & K. Ng Kwok. Physics of semiconductor devices. John Wiley & Sons, 3 edition, 2007.

[Taguchi 00] Mikio Taguchi, Kunihiro Kawamoto, Sadaji Tsuge, Toshiaki Baba, Hitoshi Sakata, Masashi Morizane, Kenji Uchihashi, Noboru Nakamura, Seiichi Kiyama & Osamu Oota. *HIT (TM) cells high-efficiency crystalline Si cells with novel structure.* Prog. Photovoltaics, vol. 8, no. 5, pages 503–513, 2000.

[Tanaka 92] M. Tanaka, M. Taguchi, T. Matsuyama, T. Sawada, S. Tsuda, S. Nakano, H. Hanafusa & Y. Kuwano. *Development of New a-Si/c-Si Heterojunction Solar Cells: ACJ-HIT (Artificially Constructed Junction-Heterojunction with Intrinsic Thin-Layer).* Jpn. J. Appl. Phys., vol. 31, pages 3518–22, 1992.

[Tardon 04] S. Tardon, M. Roesch, R. Brueggemann, T. Unold & G.H. Bauer. *Photoluminescence studies of a-Si:H/c-Si-heterojunction solar cells.* J. Non-Cryst. Sol., vol. 338-340, pages 444–447, 2004.

[Tejedor 78] C. Tejedor & F. Flores. *A simple approach to heterojunctions.* J. Phys. C Solid State, vol. 11, pages L19–23, 1978.

[Tersoff 84] J. Tersoff. *Theory of semiconductor heterojunctions: The role of quantum dipoles.* Phys. Rev. B, vol. 30, pages 4874–7, 1984.

[Thanailakis 75] A. Thanailakis. *Contacts between simple metals and atomically clean silicon.* J. Phys. C Solid State, vol. 8, page 655, 1975.

[Thanailakis 76] A. Thanailakis & A. Rasul. *Transition-metal contacts to atomically clean silicon.* J. Phys. C Solid State, vol. 9, page 337, 1976.

[Trupke 03] T. Trupke, M.A. Green, P. Wuerfel, P.P Altermatt, A. Wang, J. Zhao & R. Corkish. *Temperature dependence of the radiative recombination coefficient of intrinsic crystalline silicon.* J. Appl. Phys., vol. 94, pages 4930–4937, 2003.

[Trupke 04] T. Trupke, R.A. Bardos, F. Hudert, P. Wuerfel, J. Zhao, A. Wang & M.A. Green. *Effective excess carrier lifetimes exceeding 100 milliseconds in float zone silicon determined from photoluminescence.* In Proceedings of the 19th European Photovoltaic Solar Energy Conference, Paris, France, 2004.

[Tsu 73] R. Tsu & L. Esaki. *Tunneling in a finite superlattice.* Appl. Phys. Lett., vol. 22, page 562, 1973.

[Unold 00] T. Unold, M. Rösch & G. H. Bauer. *Defects and transport in a-Si:H/c-Si heterojunctions.* J. Non-Cryst. Sol., vol. 266-269, no. Part 2, pages 1033–1037, May 2000.

[Vaillant 86] F. Vaillant & D. Jousse. *Recombination at dangling bonds and steady-state photoconductivity in a-Si:H.* Phys. Rev. B, vol. 34, page 4088, 1986.

[van Sark 12] W.G.J.H.M. van Sark, F. Roca & L. Korte. Physics and technology of amorphous-crystalline heterostructure silicon solar cells. Springer, 2012.

[Varache 12a] R. Varache, W. Favre, L. Korte & J.P. Kleider. *Influence of the amorphous/crystalline silicon heterostructure properties on planar conductance measurements.* J. Non-Cryst. Sol., vol. 358, pages 2236–2240, 2012.

[Varache 12b] R. Varache, J.P. Kleider, W. Favre & L. Korte. *Band bending and determination of band offsets in amorphous/crystalline silicon heterostructures from planar conductance measurements.* J. Appl. Phys., vol. 112, page 123717, 2012.

[Varache 12c] R. Varache, J.P. Kleider, M.E. Gueunier-Farret & L. Korte. *Silicon heterojunction solar cells: optimization of emitter and contact properties from analytical calculation and numerical simulation.* Mater. Sci. Eng. B - Adv., vol. available online, 2012.

[Vasileska 96] D. Vasileska, P. Bordone, T. Eldridge & D.K. Ferry. Physica B, vol. 227, page 333, 1996.

[Vexler 01] M.I. Vexler, A.F. Shulekin, C. Dieker, V. Zaporojtschenko, H. Zimmermann, W. Jaeger, I.V. Grekhov & P. Seegebrecht. Solid State Electron., vol. 45, pages 19–25, 2001.

[Vexler 05] M.I. Vexler, S. E. Tyaginov & A. F. Shulekin. *Determination of the hole effective mass in thin silicon dioxide film by means of an analysis of*

characteristics of a MOS tunnel emitter transistor. J. Phys. - Condens. Mat., vol. 17, page 8057, 2005.

[Willemen 98] J. A Willemen. *Modelling of amorphous silicon single- and multi-junction solar cells.* PhD thesis, Technical University Delft, 1998.

[Wolf 12] S. De Wolf, C. Ballif & M. Kondo. *Kinetics of a-Si:H bulk defect and a-Si:H/c-Si interface-state reduction.* Phys. Rev. B, vol. 85, page 113302, 2012.

[Wronski 89] C. R. Wronski, S. Lee, M. Hicks & S. Kumar. *Internal photoemission of holes and the mobility gap of hydrogenated amorphous silicon.* Phys. Rev. Lett., vol. 63, pages 1420–3, 1989.

[Wronski 92] C.R. Wronski. J. Non-Cryst. Sol., vol. 141, page 16, 1992.

[Wuerfel 95] P. Wuerfel. Physik der solarzellen. 1995.

[Yang 93] K. Yang, J. R. East & G. I. Haddad. *Numerical modeling of abrupt heteojunctions using a thermionic-field emission boundary condition.* Solid State Electron., vol. 36, page 321, 1993.

[Zhao 08] L. Zhao, C. L. Zhou, H. L. Li, H. W. Diao & W. J. Wang. *Role of the work function of transparent conductive oxide on the performance of amorphous/crystalline silicon heterojunction solar cells studied by computer simulation.* Phys. status solidi A, vol. 205, no. 5, pages 1215–21, 2008.

Acknowledgements

A PhD thesis is the result of the interaction between the supervised candidate and his supervisors. Therefore, I would like to thank the people present around me to carry out the scientific research. On the French side, I thank Dr. Jean-Paul Kleider for having welcomed me in his research group at LGEP. In particular, very fundamental discussions on the physical aspects of my work were extremely stimulating and satisfied my wish to think about the details of solar cells functioning. He was always very helpful for administrative questions. My acknowledgements also go to Marie-Estelle Gueunier-Farret who co-supervised my work, and who gave me her support for questions dealing with tunneling and simulations. On the German side, I would like first to acknowledge Prof. Bernd Rech for receiving me at the Silizium-Photovoltaik department at HZB, first as a master student and then as a PhD student. I am very grateful to Lars Korte for supervising me and for having oriented my work. His experience on French-German relationships was often of great help. I thank these people also for helping organizing the co-supervised PhD program and for the detailed proof-reading of the manuscript.

Thanks to Dr. Ivan Gordon, Dr. Stefaan de Wolf, Prof. Bernd Szyszka and Prof. Frédéric Aniel for judging my work.

Many thanks to all the colleagues, in France and Germany, who brought a significant contribution to this work: Wilfried Favre for his introduction to most of characterization techniques, Caspar Leendertz for very helpful discussions on theory and simulations, Robert Rössler for his insights on TCOs and contact properties, Djicknoum Diouf for his help with AFORS-HET, Orman Gref for guiding me at HZB during the first months, and many others. The support of engineers and technicians is priceless in scientific research. Therefore I am extremely grateful towards Ehrad Conrad for *a*-Si:H layers deposition, Kerstin Jacob and Anja Scheue for chemical treatments, Aurore Brézard for her assistance with experiments, Tobias Haenel for spectral response measurements, and all the people who punctually helped me in my projects: Tim Schulze, Nicola Mingirulli, Maurizio Roczen, Amaru Toefflinger, ... More generally, many thanks to all my colleagues in both institutes for the nice atmosphere at work: Vanessa, Boris, Stefanie, Veit, Jennifer, Irène, etc.
My thoughts also go to Dr. Hab. Manfred Schmidt from who I gained a lot in the understanding of amorphous silicon in solar cells. Dr. Heike Angermann kindly shared her experience on chemical treatments of silicon wafers, and Dr. Christophe Longeaud was always willing to share his outstanding knowledge on amorphous silicon.
Several partners contributed to the realisation of several projetcs: I am obliged in particular towards Dr. Pere Roca i Cabarrocas (LPICM - École Polytechnique), Prof. Nazir H. Kherani, Basia Halliop and Pratish Mahtani (University of Toronto, Canada), and Delfina Muñoz and Silvia Martin de Nicolas (INES - CEA).

This joint PhD program who have not been possible without the help of the administrative

team at LGEP, Marion Krusche at HZB and Jana Peich at TUB, who helped me during all these years to accommodate to the German administration.

This is not all about scientific research: these three years have been the opportunity for me to discover Germany, or more precisely Berlin, and I thank all my friends and flatmates who made my stays in Berlin such an enjoyable time: Achim, Manuel, Aline, Charlotte, John, Anca, Jenna and many others. At this point, the patience of everyone (at work and in social life) regarding my constently improving skills in German must be underlined. My thoughts also to my old friends Pierre, Louis, Moty, Adeline, Tatave, Fabien, Mathieu, Thomas (who has a responsibility in my orientation!), who follow me since a lot of years.

Enfin, ces quelques lignes ne pourront pas décrire combien je remercie ma famille, et en particulier mes parents, pour m'avoir inculqué les qualités nécessaires à ce parcours, et pour m'avoir soutenu, dans tous les sens du terme, pendant ces longues années d'étude.
Und natürlich, danke an Paula, für die unfehlbare Geduld.

Publications of the author

Peer-reviewed articles

R1: R. Varache, J. P. Kleider, W. Favre and L. Korte, *Band bending and determination of band offsets in amorphous/crystalline silicon heterostructures from planar conductance measurements*, J. Appl. Phys., vol. 112, issue 12, pages 123717-1 (2012)

R2: R. Varache, J.P. Kleider, M.E. Gueunier-Farret and L. Korte, *Silicon heterojunction solar cells: optimization of emitter and contact properties from analytical calculation and numerical simulation*, Mater. Sci. Eng. B - Adv., available online (2012)

R3: R. Varache, W. Favre, L. Korte and J.P. Kleider, *Influence of the amorphous/crystalline silicon heterostructure properties on planar conductance measurements*, J. of Non-Cryst. Sol., vol. 358, pages 2236-2240 (2012)

R4: B. Halliop, M.F. Salaun, W. Favre, R. Varache, M.E. Gueunier-Farret, J.P. Kleider and N.P. Kherani, *Interface properties of amorphous-crystalline silicon heterojunctions prepared using DC saddle-field PECVD*, J. of Non-Cryst. Sol., vol. 358, pages 2227-2231 (2012)

Conference proceeding papers

P1: R. Varache, H. Angermann, L. Korte, M.E. Gueunier-farret and J.P. Kleider, *Controlled interfacial native oxide for amorphous silicon/crystalline silicon heterojunction solar cells*, Proc. 26th EU-PVSEC, Frankfurt, Germany (2012)

P2: R. Varache, B. Halliop, W. Favre, N. Kherani and J.P. Kleider, *Influence of the undoped amorphous silicon passivation layer on a-Si:H/c-Si heterojunction from planar conductance and modulated photoluminescence measurements*, Proc. 26th EU-PVSEC, Frankfurt, Germany, (2012)

P3: H. Angermann, K. Wolke, A. Laades, U. Stürzebecher, J. Kegel, R. Varache, O. Gref, C. Gottschalk and B. Stegemann, *Conditioning of textured Si solar cell substrates by wet-chemical oxides: evaluation by Surface Photovoltage (SPV) measurements*, Proc. 26th EU-PVSEC, Frankfurt, Germany (2012)

Conference presentations

P1: 26th European photovoltaic solar energy conference (EU-PVSEC), Frankfurt, Germany, Poster presentation (2012)

P2: 26th European photovoltaic solar energy conference (EU-PVSEC), Frankfurt, Germany,

Poster presentation (2012)

R2: European Material research society Spring meeting 2012 (E-MRS), Strasbourg, France, Poster presentation (2012)

R3: 24th International conference on amorphous and nanocrystalline semiconductors (ICANS), Nara, Japan, Oral presentation (2011)

R4: 24th International conference on amorphous and nanocrystalline semiconductors (ICANS), Nara, Japan, Poster presentation (2011)

Curriculum vitæ

Education

2006-2009: Graduated from University Paris-Sud 11 - Magister of Fundamental Physics - distinction: "very good"; rank: 1rst

- 2008-2009 : MSc (2nd year) in Solid State Physics at Joseph Fourier University (Grenoble, France)
- 2007-2008 : First year of Master of Science at University of Edinburgh, Scotland, as an exchange student
- 2006-2007 : Bachelor of Science in Fundamental Physics at University Paris 11

2004-2006: Preparation for national competitive entrance exams to leading French "grandes écoles", specializing in mathematics and physics (Lycée Blaise Pascal, Clermont-Ferrand, France)

2004: Scientific Baccalauréat

Professional experience

October 2009: Phd as a joint program between the Laboratoire de Génie Electrique de Paris (Unviersity Paris-Sud 11; Pr. Jean-Paul Kleider) and the Helmholtz Zentrum Berlin (Technical University Berlin; Pr. Bernd Rech, Dr. Lars Korte): Development, characterization and modeling of interfaces for high efficiency silicon heterojunction solar cells

April-June 2009: Master thesis at Helmholtz Zentrum Berlin: Development and characterization of ultra-thin silicon germanium layers for photovoltaic applications

2007-2008: Trainee at Centre for Science at Extreme Conditions, Edinburgh, Scotland: Study of materials under high pressure and high temperature using diamond anvil cells

May-June 2007: Trainee at Laboratory for Science of Materials for Electronics (LASMEA, Clermont-Ferrand, France): Exciton-carrier scattering in 2D semiconductor quantum wells